

# QUANTIFIABLE BREAST CANCER CELL CHARACTERISTICS AND THEIR LINK TO THE METASTATIC CASCADE

by

KYNDRA S. HIGGINS

(Under the Direction of Cheryl T. Gomillion)

## ABSTRACT

Early detection of breast cancer is associated with a high survival rate of 99%; however, this rate decreases significantly (32%) once the cancer has metastasized. Unfortunately, current methods for detecting metastatic breast cancer are limited, and metastasis will not be identified until after the disease has spread. To enhance diagnostic capabilities, a deeper understanding of the biological mechanisms driving metastasis is urgently needed. One hallmark of metastasis is the epithelial-to-mesenchymal transition, during which cancer cells shift from an epithelial phenotype, characterized by a cuboidal shape and strong adhesion to the basement membrane, to a more elongated, mesenchymal phenotype. This transition in the cells reflects a tradeoff between cellular proliferation and invasiveness. While two-dimensional cell morphology (i.e. cell shape) has been identified as a quantifiable indicator of cell function, debate remains on which cellular structures are key to migration and invasion from the primary tumor. In this study, eight mammary cell lines, including five triple-negative breast cancer lines, a particularly aggressive subtype, were analyzed to produce a comprehensive profile of cancer cell behavior. Morphological

features were compared with dynamic cellular activities like proliferation, migration, and cell-to-cell connectivity.

This work employs a quantitative approach, using an impedance-based assay for real-time analysis of proliferation and migration, offering improvements over traditional methods. High-throughput imaging and computational analysis were used to extract and quantify morphological features of the cells and their nuclei. The analysis revealed a diverse spectrum of morphological traits and aggressive behaviors across all cell lines. Overall, cell morphology was linked to behaviors such as migration, although the relationship was more complex and abstract than previously hypothesized. The findings from this work offer new insights into the cellular traits that influence breast cancer metastasis and establish a scalable framework for evaluating cancer cell behavior. By integrating detailed morphological and biophysical profiling with minimal sample input, this study contributes to the development of more efficient and clinically applicable investigative tools.

INDEX WORDS: Breast Cancer Metastasis, Epithelial-to-Mesenchymal Transition,  
Morphology, Bioelectronic Assay, Electric Cell-substrate  
Impedance Sensing

QUANTIFIABLE BREAST CANCER CELL CHARACTERISTICS AND THEIR  
LINK TO THE METASTATIC CASCADE

by

KYNDRA S. HIGGINS

B.S., University of Georgia, 2020

A Dissertation Submitted to the Graduate Faculty of The University of Georgia in Partial  
Fulfillment of the Requirements for the Degree

DOCTOR OF PHILOSOPHY

ATHENS, GEORGIA

2025

© 2025

Kyndra S. Higgins

All Rights Reserved

QUANTIFIABLE BREAST CANCER CELL CHARACTERISTICS AND THEIR  
LINK TO THE METASTATIC CASCADE

by

KYNDRA S. HIGGINS

Major Professor:	Cheryl T. Gomillion
Committee:	Karen J.L. Burg
	Melissa Davis
	Melissa Hallow
	William Kisaalita
	Ross Marklein

Electronic Version Approved:

Ron Walcott  
Vice Provost for Graduate Education and Dean of the Graduate School  
The University of Georgia  
August 2025

## DEDICATION

I would like to dedicate this to everyone who has supported me and helped carry me through this journey. Your love, encouragement, and kindness have meant more than you know.

## ACKNOWLEDGEMENTS

I would like to thank all of my committee members for your valuable guidance and support throughout this project. I know how busy you all are, and I deeply appreciate the time and expertise each of you contributed. Your diverse backgrounds and perspectives truly enriched this work.

Thank you to Dr. Marklein and Kanupriya Daga from the Marklein lab for your assistance with cell staining, imaging, and CellProfiler protocols. Your help was essential to the success of this research.

I want to especially thank Dr. Gomillion for being an incredible mentor and a wonderful person to work with. I would not be where I am today without your constant support. You've helped me grow from a hesitant undergraduate into a confident graduate student—and now, a doctor. I know I'm not alone in saying that working in your lab has been an incredible experience. I feel lucky to have spent the last six years (wow, is that a new record?) under your guidance.

To my lab members, past and present—thank you for your support, friendship, and insight. Whether I needed help troubleshooting an experiment or just a kind word after a hard day, you've always been there. I'm truly grateful to be part of such a caring and collaborative group. Damion, forever my lab manager, your mentorship and willingness to lend a hand (even during late-night experiments) has meant so much to me. I've learned so much from you.

Finally, to my friends, family, and my partner, Evan—thank you for always being there. Whether feeding me, spending time with me, or simply holding my hand through the chaos, your love and support have been everything. I'm endlessly grateful to have you in my life.

## TABLE OF CONTENTS

	Page
ACKNOWLEDGEMENTS .....	v
LIST OF TABLES .....	ix
LIST OF FIGURES .....	x
 CHAPTER	
1 INTRODUCTION AND STUDY OVERVIEW .....	1
1.1 Introduction.....	1
1.2 Study Overview .....	6
1.3 References .....	9
2 IN VITRO MODELS OF BREAST CANCER: CURRENT CHALLENGES AND FUTURE PROSPECTS TOWARDS RECAPITULATING THE MICROENVIRONMENT AND MIMICKING KEY PROCESSES.....	11
2.1 Abstract .....	12
2.2 Introduction.....	13
2.3 Processes and Characteristics Influencing Cancer Progression.....	14
2.4 In Vitro Modeling of Breast Cancer .....	29
2.5 Future Outlook .....	52
2.6 Conclusion .....	56
2.7 References .....	58
3 DEVELOPMENT AND VALIDATION OF AN IMPEDANCE-BASED ASSAY FOR BREAST CANCER CELL CHARACTERIZATION.....	72



3.1	Abstract .....	73
3.2	Background .....	75
3.3	Materials and Methods.....	79
3.4	Results.....	84
3.5	Discussion .....	90
3.6	Conclusion .....	96
3.7	References .....	97
4	ELECTRICAL IMPEDANCE AS A BIOMARKER FOR BREAST CANCER CELL TYPE DISCRIMINATION .....	102
4.1	Abstract .....	103
4.2	Introduction.....	104
4.3	Materials and Methods.....	106
4.4	Results.....	110
4.5	Discussion .....	118
4.6	Conclusion .....	120
4.7	References .....	121
5	TWO-DIMENSIONAL SINGLE CELL MORPHOLOGY AS AN INDICATOR OF BREAST CANCER AGGRESSIVENESS .....	125
5.1	Abstract .....	126
5.2	Introduction.....	127
5.3	Materials and Methods.....	129
5.4	Results.....	133
5.5	Discussion .....	143

5.6 Conclusion .....	147
5.7 References .....	149
6 DERIVATION AND ASSESSMENT OF DISTINCT MORPHOLOGICAL SUBTYPES WITHIN THE AGGRESSIVE MDA-MB-231 BREAST CANCER CELL LINE .....	153
6.1 Abstract .....	154
6.2 Introduction .....	156
6.3 Materials and Methods .....	157
6.4 Results .....	162
6.5 Discussion .....	169
6.6 Conclusion .....	173
6.7 References .....	174
7 CONCLUDING REMARKS AND RECOMMENDATIONS FOR FUTURE WORK. 177	
7.1 Concluding Remarks .....	177
7.2 Recommendations for Future Work .....	182
7.3 References .....	187
APPENDICES	
A SUPPLEMENTARY MATERIALS FOR CHAPTER 3 .....	189
B SUPPLEMENTARY MATERIALS FOR CHAPTER 4 .....	192
C SUPPLEMENTARY MATERIALS FOR CHAPTER 5 .....	194
D SUPPLEMENTARY MATERIALS FOR CHAPTER 6 .....	196
E SUPPLEMENTARY MATERIALS FOR CHAPTER 7 .....	199

## LIST OF TABLES

	Page
Table 2.1: Effects of genetic variants on the tumors and surrounding tissue .....	18
Table 2.2: Review of literature on prominent bioprinted breast cancer metastasis models .....	47
Table 2.3: Review of literature on prominent breast cancer microfluidic models.....	51
Table 4.1: Mammary cell line information .....	107

## LIST OF FIGURES

	Page
Figure 1.1: Summary of research aims and methods .....	7
Figure 2.1: Breast cancer metastasis .....	15
Figure 2.2: Breast cancer subtypes .....	17
Figure 2.3: Four different morphologies of breast cancer cells .....	22
Figure 2.4: The epithelial-to-mesenchymal transition .....	23
Figure 2.5: Schematic diagram of the mature mammary gland anatomy .....	25
Figure 2.6: Schematic comparing normal mammary extracellular matrix to breast tumor extracellular matrix .....	26
Figure 2.7: Examples of migration assay methods .....	31
Figure 2.8: Spheroid assembling techniques and characteristics.....	38
Figure 2.9: Acoustofluidic spheroid assembly.....	39
Figure 2.10: Schematic showing examples of three-dimensional bioprinters .....	41
Figure 2.11: Bioprinting with decellularized tissue extracellular matrix .....	46
Figure 2.12: Dual lumen rods to study tumor cell interaction with lymphatic vessel .....	50
Figure 2.13: Advantages and limitations of 3D in vitro modeling methods.....	54
Figure 3.1: Cell impedance concepts .....	79
Figure 3.2: Schematic of the experimental flow .....	82
Figure 3.3: Imaging and impedance monitoring of breast cancer cell dynamics .....	86
Figure 3.4: Wound closure over 36 hours.....	87

Figure 3.5: Impedance and barrier integrity across the full experimental timeline .....	88
Figure 3.6: Cell spread is more pronounced in elongated breast cancer cell lines .....	89
Figure 3.7: Breast cancer cell monolayer barrier integrity .....	90
Figure 4.1: Epithelial-mesenchymal characterization of breast cancer cell lines .....	111
Figure 4.2: Representative images of mammary cell lines with impedance and transepithelial electrical resistance values after 36 hours of proliferation .....	114
Figure 4.3: Rate of migration and impedance measurements during wound healing assay .....	116
Figure 4.4: Impedance and transepithelial electrical resistance compared to the rate of wound closure .....	117
Figure 5.1: Representative images of stained mammary cell lines .....	134
Figure 5.2: Mammary morphology features .....	135
Figure 5.3: Principal component analysis (PCA) of cell and nuclear morphology across mammary cell lines .....	137
Figure 5.4: Features driving separation between epithelial-to-mesenchymal transition (EMT) and normal states .....	139
Figure 5.5: A potential link between migration and cell morphology .....	141
Figure 5.6: Heatmap of the first 10 principal components derived from average cell morphology data across 8 mammary cell lines .....	142
Figure 6.1: Clonal colony expansion .....	163
Figure 6.2: Clonal colony characterization using CellProfiler .....	164
Figure 6.3: Principal component analysis (PCA) of morphological features in MDA-MB-231 clonal colonies .....	166
Figure 6.4: Morphology-based grouping of clonal colonies via k-means clustering .....	167

Figure 6.5: Functional differences among clonal colonies in proliferation, barrier integrity, and migration .....	169
Figure 7.1: Breast cancer cells disrupt endothelial barrier integrity .....	184

## CHAPTER 1

### INTRODUCTION AND STUDY OVERVIEW

#### 1.1 Introduction

##### 1.1.1 Breast Cancer and the Metastatic Cascade

Breast cancer is the most lethal cancer in women worldwide <sup>1</sup>, with roughly 1 in 8 U.S. women diagnosed within their lifetime. When detected early, the rate of breast cancer survival is very high (99%), however that rate decreases significantly (30%) once the cancer has metastasized to other parts of the body, such as the brain, lungs, bone, and liver <sup>2</sup>. Thus, there is still a great need to study breast cancer pathophysiology to better predict and prevent breast cancer metastasis.

Currently, breast cancer aggressiveness is determined by a variety of factors, like tumor size, receptor status, proportion of proliferating cancer cells (Ki67 index), and family history. There have been significant strides towards the identification and detection of metastatic breast cancer through investigation of genomic, proteomic, and metabolomic profiling of samples to identify potential biomarkers for breast cancer metastasis correlated to clinical data. Advances in these methods, combined with earlier and more frequent screening, have contributed to a steady increase in breast cancer survival over the last three decades <sup>2</sup>. However, effective methods to detect metastatic breast cancer are still limited and ultimately detection will not occur until after the cancer has already spread, resulting in crucial time lost towards treatment. To improve diagnostic capabilities and ultimately patient outcomes, a deeper understanding of the underlying mechanisms that drive the metastatic process is urgently needed. Specifically, in this work multiple factors are explored, including *in vitro* cell migration, the transition of cells from epithelial to mesenchymal phenotype, and cell morphology.

### 1.1.2 Two-Dimensional (2D) Migration as an Indicator for Metastasis

Once cancer cells have implanted at their primary location and a tumor is formed, the first step of metastasis begins with local invasion of the basement membrane and cell migration out from the tumor. To migrate into surrounding tissue, breast cancer cells must turn over their focal adhesions (FAs); thus, migration speed depends on the strength of attachment. Invasive cancer cells have more dynamic FAs than their noninvasive counterparts<sup>3</sup>, and decreased adhesion strength corresponds to increased metastatic potential<sup>4</sup>. Therefore, 2D migration could be a suitable metric for measuring cancer cell aggressiveness.

A wound closure assay, also known as a wound healing assay or scratch assay, is a common *in vitro* approach used to study cancer metastasis. In this method, cancer cells are seeded at the bottom of a well plate and grown to confluence. Once confluent, a physical scratch is made through the cell layer, removing cells that were once present in the line of the pipette scratch. Over a set time, the remaining cancer cells may migrate towards each other to close the gap (“heal” the wound). The distance traveled by the cancer cells and the time it takes to close the gap are indicators of a cancer cell’s migratory potential and can be used to determine metastatic potential.

While wound healing assays are a common and effective tool in evaluating breast cancer cell migration, they often involve data collection via imaging over set time points or video recording. These methods often rely on image processing software to generate quantitative data, which can be labor-intensive and imprecise. To better study the factors influencing cancer metastasis, there exists a significant need for a more modern, quantitative approach to measuring cell migration, which will yield earlier, more reliable and time-efficient identification of metastatic cells. Impedance-based wound healing assays address these challenges by providing a more



streamlined, real-time measurement of wound closure, offering an improvement over traditional image-based protocols for assessing migratory and metastatic potential of cancer cells.

### 1.1.3 Electric Cell-substrate Impedance Sensing (ECIS)

Bioelectronic cell impedance assays, also called ECIS analyses, are quickly gaining popularity as a label-free, non-invasive, and non-terminal way to continuously observe cell behavior. In ECIS, a small alternating current ( $I$ ) is applied across an electrode configuration at the bottom of a tissue culture surface. This results in a potential ( $V$ ) across the electrodes, which is measured by the ECIS instrument. The impedance ( $Z$ ) is then determined by Ohm's law, where  $Z = V/I$ <sup>5</sup>.

Cells are added to the electrode-fitted culture surface, often with the aid of a coating substrate, like poly-lysine, to enhance cell adhesion. Once attached, cells act as insulators, increasing the impedance. As cells grow and spread across the electrodes, they further impede current flow, allowing a variety of cell characteristics to be measured. When cell function changes as a response to the environment (e.g. growth factors, cytokines, hypoxia, cytotoxic agents), so does the impedance. At a higher alternating current (AC) frequency, the current predominantly flows through transcellular pathways, measuring characteristics directly relating to the cells, like cell coverage and morphology. At lower AC frequencies, the current flows via paracellular pathways. This evaluates cell barrier integrity, a particularly useful metric in cancer studies where migration and invasion leads to a degradation of tight junctions between cancer cells and within the endothelium of blood and lymph vessels<sup>6-8</sup>.

Several ECIS systems are commercially available from companies like Applied BioPhysics and Axion Biosystems. While many researchers build custom systems<sup>9-12</sup>, these often lack cross-

comparability. Therefore, this work was done using the Maestro Z (Axion Biosystems), which features a 96-well plate format with an electrode embedded in the culture surface of each well. ECIS assay techniques have predominantly been used with breast cancer cells to quantify drug interactions<sup>11,13-15</sup>, however an ECIS study that can evaluate multiple breast cancer cell behaviors concurrently has great diagnostic potential, and is, therefore, explored in this work.

#### 1.1.4 Epithelial-to-Mesenchymal Transition

In the tumor microenvironment, metastasis is influenced by physical cues, such as proteins present in the extracellular matrix (ECM). The diverse set of proteins, polysaccharides and glycoproteins in the ECM drives invasion and migration to secondary sites. A cancer cell's increase in invasiveness is often associated with a transition from an epithelial-like phenotype, characterized by a cuboidal shape and strong adhesion to the basement membrane ECM, to a more elongated, mesenchymal-like phenotype. This process, referred to as the epithelial-to-mesenchymal transition (EMT), involves a tradeoff between cellular proliferation and invasiveness. EMT is regulated at the epigenetic level, where markers like E-cadherin, desmoplakin, and keratin are associated with an epithelial-like state and N-cadherin, vimentin, and fibronectin are associated with a mesenchymal-like state<sup>16</sup>. Additionally, cells switch from having more cell-cell adhesion in an epithelial state, to predominantly cell-matrix adhesion in a mesenchymal state.

Although EMT is often conceptualized as a binary switch, where cancer cells are either completely epithelial or mesenchymal in phenotype, most cancer cells rarely achieve a fully mesenchymal phenotype, characterized by expression of markers like alpha-smooth muscle actin ( $\alpha$ -SMA) and fibroblast-specific protein 1 (Fsp-1)<sup>16,17</sup>. EMT is one of the most critical processes

in tumor progression, linking cancer cell morphology to tumor phenotype, gene expression, and metastatic behavior.

#### 1.1.5 Cell Morphology

Cell shape has long been proposed as a mediating factor in cell migration abilities<sup>18,19</sup> and is an easily quantifiable readout of the molecular underpinnings influencing cancer progression. Breast cancer cell shape can predict ECM three-dimensional (3D) invasion, while morphological heterogeneity can indicate tumor cell plasticity and malignant progression<sup>16,20</sup>. A majority of breast cancer originates from epithelial cells, which in non-malignant tissue are organized, maintain tissue polarity, and eventually halt proliferation. In contrast, malignant cells lose polarity, adopt a disorganized architecture, and exhibit uncontrolled growth.

Cells with an epithelial-like morphology are more differentiated, and have tight cell-to-cell junctions, leading to a lower proclivity for migration. Meanwhile, mesenchymal-like cells overexpress genes associated with tumor aggressiveness and invasiveness, display a high mitotic count, and have less tight-junctions than cells with an epithelial-like morphology<sup>21</sup>. Luminal breast cancer cells, which are hormone receptor positive, tend to display an epithelial-like morphology, whereas triple-negative breast cancer cells are more often mesenchymal-like<sup>22</sup>. Nonetheless, significant heterogeneity exists within these subtypes and a deeper look into this variability is necessary as breast cancer cell morphology grows as a means of evaluating cell behavior and cancer progression. For example, Hapach et. al. separated two subpopulations within the commonly used MDA-MB-231 triple-negative breast cancer cell line and found that, in an *in vivo* mouse model, each subpopulation exploits different pathways to metastasize, respective to their

epithelial/mesenchymal phenotype <sup>23</sup>. These findings underscore the importance of studying morphology at the single-cell level to better understand metastasis.

Cell shape is an easily visualized feature that often reflects overall cellular function more holistically than monitoring specific molecular outputs. Single-cell measurements are particularly influential as they may better correlate key behaviors like migration and metabolic activity, both of which can vary widely even within the same cell population. Overall, examining breast cancer cell morphology provides critical insights into the biological mechanisms driving tumor progression and metastatic potential, offering a valuable lens through which to better predict, monitor, and ultimately target aggressive cancer behaviors.

## **1.2 Study Overview**

### **1.2.1 Objective and Hypothesis**

The overall objective of this research is to validate single-cell morphology as a readout associated with cancer aggressiveness and metastatic potential. To support this work, a novel bioelectronic impedance-based assay system will first be implemented to study cell behaviors (e.g. proliferation, motility, barrier function, etc.) and to record quantitative metrics for distinct cell profiling. Subsequently, these quantitative impedance-based metrics will be linked to single-cell morphological features, towards understanding the relationship between these metrics and cell function. The motivation for exploring morphology as a metastasis predictor stems from the inaccuracy that current methods have in predicting metastasis and the need for a more encompassing approach of defining cell migration behavior. Using a combination of impedance spectroscopy and fluorescent image analysis, the studies in this dissertation are designed to test the hypothesis that cell morphology can be used as a metric for predicting cell migratory potential

and that specific morphological subtypes within the most aggressive breast cancer cell lines contribute to their aggressiveness.

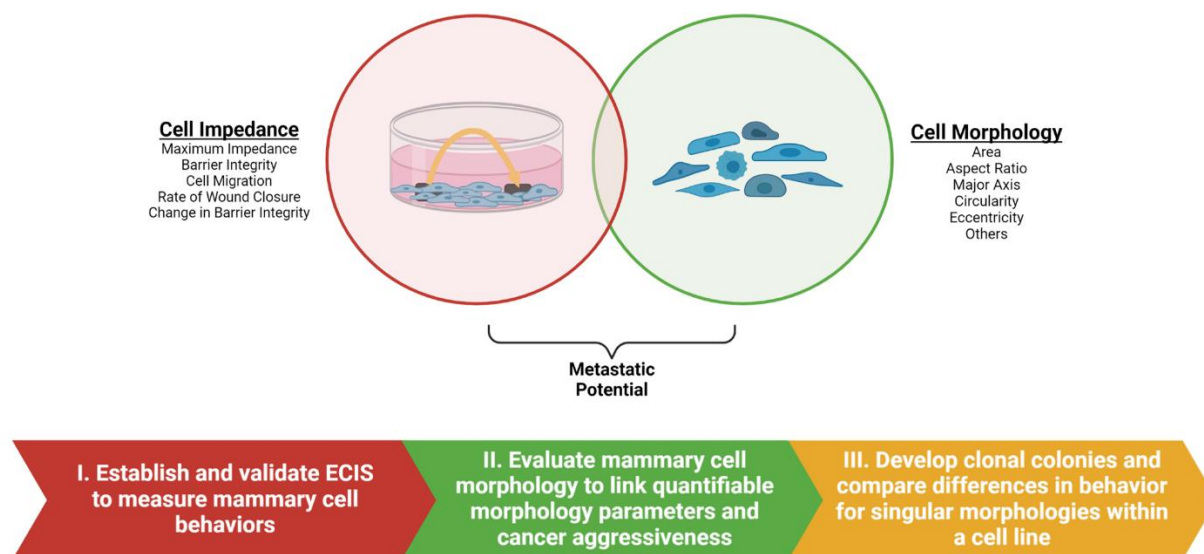


**Figure 1.1:** Summary of research aims and methods. This dissertation investigates how cell morphology relates to dynamic behaviors associated with cancer aggressiveness. Using electric cell-substrate impedance sensing (ECIS), cell behaviors such as proliferation, migration, and barrier integrity were quantitatively measured. These impedance-based readouts were then correlated with single-cell morphology features to identify characteristics influencing metastatic potential. The study is organized around three main aims: (I) Establish an ECIS assay to characterize mammary cell behaviors; (II) Quantitatively analyze single-cell morphology and correlate these metrics with cancer-relevant behaviors; (III) Generate clonal populations from the aggressive MDA-MB-231 cell line to assess behavioral and morphological heterogeneity within a single genetic background.

### 1.2.2 Chapter Organization

The chapters in this dissertation are organized to present a progressive approach to studying breast cancer morphology and its link to metastasis. Chapter 2 is a literature review, under review for publication in *Advanced Biology*, that discusses current challenges in breast cancer modeling, highlights the need for more quantitative and reproducible systems, and introduces the promise of bioelectronic platforms for studying breast cancer behaviors. Chapter 3 describes the development

of an impedance-based migration assay for the bioelectronic analysis of breast cancer behaviors. This initial study, submitted to *Journal of Biological Engineering*, validates the feasibility and sensitivity of using Electric Cell-Substrate Impedance Sensing (ECIS) to quantify key cell behaviors, including proliferation, migration, and cell-cell barrier function, through an in-depth analysis of mammary cell behavior using small cell populations. Chapter 4 builds on this work by applying the bioelectronic assay to six breast cancer cell lines and two non-cancerous mammary cell lines. This study, to be submitted to *Lab On A Chip*, characterizes the growth and migratory behaviors of these lines and proposes that high-frequency impedance and Trans-Epithelial/Endothelial Electrical Resistance (TEER) measurements can serve as indicators of cellular aggressiveness. Chapter 5 shifts to high-throughput image analysis to quantify cell shape and other key morphological features, exploring their relationship to cancer aggressiveness. This chapter identifies the morphology features that most significantly correlate with epithelial-to-mesenchymal transition (EMT) and cellular normalcy and will be submitted to *Computers in Biology and Medicine*. Chapter 6 focuses on cellular heterogeneity by generating clonal colonies from a single aggressive breast cancer cell line. This work links variations in cell morphology among colonies to differences in their migratory behaviors, providing another layer of insight into morphology's connection to cancer aggressiveness. Chapter 6 is being prepared for submittal to *Biotechnology and Bioengineering*. Finally, Chapter 7 presents concluding remarks and offers future directions to extend the findings of this comprehensive study. Together, these chapters present a detailed overview of current breast cancer modeling strategies and propose an innovative framework for quantifying and understanding metastatic behavior.

### 1.3 References

1. Sung, H., *et al.* Global cancer statistics 2020: GLOBOCAN estimates of incidence and mortality worldwide for 36 cancers in 185 countries. **71**, 209-249 (2021).
2. Siegel, R.L., Miller, K.D., Wagle, N.S. & Jemal, A.J.C.C.J.C. Cancer statistics, 2023. **73**, 17-48 (2023).
3. Bijian, K., *et al.* Targeting focal adhesion turnover in invasive breast cancer cells by the purine derivative reversine. **109**, 2810-2818 (2013).
4. Indra, I., *et al.* An in vitro correlation of mechanical forces and metastatic capacity. **8**, 015015 (2011).
5. Hedayatipour, A., Aslanzadeh, S., McFarlane, N.J.B. & Bioelectronics. CMOS based whole cell impedance sensing: Challenges and future outlook. **143**, 111600 (2019).
6. Ma, X., *et al.* Claudin-4 controls the proliferation, apoptosis, migration and in vivo growth of MCF-7 breast cancer cells. **34**, 681-690 (2015).
7. Wu, J., *et al.* RBM38 is involved in TGF- $\beta$ -induced epithelial-to-mesenchymal transition by stabilising zonula occludens-1 mRNA in breast cancer. **117**, 675-684 (2017).
8. Kim, T., *et al.* Down-regulation of claudin-2 in breast carcinomas is associated with advanced disease. **53**, 48-55 (2008).
9. Pan, Y., *et al.* 3D microgroove electrical impedance sensing to examine 3D cell cultures for antineoplastic drug assessment. **6**, 1-10 (2020).
10. Hedayatipour, A., *et al.* A wearable CMOS impedance to frequency sensing system for non-invasive impedance measurements. **14**, 1108-1121 (2020).
11. Nguyen, A., Yoshida, M., Goodarzi, H. & Tavazoie, S.F.J.N.c. Highly variable cancer subpopulations that exhibit enhanced transcriptome variability and metastatic fitness. **7**, 11246 (2016).
12. Tran, T.B., Baek, C. & Min, J.J.P.o. Electric cell-substrate impedance sensing (ECIS) with microelectrode arrays for investigation of cancer cell–fibroblasts interaction. **11**, e0153813 (2016).
13. Liu, Q., *et al.* Impedance studies of bio-behavior and chemosensitivity of cancer cells by micro-electrode arrays. **24**, 1305-1310 (2009).
14. Crowell, L.L., Yakisich, J.S., Aufderheide, B. & Adams, T.N.J.M. Electrical impedance spectroscopy for monitoring chemoresistance of cancer cells. **11**, 832 (2020).

15. Yang, Y., *et al.* Monitoring the heterogeneity in single cell responses to drugs using electrochemical impedance and electrochemical noise. **12**, 2558-2566 (2021).
16. Weinberg, R.A. *The biology of cancer*, (Garland science, 2013).
17. Lambert, A.W., Pattabiraman, D.R. & Weinberg, R.A.J.C. Emerging biological principles of metastasis. **168**, 670-691 (2017).
18. Keren, K., *et al.* Mechanism of shape determination in motile cells. **453**, 475-480 (2008).
19. Lee, J., Ishihara, A., Theriot, J.A. & Jacobson, K.J.N. Principles of locomotion for simple-shaped cells. **362**, 167-171 (1993).
20. Baskaran, J.P., *et al.* Cell shape, and not 2D migration, predicts extracellular matrix-driven 3D cell invasion in breast cancer. **4**, 026105 (2020).
21. Lehmann, B.D., *et al.* Identification of human triple-negative breast cancer subtypes and preclinical models for selection of targeted therapies. **121**, 2750-2767 (2011).
22. Geoffroy, M., *et al.* Pro-apoptotic effect of  $\Delta 2$ -TGZ in “claudin-1-low” triple-negative breast cancer cells: involvement of claudin-1. **165**, 517-527 (2017).
23. Hapach, L.A., *et al.* Phenotypic heterogeneity and metastasis of breast cancer cells. **81**, 3649-3663 (2021).



## CHAPTER 2

# IN VITRO MODELS OF BREAST CANCER: CURRENT CHALLENGES AND FUTURE PROSPECTS TOWARDS RECAPITULATING THE MICROENVIRONMENT AND MIMICKING KEY PROCESSES

---

Higgins, K. S., Yu, A.J., and Gomillion, C. T. Submitted to *Advanced Biology*.

## 2.1 Abstract

Each year, approximately 1.6 million women are diagnosed with breast cancer worldwide<sup>1</sup>. Of these cases, 0.5 million cases result in death with over 90% of these deaths resulting from metastasis. Since it is one of the top 5 cancers with the highest mortality rates, the development of breast cancer models that are physiologically relevant to the human body is severely needed. This includes models of the breast tissue microenvironment, the microenvironment of metastatic sites (e.g. brain, lungs, bone, liver), and models specifically mimicking each individual step of the cancer metastatic cascade. This review focuses on models of the primary tumor environment for studying cell invasion and spread within the mammary tissue, prior to metastatic outgrowth. Using a combination of methods such as migrations assays, tumor spheroids, three-dimensional (3D) printed biomaterials, and microfluidic designs, a variety of *in vitro* modeling methods exist to recapitulate specific aspects of the tumor microenvironment and understand sources of tumor heterogeneity. An effective model can be specified to each patient, eliminating the need for human trials. Subsequently, as the mechanisms involved in breast cancer metastasis are studied utilizing more effective *in vitro* models, targeted therapeutics can be discovered, thus advancing clinical treatment strategies.

## 2.2 Introduction

Breast cancer is the second most lethal cancer for women in the U.S., with 1 in 8 women diagnosed within their lifetime. When caught early, the rate of breast cancer survival is very high (99%), however that rate drops significantly (27%) once the cancer has metastasized to other parts of the body, like the brain, lungs, bone, and liver <sup>2</sup>. Unfortunately, effective methods to detect metastatic cancer are limited. If not identified at the original breast cancer diagnosis, detection of metastatic breast cancer will not happen until after the cancer has spread to other parts of the body, resulting in delayed treatment and often, more advanced/detrimental cancer cases. Thus, there exists a critical need for earlier more reliable methods for detecting metastatic cancer. Towards this goal, significant research is being performed to understand breast cancer pathophysiology.

Three-dimensional (3D) *in vitro* models have emerged as powerful tools in breast cancer research because they more accurately recapitulate the architecture, cellular interactions, and microenvironment of human tumors than traditional two-dimensional (2D) cell cultures or animal-based models. This enhanced physiological relevance allows researchers to better investigate key processes like tumor growth, invasion, and metastasis, improving the ability to identify early biomarkers of disease and evaluate the efficacy of potential therapies in a setting that closely mimics *in vivo* conditions. This review explores the challenges associated with current 3D *in vitro* breast cancer models while highlighting the advantages that 2D cultures continue to offer. It specifically examines the complexity and physiological relevance of 3D systems, with a focus on modeling breast cancer outgrowth from the primary tumor. While metastasis is a critical aspect of breast cancer progression, this review will specifically focus on 3D *in vitro* models of the primary tumor to better understand the early events of tumor outgrowth and local invasion, which are foundational to metastatic spread. For comprehensive insight into 3D models of common

metastatic sites like bone, lung, liver, and brain, readers are directed to existing reviews that delve into the complexity of modeling metastatic microenvironments <sup>3-6</sup>.

## **2.3 Processes and Characteristics Influencing Cancer Progression**

### **2.3.1 Cellular Events Preceding Metastasis and the Metastatic Cascade**

Although the metastasis of cancer cells is the leading cause of death in cancer patients, the process is still poorly understood. This can be attributed to cancer heterogeneity, where a variety of factors influence its spread throughout the body. Each step in this cycle is dynamic and thus difficult to study. Once cancer cells have implanted at their primary location and a tumor is formed, the first step of metastasis (Figure 2.1) begins with invasion and angiogenesis. The hypoxic center of solid cancer tumors leads to the upregulation of hypoxia-inducible factors <sup>7</sup>. This upregulation promotes vascular endothelial growth factor (VEGF) which encourages the endothelial cells in the veins to grow toward the tumor tissue. The growth and creation of vasculature supplies the tumor with nutrients and oxygen <sup>8</sup> and gives the cancer cells an exit point from which to escape.

Once angiogenesis has vascularized the primary tumor, tumor cells enter these newly formed vessels in a process called intravasation. Tumor cells secrete extracellular matrix (ECM) destructing enzymes, like matrix metalloproteinases (MMPs) MMP-2 and MMP-9, to invade local stroma, reach the blood or lymph vessel, and intravasate <sup>7</sup>. These MMPs can degrade the collagen in the basement membrane which allow easy access for intravasation <sup>9</sup>. Although not all breast cancer cells actively secrete MMPs, collective invasion enables non-invasive follower cells to migrate alongside proteolytically active leader cells <sup>10</sup>. These leader cells degrade and remodel the ECM, creating invasion paths that facilitate the coordinated movement of multicellular strands, thereby promoting collective metastasis. Thus, breast cancer cells can locally invade surrounding

tissue through two distinct yet occasionally interconnected modes of migration: collective invasion and single-cell dissemination <sup>11</sup>.

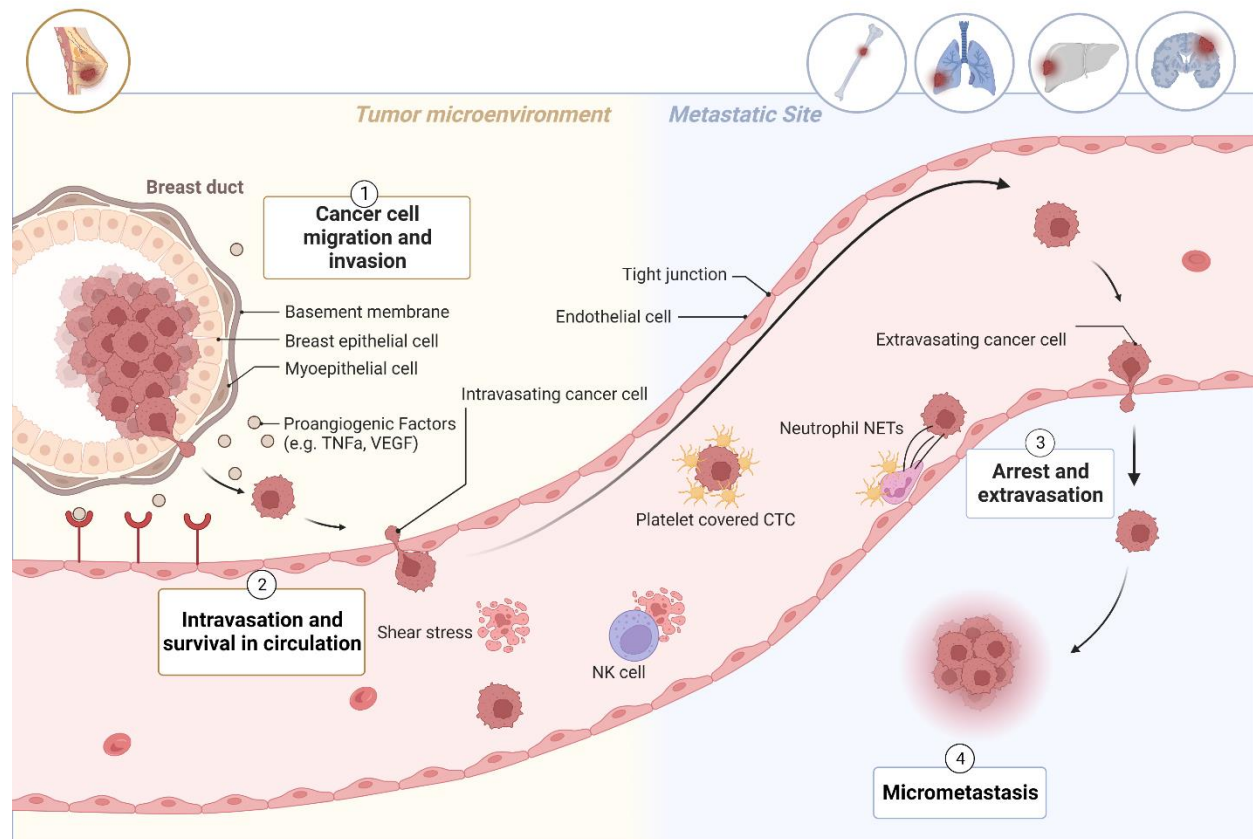


**Figure 2.1:** Breast cancer metastasis. Breast cancer cells must first detach themselves from the primary tumor, then enter the circulation (intravasation), and travel through the body via blood vessels. Here, shear stress and natural killer (NK) cells may induce apoptosis. They then leave these vessels (extravasation) and colonize a new organ (often the bone, lung, liver, and brain) where they multiply and eventually develop into secondary tumors (metastases). Adapted from “Breast Cancer to Brain Metastasis”, by BioRender.com (2022). Reproduced with permission. Retrieved from <https://app.biorender.com/biorender-template>.

Once the disseminated cancer cells (DTCs) enter the bloodstream, they begin circulation. While cancer cell circulation is a relatively short process, with cells reaching other organs in minutes, cells must survive a variety of challenges, like anoikis and immune detection. While in

circulation, platelets and neutrophils have been shown to aid in cancer cell concealment and extravasation<sup>12-14</sup>.

Once CTCs arrest along the vessel wall, they are able to perform extravasation, utilizing chemokines like epidermal growth factor, CXCL12, and hepatocyte growth factor to penetrate through vascular network<sup>15,16</sup>. While this is considered a rate-limiting step, the phenotypic plasticity of cancer cells allows them to adapt and respond to their new environment. Foreign cancer cells must acclimate to the new microenvironment, different from the original or primary tumor site, and create an atmosphere in which they can grow, utilizing local gene mediators to enhance their own signaling for survival<sup>7</sup>. The seed and soil hypothesis by Paget states that DTCs (seed) can metastasize so long as they reach an environment (soil) that is amiable enough for their survival and proliferation.

### 2.3.2 Tumor Cell Receptor Status

Traditionally there are four subtypes, as shown in Figure 2.2, based on receptor status of the estrogen receptor (ER), progesterone receptor (PR) and human epidermal growth factor receptor 2 (HER2)<sup>7</sup>. The ER+ subtype, also known as luminal (LUM), comprises roughly 80% of breast cancer cases<sup>17</sup>. Luminal subtypes can be LUM-A or LUM-B, with LUM-B breast cancer having a poorer prognosis since HER2 overexpression is shown to downregulate ER expression<sup>18</sup>. The HER2+ subtype represents about 5% of cases and is considered HER2 “positive” because it carries the receptor for the oncogene ERBB2. This HER2 overexpression is associated with the breakdown of cell-to-cell junctions, meaning HER2+ cancers generally have a worse prognosis than luminal breast cancers<sup>19</sup>. Lastly, the triple negative breast cancer subtype, or basal-like breast cancer, accounts for 10% of breast cancer cases and is the most metastatic and deadly of the three

subtypes. Triple negative breast cancer gets its name from negative status of all three receptors <sup>20</sup>. The lack of these receptors makes this cancer subtype the most difficult to treat since many therapies target these receptors. As a result, treatment options are limited to surgical removal of the breast tissue (e.g. mastectomy, partial mastectomy) and therapies like chemotherapy, radiotherapy, CDK4/CDK6 inhibitors, immune checkpoint inhibitors, and PARP inhibitors <sup>21,22</sup>. Interestingly, the androgen receptor (AR) has been increasingly recognized for its role in breast cancer and may provide prognostic and therapeutic value. While AR expression modifies ER signaling and is associated with improved survival outcomes for LUM subtypes, quadruple-negative breast cancers (ER-, PR-, HER2-, AR-) are an aggressive subtype exhibited mainly in African-American 54(AA) women <sup>23-25</sup>.

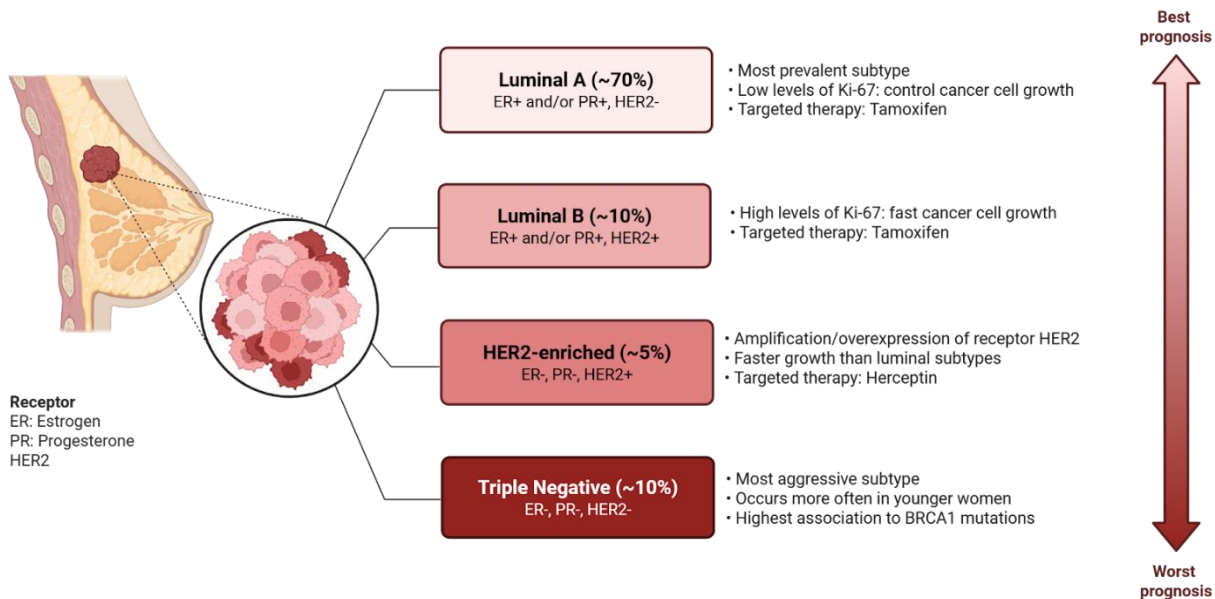


**Figure 2.2:** Breast cancer subtypes. Prevalence (%) of breast cancer subtypes in the United States from 2017 to 2021, based on data from Giaquinto et al. (2024). Note: Percentages may not total 100% due to cases with unknown subtypes. Created in BioRender. Gomillion, C. (2025) <https://BioRender.com/a06c982>

### 2.3.3 Genetics and Epigenetics

It is well established that breast cancer is inherited as a polygenic disease where pathogenic variants in breast cancer oncogenes collectively present an increased risk of metastasis and fatality. 15-20% of breast cancer cases are familial, meaning one or more first- or second-degree relatives have the disease <sup>26,27</sup>. Thus, it is important to understand the genetic and epigenetic influences on breast cancer progression and how they affect interaction with the tumor microenvironment in a model setting. Pathogenic variants of BRCA1, BRCA2, TP53, STK11, CDH1, and PTEN are strongly associated with breast cancer, accounting for approximately 20% of all familial risk <sup>28</sup>. The presence of these variants can lead to the recruitment of tumor-associated cells, systemic inflammation, and epithelial-to-mesenchymal transition (EMT, discussed in more detail later). A detailed list of their documented effects on the behavior of the breast tumor and the peritumoral environment are in Table 2.1.

**Table 2.1:** Effects of genetic variants on the tumors and surrounding tissue

<b>Mutated Gene</b>	<b>Response</b>	<b>References</b>
BRCA1	EMT <sup>a</sup> MSC <sup>b</sup> -activation Fibroblast-activation	29-31
BRCA2	EMT	29,32
TP53	TAM <sup>c</sup> -stimulation	33
STK11	Autophagy Proliferation Aerobic Glycolysis Cell Polarity	34-39
CDH1	EMT	40,41
PTEN	EMT Proliferation	42,43

<sup>a</sup> Epithelial-to-mesenchymal transition, <sup>b</sup> Mesenchymal stromal cell, <sup>c</sup> Tumor-associated macrophage



While 5-10% of breast cancers occur due to genetic mutations and 15-20% are considered familial, a majority of breast cancer cases are thought to be heavily influenced by epigenetics <sup>28</sup>. Unlike genetics, which cannot be easily altered, epigenetics have the ability to alter gene expression, operating much like a binary switch to turn gene expression "on" or "off". Epigenetic changes can be influenced by environment and lifestyle factors, thus explaining how breast cancer risk is positively associated with environmental pollutants <sup>44,45</sup>, tobacco smoking <sup>46</sup>, alcohol consumption <sup>47</sup>, obesity <sup>48,49</sup>, psychological stress <sup>50</sup>, lack of exercise <sup>48</sup>, and aging <sup>51</sup>. Although chronological age is a major risk factor for many cancers, rapid biological aging can occur at different rates in people. An accelerated biological age has been shown to be statistically significant in incidence of invasive breast cancer <sup>51</sup>. Additionally, given that the breast tissue is comprised mostly of highly secretory adipose tissue, it is especially important to highlight the effects of obesity on breast cancer risk and metastasis. Obesity promotes low-grade inflammation and can lead to epigenetic dysregulation and changes in cytokine production <sup>52,53</sup>. This, in turn, alters the phenotypes of immune cells and tumor-associated stromal cells, including fibroblasts, macrophages, and endothelial cells. Adipose tissue acts as a main source of estrogen biosynthesis in postmenopausal women, potentially explaining the strong causal relationship between obesity and postmenopausal breast cancers. Unfortunately, evaluations of the biological mechanisms underlying obesity and breast cancer have been conducted predominantly in populations with European and Asian ancestry and meta-analyses that examine this association in other racial/ethnic groups are severely lacking <sup>54</sup>. AA women tend to be diagnosed at a younger age than non-Hispanic White women and are diagnosed with higher rates of TNBC often yielding a worse prognosis. After adjusting for socioeconomic status, disparities in breast cancer risk for AA populations are reduced but not eliminated, suggesting that common genetic variants and epigenetic effects differ

according to genetic ancestry. Current research has focused on the pathogenic variants of TP53 found in AA populations <sup>55-58</sup>, as well as the Duffy Antigen Receptor for Chemokines (DARC or ACKR1) as a variant prevalent among those with Western Sub-Saharan African ancestry <sup>59-61</sup>. This gene expression is significant, as tumors that express the DARC variant exhibit a specific immune response, helping better define the tumor environment and implications for tumor therapeutic response. Finally, groups at University of California Los Angeles and Rutgers University have published a variety of papers suggesting the use of genetic variants of adipokines leptin and adiponectin as obesity-associated biomarkers for AA women, with lower expression of the leptin receptor linked to TNBC especially among AA women <sup>62-64</sup>. These protein coding genes and their corresponding receptors can explain, in part, how obesity can accelerate breast cancer progression. As more efforts have been made to improve our knowledge on the basis of health/disease in diverse populations, we will continue to understand the intricacies of genetics in association to breast cancer metastasis.

#### 2.3.4 Cancer Cell Morphology

Cell shape has long been proposed as a mediating factor in cell migration abilities <sup>65,66</sup> and is an easily quantifiable readout of the molecular underpinnings influencing cancer progression. Breast cancer cell shape can predict ECM three-dimensional (3D) cell invasion, whereas morphological heterogeneity can indicate tumor cell plasticity and malignant progression <sup>67,68</sup>. Nomenclature and cell line classification based on morphology are widely inconsistent, therefore this section will focus on the distinctions between epithelial-like and mesenchymal-like breast cell morphologies <sup>18</sup>.

A majority of breast cancer originates from epithelial cells. In non-malignant tissue, these epithelial cells are organized, maintain tissue polarity, and halt division after a period. This is compared to malignant cells that have a loss of tissue polarity, a disorganized architecture, and fail to halt growth. Cells with an epithelial-like morphology are more differentiated, and have tight cell-to-cell junctions, leading to a lower proclivity for migration. Meanwhile, mesenchymal-like cells have an overexpression of genes associated with tumor aggressiveness and invasiveness, tend to have a very high mitotic-count, and have less tight-junctions than cells with an epithelial-like morphology <sup>69</sup>. While luminal cells are typically epithelial-like, HER2-enriched subpopulations can encompass both epithelial-like and mesenchymal-like morphological features. Triple-negative breast cancer cells are more likely to have a mesenchymal-like morphology however there is enormous heterogeneity among these cell lines. Hapach et. al. separated two subpopulations within the commonly used MDA-MB-231 cell line and found that, in an *in vivo* mouse model, each subpopulation exploits different pathways to metastasize, respective to their epithelial/mesenchymal phenotype <sup>70</sup>. In 2D tissue culture, luminal-like cells demonstrate the classic cobblestone morphology and expression of cell–cell adhesion molecules such as E-cadherin, whereas cells with a mesenchymal-like appearance expressed markers of EMT transition such as vimentin <sup>71</sup>.

It should be noted that 2D morphology of cell lines differs from those grown in 3D culture. Kenny et. al. showed breast cancer cells cultured on a 3D layer of Matrigel displayed four different morphologies: round, mass, grape-like and stellate <sup>72</sup>. These morphologies, shown in Figure 2.3, not only correlated with the cell lines' protein expression and gene expression profiles, but they found distinct 3D morphologies were associated with breast cancer cell invasiveness and metastatic tendencies. Specifically, every cell line in the stellate group was shown to perform in

invasion, suggesting more elongated morphology perform much higher rates of invasion than other groups. While 3D morphologies have more physiological relevance than 2D, imaging and quantification of 2D morphology is much simpler. As breast cancer cell morphology grows as a means of evaluating cell behavior and cancer progression, a deeper look into the differences between 2D and 3D cell shape will be necessary. In all, epithelial-like cells have more cell-cell contact points, while mesenchymal-like cells can host more cell-matrix adhesion points. More aggressive breast cancers can exploit a process known as EMT to switch between phenotypes, giving these cells more adaptability during steps of the metastatic cascade.

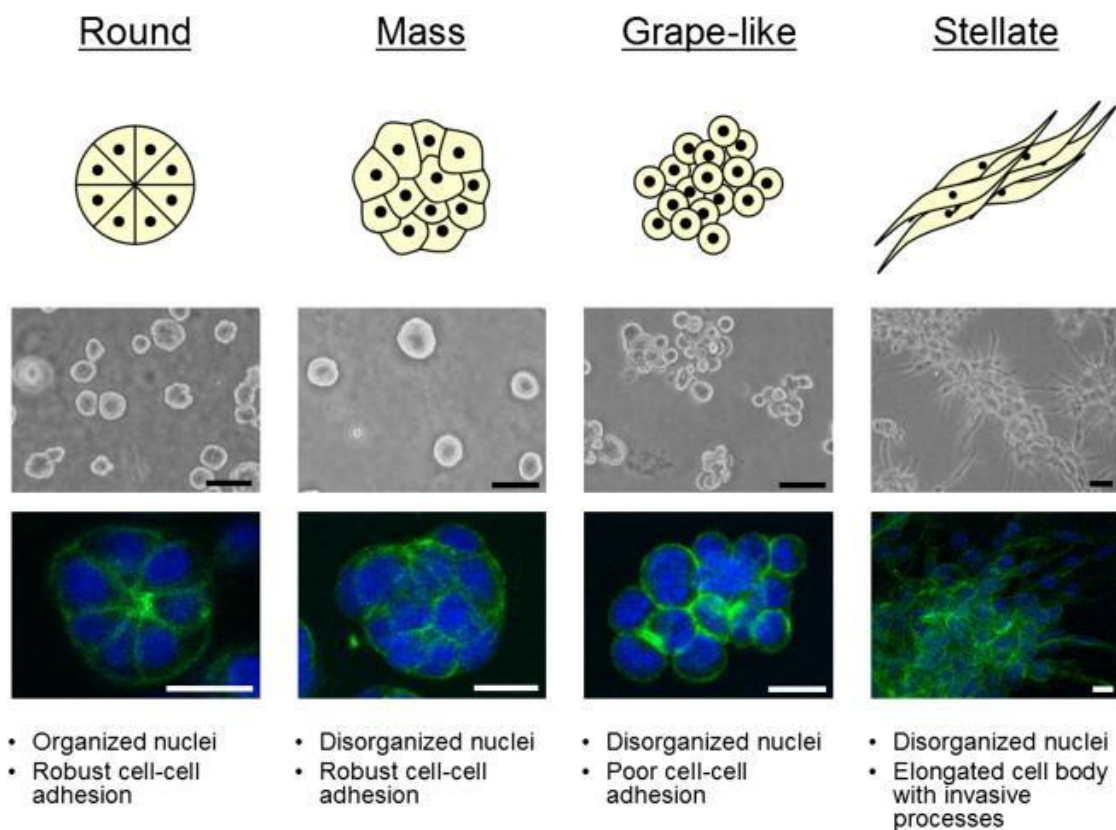


**Figure 2.3:** Four different morphologies of 3D in vitro breast cancer cells. 3D cultures were stained with F-actin (green) and nuclei were counterstained with DAPI (blue). Reproduced with permission.<sup>64</sup> 2007, Elsevier.

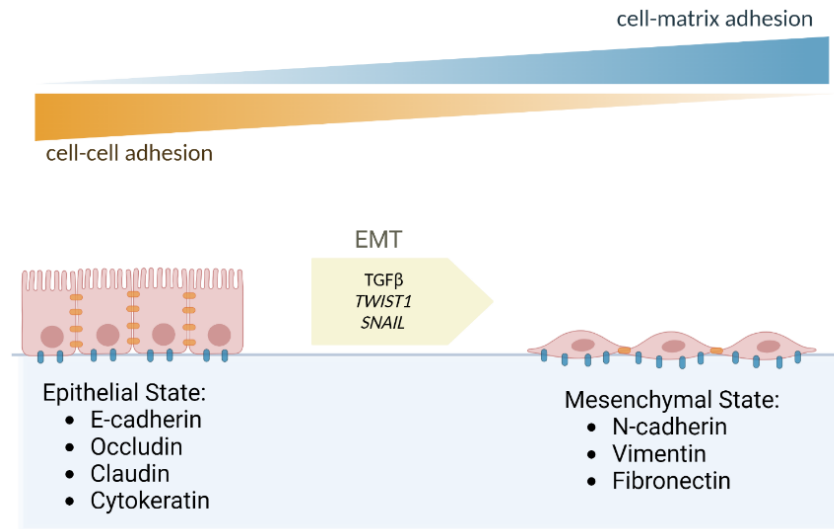


**Figure 2.4:** The epithelial-to-mesenchymal transition. In an epithelial state, cells have a higher presence of cell-cell adhesion sites (shown as orange), like tight junctions and adherens junctions, and a lower presence of cell-matrix adhesion sites. When cells undergo epithelial-to-mesenchymal transition (EMT), with the help of TGF $\beta$ , TWIST1, and SNAIL, they lose some cell-cell adhesion and gain more cell-matrix adhesion. Created with biorender.com.

### 2.3.5 Epithelial-to-Mesenchymal Transition

A cancer cell's increase in invasiveness is often associated with a transition from epithelial-like cells, that maintain a cuboidal shape and adhere to the basement membrane, to more elongated mesenchymal-like cells. There is an observed tradeoff between the cells' proliferation and invasiveness for this process, EMT. This change occurs on an epigenetic level where markers like E-cadherin, desmoplakin, and keratin are associated with an epithelial-like state and n-cadherin, vimentin, and fibronectin are associated with a mesenchymal-like state <sup>68</sup>. Additionally, cells switch from having more cell-cell adhesion in an epithelial state, to more cell-matrix adhesion in a mesenchymal state (Figure 2.4). The EMT is often viewed as a binary switch, where cancer cells are either completely epithelial or mesenchymal in phenotype. Rarely do cells express a “completely mesenchymal“ state by expressing markers like alpha-smooth muscle actin (a-SMA) and fibroblast-specific protein 1 (Fsp-1) <sup>68,73</sup>. EMT is one of the most significant processes in

tumor progression and its link to tumor phenotype, gene expression, and the tumor microenvironment are discussed throughout this paper. The reverse process, mesenchymal-to-epithelial transition (MET) is suggested to be involved in the implantation of cells at a new tumor site.

### 2.3.6 Properties of the Tumor Microenvironment

#### *Breast Anatomy*

While a majority of this review focuses on the cellular interactions between the tumor and surrounding peritumoral environment, it is important to consider the breast anatomy as a whole. The breast is composed of glandular, fatty, and connective tissues and is divided into around 15 to 20 lobes that can be further broken down into lobules. Ducts connect these structures together while fibrous stroma, blood vessels, and lymph vessels make up the rest of the breast anatomy (Figure 2.5). The purpose of the stroma, which includes adipocytes, fibroblasts, endothelial cells, immune cells, and ECM, is to provide support and protection <sup>20</sup>, however these cells can be exploited to aid in tumor migration and invasion via cytokine secretion. Fibroblasts synthesize and secrete ECM components however when cancer cells defunctionalize these processes, ECM stiffness increases.

#### *ECM Stiffness*

The ECM is an intricate network of macromolecules organized to form a structurally stable composite for cells to grow on. It contributes to the mechanical properties of tissues and is a reservoir of growth factors and bioactive molecules. ECM within the breast tissue is comprised of collagens, fibronectin, laminins, proteoglycans, and matricellular proteins, with collagen

amounting up to 90% of ECM components <sup>74</sup>. While normal mammary epithelium is soft, with an ECM stiffness around 0.15-0.20 kPa, invasive breast tumors are stiff, with an ECM stiffness around 1.0-4.0 kPa <sup>75</sup>. Hypoxic regions are present in many solid tumors, as oxygen availability is limited due to rapid tumor growth and disordered vasculature. As shown in Figure 2.6, the hypoxic tumor microenvironment increases ECM stiffness by excess deposition and crosslinking of collagen, though specific pathways linking hypoxia and ECM stiffness are not well understood

76 .

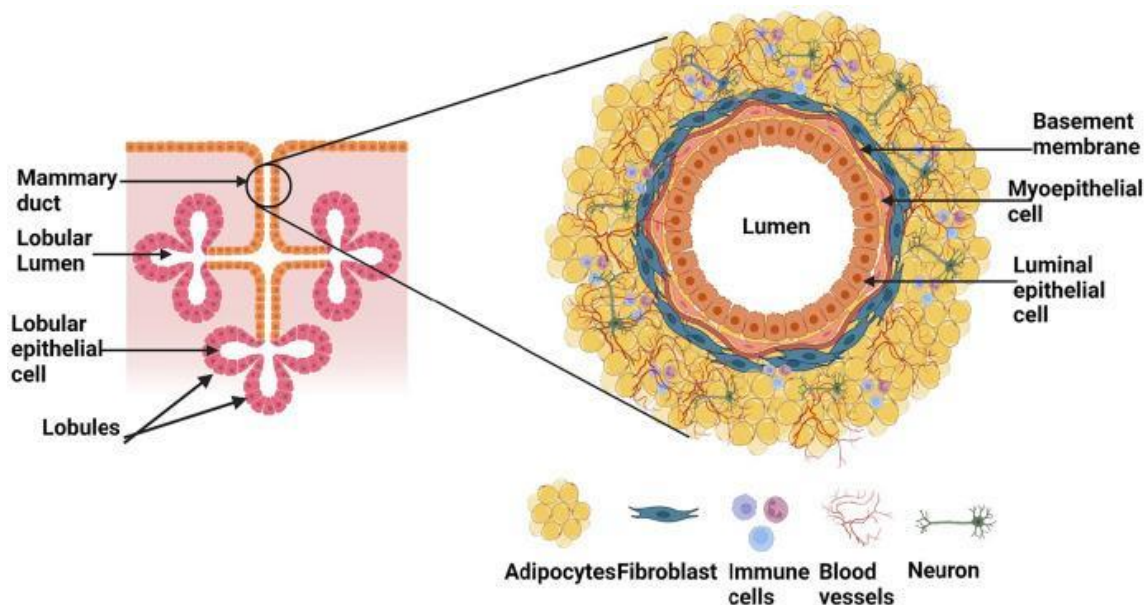


**Figure 2.5:** Schematic diagram of the mature mammary gland anatomy, composed of an epithelial compartment of polarized luminal epithelial cells that line the duct and alveoli. Surrounding the luminal epithelial cells are myoepithelial cells and a basement membrane. The epithelial compartment is embedded within a stroma composed of adipocytes, immune cells, blood vessels, fibroblasts, and neurons. Reproduced with permission.<sup>66</sup> 2022, Elsevier.

Cell-ECM interactions are mediated via cell surface receptors, like integrin-based cell adhesions and calcium ion channels. These mechanosensitive structures act to transmit mechanical signals into a cell readable format, often leading to breast cancer phenotypic changes and more aggressive invasion and proliferation. The TRPV4 channel in particular has emerged as a significant member in the TRPV family contributing to EMT and microenvironment stiffness.

Azimi et. al. demonstrated that calcium influx through the TRPV4 pathway is able to trigger EMT events. Upon pharmacological activation of TRPV4 in breast cancer cells with a traditionally epithelial morphology (MDA-MB-468), there was a significant increase in mRNA levels of mesenchymal markers vimentin and N-cadherin as well as a downregulation in epithelial marker E-cadherin <sup>77</sup>. Separate studies have also shown TRPV4 can potentiate invasion of breast cancer cells through calcium-dependent activation of the ATK pathway, leading to changes in actin dynamics and downregulation of E-cadherin <sup>78,79</sup>. Within the tumor microenvironment, TRPV4 can affect collagen remodeling, modifying ECM stiffness and potentially causing fibrosis <sup>80-82</sup>.

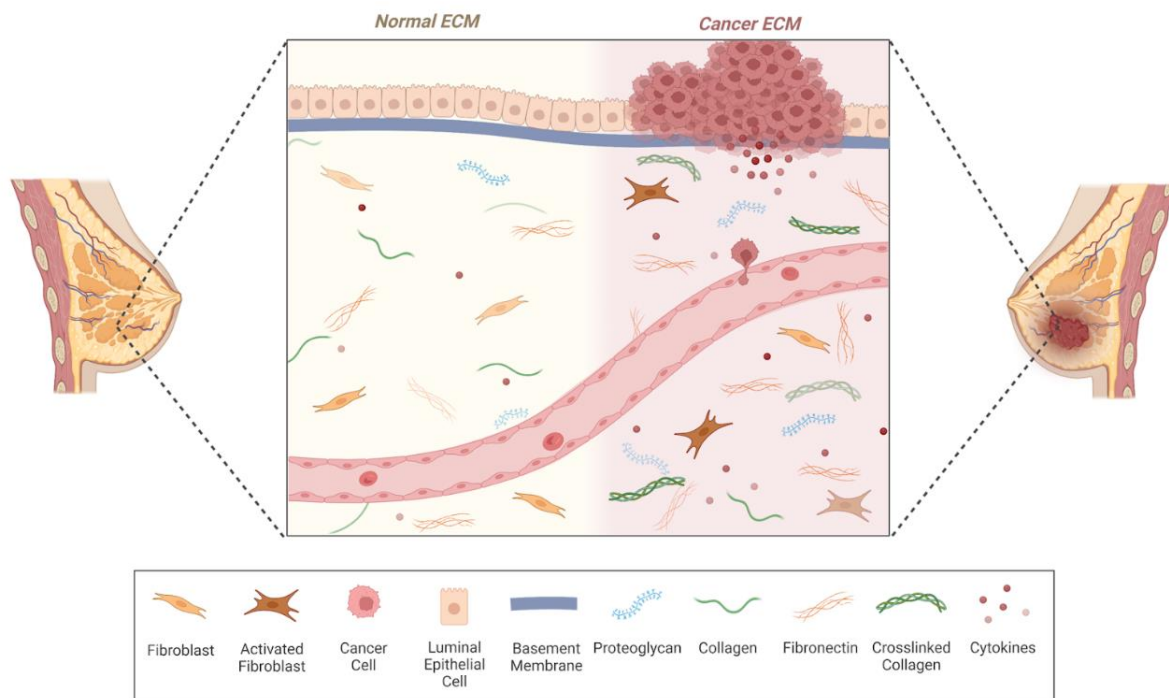


**Figure 2.6:** Schematic comparing normal mammary ECM to breast tumor ECM. Healthy breast ECM is comprised mostly of collagen with proteoglycan and fibronectin and other ECM proteins also present. Under cancerous conditions, there is an excess of ECM crosslinking, an increase in cytokine secretion, and activated fibroblasts work to reshape the ECM. This, together, gives tumor-associated ECM a higher mechanical stiffness than normal mammary ECM. Created with biorender.com.



The mechanosensing abilities of breast cancer cells are also mediated by integrin-based adhesion, which have the ability to interact with collagen and laminin in the ECM<sup>83-85</sup>. ECM-binding integrin focal adhesion kinase (FAK) regulates proliferation, migration, and adhesion and high FAK levels are associated with TNBC and increased matrix stiffness<sup>86</sup>. Tumor FAK plays a role in TNBC angiogenesis and is a significant predictor of overall survival in patients<sup>87,88</sup>. Stromal fibroblast-derived periostin can activate FAK-Src kinases through integrin-mediated signaling, which results in the activation of the YAP/TAZ pathway and, subsequently, IL-6 expression in tumor cells<sup>89</sup>. Additionally, FAK signaling has been shown to promote the secretion of enriched exosomes in a YAP/TAZ pathway-dependent manner, while FAK deletion significantly suppressed breast cancer metastasis in *in vivo* mouse models<sup>76,90</sup>. Integrin-mediated mechanotransduction regulates the transcriptional activity of YAP/TAZ which, in turn, modulates cell proliferation and differentiation<sup>85</sup>. While it is well established that a stiffer ECM is associated with more aggressive breast cancer, future advances in mechanobiological techniques will shed more light on tumor mechanosensing and the pathways exploited during metastasis.

### *Biochemical Remodeling of the Stroma*

In addition to mechanical stimuli in the tumor microenvironment, biochemical stimuli play a significant role in the severity and progression of breast cancer. In this environment, many cytokines exist to increase inflammation, promote angiogenesis, and contribute to the motile behavior of cancer cells.

VEGF is an angiogenic and proinflammatory cytokine. While the complex mechanism that alters the balance between angiogenic inducers and angiogenic inhibitors is still a subject of study, the known effect is an increase in growth factors, like VEGF. This in turn encourages the formation

of new blood vessels from pre-existing capillaries, providing a means for cancer cell metastasis. As a result, elevated levels of VEGF are symptomatic of the aggressive nature of the tumor and are linked to a poorer prognosis <sup>91</sup>. Closely associated with VEGF is tumor necrosis factor alpha (TNF $\alpha$ ), which reduces type I collagen gene expression in the tumor microenvironment. This has an antifibrotic effect on the tumor environment and encourages breast cancer motility.

To complete invasion and begin the process of metastasis, matrix degrading enzymes, like matrix metalloproteinases (MMPs), are used. MMP-2 and MMP-9 are matrix degrading enzymes known to influence breast cancer development, invasion, and metastasis <sup>92</sup>. Increased levels of MMP-9 expression was observed in breast cancer tissue compared to healthy breast tissue, as well a correlation between high expression and higher tumor histological grade and higher incidence of metastasis and relapse <sup>93</sup>. Separately, a meta-analysis of 41 studies revealed an overexpression of MMP-2 was associated with an unfavorable overall survival, while MMP-9 expression was associated with shorter overall survival <sup>94</sup>. Evidence also shows a lesser studied, membrane-bound membrane type-1 MMP (MT1-MMP) is a significant driver of breast cancer invasion and aids in matrix degradation <sup>95</sup>.

An interesting growth factor, for its initial cancer inhibition but late-stage cancer promotion, is transforming growth factor beta (TGF- $\beta$ ). TGF- $\beta$  is a cytokine and major regulator in many processes, including proliferation, differentiation, migration, adhesion, immunity, and apoptosis. In breast cancer, TGF- $\beta$  is thought to play a dual role, inhibiting cancer growth early on and later aiding in EMT <sup>96</sup>. Cell-cycle arrest is caused by TGF- $\beta$  in early breast cancer stages by inhibiting cyclin-dependent kinases and restricting ER alpha-mediated proliferation <sup>97</sup>. Often times, TNBCs are resistant to these growth-inhibitory effects, contributing to their aggressiveness.

As previously stated, an increase in inflammation of the tumor's surrounding tissue environment aids in the initiation and promotion of invasion, angiogenesis, and eventually metastasis. The interest in breast cancer and obesity stems from the observation that an increase in adipose tissues around the tumor also increases an inflammatory response by the body. Adipose tissue is a part of the endocrine system, secreting adipokines, like leptin, resistin, adiponectin, TNF- $\alpha$ , and interleukin-6 (IL-6). When this tissue becomes dysfunctional, like with obesity, this leads to elevated levels of adipokines and an increase in free fatty acids (FFA). High levels of FFAs provoke an upregulation of inflammatory signaling through nuclear factor kappa B (NF- $\kappa$ B) transcription<sup>98,99</sup>. The environment surrounding the tumor is then populated with inflammatory cells such as tumor-associated macrophages (TAMs), neutrophils, and mast cells. These inflammatory cells aid in tumor growth and angiogenesis as they encourage pro-inflammatory, pro-angiogenic factors like VEGF, TNF, IL-1 and IL-6<sup>8,100</sup>. Therefore, angiogenesis is already encouraged by the hypoxic center of tumor cells but in an environment with plenty of adipose tissue, generates a positive feedback loop. Cytokines like TGF- $\beta$  and IL-10 are also used by TAMs and tumor-induced regulatory T cells to suppress immune response<sup>101,102</sup>. While the paracrine signaling associated with the tumor microenvironment is incredibly complex and involves many pathways and cell-cell interactions, these influences on breast cancer progression should be considered when constructing a system to model steps of the metastatic cascade.

## **2.4 *In Vitro* Modeling of Breast Cancer**

### **2.4.1 2D *In Vitro* Modeling Approaches**

2D *in vitro* models offer a range of advantages for studying breast cancer metastasis, making them indispensable tools in both basic and translational research. Their simplicity and cost-

effectiveness allow for rapid experimental setup and high-throughput screening, while their reproducibility and scalability make them ideal for comparative studies across labs. In the context of metastasis research, 2D models are primarily used for adhesion and migration assays.

Adhesion assays typically involve culturing cancer cells on tissue culture polystyrene coated with specific ECM proteins. Cell attachment is then measured over a short time period, typically around 30 minutes. The choice of ECM protein can reveal different aspects of the metastatic process. For instance, breast cancer cell adhesion to laminin-411 or laminin-511—two proteins abundant in the sub-endothelial basement membrane—can provide insights into intravasation and extravasation capabilities, respectively <sup>103</sup>.

Migration is another key process in metastasis and is commonly assessed using wound healing (scratch) assays or transwell migration assays (Figure 2.7). After tumor formation at the primary site, metastasis begins with local invasion through the basement membrane and migration into surrounding tissues. This migration requires turnover of focal adhesions (FAs), and the rate of cell migration is linked to FA dynamics. Invasive breast cancer cells tend to have more dynamic FAs than their non-invasive counterparts <sup>104</sup>, and reduced adhesion strength has been associated with increased metastatic potential <sup>105</sup>. Therefore, 2D migration assays serve as useful proxies for assessing cancer cell aggressiveness.

The wound healing assay, also known as the scratch assay, is a classic *in vitro* model used to study cancer cell migration. In this method, shown Figure 2.7D, cancer cells are seeded into a well plate and allowed to grow to confluence. A scratch is then made across the cell monolayer, removing cells along the scratch line. Over time, the remaining cells migrate to close the gap. The rate and extent of this closure reflect the cells' migratory and metastatic potential.

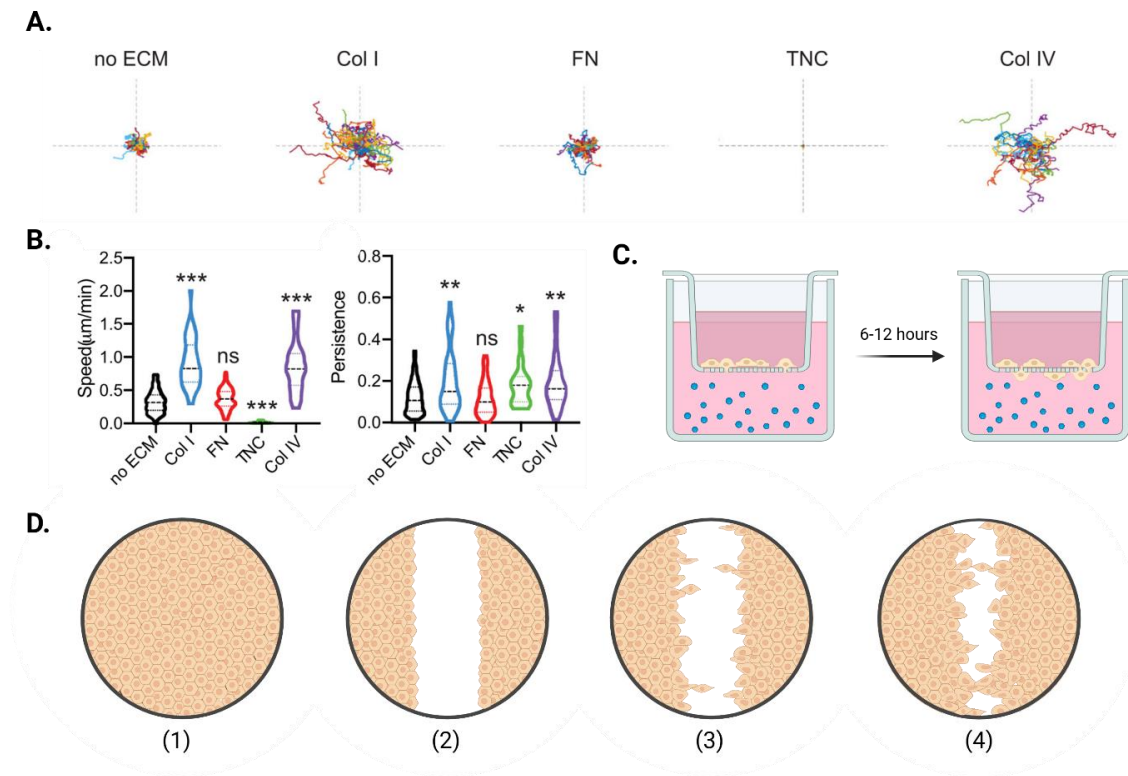


**Figure 2.7:** Examples of migration assay methods. A) Time-lapse microscopy tracks single-cell movement across different groups (e.g., on distinct ECM substrates).<sup>67</sup> B) Cell speed and persistence can be quantified from time-lapse videos and averaged to compare migration patterns across conditions. C) Transwell assays assess migration by separating cancer cells (in the top insert) from a chemoattractant (in the bottom well), measuring movement through a porous membrane. D) Wound healing (scratch) assays create a physical gap in a cell monolayer, and migration is measured by the rate at which cells close the exposed area. 2020, AIP.

Another common assay is the transwell or Boyden chamber assay (Figure 2.7C). In this setup, a chemoattractant is placed in the lower chamber, and cancer cells are seeded in an upper insert separated by a porous membrane (typically 4–8 μm in pore size). Migratory cells move through the pores to the underside of the membrane, where they can be imaged and quantified. Although 2D models are less complex than 3D systems, they have played a foundational role in cancer cell research and continue to offer valuable insights into the molecular mechanisms that govern cell adhesion, migration, and metastatic potential.

### *Advantages and Insights Gained from 2D Models*

The widespread use of 2D models has resulted in well-established protocols and a wealth of historical data, providing a strong foundation for hypothesis generation and validation. Unlike 3D models, 2D systems have more established protocols, making high throughput analysis easier. Additionally, easier image analysis allows for better study of EMT, including the regulation of key molecular markers like E-cadherin, vimentin, and Snail, which are central to metastatic progression. For instance, studies have demonstrated that treatment with TGF- $\beta$ 1 in 2D cultures induces EMT, characterized by decreased E-cadherin and increased vimentin expression, leading to enhanced migratory capabilities of breast cancer cells<sup>106-108</sup>.

Moreover, 2D systems are instrumental in dissecting the roles of cell adhesion molecules, MMPs, and pro-metastatic cytokines, all of which contribute to tumor cell invasion and dissemination<sup>92,109</sup>. Time-lapse microscopy allows for dynamic tracking of cell migration and invasion, while high-throughput imaging and morphometric analysis enable quantitative profiling of metastatic phenotypes, including cell shape, motility, and protrusion dynamics. These image-based approaches were combined in a study by the Oudin Lab, that validated 2D cell morphology as a predictor of tumorigenicity and metastasis *in vivo* across multiple triple-negative breast cancer cell lines<sup>110</sup>. The compatibility of 2D cultures with automated imaging systems facilitates high-content screening approaches, allowing for the rapid assessment of numerous parameters across large datasets and accelerating the discovery of new metastatic processes. Coupled with transcriptomic and proteomic profiling, 2D cultures provide valuable molecular signatures of metastatic behavior that inform both mechanistic insights and therapeutic development.

### *Limitations of 2D In Vitro Approaches*

Despite the importance of 2D *in vitro* studies in uncovering fundamental aspects of breast cancer metastatic behavior, they can present notable limitations. Primarily, they lack the 3D architecture and resulting mechanical cues that are critical for accurately modeling tumor progression and cellular responses. These simplified environments fail to fully recapitulate the complex tumor microenvironment, like ECM remodeling, though the use of ECM coatings and biomimetic substrates can partially mimic the basement membrane to support cell adhesion and polarity<sup>67,111,112</sup>. Additionally, 2D platforms offer an oversimplified representation of the multi-step metastatic process and are often used to measure early metastatic behaviors, like EMT, migration, and adhesion. To address some of these limitations, recent advances such as microfabrication and surface patterning have enabled more precise studies of directional migration by guiding cell movement along defined paths<sup>113-115</sup>. In parallel, co-culture approaches incorporating immune or stromal cells help simulate key aspects of tumor-immune interactions within a controlled 2D environment<sup>116,117</sup>. Nevertheless, many 2D models continue to exhibit poor correlation with *in vivo* metastatic behavior and offer limited predictive power for clinical outcomes, underscoring the need for more physiologically relevant systems.

### *The Transition from 2D to 3D*

2D breast cancer models serve as a valuable foundation for dissecting fundamental mechanisms of metastasis, like cell migration, invasion, and EMT, under controlled and reproducible conditions. These systems remain valuable for their high-throughput capabilities and ease of imaging. By first identifying key molecular drivers in 2D and then validating their

functional relevance in 3D systems, we can bridge the gap between simplicity and biological complexity, enabling a more comprehensive understanding of metastatic progression.

#### 2.4.2 3D *In Vitro* Models

##### *ECM-associated Proteins*

Many ECM proteins exist on the market to model 3D breast cancer cell outgrowth from the primary tumor and are chosen to fit the needs of the model. To emphasize the role that tumor ECM plays in cancer progression, this review will highlight the use of ECM-associated proteins in a hydrogel format, however alternative models are discussed in detail in many reviews <sup>76,118</sup>. Breast ECM-associated proteins, like collagen, fibronectin, and laminin are used in 3D *in vitro* models for their excellent biocompatibility and ability to effectively recapitulate the biochemistry of the tumor microenvironment. Given that collagen makes up around 90% of the breast ECM, it's a good choice for its biomimetic capabilities. Collagen is made up of many polypeptides called alpha chains which are rich in proline and glycine. Three of these alpha chains will become twisted to form stiff triple helical structures that aggregate to form collagen fibrils. These fibrils will arrange in tissue-specific formations which allow for the identification of the collagen type. Collagen has been used in many studies to examine the effects of collagen fiber alignment on cancer cell morphology and invasion through contact guidance <sup>119</sup>. In a 2020 paper, Gong et. al. developed a method to fabricate collagen bundles by heating up the collagen mixture prior to agitation <sup>120</sup>. This results in the collagen bundling together, mimicking the stiffening and alignment that collagen I undergoes *in vivo* during cancer progression. Collagen has also been used to replicate age in the microenvironment. Yang et. al. developed a 3D scaffold made up of collagen extracted from young and aged mouse tail tendons aiming to mimic age-related changes in breast



tissue. The collagen from two different age groups were able to demonstrate the young vs aged phenotype of increased microenvironment stiffness and motility. The ability to use natural ECM proteins from intentionally chosen sources highlights the potential to leverage the vast tunability of 3D *in vitro* modeling. Breast cancer spheroids of invasive ductal carcinoma have also proven to reinforce ECM alignment via LOXL3 secretion <sup>121</sup>. Ligands for cancer cell integrin receptors exist in proteins like collagens, laminin, fibronectin and are used to identify new signaling pathways that may be exploited. Park et. al. created a TNBC model using MDA-MB-231 cells to demonstrate that increased fibronectin levels in 3D suspension culture facilitates cancer cell attachment and spread using integrins  $\beta$ -5 and Src with targeted Src-based therapies being actively pursued <sup>122,123</sup>.

Biomaterials are any type of material that can interact with biological systems <sup>124</sup>. *In vitro* models often rely on naturally and synthetically derived biomaterials to serve as matrices, hydrogels, and scaffolds, among other applications. Naturally derived biomaterials can be sourced from proteins, polysaccharides, glycosaminoglycans, and decellularized tissues <sup>125</sup>. Conversely, synthetically derived biomaterials are engineered specifically for their ability to interact with biological systems and can be attuned to meet specific standards for molecular weight, degradation rates, strength, and spatial structure <sup>126</sup>. The utility of synthetic biomaterials arises from its controlled composition which reduces unintended results in cell culture experiments. Overall, using a composite of natural and synthetic biomaterials creates a biomimetic structure with tunable mechanical and chemical properties.

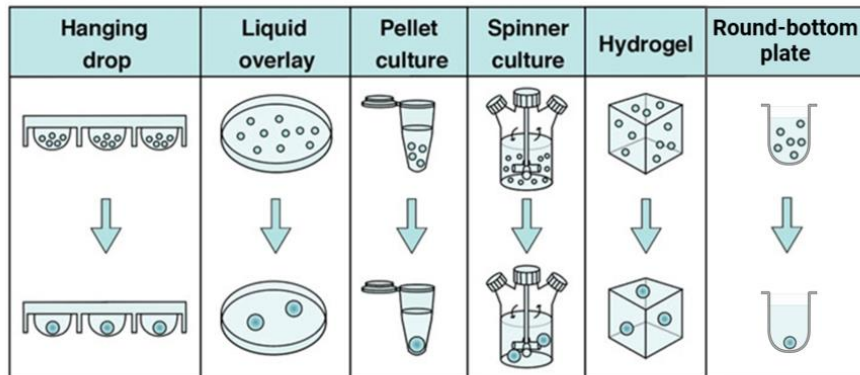
## *Spheroids*

Tumor spheroids are spherical cellular clumps that are either self-assembling or are forced to aggregate. Their architecture resembles that of the tumor and is often used to assess cell-cell communication in a complex 3D system. While some spheroid shaping techniques encourage cells to self-assemble, like hanging drop, liquid overlay, and ultra-low attachment (ULA) round-bottom plates, methods like centrifugation, spinner flasks, and rotating bioreactors use force to encourage cell-cell assemblage (Figure 2.8A). Spheroids are often constructed from single cell populations, for their ease of use and accessibility. These spheroids are called multicellular tumor spheroids. One of the first scaffold-free methods of creating tumor spheroids is outlined in the protocol by Foty<sup>127</sup> which uses a small cancer cell suspension that is pipetted to a lid of a 10cm plate and then gently placed back onto the plate. Once the cells have aggregated, the tumor spheroids can be harvested and grown out or used immediately. The liquid overlay technique (LOT) uses a non-adherent coating in a cell culture plate with a cell suspension in media that is seeded over this coating. This method negates the need for round-bottom plates as the non-adherent coating forces the cells to self-aggregate. An important consideration for using tumor spheroids as a breast cancer model is the ability to replicate hallmark phenotypes consistent with the breast cancer subtype. Dhandapani et al used the LOT to create tumor spheroids in the MCF-7 and MDA-MB-231 cell lines<sup>128</sup>. In this work, they were able to capture the EMT and cancer stemness in the triple-negative breast cancer line and replicate the same immune effects of doxorubicin treatment as *in vivo* studies, which highlights the spheroids ability to be used as an effective drug testing model. Another popular method is using ULA round-bottom plates to mimic the same self-aggregation technique of hanging-drop, but in a more streamlined way that can sustain larger cell seeding volumes. In the paper by Malhão et al, four breast cancer cell lines were aggregated using 96-well

ULA plates. It is mentioned that although this method is fast, cost-effective, and reproducible, there still lacks significant literature on the characterization of breast cancer tumor spheroids <sup>129</sup>. Alternatively, surgical resections of breast cancer tissue can be used to create tissue-derived spheroids that are often enriched with cancer stem cells. While this method better captures tumor complexity, this process has traditionally been difficult due to low cell number and high amount of nonmalignant tissue within the samples <sup>130</sup>.

Spheroid diameter can range anywhere from 200-750  $\mu\text{m}$ , depending on cell type and culture conditions <sup>131,132</sup>. Spheroids larger than 400  $\mu\text{m}$  in diameter develop oxygen gradients representing the hypoxic core of aggressive breast cancers <sup>133</sup>. As previously discussed, intratumoral hypoxia is associated with a more aggressive phenotype and an upregulation of hypoxia-inducible factors which support tumor growth and malignant progression (Figure 2.8B). Homotypic spheroids, meaning the spheroid is composed of one cell type, have a simplified tumor environment that can isolate the cell-cell interactions of the breast cancer cells themselves. For example, Huang et. al. exposed MDA-MB-231 spheroids to static conditions and interstitial flow and found e-cadherin expression significantly decreased in flow conditions, elucidating the relationship between tumor interstitial flow and metastatic cancer motility <sup>134</sup>. Heterotypic spheroids are used to evaluate the complex cell-cell interactions of breast cancer cells with the surrounding tumor stroma. Tumor associated cells, like fibroblasts and mesenchymal stromal cells, can be integrated in spheroids to model the heterotypic cell-cell interactions that so heavily influence tumor progression <sup>135-137</sup>. Lastly spheroids can be encapsulated in ECM proteins as a means of studying cell-matrix interactions and tumor invasion. For example, Karrobi et. al. used MCF10A and MDA-MB-231 spheroids in a collagen matrix to understand the shift toward oxidative phosphorylation in cells in contact with the ECM <sup>138</sup>.

A.



B.

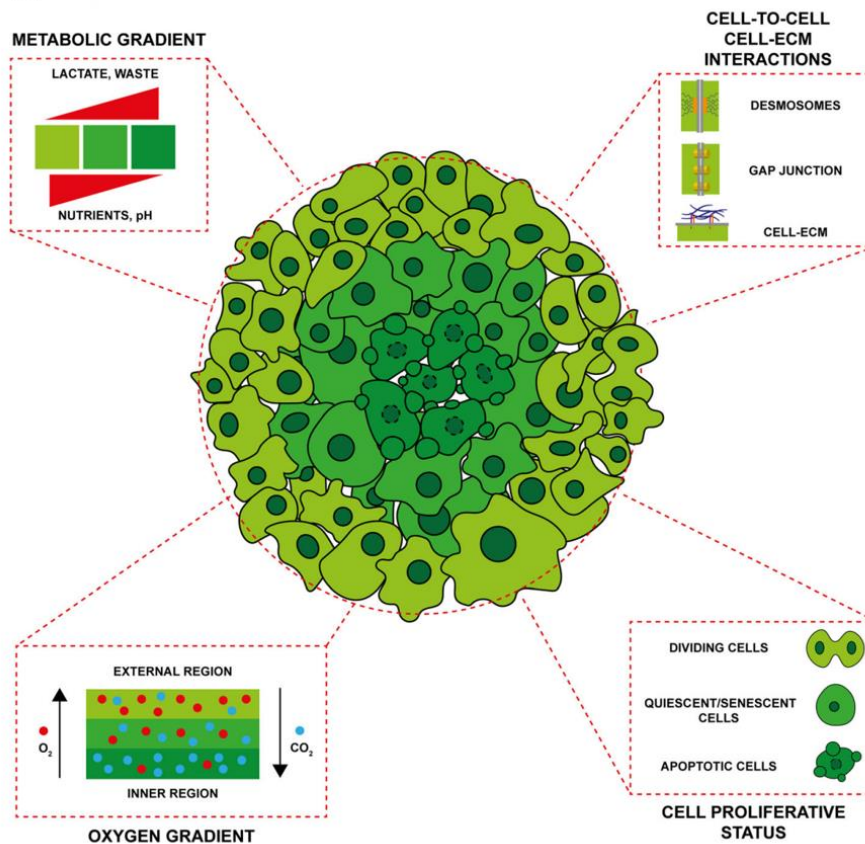


**Figure 2.8:** Spheroid assembling techniques and characteristics. A) Simplified diagram of different self-assembling and forced assembling spheroid methods. B) Diagram showing the gradients and cell heterogeneity within a large tumor spheroid. Adapted with permission.<sup>110</sup> 2020, BMC.

Spheroid models can vary in complexity with future sections involving 3D printed and microfluidic spheroid systems. While this method is the foundation for many breast cancer models, it suffers from poor controllability and challenges in replicating large tumors due to their lack of vasculature. Spheroids possess chemical gradients starting at 200  $\mu\text{m}$  in diameter. Given their variability in tumor shape and volume, spheroid behavior, like proliferative status<sup>139</sup>, can be very different, leading to poor reproducibility. Future research includes methods of standardization and uniform spheroid fabrication. One research group developed an imaging-based approach to select homogenous populations of large spheroids, though the process is time intensive and this process eliminated around 30% of spheroids after one week of culture<sup>140</sup>. Meanwhile, new manufacturing methods like acoustofluidic vibration, shown in Figure 2,9, are used to fabricate uniformly sized spheroids with high throughput<sup>141,142</sup>.

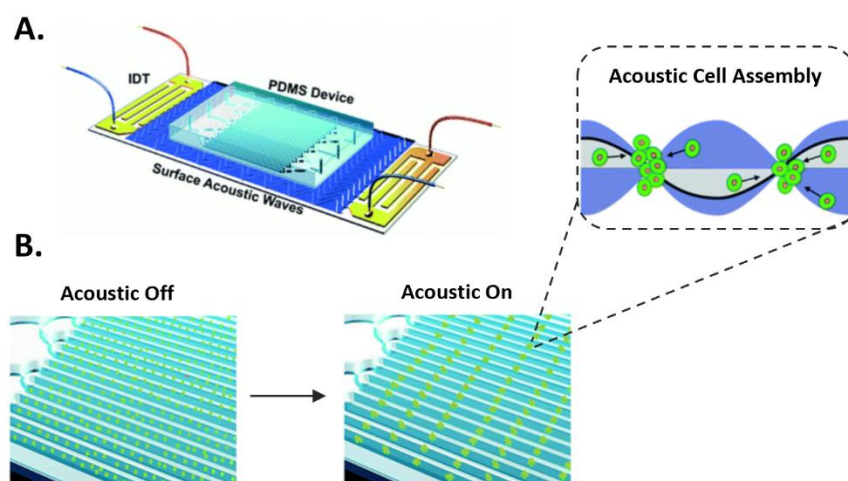


**Figure 2.9:** Acoustofluidic spheroid assembly. A) Schematic of high-throughput acoustofluidic cell spheroid assembly. This device contains a disposable PDMS components with multiple cell assembly channels and a reusable surface acoustic wave generator. B) Schematic of acoustic cell assembly where cells are randomly distributed throughout the microchannel, then aggregate into cell clusters with acoustics. Adapted with permission.<sup>120</sup> 2019, The Royal Society of Chemistry.

### *Bioprinted Structures*

The use of bioprinters to create 3D models has grown due to their ability to provide intentional structural organization with definite composition <sup>143</sup>. The three main types of 3D bioprinters are distinguished by their printing methods: line printing, drop-by-drop printing, or layer-by-layer printing (Figure 2.10). In line printing, a form of microextrusion, the bioprinter extrudes a continuous line of biomaterial or hydrogel through a syringe and needle. This method allows the bioprinter to print freely in the X and Y directions, while moving vertically in the Z direction to build upon the print or change locations on the platform. Some 3D bioprinters feature dual-head attachments or multiple nozzles, enabling them to print with different materials simultaneously <sup>144</sup>. In a study by Desigaux et. al., a 3D micro-extrusion bioprinted-based model was created using photo-polymerizing bioinks made up of cancer and stromal cells. The authors developed a model to observe the influences of stromal cells on the ECM and its ability to affect tumor response to radiation therapy. Using naturally derived ECM proteins such as methacrylated collagen and hyaluronic acid that were functionalized with a laminin-derived peptide. Using this 3D bioprinting method with this bioink, the authors were able to display a novel aspect of maturation in their 3D model, demonstrated by cancer associated fibroblast (CAF)-induced remodeling of the ECM. This study also highlights the potential for 3D *in vitro* models to be used as preclinical models for other cancer treatments such as radiation therapy.

Drop-by-drop printing can be either inkjet based or laser based <sup>143</sup>. Inkjet 3D printing differs from line printing in that it uses droplets rather than a continuous line. Inkjet printers can be used with a hydrogel support bath, which functions to support the print at certain temperatures and liquifies when raised to normal body temperature, allowing for easy release of the print <sup>144</sup>. In

laser-based 3D printing, also known as stereolithography, a photosensitive biomaterial is cured by a laser as it is printed, after the print is completed <sup>144</sup>.

Layer-by-layer (LBL) bioprinting refers to the process of 3D depositing of bioink that builds off of each successive layer. This type of printing is generally done following the design of a precise binary model of the structure. A sub-type of layer-by-layer printing is photo-patterning, which uses photo-crosslinkable hydrogels to cure each layer as it is added. Similar to traditional 3D-printing, photo-patterning is a form of additive manufacturing that is biocompatible for the uses of tissue engineering, drug discovery, and translational medicine. As each layer of bioink is printed, the hydrogel is cured to strengthen its stability before the subsequent layers are printed. The ability to have a tunable bioink that can be adjusted, either by adjusting the hydrogel composition or curing time, to better suit the model is advantageous over other methods that are less modifiable.

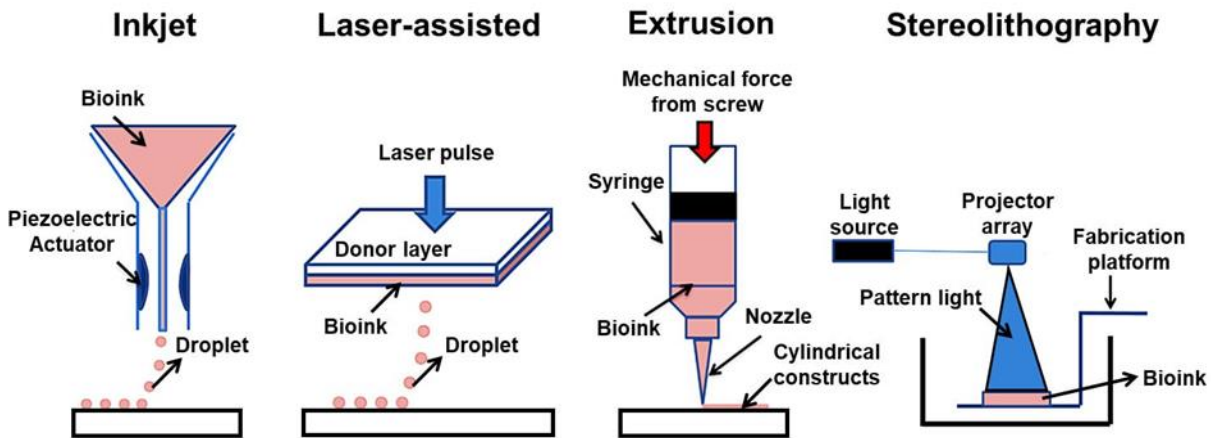


**Figure 2.10:** Schematic showing examples of three-dimensional bioprinters. Inkjet and its derivation, laser-assisted bioprinters, primarily use droplets whereas extrusion-based and stereolithography use continuous streams of bioink. Of the four bioprinting methods, the latter two are newer and offer advantages over the inkjet and laser-assisted methods because of their ability to create larger scale 3D structures, printing optimizations (temperature, viscosity, and applied stress), and higher resolution. Reproduced with permission <sup>145</sup>. 2019, Hapres.

Regardless of the printing method used, crosslinking, which transforms the solution into a stable structure, is a crucial step. The cross-linking agent should be non-toxic, ideally affecting only the hydrogel or bioink during the curing process, while preserving the integrity of the cells or biofactors. Crosslinking can be achieved through chemical or physical methods, including pH-driven, temperature-responsive, photo-crosslinking, electric field-responsive, magnetic-responsive, and ionic crosslinking techniques.

Using this high-resolution fabrication technique, biomimetic breast cancer models are designed with controlled structural and mechanical properties, like porosity, permeability, and stiffness. Commonly used natural structures are gelatin, alginate, collagen, hyaluronic acid, fibronectin, chitosan, and Matrigel. Collagen is a great option for physiologically similar conditions given it is the most abundant protein in the tumor ECM and allows for cell attachment via glycoproteins and integrins. Two of the most popular naturally derived biomaterials for bioink are gelatin and alginate. Gelatin allows for high cell adhesion and low inflammation induction, while alginate has high thermal stability and easier cell encapsulation. Gelatin is a derivation of collagen via basic or acidic hydrolysis, therefore its behavior is pH driven. Gelatin is also thermoreversible because it gels at room temperature and liquefies at higher temperatures <sup>146</sup>. This property of gelatin makes it ideal to use as a bioink because it can be heated in the nozzle of the bioprinter and extruded into 3D scaffolds that solidify as it cools. While polymeric gelatin is naturally equipped with arginylglycylaspartic acid (RGD) sequences which promote cell surface adhesion via integrins, its mechanical properties fall short to those desirable in application. Due to its lack of stiffness at bodily temperature and low yield strength, natural polymeric gelatin alone is not a viable option for a printing material <sup>126</sup>. Alginate is derived from brown algae and is crosslinked by divalent cations. Alginate is arguably the most used biomaterial for 3D printing due



to its biocompatibility, control over mechanical properties, and ability to form highly porous structures for cell regeneration <sup>146</sup>. Used together, gelatin-alginate composites are a common bioink with ideal physical and biological properties under printing stresses.

Hyaluronic acid is the major component of cartilage ECM and is very hydrophilic. In a study by González-Callejo et. al, a blend of decellularized extracellular matrix from breast tissue and methacrylated hyaluronic acid with tumor-derived cells and non-cancerous stromal cells, were bioprinted as two separate but adjoining compartments and heat cross-linked to create a tumor-stroma model <sup>147</sup>. Chitosan is derived from the exoskeleton of arthropods. The chemical structure of chitosan is like glycosaminoglycans (GAGs) which are another large component of the ECM. The structure contains highly negative charges and can bring a lot of water into the hydrogel. Chitosan hydrogels are often used as a biomaterial to produce bone or cartilage-like scaffolds. Matrigel has the advantage of being printed to form scaffolds with an editable architecture through the addition of other hydrogel components, though it has batch-to-batch differences, making it unsuitable for production of hydrogels with a defined ECM. All of these natural materials have high biocompatibility and are ideal for cell encapsulation but generally have lower mechanical strength and lower stability at 37°C than polymers like PCL, PEG, and PLA (commonly used as a scaffold for cells to grow on). Therefore, a significant drawback in bioprinting is that materials used must be biocompatible as well as stable under printing stresses. However, synthetic polymers can be functionalized by mixing scaffolds with certain ECM components <sup>148</sup>. In a study by Jaidev et. al, polyethyleneimine and citric acid were conjugated to PLA scaffolds and then soaked in simulated body fluids to coat the surface with calcium-deficient hydroxyapatite (HA) <sup>149</sup>. The surface modification allowed the 3D printed PLA to become a synthetically derived biomimetic scaffold for bone regeneration.

Different materials have been adapted to overcome this issue. For instance, additives, like hydroxyapatite, can increase the mechanical strength of bioinks, like alginate, while mimicking the microcalcifications found within breast tissue<sup>150</sup>. Alternatively, there has been a recent trend in bioprinting with decellularized tissue ECM for their ability to recapitulate *in vivo* processes. As an interesting example shown in Figure 2.11, Blanco-Fernandez et. al. incorporated porcine breast tissue-derived matrices into a GelMA-alginate bioink, to print cell-laden hydrogels with similar adhesion sites, viscoelasticity, mechanical properties, and architecture to the TME<sup>151</sup>. By seeding MCF7 cells into this model, spheroid formation was observed as well as a lower e-cadherin expression, higher tumor marker expression, and lower chemo-responsiveness than 2D cultures. They even exhibited a way to incorporate a stromal-cell laden outer layer without the bioinks merging together. A separate study by Horder et. al. designed a 3D printed spheroid model to evaluate the relationship between the tumor and adipose tissue. After differentiating adipose-derived stromal cells in adipogenic culture for 21 days, a breast cancer cell (MDA-MB-231) compartment was printed onto the adipose tissue constructs where a reduction of lipid content and remodeling of ECM was observed over nine days<sup>152</sup>.

While bioprinting is a promising avenue for 3D *in vitro* breast cancer models, issues like cell stress, limited bioink options, and the need for costly/repetitive process optimization are challenges that must be overcome before the true potential of bioprinted models can be tapped. Maintaining cell viability throughout the printing process is crucial when culturing live cells. Excessive mechanical stress during printing can lead to cell death and if the printing speed and viscosity are too high, the excessive pressure on the hydrogel will shear the cells. Additionally, hydrodynamic pressures and capillary forces can cause apoptosis when the cells land on the printing surface. These forces can be minimized by adjusting the printing speed and changing the

hydrophobic or hydrophilic tendencies of the printing surface <sup>153</sup>. Furthermore, low print speeds can reduce the viability of cells as the cells cannot be maintained long term without proper maintenance medium. Another technique to address this is computational modeling of printing and post-printing dynamics. Mohammadrezaei et. al. developed a predictive model to understand the post-printing proliferation and migration of cancer cells in commonly used gelatin/alginate structures. Their *in silico* data was comparable to their *in vitro* data obtained from MDA-MB-231 cells in 4% gelatin/4% alginate constructs <sup>154</sup>. Meanwhile, others have utilized machine learning to anticipate cell viability under different printing parameters <sup>155</sup>, like UV crosslinking time, and bioink printability <sup>156</sup>.

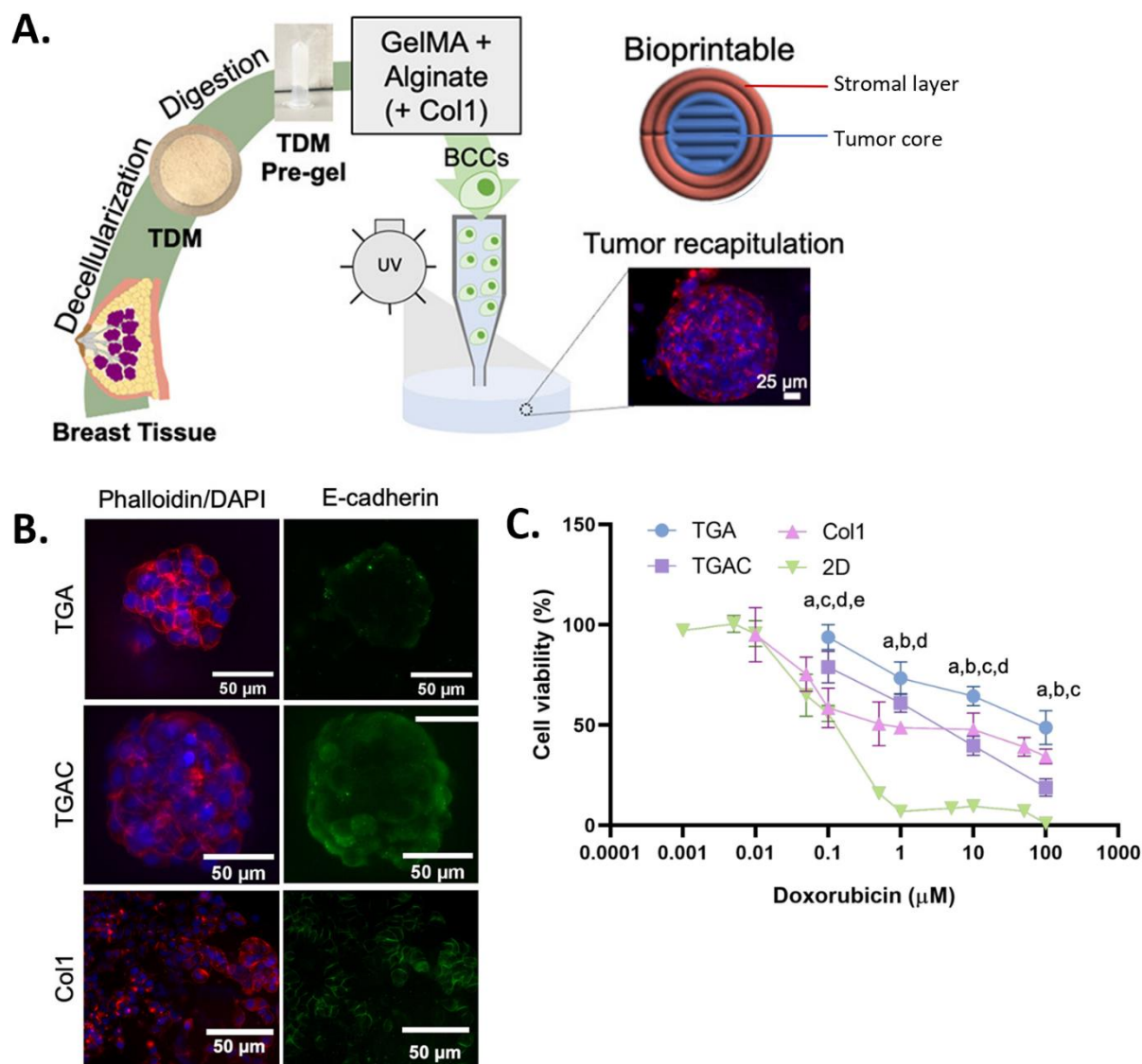


**Figure 2.11:** Bioprinting with decellularized tissue ECM A) Process of making bioink and printing tumor coculture with an MCF7 tumor core and human adipose-derived mesenchymal stromal cell (hAMSC)-laden stromal layer. Porcine breast tissue was decellularized to make a tissue-derived matrix (TDM). The TDM was subsequently combined with GelMA and alginate, and for the TGAC group, collagen I, and cells were encapsulated in this bioink for printing. B) MCF-7 stained with phalloidin–rhodamine (red), nuclei are counterstained with DAPI (blue). Expression of E-cadherin (green) in MCF-7 clusters is most prominent in hydrogels containing collagen I. All images taken after 14 days of culture. C) MCF7 cell viability 48 hours after doxorubicin treatment, where all 3D cultures show lower chemoresponsiveness than 2D MCF7 culture. Adapted with permission.<sup>130</sup> 2022, American Chemical Society.

**Table 2.2:** Review of literature on prominent bioprinted breast cancer metastasis models

Goal of Study	Design	Advantages	Limitations	Printing Parameters	Reference
Develop 3D printed scaffold that mimics key cell responses of patient-derived scaffold (PDS) cultured cells and to use these as tumor models for cancer drug screening	8% w/v alginate grid lattice scaffold enriched with periostin and hydroxyapatite (HA)  <u>Cells:</u> MCF7 and MDA-MB-231 cell lines	Cells cultured on the 3D printed scaffold (3DPS) exhibited similar phenotype to those cultured on PDS  HA rendered a stiffer material, increasing the ratio of cancer stem cells	Cells were not able to infiltrate the 3DPS, as observed in PDS  MCF7 cell attachment was initially lower in the 3DPS as compared to the PDS	10°C - 20°C temperature 0.6 bar pressure 35 mm s <sup>-1</sup> speed 0.45-0.50 mm needle offset 400 µm needle diameter *crosslinked with CaCl <sub>2</sub>	<sup>150</sup>
Incorporate alginate and GelMA to decellularized porcine breast tissue-derive matrices (TDM) to fabricate bioinks with suitable mechanical properties for 3D bioprinting and appropriate tumor recreation	2% TDM hydrogel, 2.5% GelMA, 0.5% alginate, 0.15% Collagen I, 0.1% irgacure  <u>Cells:</u> MCF7 cells and primary human adipose-derive mesenchymal stem cells (hASCs)	Decellularized, delipidated ECM helps recapitulate in vivo processes  Stromal cell-laden outer layer surrounds	TDM is from healthy porcine and cannot fully mimic human breast cancer ECM  TDM can lack lot-to-lot reproducibility, much like Matrigel	8°C - 20°C temperature 0.25-0.50 bar pressure 3-5 mm s <sup>-1</sup> speed 51 mm tip diameter *crosslinked with 37°C, CaCl <sub>2</sub> , and UV	<sup>151</sup>
Combine breast tissue mimicking alginate hydrogels with bone mimicking polycaprolactone (PCL) scaffolds to illustrate how primary tumor stiffness and ECM composition direct invasion and metastasis to bone	Alginate-gelatin hydrogels (of varying concentrations) atop a mineralized  PCL/hydroxyapatite biohybrid scaffold  <u>Cells:</u> MDA-MB-231, breast cancer bone homing MDA-IV, and Saos-2	Describes the relationship between two different tissue sites and how breast cancer cells interpret signals across tissue sites	Simplifies the metastatic cascade to the primary and secondary tumor sites, ignoring travel through vasculature	130°C temperature 6.5 bar pressure 0.6 mm s <sup>-1</sup> speed	<sup>157</sup>
Assess the printability of hASC spheroids and their ability to differentiate into adipose-like microtissues within the printed constructs, which is further used as the basis for a 3D breast cancer-adipose tissue model.	Hyaluronic acid hydrogels of varying concentrations  <u>Cells:</u> Primary hASCs and MDA-MB-231	Focuses on the relationship between adipose tissue and the tumor	MDA-MB-231 cell-laden hydrogels are printed atop the adipose tissue, and are not encapsulated by the construct	1-5 bar pressure 250-330µm nozzle diameter *crosslinked with UV	<sup>152</sup>

Many of the models discussed so far are static and can lead to an accumulation of biochemical waste around the tumor model (particularly with spheroids), ultimately affecting cell viability. The next section will discuss dynamic microfluidic models that are able to circumvent some of these limitations and better recapitulate the nutrient diffusion in tumor microenvironments.

### *Microfluidics*

Microfluidic models are often fabricated by constructing microchannels on a chip and integrating various microelements into these channels to precisely control the pressure, flow rate, and flow direction. They can be used to look at gradients in interstitial fluid (IF) pressure, pH, nutrients, and oxygen and together, allow for the study of dynamic aspects of tumor progression. Given the micro size of these models, they permit real-time imaging of cellular dynamics like invasion and migration and are ideal for modelling breast cancer interaction with vasculature.

Microfluidic arrays are high throughput, enabling multiple conditions and hundreds of replicates on a single chip. This can be used to evaluate a range of biochemical and biophysical cues, like flow rates, pressure and oxygen. Fridman et. al. used this as a means to study breast cancer cell chemoresistance under an oxygen gradient ranging from 1% oxygen (hypoxia) to 20% (normoxia) <sup>158</sup>. They found that increased reactive oxygen species production under hypoxic conditions led to drug cytotoxicity levels that are similar to *in vivo* findings, demonstrating the importance of tumor hypoxia in tumor aggressiveness.

The most widely used model recreates invasive ductal carcinoma (the most common type of breast cancer) in the lumen by molding ECM around a rod that is later removed to create an open cavity that can be filled with cancer cells. Media can then flow through this cavity, similar to

the tumor *in vivo*, while providing the option to image cell invasion into the surrounding ECM. Moon et. al. developed a microfluidic structure with a ductal structure of cancer epithelial cells surrounded with a 3D collagen matrix <sup>159</sup>. Invasion of two triple-negative cancer lines (MDA-MB-231, SUM-159T) was clearly observable, while the luminal MCF7 cells did not. One major advantage is that different cell types can be co-cultured long term in a controlled microenvironment, allowing for the bidirectional crosstalk between cancer cells and other tumor-associated cells to be fully evaluated. Models incorporating fibroblasts and tumor-associated macrophages have been used to evaluate breast cancer cell invasiveness in response to tumor-associated stromal cells <sup>160,161</sup>, while an additional lumen cavity can be lined with endothelial cells to observe cancer migration toward vasculature and conditioning of lymphatic vessels <sup>162,163</sup>. Ayuso et. al. created a chamber with dual lumen rods as seen in Figure 2.12 and, through imaging and RT-qPCR, found that MCF7 and MDA-MB-231 cells alone do not negatively impact the physical integrity of the vessel or endothelial cell maintenance, but do trigger lymphangiogenic sprouting <sup>163</sup>.

While microfluidic models can recapitulate many aspects of the TME *in vivo*, some issues persist. For instance, the direction of flow for cell growth may not always mimic that inside the body. A study by Seibel et. al. seeded a microtumor of MDA-MB-231 cells across from a vascularized lumen in collagen I to study breast cancer invasion and escape through lymph vessels <sup>164</sup>. While flow towards the tumor was created by the hydrostatic pressure of an upstream well above the lymph channel, this is a non-physiological flow direction. Additionally, the size of microfluidic models means that only small tumors can be studied in this capacity, neglecting the effects of necrotic tumor cores in metastasis signaling. Finally, there is rarely consistency in model designs, leading to issues with reproducibility.

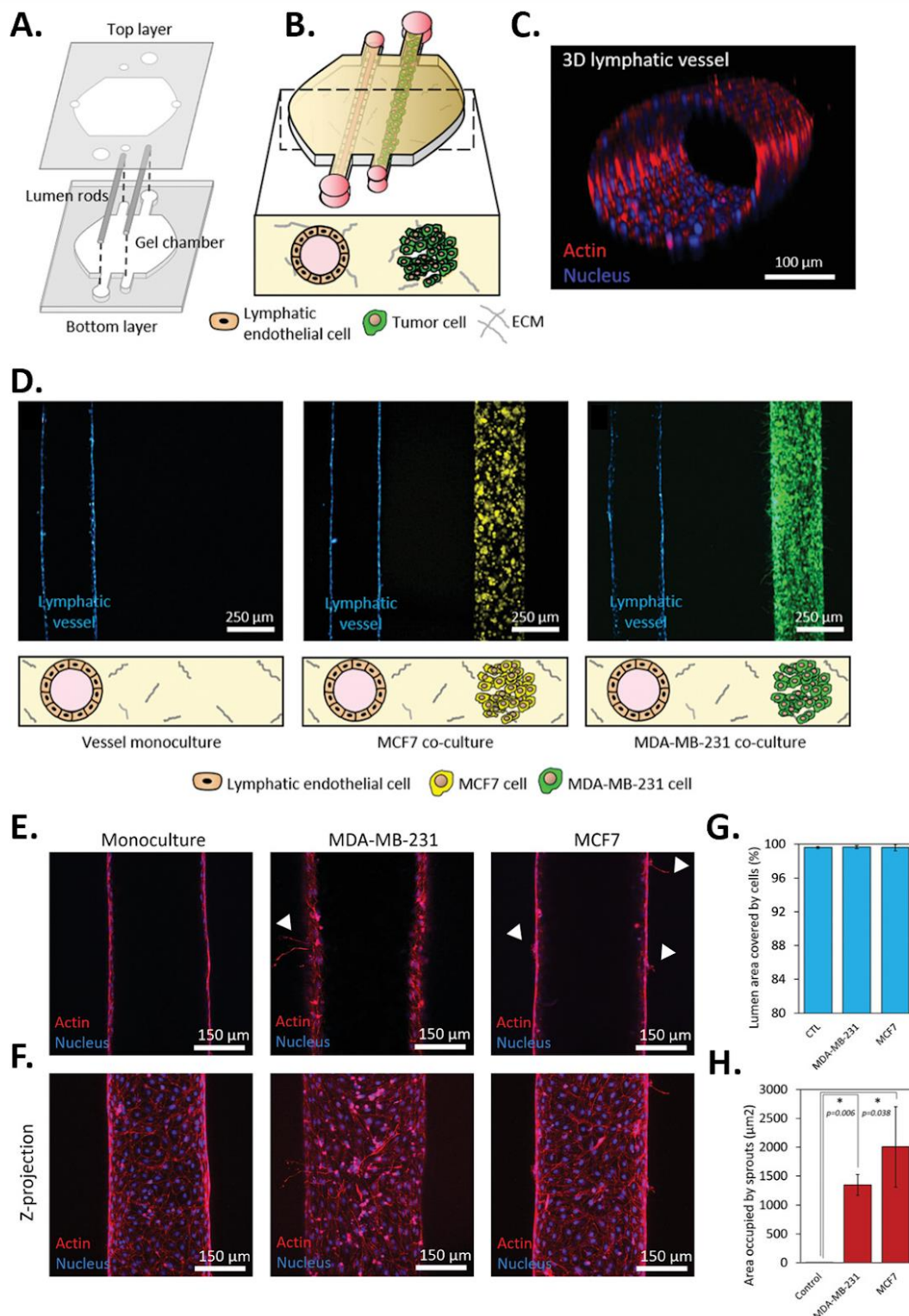


**Figure 2.12:** Dual lumen rods to study tumor cell interaction with lymphatic vessel A) Schematic of the breast tumor-lymphatic microfluidic device. The device consists of two polydimethylsiloxane (PDMS) layers. The bottom layer contains a chamber and microchannels for



suspending two adjacent lumen rods. The top layer contains the ports for fluid exchange. B) Cell culture in the device allows the formation of a lumen lined with primary human lymphatic endothelial cells (HLECs) and a second lumen filled with breast cancer cells. C) Representative confocal image of a 3D lymphatic vessel. D) Representative images of vessel monoculture, coculture with MCF7 cells (in yellow), and coculture with MDA-MB-231 cells (in green) in the device. E) Confocal images showing the middle plane of lymphatic vessels in monoculture and coculture with MCD7 and MDA-MB-231 cells. F) Z-projected images of lymphatic vessels in monoculture and coculture with MCF7 and MDA-MB-231 cells. G) Quantification of cell coverage for each culture condition showing an average percentage of cell coverage >99% for all conditions. H) Crosstalk with the breast cancer cells induced lymphangiogenic sprouting in the vessels. There were no observable sprouts in the monoculture control. Three individual vessels (n = 3) were measured for each culture condition to determine the average permeability value (mean  $\pm$  s.d.). Adapted with permission<sup>163</sup>. 2019, Wiley-VCH

**Table 2.3:** Review of literature on prominent breast cancer microfluidic models

Design	Biological Observations/ Advantages	Limitations	Reference
Parallel 3D lumen configuration mimicking vascular endothelial and mammary epithelial respectively; migration ports connecting each channel  <u>Cells:</u> MCF10A, MCF7, MDA-MB-231	Cells in microfluidic channels consume nutrients and accumulate waste products due to a 3- to 4-fold increase in cell density compared to 2D culture  Allows for migration from both sides, potentially representing cancer invasion and angiogenesis	Does not incorporate perfusion and shear flow over the endothelium  There is no outer layer of myoepithelial cells around the inner luminal epithelial cells	<sup>162</sup>
Tumor region bordered by a stromal outer region of fibroblasts encapsulated in 1:1 mixture of Matrigel and collagen I  <u>Cells:</u> SUM-159, patient-derived cancer-associated fibroblasts (CAFs)	Bidirectional fibroblast-cancer migration visible  Can image cells while in hydrogel, for morphometric analysis	While markers like FAP and $\alpha$ SMA are used to identify CAFs, there is no defined single or set of molecular markers that exclusively define CAFs owing to their heterogeneity	<sup>161</sup>
An array layer of alginate-based cancer spheroids and a gas conditioning layer exposing cells to five oxygen levels ranging from hypoxia (~1%) to ambient air (~20%)  <u>Cells:</u> MCF7, macrophages	High experimental throughput with multiple oxygen levels (1000 docking sites total)  There was a significant increase in reactive oxygen species (ROS) production for both MCF7s and macrophages under 1% oxygen levels	Multilayer structure poses issues with high resolution imaging due to layer thickness and phase changes	<sup>158</sup>
Two parallel collagen channels with macrophages and cancer cells respectively, and sandwiched between nutrient supply channels perfused through a vascular endothelial layer	Model shows bidirectional crosstalk between macrophages and cancer cells  This method could dynamically explore the changes in endothelial cell permeability over time	Cellular crosstalk can involve multiple mechanisms such as exosomes, RNAs, or mechanical forces that were not investigated	<sup>160</sup>

<u>Cells:</u> MDA-MB-231, macrophages, HUVECs	TAMs encouraged the most cancer cell migration compared to other noncancerous cell lines (U937, MCF10A)		
Two layers of microchannels made of PDMS with two PCL electrospun matrices in between  <u>Cells:</u> MCF7, CAMA-1, MDA-MB-231	Shows a way to investigate cancer cell invasion, separate from proteolytic cleavage  Cells and matrix are more accessible than injectable hydrogels, and allow for more analytical approaches	This concept does not incorporate ECM and fails to acknowledge the biochemical influences on invasion  Does not co-culture additional cells with cancer cells	165

## 2.5 Future Outlook

While 3D breast cancer models have come very far and are highly refined modeling systems as compared to 2D *in vitro* or 3D *in vivo* models, there are still improvements to be made. A summary of each 3D modeling technique discussed thus far is presented in Figure 2.13, highlighting the distinct advantages and limitations associated with each approach. These specific characteristics should be carefully weighed when selecting a model to address a particular research question. As research needs continue to grow more complex, it is crucial to refine existing models and innovate new approaches that address current gaps. Future work is directed towards improving/developing reproducibility of results, easier quantification of data, and personalized modelling methods.

### 2.5.1 Bioelectronic Assay Systems for *In Vitro* Modeling

Towards the goal of data quantification, a relatively novel technique has emerged: bioelectronic assays. Bioelectronic assays can measure values like impedance (resistance and reactance) or capacitance by passing small electrical currents through electrodes embedded in a cell culturing platform. The flow of electrons is obstructed by the presence of cells, media, and

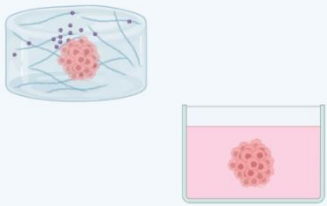
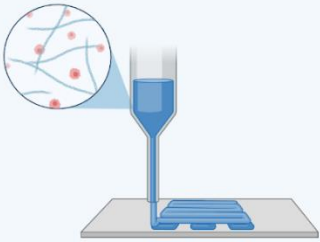
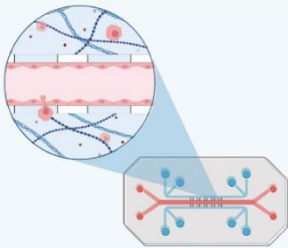
ECM materials, offering a sensitive, label-free, and non-destructive method to continuously monitor cells in real time, allowing the assessment of cellular kinetics, like proliferation and stimuli/drug response. There are a variety of commercially available electric cell-substrate impedance sensing (ECIS) systems, and many researchers build their own platforms<sup>166-169</sup>. Hedayatipour et. al. provides an in-depth explanation and evaluation of the circuit topologies used for cell impedance measurement<sup>170</sup>. This assay technique has been used with BC cells to evaluate migration<sup>171</sup>, drug interactions<sup>166,169</sup>, and communication and interaction via co-cultures<sup>168</sup> and, as more research is done, the varieties and options for ECIS assays will increase. One notable example of this is Pan et. al. who have developed a 3D microgroove impedance sensing model that can detect changes in cancer cell growth while encapsulated in Matrigel<sup>167</sup>. They found that lung cancer spheroids suspended in Matrigel exhibited a gradient in response to chemotherapeutic drug cisplatin and more chemoresistance than the same cells in 2D culture. Lee et. al. conducted a similar study using capacitance sensors using four parallel electrodes stacked along the y-axis of a well, measuring the layered cytotoxicity of doxorubicin on MCF7 cells within an alginate hydrogel<sup>172</sup>. While this method lacks the specificity of other assays, it allows for continuous maintenance of cell behavior over an extended period of time and can provide a lot of information from a small population of cells. This is particularly useful if using primary cells from a biopsy, where only a small population of cells is available, making it a possible option for personalized cancer modeling.

### 2.5.2 Organoids and Patient-specific Models

Currently, cancer treatment approaches are mostly trial-and-error, and it's not entirely known how a patient's cancer will respond to different types of treatment, for example like if drug resistance will occur. Because of this, patients are often subjected to time-consuming and arduous treatment regimens. As a result, many researchers are moving towards developing personalized 3D breast cancer models that can provide translational information about patient cancer aggressiveness and treatment options. Patient-derived tumor components can be incorporated in bioprinted and microfluidic systems to study tumor behavior and response to pharmacological compounds <sup>161,173,174</sup>, however tumor organoids are a more popular option for studying physiologically relevant drug response. Tumor organoids can be a powerful *in vitro* tool for their ability to resemble tumor tissue-specific architecture. Organoids are miniature 3D structures that mimic the functional, structural and organizational complexity of human tissues and organs and they can be a powerful *in vitro* tool for their ability to resemble tumor tissue-specific architecture. Tumor organoids can recapitulate genomic and histological features of the original tumor from which they came, hence they can be utilized for personal cancer medicine. Chen et. al. established organoids from 99 breast cancer patients with a 75% success rate, focusing on patients with high-risk clinical features, like drug-resistance and metastasis <sup>175</sup>. They found that organoid lines had inherited histological features of their parental tumor, as well as preserved receptor status and Ki-67. They were able to use these organoids to conduct high throughput drug screening with 49 drugs and found that the drug-resistant patient-derived organoids showed an especially high resistivity to a wide range of the tested drugs, demonstrating that organoids not only serve as a pre-clinical model for broader cancer studies but also can provide personalized therapy recommendations for patients with advanced disease. Overall, organoids are a promising tool for accurately modelling

tumor drug response, with 14 clinical trials actively recruiting patients at the time of publication

176-189

3D In Vitro Modelling Methods	✓ Advantages	✗ Limitations
 <p>Spheroids</p>	<ul style="list-style-type: none"> <li>• Architecture resembles tumor</li> <li>• Large spheroids recreate the hypoxic core and metabolic gradients of aggressive tumors</li> </ul>	<ul style="list-style-type: none"> <li>• Variability in tumor shape and volume affecting spheroid behavior</li> <li>• Lack of vasculature</li> </ul>
 <p>Bioprinting</p>	<ul style="list-style-type: none"> <li>• High resolution fabrication with controlled mechanical properties</li> <li>• Ideal for co-cultures with highly controlled cell-to-cell exposure</li> </ul>	<ul style="list-style-type: none"> <li>• Bioink options must be biocompatible and printing stable</li> <li>• Can be a costly and repetitive process to optimize</li> </ul>
 <p>Microfluidics</p>	<ul style="list-style-type: none"> <li>• Incorporates dynamic flow</li> <li>• Small size makes imaging easier</li> <li>• Nutrient flow allows cells to be cultured together for longer</li> </ul>	<ul style="list-style-type: none"> <li>• Model flow is not always physiologically similar</li> <li>• Difficult to standardize and scale up</li> </ul>

**Figure 2.13:** Advantages and limitations of 3D *in vitro* modeling methods. Created in BioRender. Gomillion, C. (2025) <https://BioRender.com/4xv1ccj>

### 2.5.3 *In Silica* Modeling Systems

All modeling methods discussed thus far are incredibly important to the future of breast cancer research, however they can be time consuming to iterate and resource intensive. Computational models should be used in conjunction with these *in vitro* methods to help with data analysis and predictive modelling of cell behavior under various modelling conditions. For

example, the Mohammadrezaei et. al. paper discussed earlier developed a predictive model to understand the post-printing proliferation and migration of cancer cells in commonly used gelatin/alginate structures <sup>154</sup>. In another notable paper, Baskaran et. al. studied the correlation between cell shape and ECM-driven 3D cell invasion <sup>67</sup>. Using principal component analysis and partial least squares regression, their model suggests that cell adhesion, based on cell morphology parameters like form factor, area, and eccentricity, can accurately predict 3D invasion. Computational modelling compliments high throughput 2D data collection well and facilitates a deeper understanding of cell behaviors and signaling dynamics <sup>190</sup>. Overall, computational models and machine learning can help with *in vitro* model optimization and data processing and should be used in conjunction with both 2D and 3D *in vitro* modeling platforms to determine the most significant influences on breast cancer metastasis.

## 2.6 Conclusion

Breast cancer metastasis is an incredibly complex process. Tumors are considered abnormal organs, displaying several biochemical gradients and physical properties that significantly affect cell behavior. There are multiple stromal and epithelial cells associated with the TME, and cancer cells exploit several ECM proteins present in the TME. While we understand the relationship between cancer phenotype and tumor environmental factors, like hypoxia, ECM stiffening, and cytokine secretion, the molecular/mechanical underpinnings of these processes are not fully understood. 2D models allow precise control of variables (e.g. substrate stiffness, ECM composition, growth factor gradients) but do not fully recapitulate the complexity of the tumor microenvironment, as 3D systems do. Therefore, a complementary approach should be used, combining 2D and 3D models to address research questions.

While 3D *in vitro* models aim to replicate the complexity of the TME, a critical question in the field is: how simple is complex enough? That is, how does one choose a model that provides the appropriate level of detail to address specific research questions, balancing simplicity with the need for physiological relevance? As 3D modelling techniques continue to advance, determining the appropriate level of complexity is crucial for accurately recreating tumoral tissue, while maintaining enough simplicity for easy modification and predictability. Although there is no straightforward answer to this question, breast cancer models that successfully balance these factors will play a pivotal role in advancing research and therapeutic development in the future.

## 2.7 References

1. Sung, H., *et al.* Global cancer statistics 2020: GLOBOCAN estimates of incidence and mortality worldwide for 36 cancers in 185 countries. **71**, 209-249 (2021).
2. Siegel, R.L., Miller, K.D. & Jemal, A.J.C.a.c.j.f.c. Cancer statistics, 2019. **69**, 7-34 (2019).
3. Katti, K.S., Jasuja, H., Kar, S. & Katti, D.R. Nanostructured biomaterials for in vitro models of bone metastasis cancer. *Current opinion in biomedical engineering* **17**, 100254 (2021).
4. Nuckhir, M., Withey, D., Cabral, S., Harrison, H. & Clarke, R.B. State of the art modelling of the breast cancer metastatic microenvironment: where are we? *Journal of Mammary Gland Biology and Neoplasia* **29**, 14 (2024).
5. Kolahi Azar, H., *et al.* The progressive trend of modeling and drug screening systems of breast cancer bone metastasis. *Journal of Biological Engineering* **18**, 14 (2024).
6. Fallert, L., Urigoitia-Asua, A., Cipitria, A. & de Aberasturi, D.J. Dynamic 3D in vitro lung models: applications of inorganic nanoparticles for model development and characterization. *Nanoscale* **16**, 10880-10900 (2024).
7. Jin, X. & Mu, P. Targeting breast cancer metastasis. *Breast cancer: basic and clinical research* **9**, BCBCR. S25460 (2015).
8. Nyga, A., Cheema, U. & Loizidou, M. 3D tumour models: novel in vitro approaches to cancer studies. *Journal of cell communication and signaling* **5**, 239-248 (2011).
9. Zhang, Y.S., *et al.* Bioprinting the cancer microenvironment. *ACS biomaterials science & engineering* **2**, 1710-1721 (2016).
10. Vilchez Mercedes, S.A., *et al.* Decoding leader cells in collective cancer invasion. *Nature Reviews Cancer* **21**, 592-604 (2021).
11. Parlani, M., Jorgez, C. & Friedl, P. Plasticity of cancer invasion and energy metabolism. *Trends in cell biology* **33**, 388-402 (2023).
12. Kopp, H.-G., Placke, T. & Salih, H.R.J.C.r. Platelet-derived transforming growth factor- $\beta$  down-regulates NKG2D thereby inhibiting natural killer cell antitumor reactivity. **69**, 7775-7783 (2009).
13. Coffelt, S.B., *et al.* IL-17-producing  $\gamma\delta$  T cells and neutrophils conspire to promote breast cancer metastasis. **522**, 345-348 (2015).



14. Spiegel, A., *et al.* Neutrophils suppress intraluminal NK cell-mediated tumor cell clearance and enhance extravasation of disseminated carcinoma cells. **6**, 630-649 (2016).
15. Ma, Y.-H.V., Middleton, K., You, L., Sun, Y.J.M. & Nanoengineering. A review of microfluidic approaches for investigating cancer extravasation during metastasis. **4**, 1-13 (2018).
16. Reymond, N., d'Agua, B.B. & Ridley, A.J.J.N.R.C. Crossing the endothelial barrier during metastasis. **13**, 858-870 (2013).
17. Giaquinto, A.N., *et al.* Breast cancer statistics 2024. *CA: a cancer journal for clinicians* **74**, 477-495 (2024).
18. Dai, X., Cheng, H., Bai, Z. & Li, J.J.J.o.C. Breast cancer cell line classification and its relevance with breast tumor subtyping. **8**, 3131 (2017).
19. Kyuno, D., *et al.* Role of tight junctions in the epithelial-to-mesenchymal transition of cancer cells. *Biochimica et Biophysica Acta (BBA)-Biomembranes* **1863**, 183503 (2021).
20. Moccia, C. & Haase, K. Engineering breast cancer on-chip—moving toward subtype specific models. *Frontiers in Bioengineering and Biotechnology* **9**, 694218 (2021).
21. Beykou, M., *et al.* Proteomic characterisation of triple negative breast cancer cells following CDK4/6 inhibition. **9**, 395 (2022).
22. Mandapati, A., Lukong, K.E.J.J.o.C.R. & Oncology, C. Triple negative breast cancer: approved treatment options and their mechanisms of action. 1-19 (2022).
23. Angajala, A., *et al.* Quadruple negative breast cancers (QNBC) demonstrate subtype consistency among primary and recurrent or metastatic breast cancer. **12**, 493-501 (2019).
24. Saini, G., Bhattarai, S., Gogineni, K. & Aneja, R.J.J.G.O. Quadruple-negative breast cancer: An uneven playing field. **6**(2020).
25. Kensler, K.H., *et al.* Prognostic and predictive value of androgen receptor expression in postmenopausal women with estrogen receptor-positive breast cancer: results from the Breast International Group Trial 1–98. **21**, 1-11 (2019).
26. Zheng, G., *et al.* Familial associations of female breast cancer with other cancers. **141**, 2253-2259 (2017).
27. Cobain, E.F., Milliron, K.J. & Merajver, S.D. Updates on breast cancer genetics: Clinical implications of detecting syndromes of inherited increased susceptibility to breast cancer. in *Seminars in oncology*, Vol. 43 528-535 (Elsevier, 2016).

28. Wendt, C. & Margolin, S.J.A.O. Identifying breast cancer susceptibility genes—a review of the genetic background in familial breast cancer. **58**, 135-146 (2019).
29. Plava, J., *et al.* Permanent Pro-Tumorigenic Shift in Adipose Tissue-Derived Mesenchymal Stromal Cells Induced by Breast Malignancy. **9**, 480 (2020).
30. Ghosh, S., *et al.* Tumor suppressor BRCA1 inhibits a breast cancer-associated promoter of the aromatase gene (CYP19) in human adipose stromal cells. **292**, E246-E252 (2007).
31. Hemalatha, S.K., *et al.* Brcal defective breast Cancer cells induce in vitro transformation of cancer associated fibroblasts (CAFs) to metastasis associated fibroblasts (MAF). **8**, 13903 (2018).
32. Jaspers, J.E., *et al.* BRCA2-Deficient Sarcomatoid Mammary Tumors Exhibit Multidrug ResistanceMultidrug Resistance of Sarcomatoid Mouse Mammary Tumors. **75**, 732-741 (2015).
33. Wellenstein, M.D., *et al.* Loss of p53 triggers WNT-dependent systemic inflammation to drive breast cancer metastasis. **572**, 538-542 (2019).
34. Muniraj, N., *et al.* Induction of STK11-dependent cytoprotective autophagy in breast cancer cells upon honokiol treatment. **6**, 81 (2020).
35. Faubert, B., *et al.* Loss of the tumor suppressor LKB1 promotes metabolic reprogramming of cancer cells via HIF-1 $\alpha$ . **111**, 2554-2559 (2014).
36. Chen, I., *et al.* Clinical relevance of liver kinase B1 (LKB1) protein and gene expression in breast cancer. **6**, 1-10 (2016).
37. Zyla, R.E., Hahn, E. & Hodgson, A.J.J.o.C.P. Gene of the month: STK11. **74**, 681-685 (2021).
38. Fujisawa, F., *et al.* STK11 loss drives rapid progression in a breast cancer patient resulting in pulmonary tumor thrombotic microangiopathy. **28**, 765-771 (2021).
39. Mossmann, D., Park, S. & Hall, M.N.J.N.R.C. mTOR signalling and cellular metabolism are mutual determinants in cancer. **18**, 744-757 (2018).
40. Dongre, A. & Weinberg, R.A.J.N.r.M.c.b. New insights into the mechanisms of epithelial–mesenchymal transition and implications for cancer. **20**, 69-84 (2019).
41. Corso, G., *et al.* E-cadherin deregulation in breast cancer. **24**, 5930-5936 (2020).
42. Qi, Y., *et al.* PTEN suppresses epithelial–mesenchymal transition and cancer stem cell activity by downregulating Abi1. **10**, 1-13 (2020).

43. Chen, G., *et al.* RILPL2 regulates breast cancer proliferation, metastasis, and chemoresistance via the TUBB3/PTEN pathway. **9**, 1583 (2019).
44. Cheng, I., *et al.* Association between ambient air pollution and breast cancer risk: the multiethnic cohort study. **146**, 699-711 (2020).
45. White, A.J., *et al.* Air pollution, clustering of particulate matter components, and breast cancer in the sister study: a US-wide cohort. **127**, 107002 (2019).
46. Macacu, A., Autier, P., Boniol, M., Boyle, P.J.B.c.r. & treatment. Active and passive smoking and risk of breast cancer: a meta-analysis. **154**, 213-224 (2015).
47. Jung, S., *et al.* Alcohol consumption and breast cancer risk by estrogen receptor status: in a pooled analysis of 20 studies. **45**, 916-928 (2016).
48. Kerr, J., Anderson, C. & Lippman, S.M.J.T.L.O. Physical activity, sedentary behaviour, diet, and cancer: an update and emerging new evidence. **18**, e457-e471 (2017).
49. Sung, H., *et al.* Global patterns in excess body weight and the associated cancer burden. **69**, 88-112 (2019).
50. Cui, B., *et al.* Stress-induced epinephrine enhances lactate dehydrogenase A and promotes breast cancer stem-like cells. **129**, 1030-1046 (2019).
51. Kresovich, J.K., *et al.* Methylation-based biological age and breast cancer risk. *JNCI: Journal of the National Cancer Institute* **111**, 1051-1058 (2019).
52. Bowers, L.W., *et al.* Reversing the Genomic, Epigenetic, and Triple-Negative Breast Cancer-Enhancing Effects of Obesity. **15**, 581-594 (2022).
53. Stephens, K.E., *et al.* Associations between genetic and epigenetic variations in cytokine genes and mild persistent breast pain in women following breast cancer surgery. **99**, 203-213 (2017).
54. Donovan, M.G., Wren, S.N., Cenker, M., Selmin, O.I. & Romagnolo, D.F.J.B.J.o.P. Dietary fat and obesity as modulators of breast cancer risk: Focus on DNA methylation. **177**, 1331-1350 (2020).
55. Murphy, M.E., *et al.* A functionally significant SNP in TP53 and breast cancer risk in African-American women. **3**, 5 (2017).
56. Davis, M., *et al.* Identification of distinct heterogenic subtypes and molecular signatures associated with African ancestry in triple negative breast cancer using quantified genetic ancestry models in admixed race populations. **12**, 1220 (2020).

57. Jennis, M., *et al.* An African-specific polymorphism in the TP53 gene impairs p53 tumor suppressor function in a mouse model. **30**, 918-930 (2016).
58. Levine, A.J.J.O. Spontaneous and inherited TP53 genetic alterations. **40**, 5975-5983 (2021).
59. Newman, L.A., *et al.* Hereditary susceptibility for triple negative breast cancer associated with Western Sub-Saharan African Ancestry: results from an International Surgical Breast Cancer Collaborative. **270**, 484-492 (2019).
60. Jenkins, B.D., *et al.* Atypical chemokine receptor 1 (DARC/ACKR1) in breast tumors is associated with survival, circulating chemokines, tumor-infiltrating immune cells, and African ancestry. **28**, 690-700 (2019).
61. Jinna, N., *et al.* The DARC Side of Inflamm-Aging: Duffy Antigen Receptor for Chemokines (DARC/ACKR1) as a Potential Biomarker of Aging, Immunosenescence, and Breast Oncogenesis among High-Risk Subpopulations. **11**, 3818 (2022).
62. Llanos, A.A., *et al.* Immunohistochemical analysis of adipokine and adipokine receptor expression in the breast tumor microenvironment: associations of lower leptin receptor expression with estrogen receptor-negative status and triple-negative subtype. **22**, 1-16 (2020).
63. Llanos, A.A., *et al.* Gene expression of adipokines and adipokine receptors in the tumor microenvironment: associations of lower expression with more aggressive breast tumor features. **185**, 785-798 (2021).
64. Nam, G.E., Zhang, Z.-F., Rao, J., Zhou, H. & Jung, S.Y.J.F.i.O. Interactions between adiponectin-pathway polymorphisms and obesity on postmenopausal breast cancer risk among African American women: The WHI SHARe Study. **11**, 698198 (2021).
65. Keren, K., *et al.* Mechanism of shape determination in motile cells. **453**, 475-480 (2008).
66. Lee, J., Ishihara, A., Theriot, J.A. & Jacobson, K.J.N. Principles of locomotion for simple-shaped cells. **362**, 167-171 (1993).
67. Baskaran, J.P., *et al.* Cell shape, and not 2D migration, predicts extracellular matrix-driven 3D cell invasion in breast cancer. **4**, 026105 (2020).
68. Weinberg, R.A. *The biology of cancer*, (Garland science, 2013).
69. Lehmann, B.D., *et al.* Identification of human triple-negative breast cancer subtypes and preclinical models for selection of targeted therapies. **121**, 2750-2767 (2011).
70. Hapach, L.A., *et al.* Phenotypic heterogeneity and metastasis of breast cancer cells. **81**, 3649-3663 (2021).

71. Holliday, D.L. & Speirs, V.J.B.c.r. Choosing the right cell line for breast cancer research. **13**, 1-7 (2011).
72. Kenny, P.A., *et al.* The morphologies of breast cancer cell lines in three-dimensional assays correlate with their profiles of gene expression. **1**, 84-96 (2007).
73. Lambert, A.W., Pattabiraman, D.R. & Weinberg, R.A.J.C. Emerging biological principles of metastasis. **168**, 670-691 (2017).
74. Dekker, Y., Le Dévédec, S.E., Danen, E.H. & Liu, Q.J.G. Crosstalk between hypoxia and extracellular matrix in the tumor microenvironment in breast cancer. **13**, 1585 (2022).
75. Bahcecioglu, G., Basara, G., Ellis, B.W., Ren, X. & Zorlutuna, P.J.A.b. Breast cancer models: Engineering the tumor microenvironment. **106**, 1-21 (2020).
76. Patwardhan, S., Mahadik, P., Shetty, O. & Sen, S.J.B. ECM stiffness-tuned exosomes drive breast cancer motility through thrombospondin-1. **279**, 121185 (2021).
77. Azimi, I., *et al.* Activation of the ion channel TRPV4 induces epithelial to mesenchymal transition in breast cancer cells. **21**, 9417 (2020).
78. Lee, W., *et al.* TRPV4 plays a role in breast cancer cell migration via Ca<sup>2+</sup>-dependent activation of AKT and downregulation of E-cadherin cell cortex protein. **6**, e338-e338 (2017).
79. Lee, W.H., *et al.* TRPV4 regulates breast cancer cell extravasation, stiffness and actin cortex. **6**, 27903 (2016).
80. Wang, A.Y., *et al.* DDR1 associates with TRPV4 in cell-matrix adhesions to enable calcium-regulated myosin activity and collagen compaction. **237**, 2451-2468 (2022).
81. Goswami, R., *et al.* Mechanosensing by TRPV4 mediates stiffness-induced foreign body response and giant cell formation. **14**, eabd4077 (2021).
82. Kärki, T. & Tojkander, S.J.B. Trpv protein family—from mechanosensing to cancer invasion. **11**, 1019 (2021).
83. Karamanou, K., *et al.* Evaluation of lumican effects on morphology of invading breast cancer cells, expression of integrins and downstream signaling. **287**, 4862-4880 (2020).
84. Yousefi, H., *et al.* Understanding the role of integrins in breast cancer invasion, metastasis, angiogenesis, and drug resistance. **40**, 1043-1063 (2021).
85. Paavolainen, O. & Peuhu, E. Integrin-mediated adhesion and mechanosensing in the mammary gland. in *Seminars in Cell & Developmental Biology*, Vol. 114 113-125 (Elsevier, 2021).

86. Chen, X., *et al.* A feedforward mechanism mediated by mechanosensitive ion channel PIEZO1 and tissue mechanics promotes glioma aggression. **100**, 799-815. e797 (2018).
87. Pan, M.-R., *et al.* FAK is required for tumor metastasis-related fluid microenvironment in triple-negative breast cancer. **8**, 38 (2019).
88. Shiau, J.-P., *et al.* FAK regulates VEGFR2 expression and promotes angiogenesis in triple-negative breast cancer. **9**, 1789 (2021).
89. Ma, H., *et al.* Periostin promotes colorectal tumorigenesis through integrin-FAK-Src pathway-mediated YAP/TAZ activation. **30**, 793-806. e796 (2020).
90. Wu, H.-J., Hao, M., Yeo, S.K. & Guan, J.-L.J.O. FAK signaling in cancer-associated fibroblasts promotes breast cancer cell migration and metastasis by exosomal miRNAs-mediated intercellular communication. **39**, 2539-2549 (2020).
91. Linderholm, B., Tavelin, B., Grankvist, K. & Henriksson, R.J.B.j.o.c. Does vascular endothelial growth factor (VEGF) predict local relapse and survival in radiotherapy-treated node-negative breast cancer? **81**, 727-732 (1999).
92. Cancemi, P., Buttacavoli, M., Roz, E. & Feo, S.J.I.j.o.m.s. Expression of alpha-enolase (ENO1), Myc promoter-binding protein-1 (MBP-1) and matrix metalloproteinases (MMP-2 and MMP-9) reflect the nature and aggressiveness of breast tumors. **20**, 3952 (2019).
93. Yousef, E.M., Tahir, M.R., St-Pierre, Y. & Gaboury, L.A.J.B.c. MMP-9 expression varies according to molecular subtypes of breast cancer. **14**, 1-12 (2014).
94. Jiang, H. & Li, H.J.B.c. Prognostic values of tumoral MMP2 and MMP9 overexpression in breast cancer: A systematic review and meta-analysis. **21**, 1-13 (2021).
95. Castagnino, A., *et al.* Coronin 1C promotes triple-negative breast cancer invasiveness through regulation of MT1-MMP traffic and invadopodia function. **37**, 6425-6441 (2018).
96. Zu, X., *et al.* Transforming growth factor- $\beta$  signaling in tumor initiation, progression and therapy in breast cancer: an update. **347**, 73-84 (2012).
97. Allington, T.M. & Schiemann, W.P.J.C.T.O. The Cain and Abl of epithelial-mesenchymal transition and transforming growth factor- $\beta$  in mammary epithelial cells. **193**, 98-113 (2011).
98. Poletto, A.C., *et al.* Oleic and linoleic fatty acids downregulate Slc2a4/GLUT4 expression via NF $\kappa$ B and SREBP1 in skeletal muscle cells. **401**, 65-72 (2015).

99. Rutledge, A.C. & Adeli, K.J.N.r. Fructose and the metabolic syndrome: pathophysiology and molecular mechanisms. **65**, S13-S23 (2007).
100. Yang, J., Bahcecioglu, G. & Zorlutuna, P.J.B. The extracellular matrix and vesicles modulate the breast tumor microenvironment. **7**, 124 (2020).
101. Sarkar, T., *et al.* FOXP3/HAT1 axis controls treg infiltration in the tumor microenvironment by inducing CCR4 expression in breast cancer. **13**, 20 (2022).
102. Munir, M.T., *et al.* Tumor-associated macrophages as multifaceted regulators of breast tumor growth. **22**, 6526 (2021).
103. Graf, F., Horn, P., Ho, A.D., Boutros, M. & Maercker, C. The extracellular matrix proteins type I collagen, type III collagen, fibronectin, and laminin 421 stimulate migration of cancer cells. *The FASEB Journal* **35**, e21692 (2021).
104. Bijian, K., *et al.* Targeting focal adhesion turnover in invasive breast cancer cells by the purine derivative reversine. **109**, 2810-2818 (2013).
105. Indra, I., *et al.* An in vitro correlation of mechanical forces and metastatic capacity. **8**, 015015 (2011).
106. Hao, Y., Baker, D. & ten Dijke, P. TGF- $\beta$ -Mediated Epithelial-Mesenchymal Transition and Cancer Metastasis. **20**, 2767 (2019).
107. Li, Z.-X., *et al.* TGF- $\beta$ 1 promotes human breast cancer angiogenesis and malignant behavior by regulating endothelial-mesenchymal transition. *Frontiers in Oncology* **12**, 1051148 (2022).
108. Wu, J., *et al.* RBM38 is involved in TGF- $\beta$ -induced epithelial-to-mesenchymal transition by stabilising zonula occludens-1 mRNA in breast cancer. **117**, 675-684 (2017).
109. Niu, J., *et al.* DKK1 inhibits breast cancer cell migration and invasion through suppression of  $\beta$ -catenin/MMP7 signaling pathway. **19**, 1-13 (2019).
110. Conner, S.J., *et al.* Cell morphology best predicts tumorigenicity and metastasis in vivo across multiple TNBC cell lines of different metastatic potential. *Breast Cancer Research* **26**, 43 (2024).
111. Byrne, C.E., *et al.* Evaluation of extracellular matrix composition to improve breast cancer modeling. *Tissue Engineering Part A* **27**, 500-511 (2021).
112. Barney, L.E., *et al.* A cell-ECM screening method to predict breast cancer metastasis. *Integrative Biology* **7**, 198-212 (2015).

113. Ermis, M., Antmen, E., Kuren, O., Demirci, U. & Hasirci, V. A cell culture chip with transparent, micropillar-decorated bottom for live cell imaging and screening of breast cancer cells. *Micromachines* **13**, 93 (2022).
114. Vu, H.H., Nguyen, N.-T., Yadav, S., Nguyen, T.T.H. & Kashaninejad, N. Roles of Micropillar Topography and Surface Energy on Cancer Cell Dynamics. *Technologies* **12**, 130 (2024).
115. Hosseinkazemi, H. Staats-und Universitätsbibliothek Hamburg Carl von Ossietzky (2024).
116. Biriz, N. & Canturk, Z. Investigation of the immunological effects of escitalopram oxalate in the breast cancer co-culture model. *Asian Biomedicine: Research, Reviews and News* **18**, 133 (2024).
117. Nordin, F.J., *et al.* Immunomodulatory potential of Clinacanthus nutans extracts in the co-culture of triple-negative breast cancer cells, MDA-MB-231, and THP-1 macrophages. *PLoS One* **16**, e0256012 (2021).
118. Li, W., *et al.* Multiple comparisons of three different sources of biomaterials in the application of tumor tissue engineering in vitro and in vivo. **130**, 166-176 (2019).
119. Brett, E.A., Sauter, M.A., Machens, H.-G., Duscher, D.J.C. & Metabolism. Tumor-associated collagen signatures: pushing tumor boundaries. **8**, 1-5 (2020).
120. Gong, X., Kulwatno, J. & Mills, K.J.A.B. Rapid fabrication of collagen bundles mimicking tumor-associated collagen architectures. **108**, 128-141 (2020).
121. Koorman, T., *et al.* Spatial collagen stiffening promotes collective breast cancer cell invasion by reinforcing extracellular matrix alignment. **41**, 2458-2469 (2022).
122. Park, H.-J. & Helfman, D.M.J.S.r. Up-regulated fibronectin in 3D culture facilitates spreading of triple negative breast cancer cells on 2D through integrin  $\beta$ -5 and Src. **9**, 1-14 (2019).
123. Luo, J., *et al.* SRC kinase-mediated signaling pathways and targeted therapies in breast cancer. **24**, 1-17 (2022).
124. Agrawal, R., Kumar, A., Mohammed, M.K. & Singh, S. Biomaterial types, properties, medical applications, and other factors: a recent review. *Journal of Zhejiang University-SCIENCE A* **24**, 1027-1042 (2023).
125. Brovold, M., *et al.* Naturally-derived biomaterials for tissue engineering applications. *Novel biomaterials for regenerative medicine*, 421-449 (2018).



126. Datta, P., Dey, M., Ataie, Z., Unutmaz, D. & Ozbolat, I.T. 3D bioprinting for reconstituting the cancer microenvironment. *NPJ precision oncology* **4**, 18 (2020).
127. Foty, R. A simple hanging drop cell culture protocol for generation of 3D spheroids. *Journal of visualized experiments: JoVE*, 2720 (2011).
128. Dhandapani, H., Siddiqui, A., Karadkar, S. & Tayalia, P. In vitro 3D spheroid model preserves tumor microenvironment of hot and cold breast cancer subtypes. *Advanced Healthcare Materials* **12**, 2300164 (2023).
129. Malhão, F., Macedo, A.C., Ramos, A.A. & Rocha, E. Morphometrical, morphological, and immunocytochemical characterization of a tool for cytotoxicity research: 3D cultures of breast cell lines grown in ultra-low attachment plates. *Toxics* **10**, 415 (2022).
130. Hofmann, S., Cohen-Harazi, R., Maizels, Y. & Koman, I.J.T.c.r. Patient-derived tumor spheroid cultures as a promising tool to assist personalized therapeutic decisions in breast cancer. **11**, 134 (2022).
131. Perche, F., Torchilin, V.P.J.C.b. & therapy. Cancer cell spheroids as a model to evaluate chemotherapy protocols. **13**, 1205-1213 (2012).
132. Zhao, L., *et al.* A 3D printed hanging drop dripper for tumor spheroids analysis without recovery. **9**, 19717 (2019).
133. Riffle, S., Hegde, R.S.J.J.o.E. & Research, C.C. Modeling tumor cell adaptations to hypoxia in multicellular tumor spheroids. **36**, 1-10 (2017).
134. Huang, Y.L., *et al.* Tumor spheroids under perfusion within a 3D microfluidic platform reveal critical roles of cell-cell adhesion in tumor invasion. **10**, 1-11 (2020).
135. Lao, Z., *et al.* Improved methods to generate spheroid cultures from tumor cells, tumor cells & fibroblasts or tumor-fragments: Microenvironment, microvesicles and MiRNA. **10**, e0133895 (2015).
136. Lamichhane, S.P., *et al.* Recapitulating epithelial tumor microenvironment in vitro using three dimensional tri-culture of human epithelial, endothelial, and mesenchymal cells. **16**, 1-12 (2016).
137. Majety, M., Pradel, L.P., Gies, M. & Ries, C.H.J.P.o. Fibroblasts influence survival and therapeutic response in a 3D co-culture model. **10**, e0127948 (2015).
138. Karrobi, K., *et al.* Fluorescence Lifetime Imaging Microscopy (FLIM) reveals spatial-metabolic changes in 3D breast cancer spheroids. **13**, 3624 (2023).
139. Zaroni, M., *et al.* Modeling neoplastic disease with spheroids and organoids. **13**, 1-15 (2020).

140. Zandoni, M., *et al.* 3D tumor spheroid models for in vitro therapeutic screening: a systematic approach to enhance the biological relevance of data obtained. **6**, 19103 (2016).
141. Chen, B., *et al.* High-throughput acoustofluidic fabrication of tumor spheroids. **19**, 1755-1763 (2019).
142. Wu, Z., *et al.* Scaffold-free generation of heterotypic cell spheroids using acoustofluidics. **21**, 3498-3508 (2021).
143. Blaeser, A., Campos, D.F.D. & Fischer, H. 3D bioprinting of cell-laden hydrogels for advanced tissue engineering. *Current Opinion in Biomedical Engineering* **2**, 58-66 (2017).
144. Albritton, J.L. & Miller, J.S. 3D bioprinting: improving in vitro models of metastasis with heterogeneous tumor microenvironments. *Disease models & mechanisms* **10**, 3-14 (2017).
145. Loai, S., *et al.* Clinical perspectives on 3D bioprinting paradigms for regenerative medicine. (2019).
146. Pati, F., Gantelius, J. & Svahn, H.A. 3D bioprinting of tissue/organ models. *Angewandte Chemie International Edition* **55**, 4650-4665 (2016).
147. González-Callejo, P., *et al.* 3D bioprinted breast tumor-stroma models for pre-clinical drug testing. *Materials Today Bio* **23**, 100826 (2023).
148. Shi, W., He, R. & Liu, Y. 3D printing scaffolds with hydrogel materials for biomedical applications. *Eur. J. Biomed. Res* **1**, 3-8 (2015).
149. Jaidev, L. & Chatterjee, K. Surface functionalization of 3D printed polymer scaffolds to augment stem cell response. *Materials & Design* **161**, 44-54 (2019).
150. Svanström, A., *et al.* Optimized alginate-based 3D printed scaffolds as a model of patient derived breast cancer microenvironments in drug discovery. **16**, 045046 (2021).
151. Blanco-Fernandez, B., *et al.* Bioprinting decellularized breast tissue for the development of three-dimensional breast cancer models. **14**, 29467-29482 (2022).
152. Horder, H., *et al.* Bioprinting and differentiation of adipose-derived stromal cell spheroids for a 3D breast cancer-adipose tissue model. **10**, 803 (2021).
153. Knowlton, S., Onal, S., Yu, C.H., Zhao, J.J. & Tasoglu, S. Bioprinting for cancer research. *Trends in biotechnology* **33**, 504-513 (2015).

154. Mohammadrezaei, D., *et al.* Predicting and elucidating the post-printing behavior of 3D printed cancer cells in hydrogel structures by integrating in-vitro and in-silico experiments. **13**, 1211 (2023).
155. Xu, H., *et al.* Prediction of cell viability in dynamic optical projection stereolithography-based bioprinting using machine learning. 1-11 (2022).
156. Lee, J., Oh, S.J., An, S.H., Kim, W.-D. & Kim, S.-H.J.B. Machine learning-based design strategy for 3D printable bioink: elastic modulus and yield stress determine printability. **12**, 035018 (2020).
157. Shah, L., Latif, A., Williams, K.J., Mancuso, E. & Tirella, A.J.A.H.M. Invasion and secondary site colonization as a function of in vitro primary tumor matrix stiffness: breast to bone metastasis. **12**, 2201898 (2023).
158. Fridman, I.B., Ugolini, G.S., VanDelinder, V., Cohen, S. & Konry, T.J.B. High throughput microfluidic system with multiple oxygen levels for the study of hypoxia in tumor spheroids. **13**, 035037 (2021).
159. Moon, H.-r., *et al.* Subtype-specific characterization of breast cancer invasion using a microfluidic tumor platform. **15**, e0234012 (2020).
160. Mi, S., *et al.* Three-dimensional microfluidic tumor–macrophage system for breast cancer cell invasion. **116**, 1731-1741 (2019).
161. Truong, D.D., *et al.* A Human Organotypic Microfluidic Tumor Model Permits Investigation of the Interplay between Patient-Derived Fibroblasts and Breast Cancer Cells Patient-Derived Fibroblasts Promote Cancer Invasion Behavior. **79**, 3139-3151 (2019).
162. Devadas, D., Moore, T.A., Walji, N. & Young, E.W.J.B. A microfluidic mammary gland coculture model using parallel 3D lumens for studying epithelial-endothelial migration in breast cancer. **13**, 064122 (2019).
163. Ayuso, J.M., Gong, M.M., Skala, M.C., Harari, P.M. & Beebe, D.J.J.A.h.m. Human tumor-lymphatic microfluidic model reveals differential conditioning of lymphatic vessels by breast cancer cells. **9**, 1900925 (2020).
164. Seibel, A.J., *et al.* Role of Lymphatic Endothelium in Vascular Escape of Engineered Human Breast Microtumors. 1-17 (2022).
165. Eslami Amirabadi, H., *et al.* Characterizing the invasion of different breast cancer cell lines with distinct E-cadherin status in 3D using a microfluidic system. **21**, 1-11 (2019).
166. Liu, Q., *et al.* Impedance studies of bio-behavior and chemosensitivity of cancer cells by micro-electrode arrays. **24**, 1305-1310 (2009).

167. Pan, Y., *et al.* 3D microgroove electrical impedance sensing to examine 3D cell cultures for antineoplastic drug assessment. **6**, 1-10 (2020).
168. Tran, T.B., Baek, C. & Min, J.J.P.o. Electric cell-substrate impedance sensing (ECIS) with microelectrode arrays for investigation of cancer cell–fibroblasts interaction. **11**, e0153813 (2016).
169. Anh-Nguyen, T., Tiberius, B., Pliquett, U. & Urban, G.A. An impedance biosensor for monitoring cancer cell attachment, spreading and drug-induced apoptosis. *Sensors and Actuators A: Physical* **241**, 231-237 (2016).
170. Hedayatipour, A., Aslanzadeh, S., McFarlane, N.J.B. & Bioelectronics. CMOS based whole cell impedance sensing: Challenges and future outlook. **143**, 111600 (2019).
171. Láng, O., Köhidai, L. & Wegener, J.J.E.c.r. Label-free profiling of cell dynamics: A sequence of impedance-based assays to estimate tumor cell invasiveness in vitro. **359**, 243-250 (2017).
172. Lee, S.-M., *et al.* Real-time monitoring of 3D cell culture using a 3D capacitance biosensor. **77**, 56-61 (2016).
173. Wu, Z., *et al.* Rapid microfluidic formation of uniform patient-derived breast tumor spheroids. **3**, 6273-6283 (2020).
174. Sharifi, M., *et al.* 3D bioprinting of engineered breast cancer constructs for personalized and targeted cancer therapy. **333**, 91-106 (2021).
175. Chen, P., *et al.* Patient-Derived Organoids Can Guide Personalized-Therapies for Patients with Advanced Breast Cancer. **8**, 2101176 (2021).
176. Feasibility Study for the Generation of Organoids From Male Breast Tumors. (eds. San Giovanni Addolorata, H., Weizmann Institute of Science, I. & Hospital, S.A.) (2025).
177. Collection of Specimens and Clinical Data for Patients With Recurrent or Metastatic Breast Cancer or Male Breast Cancer. (2024).
178. Drug Sensitivity Based on Hydrothorax and Ascite Organoids Derived from Metastatic Breast Cancer. (2024).
179. Efficacy of Personalized Tumorogram-based Therapy in Cancer Established From Patient-derived Biological Avatar: Proof-of-concept Study. (2024).
180. Patient Derived Organoid-guided Personalized Treatment Versus Treatment of Physician's Choice in Patients With Relapsed and Refractory Breast Cancer : a Multicenter, Randomized, Controlled Phase III Trial. (2024).

181. Clinical Exploratory Study on Predicting Drug Sensitivity for Breast Cancer Treatment Using Simulated Organoid Models. (2024).
182. Consistency of Organoids Based Drug Sensitivity and Efficacy of Neoadjuvant Chemotherapy in Breast Cancer. (2023).
183. Organoid-Guided Functional Precision Therapy Versus Treatment of Physician's Choice in Previously Treated HER2-negative Advanced Breast Cancer: A Phase II, Multicenter, Open-label, Randomized Controlled Trial. (eds. First Affiliated Hospital, S.Y.-S.U., Sun Yat-sen, U. & Shantou Central, H.) (2023).
184. Breast Cancer Subtype Characterization Through Patient's Derived Organoids". (BCinsightPDO). (2023).
185. Towards Functional Precision Oncology to Predict, Prevent, and Treat Early Metastatic Recurrence of Triple Negative Breast Cancer. (ed. United States Department of, D.) (2022).
186. Establishment of an ex Vivo Tumor Collection of Triple-negative Breast Cancers in Order to Validate the Interest of Innovative Therapies and the Search for Predictive Biomarkers of Response to Treatment. (2022).
187. Developing Breast (Cancer) Organoids. (eds. Maastricht University Medical, C. & Maastricht, U.) (2022).
188. The Roswell Park Ciclib Study: A Prospective Study of Biomarkers and Clinical Features of Advanced/Metastatic Breast Cancer Treated With CDK4/6 Inhibitors. (2020).
189. Prospective Evaluation of Freshly Implanted Cancers in Mice to Test Drug Response in Matching Host. (2016).
190. Momoli, C., *et al.* The Evolution of Anticancer 3D In Vitro Models: The Potential Role of Machine Learning and AI in the Next Generation of Animal-Free Experiments. *Cancers* **17**, 700 (2025).

CHAPTER 3

DEVELOPMENT AND VALIDATION OF AN IMPEDANCE-BASED ASSAY FOR  
BREAST CANCER CELL CHARACTERIZATION

---

Higgins, K. S. and Gomillion, C. T. Submitted to *Journal of Biological Engineering*.

### 3.1 Abstract

Cellular impedance-based assays offer a sensitive, label-free, and non-destructive method to continuously monitor cells in real time, allowing the assessment of both kinetics and degree of migration for breast cancer cells. A scratch assay is one of the most commonly used methods for testing cell migration in a two-dimensional (2D) monolayer culture. Traditional methods to evaluate 2D cancer migration commonly use image analysis to determine the rate of wound closure over a set of timepoints as an indicator of migratory/metastatic potential for cancer cells. An impedance-based assay system was employed towards establishing a modified wound healing assay technique that can measure wound coverage and therefore, 2D cancer migration continuously. This method can also be used to measure a variety of cell characteristics, including proliferation and epithelial barrier integrity.

Using the Maestro Z Live-cell Analysis System by Axion Biosystems, cell spread, related to single cell morphology, and cell proliferation were observed for multiple breast cancer cell lines. A distinct quantifiable difference in the behavior of aggressive triple-negative breast cancer cells (HCC1806, MDA-MB-231), compared to less aggressive luminal MCF7 cells was determined. With an established assay method, cells were then treated with pro-inflammatory cytokine leptin, which plays a crucial role in metabolism and epithelial to mesenchymal transition (EMT), to verify assay sensitivity. The effects of leptin concentration in media were measurable for MCF7 and HCC1806 cells, and cell barrier integrity was significantly higher in the luminal MCF7 cells as compared to the more aggressive triple-negative cell lines. Cell migration to close a physical wound was measured over 36 hours, with the modified wound healing assay providing quantifiable evidence that the more aggressive breast cancer cells migrated to close the gap.

This work validates the use of cellular impedance-based assay systems to evaluate multiple cell characteristics. In a single experiment, cell spread onto the substrate, cell proliferation, cell-cell barrier integrity, and 2D cell migration were able to be quantified. These findings parallel previously published data on cell migration of the cell lines used, while highlighting the role of leptin in cancer behavior. The potential for bioelectronic impedance assay systems is also demonstrated.



### 3.2 Background

Breast cancer is the second most lethal cancer in women. When detected early, the rate of breast cancer survival is high (99%), however that rate decreases significantly (27%) once the cancer has metastasized to other parts of the body, such as the brain, lungs, bone, and liver <sup>1</sup>. Unfortunately, effective methods to detect metastatic cancer are limited. If not identified at the original breast cancer diagnosis, detection of metastatic breast cancer will not happen until after the cancer has spread to other parts of the body, resulting in delayed treatment and often, more advanced/detrimental cancer cases. Thus, early identification and determination of metastatic cancer could significantly alter therapeutic approaches worldwide.

There have been significant strides towards the identification and detection of metastatic breast cancer through the investigation of genomic, proteomic, and metabolomic profiling of samples to identify potential biomarkers for breast cancer metastasis correlated to clinical data. In these instances, there is reliance on multiple analytical methods for sample analysis (i.e. nuclear magnetic resonance (NMR) and mass spectrometry (MS) for metabolomics), which can be labor intensive and subject to delayed information processing since correlating clinical data may not always be readily obtained. Key factors known to influence breast cancer metastasis are receptor subtype, environment, and motility. Therefore, a method that allows for evaluation of these factors, while yielding an earlier, more reliable, and time-efficient approach for identification of metastatic cells is needed. This research validates the use of a novel bioelectronic assay to characterize breast cancer cell motility and response to biochemical stimuli *in vitro*.

Breast cancer metastasis remains one of the leading causes of death for women with cancer, accounting for 70% of breast cancer deaths, largely because methods to predict metastasis are limited. Metastasis remains difficult to predict, in part, due to cancer heterogeneity. Three subtypes

of breast cancer can be determined by their receptor status of the estrogen receptor (ER), progesterone receptor (PR), and human epidermal growth factor receptor-2 (HER2). This determines treatment and is correlated to how aggressive/metastatic a cancer may be. The most aggressive type of breast cancer is triple negative cancer (ER-, PR- and HER2-). This subtype has a high chance of metastasis; therefore, this research includes two different human breast cancer cell lines that are defined as triple negative.

In addition to receptor status, environmental factors can also influence a cancer cell's behavior. Proinflammatory cytokines like leptin, Interleukin (IL)-1 $\beta$ , IL-6, or tumor necrosis factor (TNF)- $\alpha$  encourage blood vessel formation (angiogenesis) towards the tumor site, a primary step in the metastatic cascade <sup>2,3</sup>. Leptin, in particular, can bind to breast cancer cells and trigger proliferation, invasion, and migration through oncogenic signaling pathways like mitogen-activated protein kinase (MAPK), phosphatidylinositol 3-kinase (PI3K), and janus kinase/signal transducers and activators of transcription (JAK/STAT) <sup>4,5</sup>. Additionally, leptin levels have been shown to be significantly higher in breast cancer cases with lymph node metastasis, compared to no metastasis <sup>6</sup>. In this work, we aim to establish the utility of a bioelectronic impedance-sensing assay as an alternate *in vitro* approach applicable for studying cell migration and assessing metastatic potential of cancer cells by demonstrating quantifiable effects of leptin concentration on breast cancer aggressiveness, separate from leptin-induced immune response <sup>7,8</sup> *in vitro*.

A wound closure assay, also known as a wound healing assay or scratch assay, is an example of an *in vitro* assay to study cancer metastasis. In this method, cancer cells are seeded at the bottom of a well plate and grown to confluence. Once confluent, a physical scratch through the cancer cell monolayer is made, creating a gap. Over a set period, the cancer cells will migrate towards each other to close the gap or “heal” the wound. The distance traveled by the cancer cells

and the time it takes to close the gap is viewed as a cancer cell's migratory potential and can be used to determine metastatic likelihood. While wound healing assays are a common and effective tool in evaluating breast cancer cell migration, they rely heavily on periodic imaging or video recording for data collection, which require time-intensive processing and can limit throughput precision<sup>9</sup>.

To overcome these limitations, impedance-based techniques, such as Electric Cell-substrate Impedance Sensing (ECIS), offer a compelling alternative for monitoring cell migration and behavior in real time<sup>10,11</sup>. Bioelectronic systems, like ECIS, are quickly gaining popularity as a label-free, non-invasive, and non-terminal method that continuously measures changes in electrical impedance to quantify several aspects of cell behavior. In this technique, a small alternating current (I) is applied across an electrode configuration at the bottom of a tissue culture surface. This results in a potential (V) across the electrodes which is measured by the ECIS instrument. The impedance (Z) is then determined by Ohm's law where  $Z = V/I$ <sup>12</sup>. By tracking impedance changes as cells adhere, proliferate, and migrate, ECIS provides continuous, quantitative data without the need for frequent imaging.

As cells adhere onto the electrode-coated surface and proliferate, they act as insulators, increasing impedance (Figure 3.1). Alterations in impedance reflect key cellular characteristics, including surface coverage, morphology, and adhesion, as shown in Figure 3.1B. When cell function shifts in response to the environment (e.g. growth factors, cytokines, hypoxia, cytotoxic agents), so do the impedance readings. At higher alternating current (AC) frequencies, the current travels via transcellular pathways (Figure 3.1B), providing information about cellular surface coverage and morphology. Conversely, at lower AC frequencies, the current flows via paracellular pathways. To quantify this, trans-endothelial/epithelial electrical resistance (TEER) is widely used

as a robust and established method for assessing barrier function in epithelial and endothelial monolayer cultures<sup>13,14</sup>. This measurement is particularly relevant in cancer studies, where loss of barrier integrity reflects the degradation of tight junctions during tumor cell migration and invasion through both epithelial layers and vascular endothelium<sup>15-17</sup>.

Given its advantages, ECIS is increasingly being adopted in cancer research. Several commercial systems are available from companies like Applied BioPhysics and Axion Biosystems, while many researchers also develop custom setups tailored to their experimental needs<sup>18-21</sup>. Individual systems often lack cross-study comparability, therefore this work utilizes the commercially available Maestro Z system (Axion Biosystems)<sup>22,23</sup>, ensuring consistency and reproducibility. Although ECIS has been used predominantly with breast cancer cells to quantify drug interactions<sup>20,24-26</sup>, a system that integrates multiple behavioral readouts using ECIS can significantly advance efforts to diagnose and characterize metastatic potential in breast cancer.

To better identify metastatic cancer cells more efficiently in 2D culture, we propose to leverage cell impedance for a “smart” *in vitro* modeling approach to interrogating the relationship between specific attributes of cancer cells and their metastatic potential. Such an approach provides a modern, quantitative framework for studying cancer cell migration and metastasis and, because of its 96-well plate format, small numbers of cells are utilized, making it practical for clinical settings where biopsies of human tissues do not typically yield a large quantity of cells for culturing<sup>27</sup>. Specifically, we first determined the feasibility of a quantitative impedance-based assay to characterize cancer cell proliferation and migration. The assay approach was then applied to measure the effects of leptin on breast cancer cell behavior to demonstrate assay sensitivity and understand how migration is affected by varying leptin concentrations. Overall, the approach

established in this work allows for the collection of an array of data within a single experiment, streamlining the process of cancer cell characterization.

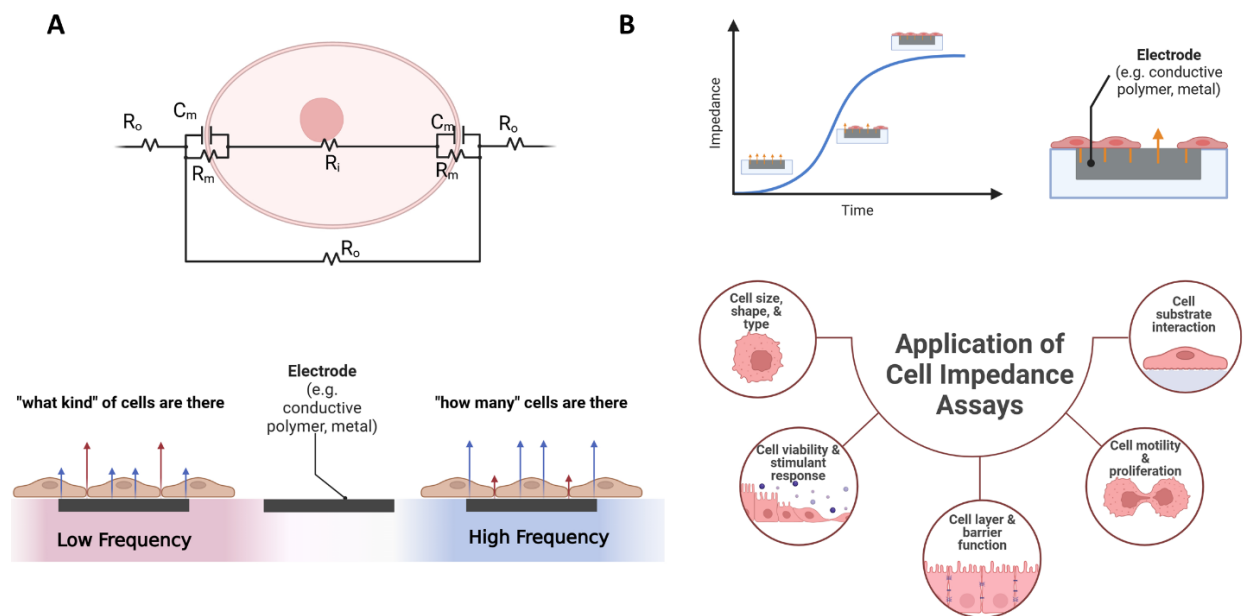


**Figure 3.1:** Cell impedance concepts. A) Electrical circuit of an animal cell, where  $R_o$  is resistance of the surrounding media,  $R_m$  is the resistance of the membrane,  $C_m$  is the capacitance of the cell membrane, and  $R_i$  is the resistance of the protoplasm. The lipid bilayer of the cell membrane works in both a capacitive and resistive role, which both contribute to impedance. The flow of electrical signals through a cell monolayer at different alternating current (AC) frequencies. At low frequencies, current primarily travels through paracellular pathways (red arrow), reflecting barrier integrity and providing information about cell phenotype or “what kind” of cell. At high frequencies, current predominantly passes transcellularly (blue arrows), correlating with cell coverage and “how many” cells there are. B) Applications of cell impedance assays for monitoring various cellular behaviors. As cells cover the electrode surface, impedance increases. Different factors can be measured, depending on frequency, allowing for many practical applications of this technology. Created with BioRender.com

### 3.3 Materials and Methods

#### 3.3.1 Reagents and Cell Lines

Poly-D-lysine lyophilized powder (Sigma Aldrich) was dissolved in sterilized deionized (DI) water to form a 21.3  $\mu$ M solution. This solution was stored at  $-20^{\circ}\text{C}$  and thawed on ice when needed. To prepare leptin, the adipokine used as a cell stimulant, human leptin (Sigma Aldrich)

was reconstituted in sterilized DI water to make a 0.5 µg/mL solution and 1.5 µg/mL solution. Leptin solutions were stored at 4°C for short term storage and -20°C for longer storage.

MCF7, HCC1806, and MDA-MB-231 cells were purchased from American Type Culture Collection (ATCC). Characteristics of the cells include: MCF7 cells (metastatic adenocarcinoma, ER+, PR+); HCC1806 cells (triple negative ER-/PR-/HER2-), African American donor); and MDA-MB-231 (triple negative (ER-/PR-/HER2-), Caucasian donor). All three cell line populations were expanded as a monolayer in 75 cm<sup>2</sup> flasks (Falcon) at 37°C and 5% CO<sub>2</sub> atmosphere in Dulbecco's Modified Eagle Medium (DMEM) supplemented with 10% fetal bovine serum (R&D Systems) and 1% penicillin/streptomycin (Gibco), referred to as DMEM-Complete. Three days before data collection began, cell media was changed every day and 200 µL of stimulant was added. This stimulant was either sterile DI water for the control groups, 0.5 µg/mL leptin for the normal concentration groups, or 1.5 µg/mL leptin for the high concentration groups. Cells were confirmed to be free of mycoplasma using a commercially available kit (InvivoGen).

### 3.3.2 Seeding Cells onto CytoView Plates

Experiments for this work were performed according to the plan shown in Figure 3.2. Before cells were added to the CytoView-Z 96-well electrode plates (Axion), the culture surfaces were treated with 50 µL of the poly-D-lysine solution (21.3 µM) and incubated at room temperature for 1 hour in a biosafety cabinet. Afterward, each well was washed with 50 µL of Phosphate Buffered Saline (PBS, Gibco) twice and allowed to dry in the biosafety cabinet. Cells were transferred from the 75 cm<sup>2</sup> flasks using 0.5% trypsin-EDTA (Gibco). Before seeding the cells on the electrode plate, a Media Only Baseline test was performed in the AxisZ software of the Maestro Z (Axion) by adding 100 µL of DMEM-Complete to each well of the plate and evenly

distributing 8 mL of sterile room temperature DI water to the reservoirs on the CytoView-Z plates (shown in Supplementary Figure A.4). The plate was docked in the Maestro Z instrument, and the Media Only Baseline was measured. Once the baseline was measured, the plate was transferred to a biosafety cabinet and the cells were added to the CytoView-Z plate. MDA-MB-231 cells were plated at a concentration of 75,000 cells/cm<sup>2</sup>, while MCF7 and HCC1806 cells were plated at 85,000 cells/cm<sup>2</sup> to account for varying growth rates and cell sizes. A volume of 4 µL of the stimulant was added to each well and the plate was allowed to rest in a biosafety cabinet at room temperature for 1 hour to allow cells to attach to the culture surface and avoid edge effects. Lastly, the plate was docked in the Maestro Z and cultured at 37°C and 5% CO<sub>2</sub>. Impedance and Barrier Index measurements are automatically collected upon plate engagement.

### 3.3.3 Evaluating Cell Proliferation and Barrier Integrity

Cell growth was monitored by tracking impedance through the AxisZ software associated with the Maestro Z. At 24 hours, the plate was undocked, and the cells were visually checked for confluence using an EVOS FLc microscope (Invitrogen). Shown in Figure 3.2, all medium was changed to a low-serum medium (DMEM supplemented with 2% fetal bovine serum and 1% penicillin/streptomycin) to halt growth. A volume of 4 µL of the stimuli treatment was added to each well. The CytoView-Z plate was redocked in the Maestro Z and cells continued to culture for 12 hours while their growth ceased. Impedance readings were collected on Axion's AxisZ Software approximately every minute and all data exported to Excel at the end of experiment. Barrier Index measurements were collected simultaneously with impedance during cell proliferation. Barrier integrity was then calculated in AxisZ.

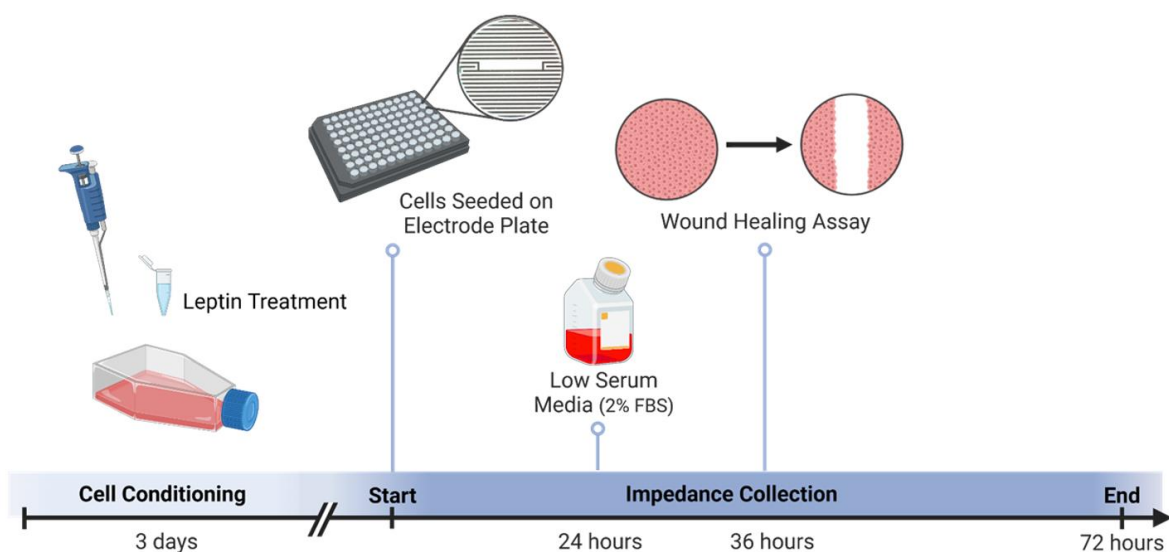


**Figure 3.2:** Schematic of the experimental flow. Created with BioRender.com

### 3.3.4 Modified Quantitative Wound Healing Assay

The CytoView-Z plate was undocked from the Maestro Z and placed in a biosafety cabinet. To create a physical wound in each well of the plate, a multi-channel micropipettor fitted with micropipette tips was used to gently scratch the plate surface in a vertical line. The media was replaced by fresh low-serum media and supplemented with 4  $\mu$ L of stimuli treatment. The plate was redocked in the impedance system. After 36 hours, the experiment was terminated.

### 3.3.5 Transwell Migration Assay

CellTracker Green (Invitrogen) was used to stain actin of each cell line immediately prior to seeding the cells on the inserts. Transwell inserts of 24-mm diameter and 8- $\mu$ m porosity (Corning Costar) were used to evaluate migration potential of each cell line. DMEM-Complete was added to the bottom wells and each cell line was seeded on individual inserts at 100,000



cells/cm<sup>2</sup> using a low-serum medium. Plates were cultured and evaluated at 6, 12, 18, and 24 hours. To image cell nuclei, 2 drops of NucBlue™ Live ReadyProbes™ Reagent (Hoechst 33342, Invitrogen) per mL of media were added to each well and allowed to incubate at room temperature for 20 minutes. After incubation, each transwell insert was gently rinsed with PBS and transferred to a well with fresh PBS. The top of each insert was gently swabbed to remove the non-migrated cells. Using the Cytation1 Cell Imaging Multi-Mode Reader (Agilent BioTek), each well was imaged in 4 locations, and the nuclei were counted using Gen5 Cell Imaging & Microscopy Software (BioTek). Object count was performed using a threshold of 9000, minimum object size of 9 microns, and maximum object size of 35 microns. The number of nuclei was used to quantify the number of migrated cells per image for each cell type.

### 3.3.6 Traditional Wound Healing Assay

MCF7, HCC1806, and MDA-MB-231 cells were seeded onto a standard 96-well plate using DMEM-Complete at the same density as the modified wound healing assay. CellTracker Green was used to stain the cell actin immediately prior to seeding the cells on the plate. At 24 hours, the cells were visually checked for confluence using an EVOS FLc microscope (Invitrogen). To halt growth, all medium was changed to a low-serum medium. The plate was returned to the incubator and cells continued to culture for 12 hours while their growth ceased. After 36 hours of culture, nuclei were stained, and cell monolayers were scratched.

To stain the nuclei, NucBlue (Invitrogen) was added to a stock of DMEM complete at a concentration of 2 drops per mL. Spent media was removed from the 96-well plate and 100 µL of NucBlue-DMEM solution was added to each well and incubated in a biosafety cabinet for 20 minutes at room temperature. To create a physical wound in each well, a multi-channel

micropipettor fitted with micropipette tips was used to gently scratch the plate surface in a vertical line. The media was replaced by fresh low-serum media and the plate was imaged using a Cytation 1 (Agilent Biotek). Each well was imaged in a two-by-three montage that was stitched into one image using Agilent Biotek's Gen5 software. The plate was imaged every 12 hours for 36 hours to visualize wound closure over time.

### 3.3.7 Data Processing and Statistical Analysis

Impedance data was exported via Microsoft Excel, where the rate of wound closure was calculated. Statistical analyses were calculated using GraphPad Prism 3.9. Statistical significances of ECIS data were determined via ordinary one-way ANOVA. Transwell migration significance was calculated using an unpaired parametric t-test.

## 3.4 Results

### 3.4.1 Determination of Quantitative Impedance Assay Feasibility

Preliminary evaluation of the efficacy of cell impedance for monitoring changes in breast cancer cell behavior was performed. Stained images demonstrating the representative morphology of the three tested breast cancer cell lines, MCF7, HCC1806, and MDA-MB-231 cells, are shown in Figure 3.3A. Each of the three cell lines were cultured using the Maestro Z Impedance Assay System, with a high frequency impedance, measured across the electrodes of each well.

Initial evaluation of the data for control cell samples without any treatment showed a distinct impedance profile for each breast cancer line, where variations in Impedance and Barrier Integrity were detected during adhesion, proliferation, and wound healing phases of the culture

period (Figure 3.3B and 3.3C, respectively). The graphs obtained show high frequency impedance averaged across the set of wells for each cell type. Key points during the culture period are reflected in the graphs, where the baseline impedance for each cell line is indicated at 0 hours, and an increase in impedance is observed as cells proliferate up to 36 hours. Interruptions in the culture process, such as media change at 24 hours or the initiation of wounds for a scratch assay at confluence (36 hours) are reflected by an immediate decrease in impedance, and subsequent increase, depending on cell response.

For the tested cell lines, as shown in Figure 3.3B, during the first six to eight hours, the MDA-MB-231 and HCC1806 impedance values plateaued. Impedance measurements during the first 36 hours of proliferation showed that the MCF7 cells reached the highest impedance for the tested cells, and the MDA-MB-231 cells maintained the lowest impedance for the entire culture period. The MCF7 cells had an average impedance of  $49.5\ \Omega$  at confluency, while the HCC1806 and MDA-MB-231 cells measured as  $34.1\ \Omega$  and  $11.8\ \Omega$  respectively. The Barrier Integrity of each breast cancer cell monolayer was measured during proliferation by quantifying the ratio between low frequency (1 kHz) resistance and high frequency (41.5 kHz) resistance. In addition to the highest impedance, the MCF7 cells also had the highest Barrier Integrity among the three cell lines tested, which remained the highest during proliferation and wound healing assay phases (Figure 3.3C).

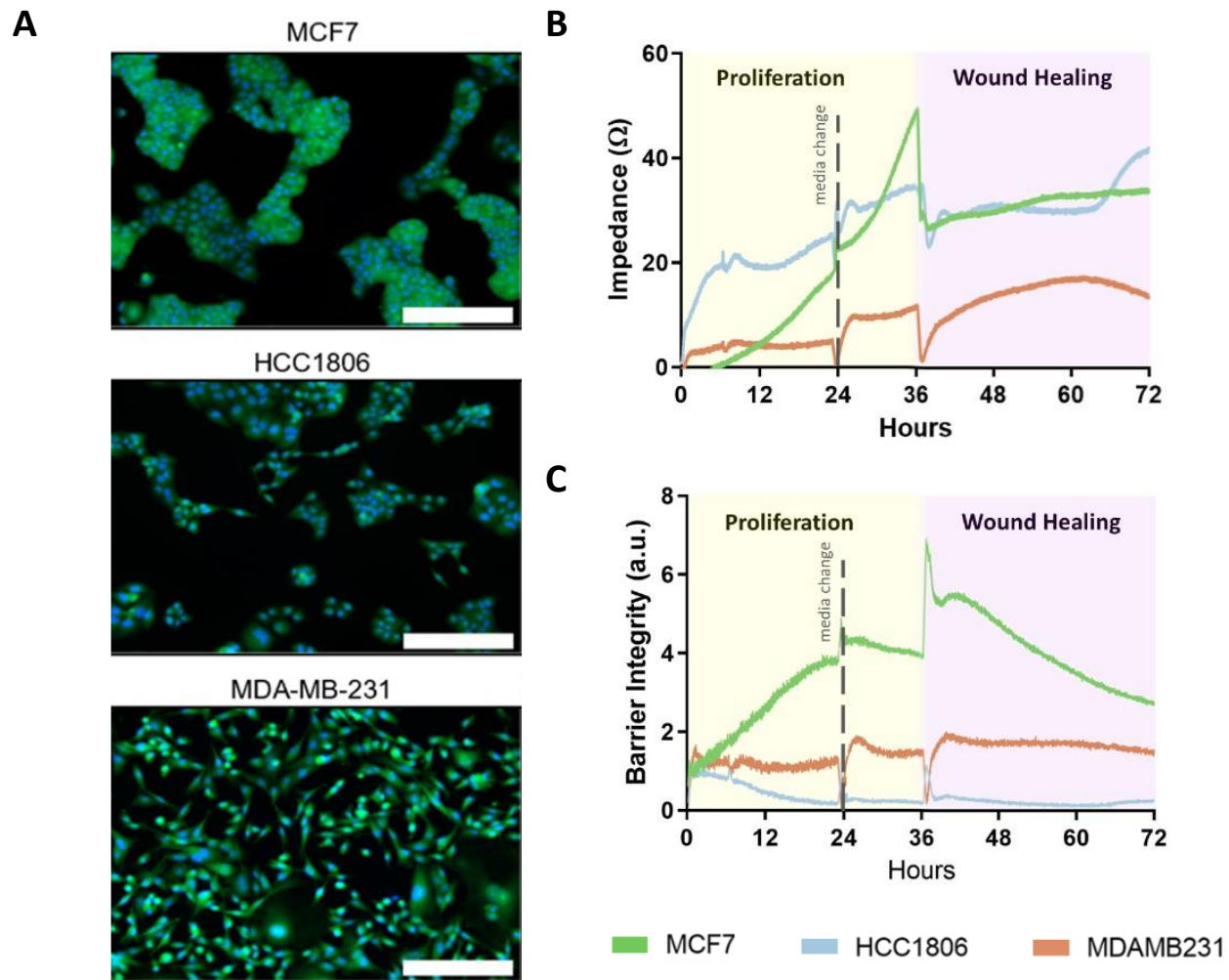


**Figure 3.3.** Imaging and impedance monitoring of breast cancer cell dynamics. A) Breast cancer cells (green) and their nuclei (blue) stained to visualize morphology. B) Application of impedance assay system for simultaneously monitoring Impedance and C) Barrier Integrity during culture. Cells were allowed to attach to plate and proliferate for 36 hours (yellow background). Then, each well was physically scratched, and wound closure was observed for another 36 hours (purple background).

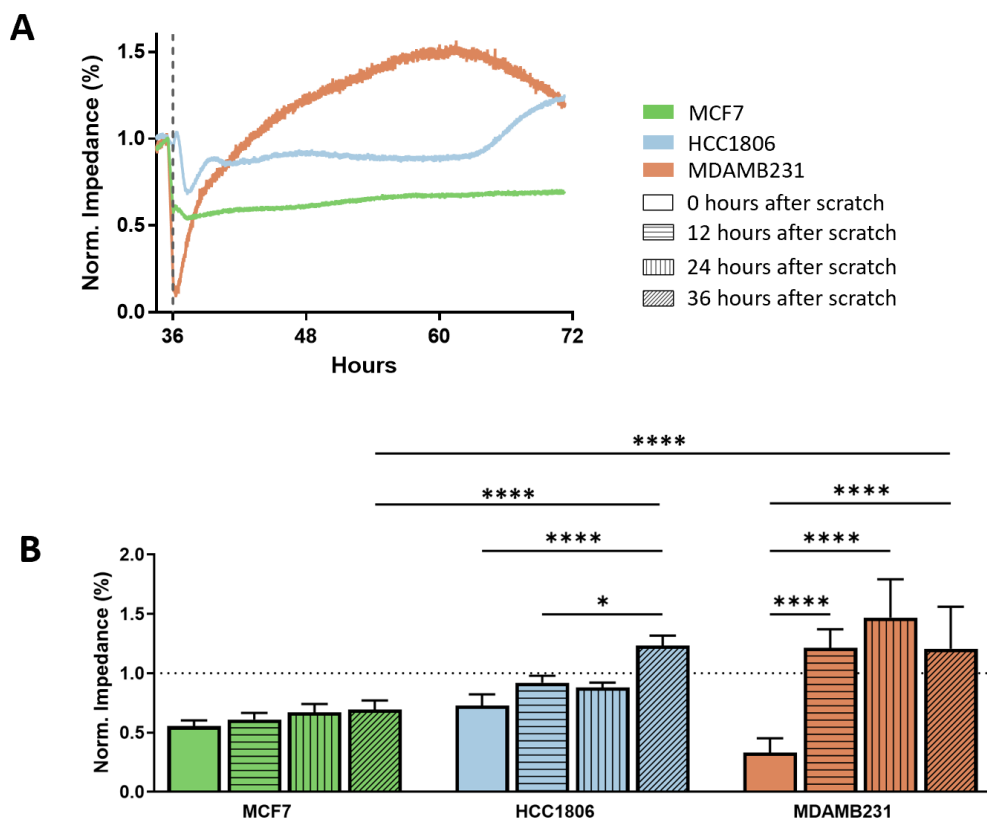


**Figure 3.4:** Wound closure over 36 hours. A) Normalized high frequency (41.5 kHz) impedance of breast cancer cells without any treatment. To visualize wound closure, impedance was normalized to the value of each well pre-scratch. B) Bar graph of wound closure, measured by normalized impedance. Graph shows normalized impedance levels directly after creating a wound and 12, 24, and 36 hours after. The grey dotted line represents the point in which the impedance matches the pre-scratch impedance. Significance between groups is denoted by asterisks: \*  $p < 0.05$ , \*\*  $p < 0.01$ , \*\*\*  $p < 0.001$ , \*\*\*\*  $p < 0.0001$ .  $n = 6$  wells per condition.

### 3.4.2 Confirmation of Quantitative Wound Healing Assay Protocol

When cells reached confluence at 36 hours, the wound healing assay was initiated by making a physical scratch within each well, and the impedance was measured for an additional 36 hours. Impedance was normalized to the point prior to creating a wound. Immediately after the scratch a decrease in impedance was observed for each cell type, as indicated in Figure 3.4A. As shown in Figure 3.4B, both triple-negative cell lines were able to close the created wounds within 36 hours, if not sooner, with the impedance for the HCC1806 and MDA-MB-231 cells reaching

or exceeding the impedance values measured before the scratch. The less aggressive MCF7 cells showed very little migration, as there was little to no change in the measured MCF7 impedance over the 36 hours. These observations were consistent with cell migration measured via a transwell migration assay and a traditional wound healing assay performed for each cell line (Supplementary Figure A.1).

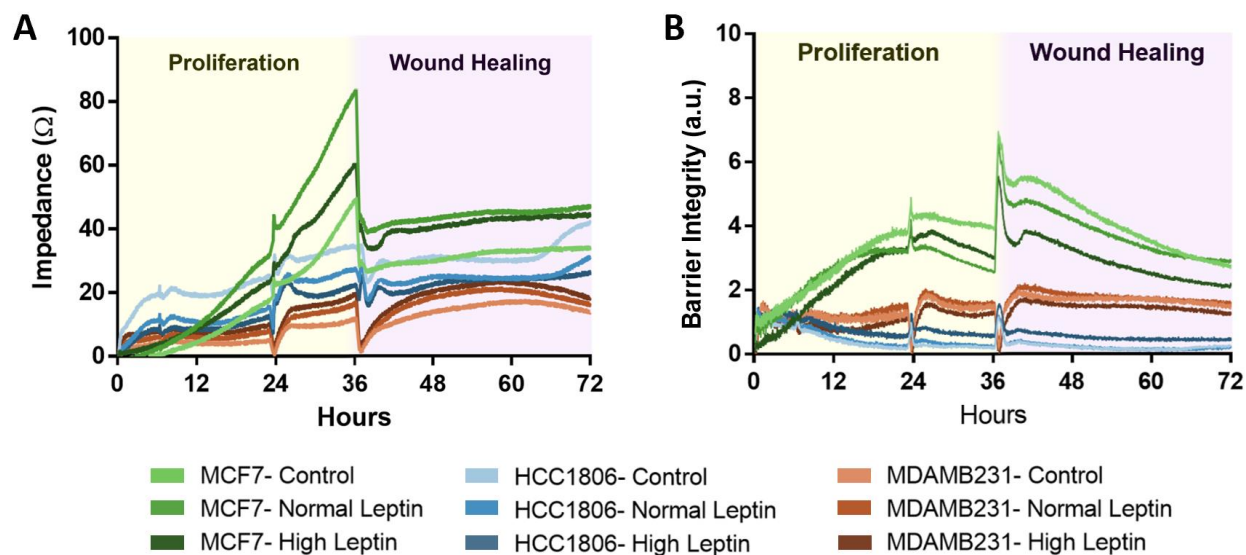


**Figure 3.5:** Impedance and barrier integrity across the full experimental timeline. A) High-frequency impedance (41.5 kHz) and B) barrier integrity measurements for three breast cancer cell lines treated with leptin at 0, 10, or 30  $\mu\text{g/mL}$ . Cells were seeded and allowed to attach and proliferate for 36 hours (yellow background). A scratch wound was then created, and wound closure was monitored for an additional 36 hours (purple background).  $n = 6$  wells per condition.

### 3.4.3 Application of Impedance Assay Protocols to Evaluate Cell Behavior

The high frequency impedance for each cell type treated with either a normal leptin concentration (10  $\mu\text{g/mL}$ ) or high leptin concentration (30  $\mu\text{g/mL}$ ) was measured and compared to control samples (Figure 3.5A). In addition, the barrier integrity of each breast cancer cell monolayer was measured simultaneously (Figure 3.5B). For each cell type, the effects of leptin on cell behavior were assessed by monitoring cells during adhesion, proliferation and wound healing phases of culture. For the MCF7 cells, their impedance and barrier integrity across all three

leptin levels was significantly higher than either triple-negative cell line. Each cell line had a significant change in impedance with response to leptin, however there was no consistent pattern of response to leptin across all three cell lines.

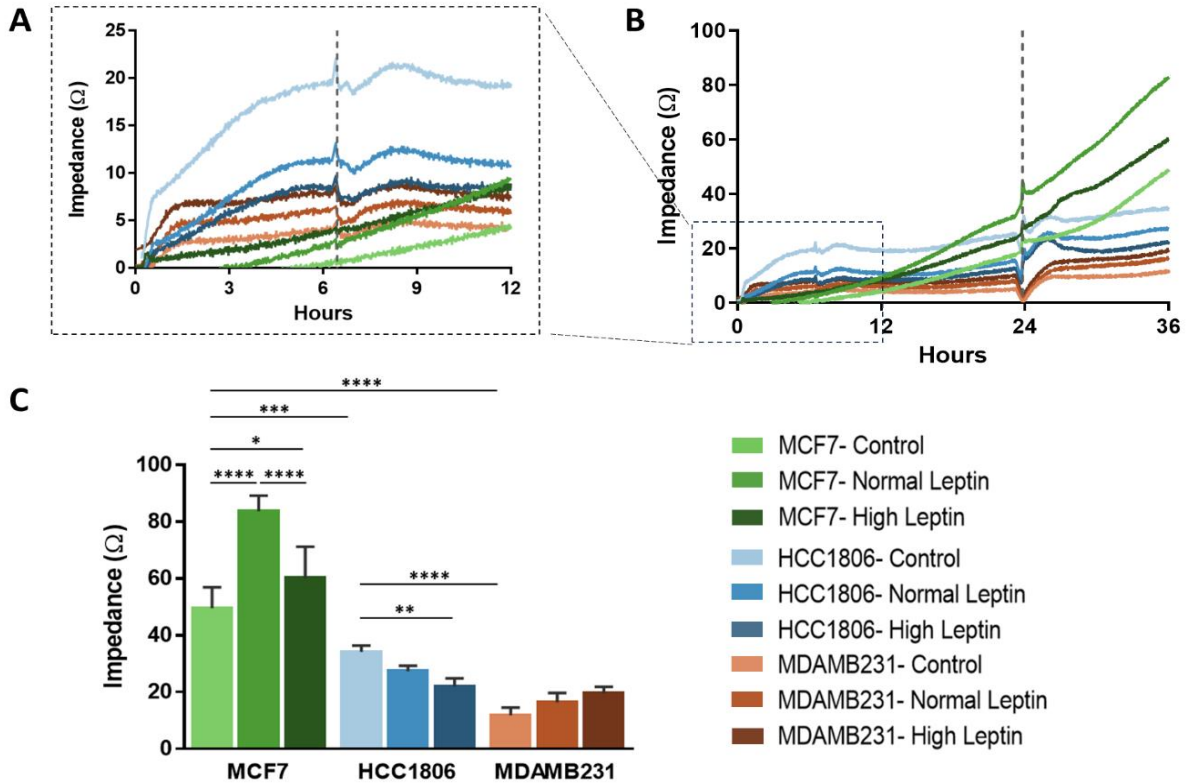


**Figure 3.6:** Cell spread is more pronounced in elongated breast cancer cell lines. A) High frequency impedance recorded in the first 12 hours of the experiment to visualize HCC1806 and MDA-MB-231 cell spread. Plate was removed from recording device at  $t = 6.5$  hours (dashed line), resulting in a data artifact. B) High frequency (41.5 kHz) impedance recorded in the first 36 hours of the experiment to visualize cell spread and proliferation. Media was changed at  $t = 24$  hours (dashed line). C) Average impedance (41.5 kHz) at  $t = 36$  hours. \* indicates a statistically significant comparison where  $p > 0.05$ . \*\* indicates a statistically significant comparison where  $p > 0.01$ . \*\*\* indicates a statistically significant comparison where  $p > 0.001$ . \*\*\*\* indicates a statistically significant comparison where  $p > 0.0001$ . (n=6)

At high cell density (t = 36 hours), MCF7 cell barrier integrity is influenced by concentration of leptin (Figure 3.7A). Additionally, a significant difference in barrier integrity across all three control groups was measured. This is linked to cell-cell adhesion and shows a significantly higher barrier integrity for the less aggressive MCF7 cells in comparison to the more aggressive triple negative cell lines (Figure 3.7B).

**Figure 3.7:** Breast cancer cell monolayer barrier integrity. A) Cell-cell barrier integrity recorded in the first 36 hours of the experiment. Media was changed at t= 24 hours (dashed line). (B) Average barrier integrity at t= 36 hours. Significance between groups is denoted by asterisks: \* p < 0.05, \*\* p < 0.01, \*\*\* p < 0.001, \*\*\*\* p < 0.0001. n = 6 wells per condition.

### 3.5 Discussion



experiment, providing knowledge of how each cell line compares with one another and how leptin affects these behaviors.

### 3.5.1 Determination of Quantitative Impedance Assay Feasibility

Cell spread and proliferation were evaluated using high frequency (41.5 kHz) impedance. At this frequency, the impedance of the cell membrane is relatively low. Thus, most of the current couples capacitively through the cell membranes. In other words, the current is traveling in a transcellular manner, providing information about the cell layer, such as confluency and surface coverage where the cells attach to the electrode surface and spread out. In the first 12 hours of culture, the impedance of each triple-negative breast cancer cell group plateaued. This was later identified as cell spread as the cells spread out and attach onto the substrate, a phenomenon that is well documented using ECIS<sup>28-30</sup>. While MCF7 cells have a cobblestone-like morphology, the triple-negative breast cancer cell lines are more elongated in shape. Therefore, it is indicated that the HCC1806 and MDA-MB-231 cell lines exhibited a plateau in their impedance readings as the cells work to fully attach to the plate before proliferating.

Once cells began to proliferate, the MCF7 cells grew quickly and tended to pack tightly together. Because of this, a higher number of MCF7 cells can cover the same surface area as either of the triple-negative breast cancer cell lines. This is reflected in the impedance reading at  $t = 36$  hours, when cells are at their highest density. This alone can give us insight into the growth patterns of each cell line and how cells might behave *in vivo*.

Endothelial and epithelial cells express tight junctions, allowing them to link tightly with their neighboring cells to form a selectively permeable barrier. A cancer cell's increase in invasiveness is often associated with a transition from epithelial-like cells, that maintain a cuboidal

shape and adhere to the basement membrane, to more elongated mesenchymal-like cells <sup>31,32</sup>. There is an observed tradeoff between the cells' proliferation and invasiveness for this process, the epithelial-to-mesenchymal-transition. This change occurs on an epigenetic level where markers like E-cadherin, desmoplakin, and keratin are associated with an epithelial-like state and n-cadherin, vimentin, and fibronectin are associated with a mesenchymal-like state <sup>33</sup>. A degradation of tight junctions is associated with the transition to a more mesenchymal-like state, leading to decreased barrier integrity and a proclivity for migration <sup>34</sup>.

At lower frequencies, electrical signal passes through paracellular pathways, measuring the integrity and permeability of a cell monolayer. While this measurement, referred to as trans-epithelial electrical resistance (TEER) typically requires a fully confluent monolayer to accurately measure barrier function, the Maestro Z normalizes this data to cell surface coverage, measured with high frequency (41.5 kHz) resistance (Equation 3.1). As a result, this is a unitless measure.

$$\text{Barrier Integrity} = \frac{\text{measured resistance at 1 kHz current } [\Omega]}{\text{measured resistance at 41.5 kHz current } [\Omega]} \quad (3.1)$$

This difference in barrier integrity is observable across all three cell lines in Figure 3.3C where highly cuboidal and non-migratory MCF7 cells maintain a high normalized TEER value (i.e. barrier integrity). The more aggressive HCC1806 and MDA-MB-231 cells have a much lower barrier integrity, which associates with their morphology and aggressiveness.

### 3.5.2 Confirmation of Quantitative Wound Healing Assay Protocol

Cell migration is essential for many physiological processes including embryonic development, wound repair, angiogenesis, and tumor metastasis <sup>35</sup>. Cancer cell migration is one of

the first steps in the metastatic cascade and is commonly used to evaluate cancer cell aggressiveness.

With high frequency (41.5 kHz) cell impedance being directly related to cell surface coverage, we can use this value to determine cell migration as a form of wound closure. Impedance was normalized to the value prior to creating a wound, meaning that the wound would be effectively covered once the cell value has reached 1.0 again. Over 36 hours of wound closure, the luminal MCF7 cells did not show any measurable difference in impedance and did not migrate to close the wound at all. This is in contrast to the triple-negative breast cancer cell lines, which displayed an increase in impedance over time as they worked to close the wound. The MDA-MB-231 cells migrated the most and quickest of all three breast cancer cell lines, and eventually began to die back, resulting in a drop in impedance between 24 hours and 36 hours of migration. The non-migratory tendencies of the luminal MCF7 cell line have been mentioned previously in literature<sup>36-40</sup>. Luminal cell lines are comparably more differentiated and have a lower propensity for migration due to a higher number of tight junctions<sup>41</sup> and MCF7 cells have higher rates of claudin-1 than their triple-negative counterparts<sup>34,42</sup>. Our data correlates with published information; however, we also assessed migration potential of our specific cell populations using a more traditional transwell migration assay. Our transwell migration data mirrors our impedance-measured wound closure where the MCF7 and HCC1806 cells exhibit no migration over 24 hours, and the MDA-MB-231 cells do. Notably, the MDA-MB-231 groups displayed immediate and rapid migration with both migration assays. All of this further proves the efficacy of impedance-based cell monitoring to measure cell migration.

### 3.5.3 Application of Impedance Assay Protocols to Evaluate Cell Behavior

The sensitivity and efficacy of the quantifiable assay approaches developed here was tested by treating cultured cells with exogenous leptin added to their culture media at varying levels. It was expected that high levels of leptin, commonly associated with diseased states, would impact cell proliferation and migration, particularly for the more aggressive cell lines tested. Measurement of the impedance and barrier integrity in response to leptin treatment did successfully yield quantifiable measures, indicating that this assay approach is sensitive enough to detect subtle differences in cell behavior. However, the effects of leptin were not consistent.

Because MCF7 cells have a cobblestone morphology and grow tightly packed, their impedance across all three leptin levels was significantly higher than either triple-negative cell line. Each cell line had a significant change in impedance with response to leptin, however there was no consistent pattern of response to leptin across all three cell lines. Leptin has previously been shown to have an effect on cell breast cancer cell proliferation<sup>43-45</sup>, though there is no distinct pattern in response across cell lines. Determining leptin receptor (Ob-R) expression for each cell line may give us insight into the varied response we measured. Additionally, in this work, leptin was shown to have an effect on cell barrier integrity across all three cell lines, but particularly with the luminal MCF7 cells. Previous studies have shown that leptin can have an effect on e-cadherin expression within breast cancer cells<sup>46,47</sup>. Since MCF7 cells have a higher expression of E-cadherin, this may explain why their barrier integrity is affected more by leptin expression.

For the modified wound healing assay, since high frequency impedance corresponds to electrode surface coverage, it was used to track wound closure. When treated with leptin it was expected that high leptin concentrations would yield increased cell migration. However, while

there were differences observed between cell types and across all MCF7 cells observed, there was no measurable difference in wound closure as a response to leptin (Supplementary Figure A.2).

Leptin was shown to have no effect on cell migration in this work, although leptin has previously been shown to increase cell migration and invasion<sup>48,49</sup>. This outcome may be resultant from the concentrations of leptin used within this study in comparison to other studies. Concentration levels were determined based on a literature review of serum leptin levels<sup>6,50-55</sup>, however leptin concentrations within the fatty tumor microenvironment are likely higher. Additionally, the effect of leptin on breast cancer migration *in vivo* involves not only oncogenic signaling within the cancer cell but can lead to an inflammatory response in macrophages and T-cells in the surrounding microenvironment. By decoupling the leptin-induced cancer cell and immune cell responses, this may understate the effect that leptin plays in breast cancer progression.

#### 3.5.4 Performance and Operational Issues

Overall, this experimental method proved simple and effective in providing a large collection of data on many different cell characteristics. ECIS is non-invasive and non-terminal allowing us to evaluate cell spread, proliferation, barrier integrity, and cell motility with the same cell population. This is practical in a research setting where there is a small population of cells (e.g. derived from a biopsy). The only notable issue of this adapted wound healing assay is creating the wound without damaging the electrode imbedded within each well. This is due to the difficulty of creating an even distribution of weight across a row of wells with the multichannel pipettor. While some wells had damaged electrodes from the pipette tip, others did not show a full scratch. In later iterations of this experiment, the user applied a more even distribution of weight by holding the pipettor at its base to perform the scratch. In future work, we plan to test higher precision

wound-making tools, like the Autoscratch by Agilent. With minimal adaptations, this method can be used for an easier wound healing assay that requires less maintenance and gives a much broader view of cell behavior and migration over time.

### **3.6 Conclusion**

Breast cancer metastasis remains one of the leading causes of death in women with cancer. While wound healing assays are a common way to evaluate 2D cell migration, traditional methods rely on image processing. This method is not only more computationally intense but is less quantitative. The methods outlined above propose a modified wound healing assay that can track wound closure, as cells migrate to close the gap, with ECIS. Impedance spectroscopy is a label-free, non-terminal way to continuously observe cell behavior throughout the entire experiment. Within this experiment, we were able to measure cell response to leptin (a proinflammatory adipokine), track cell spread and proliferation, quantify cell barrier integrity, and determine 2D cell migration via a modified wound closure assay. We found leptin to be a contributing factor in cancer cell proliferation and barrier integrity, however no variation in migration was recorded between our leptin conditions. This method allowed us to characterize cancer cell behavior and will be applied to more mammary cell lines in the future to establish a library of data on established breast cancer cell lines.

### 3.7 References

1. Siegel, R.L., Miller, K.D. & Jemal, A.J.C.a.c.j.f.c. Cancer statistics, 2019. **69**, 7-34 (2019).
2. Hartman, Z.C., *et al.* Growth of Triple-Negative Breast Cancer Cells Relies upon Coordinate Autocrine Expression of the Proinflammatory Cytokines IL-6 and IL-8. *Cancer Research* **73**, 3470 (2013).
3. Martin, T.A. & Jiang, W.G.J.B.e.B.A.-B. Loss of tight junction barrier function and its role in cancer metastasis. **1788**, 872-891 (2009).
4. Buonaiuto, R., *et al.* Insight on the role of leptin: a bridge from obesity to breast cancer. **12**, 1394 (2022).
5. Linares, R.L., Benítez, J.G.S., Reynoso, M.O., Romero, C.G. & Sandoval-Cabrera, A.J.S.r. Modulation of the leptin receptors expression in breast cancer cell lines exposed to leptin and tamoxifen. **9**, 1-9 (2019).
6. Gu, L., *et al.* Association of serum leptin with breast cancer: A meta-analysis. **98**, e14094 (2019).
7. Gelsomino, L., *et al.* Knockdown of leptin receptor affects macrophage phenotype in the tumor microenvironment inhibiting breast cancer growth and progression. **12**, 2078 (2020).
8. Naik, A., Monjazez, A.M. & Decock, J.J.F.i.i. The obesity paradox in cancer, tumor immunology, and immunotherapy: potential therapeutic implications in triple negative breast cancer. **10**, 476171 (2019).
9. Bouchalova, P. & Bouchal, P. Current methods for studying metastatic potential of tumor cells. *Cancer cell international* **22**, 394 (2022).
10. Moghtaderi, H., *et al.* Electric cell-substrate impedance sensing in cancer research: An in-depth exploration of impedance sensing for profiling cancer cell behavior. *Sensors and Actuators Reports*, 100188 (2024).
11. Gomillion, C.Z., Longjing; Chvatal, Stacie. Monitoring Migration of Breast Cancer Cells using Maestro Z Real-Time Impedance Assay. in *Application Note* (ed. Biosystems, A.) (<https://www.axionbiosystems.com/resources/application-note/scratch-assay>, 2020).
12. Hedayatipour, A., Aslanzadeh, S., McFarlane, N.J.B. & Bioelectronics. CMOS based whole cell impedance sensing: Challenges and future outlook. **143**, 111600 (2019).
13. Srinivasan, B., *et al.* TEER measurement techniques for in vitro barrier model systems. *Journal of laboratory automation* **20**, 107-126 (2015).

14. Li, X., *et al.* CLDN6-mediates SB431542 action through MMPs to regulate the invasion, migration, and EMT of breast cancer cells. *International Journal of Clinical and Experimental Pathology* **13**, 1590 (2020).
15. Ma, X., *et al.* Claudin-4 controls the proliferation, apoptosis, migration and in vivo growth of MCF-7 breast cancer cells. **34**, 681-690 (2015).
16. Wu, J., *et al.* RBM38 is involved in TGF- $\beta$ -induced epithelial-to-mesenchymal transition by stabilising zonula occludens-1 mRNA in breast cancer. **117**, 675-684 (2017).
17. Kim, T., *et al.* Down-regulation of claudin-2 in breast carcinomas is associated with advanced disease. **53**, 48-55 (2008).
18. Pan, Y., *et al.* 3D microgroove electrical impedance sensing to examine 3D cell cultures for antineoplastic drug assessment. **6**, 1-10 (2020).
19. Hedayatipour, A., *et al.* A wearable CMOS impedance to frequency sensing system for non-invasive impedance measurements. **14**, 1108-1121 (2020).
20. Nguyen, A., Yoshida, M., Goodarzi, H. & Tavazoie, S.F.J.N.c. Highly variable cancer subpopulations that exhibit enhanced transcriptome variability and metastatic fitness. **7**, 11246 (2016).
21. Tran, T.B., Baek, C. & Min, J.J.P.o. Electric cell-substrate impedance sensing (ECIS) with microelectrode arrays for investigation of cancer cell–fibroblasts interaction. **11**, e0153813 (2016).
22. Biosystems, A. Impedance - General. Vol. 2024 (Author, Axionbiosystems.com, 2024).
23. Biosystems, A. Axis Z User Guide. in *Software Manual for the Maestro Impedance System* (Author, 2021).
24. Liu, Q., *et al.* Impedance studies of bio-behavior and chemosensitivity of cancer cells by micro-electrode arrays. **24**, 1305-1310 (2009).
25. Crowell, L.L., Yakisich, J.S., Aufderheide, B. & Adams, T.N.J.M. Electrical impedance spectroscopy for monitoring chemoresistance of cancer cells. **11**, 832 (2020).
26. Yang, Y., *et al.* Monitoring the heterogeneity in single cell responses to drugs using electrochemical impedance and electrochemical noise. **12**, 2558-2566 (2021).
27. Láng, O., Köhidai, L. & Wegener, J.J.E.c.r. Label-free profiling of cell dynamics: A sequence of impedance-based assays to estimate tumor cell invasiveness in vitro. **359**, 243-250 (2017).



28. Wegener, J., Keese, C.R. & Giaever, I.J.E.c.r. Electric cell–substrate impedance sensing (ECIS) as a noninvasive means to monitor the kinetics of cell spreading to artificial surfaces. **259**, 158-166 (2000).
29. Pradhan, R., Rajput, S., Mandal, M., Mitra, A. & Das, S.J.R.A. Electric cell–substrate impedance sensing technique to monitor cellular behaviours of cancer cells. **4**, 9432-9438 (2014).
30. Iwakura, T., Marschner, J.A., Zhao, Z.B., Świdarska, M.K. & Anders, H.-J.J.N.D.T. Electric cell-substrate impedance sensing in kidney research. **36**, 216-223 (2021).
31. Roy Burman, D., Das, S., Das, C. & Bhattacharya, R.J.M.B.R. Alternative splicing modulates cancer aggressiveness: role in EMT/metastasis and chemoresistance. **48**, 897-914 (2021).
32. Santos, J.M., Hussain, F.J.N. & cancer. Higher glucose enhances breast cancer cell aggressiveness. **72**, 734-746 (2020).
33. Weinberg, R.A. *The biology of cancer*, (Garland science, 2013).
34. Edechi, C.A., *et al.* Comparison of fixation methods for the detection of claudin 1 and E-cadherin in breast cancer cell lines by immunofluorescence. **70**, 181-187 (2022).
35. Kauanova, S., Urazbayev, A., Vorobjev, I.J.F.i.c. & biology, d. The frequent sampling of wound scratch assay reveals the “opportunity” window for quantitative evaluation of cell motility-impeding drugs. **9**, 640972 (2021).
36. AL-Shaeli, S.J., Ethaeb, A.M. & Gharban, H.A. Determine the glucose regulatory role of decaffeinated Green Tea extract in reduces the metastasis and cell viability of MCF7 cell line. in *AIP Conference Proceedings*, Vol. 2394 020003 (AIP Publishing LLC, 2022).
37. Niu, J., *et al.* DKK1 inhibits breast cancer cell migration and invasion through suppression of  $\beta$ -catenin/MMP7 signaling pathway. **19**, 1-13 (2019).
38. Alhawarat, F.M., *et al.* The effect of cycling hypoxia on MCF-7 cancer stem cells and the impact of their microenvironment on angiogenesis using human umbilical vein endothelial cells (HUVECs) as a model. **7**, e5990 (2019).
39. Gest, C., *et al.* Rac3 induces a molecular pathway triggering breast cancer cell aggressiveness: differences in MDA-MB-231 and MCF-7 breast cancer cell lines. **13**, 1-14 (2013).
40. Shirazi, F.H., *et al.* *Remarks in successful cellular investigations for fighting breast cancer using novel synthetic compounds*, (INTECH Open Access Publisher Croatia, 2011).

41. Dai, X., Cheng, H., Bai, Z. & Li, J.J.J.o.C. Breast cancer cell line classification and its relevance with breast tumor subtyping. **8**, 3131 (2017).
42. Geoffroy, M., *et al.* Pro-apoptotic effect of  $\Delta 2$ -TGZ in “claudin-1-low” triple-negative breast cancer cells: involvement of claudin-1. **165**, 517-527 (2017).
43. Fiorio, E., *et al.* Leptin/HER2 crosstalk in breast cancer: in vitro study and preliminary in vivo analysis. **8**, 1-11 (2008).
44. Gonzalez, R.R., *et al.* Leptin signaling promotes the growth of mammary tumors and increases the expression of vascular endothelial growth factor (VEGF) and its receptor type two (VEGF-R2). **281**, 26320-26328 (2006).
45. Yuan, H.-J., Sun, K.-W. & Yu, K.J.M.M.R. Leptin promotes the proliferation and migration of human breast cancer through the extracellular-signal regulated kinase pathway. **9**, 350-354 (2014).
46. Yan, D., Avtanski, D., Saxena, N.K. & Sharma, D.J.J.o.b.c. Leptin-induced epithelial-mesenchymal transition in breast cancer cells requires  $\beta$ -catenin activation via Akt/GSK3- and MTA1/Wnt1 protein-dependent pathways. **287**, 8598-8612 (2012).
47. Feng, H., *et al.* Leptin promotes metastasis by inducing an epithelial-mesenchymal transition in A549 lung cancer cells. **21**, 165-171 (2014).
48. Li, S.-J., *et al.* Adipocyte-derived leptin promotes PAI-1-mediated breast cancer metastasis in a STAT3/miR-34a dependent manner. **12**, 3864 (2020).
49. Gorrab, A., *et al.* Leptin promotes prostate cancer proliferation and migration by stimulating STAT3 pathway. **73**, 1217-1227 (2021).
50. Assiri, A.M., Kamel, H.F.J.O.r. & practice, c. Evaluation of diagnostic and predictive value of serum adipokines: Leptin, resistin and visfatin in postmenopausal breast cancer. **10**, 442-453 (2016).
51. Crisostomo, J., *et al.* Hyperresistinemia and metabolic dysregulation: a risky crosstalk in obese breast cancer. **53**, 433-442 (2016).
52. Georgiou, G.P., *et al.* Serum resistin is inversely related to breast cancer risk in premenopausal women. **29**, 163-169 (2016).
53. Li, G., *et al.* Magnetic resonance spectroscopy-detected change in marrow adiposity is strongly correlated to postmenopausal breast cancer risk. **17**, 239-244 (2017).
54. Rodrigo, C., *et al.* Circulating leptin, soluble leptin receptor, free leptin index, visfatin and selected leptin and leptin receptor gene polymorphisms in sporadic breast cancer. **64**, 393-401 (2017).

55. Jen, K.-L.C., Buison, A., Darga, L., Nelson, D.J.J.o.L. & Medicine, C. The relationship between blood leptin level and bone density is specific to ethnicity and menopausal status. **146**, 18-24 (2005).

CHAPTER 4

ELECTRICAL IMPEDANCE AS AN INDICATOR FOR BREAST CANCER CELL TYPE  
DISCRIMINATION

---

Higgins, K. S. and Gomillion, C. T. *To be submitted to Lab On A Chip.*

## 4.1 Abstract

Breast cancer metastasis remains the leading cause of mortality among women with breast cancer, with triple-negative breast cancer posing a particularly aggressive and poorly understood clinical challenge. This chapter investigates the use of impedance-based techniques, including Electric Cell-substrate Impedance Sensing (ECIS) and transepithelial electrical resistance (TEER), to quantitatively assess cellular behaviors associated with metastatic potential, with particular focus on factors associated with epithelial-to-mesenchymal transition (EMT). Bioelectronic impedance assay methods offer a label-free, real-time alternative to conventional wound healing assays, providing dynamic measurements of cell adhesion, surface coverage, and migratory capacity. Through the application of these techniques across a panel of mammary cell lines, we identified distinct behavioral patterns that correlate with known metastatic tendencies. Notably, impedance measurements revealed that MDA-MB-453 cells exhibit high migratory behavior despite epithelial morphology, challenging the assumption that EMT transition status alone predicts metastatic potential. These findings highlight the value of impedance and TEER as complementary tools in metastasis research and underscore the need to consider both dynamic and morphological cell features. Looking forward, integrating these techniques with image-based phenotyping and machine learning holds promise for enhancing the precision of metastatic behavior assessments.

## 4.2 Introduction

Breast cancer is the leading cause of cancer-related death among women worldwide, with over 300,00 new cases expected in the United States alone in 2025 <sup>1,2</sup>. The majority of these deaths result from metastasis, where the cancer spreads to distant organs, like the brain, lungs, liver, and bone <sup>3</sup>. Among breast cancer subtypes, triple-negative breast cancer (TNBC) accounts for approximately 10% of cases <sup>4</sup> and poses a particular challenge due to its difficulty to treat and increased aggressiveness. Specifically, TNBC tumors lack all three of the main cell receptors related to breast cancer - estrogen receptor (ER), progesterone receptor (PR), and human epidermal growth factor receptor type 2 (HER2), which results in greater difficulty treating this type of cancer with commonly available targeted therapies. In addition, TNBC has been shown to occur more frequently in younger women and is the most aggressive form of cancer, with the highest rates of metastasis and mortality. Hence, there is a significant need to better understand the metastatic behaviors of breast cancer, particularly of the TNBC subtype. Gaining insight into the mechanisms driving metastatic progression is critical for improving both diagnostic and treatment strategies towards improving TNBC patient outcomes.

One hallmark of metastasis is the epithelial-to-mesenchymal transition (EMT), a metabolic shift where epithelial cells acquire mesenchymal properties and transition from a proliferative to a migratory state. This transformation occurs on an epigenetic level where markers like epithelial cell adhesion molecule (EpCAM), desmoplakin, and keratin are associated with an epithelial-like state and n-cadherin, vimentin, and fibronectin are associated with a mesenchymal-like state <sup>5-7</sup>. This loss of polarity and cell-to-cell adhesion enhances the cells' invasive and migratory capacities, facilitating early metastatic processes <sup>8-10</sup>. Tight junction proteins like claudins, occludin, and ZO-1 are key regulators of epithelial polarity and cell-to-cell adhesion <sup>11,12</sup>, and their

downregulation is a critical step during EMT<sup>13,14</sup>. The disruption of these junctions compromises the epithelial barrier, enabling cytoskeletal remodeling and increased motility, and is especially pronounced in aggressive breast cancer subtypes like claudin-low tumors<sup>15</sup>. These changes not only promote dissemination from the primary tumor but also directly influence how cancer cells interact with and migrate through peritumoral tissue<sup>16-19</sup>.

As a tumor establishes itself at the primary site, metastasis begins with local invasion, where cancer cells breach the basement membrane and migrate into surrounding tissue. This migration requires dynamic regulation of focal adhesions (FAs), which mediate attachment between cells and the extracellular matrix (ECM). Invasive breast cancer cells have more dynamic FAs than their noninvasive counterparts<sup>20</sup>, and a decrease in adhesion strength has been shown to correspond to increased metastatic potential<sup>21</sup>. Thus, investigating changes in cell adhesion and motility can yield valuable insights into metastatic behavior and disease aggressiveness.

This study employs an impedance-based assay methodology, developed in Chapter 3, to quantify metastatic behaviors across a broad panel of mammary cell lines. By integrating impedance and resistance measurements, this approach enables the assessment of cell proliferation, surface coverage, barrier integrity, and migration within the same population of cells. Two non-cancerous lines and six breast cancer cell lines were analyzed to evaluate the relationship between EMT and cancer aggressiveness using this approach. Five TNBC lines, selected for their diverse morphological profiles, were included to investigate this question within the aggressive TNBC subtype, towards identifying key characteristics of these cells that could be used as indicators for assessing their metastatic potential. This work aims to identify novel, quantifiable patterns of behavior in TNBC cells with distinct morphologies, providing deeper insight into their aggressiveness and metastatic potential.

## 4.3 Materials and Methods

### 4.3.1 Reagents and Cell Cultures

Poly-D-lysine lyophilized powder (Sigma Aldrich) was dissolved in sterilized deionized (DI) water to form a 21.3  $\mu$ M solution. This solution was stored at -20°C and thawed on ice when needed. All cell lines were purchased from American Type Culture Collection (ATCC) and cultured at 37°C and 5% CO<sub>2</sub> atmosphere. Cell line information, including cell type, and literature-confirmed receptor status, is summarized in Table 4.1. As outlined in Supplementary Table B.1, 184B5 and MCF10A cells were cultured in Mammary Epithelial Growth Medium (MEGM; Lonza) supplemented with 1 ng/mL cholera toxin (Sigma-Aldrich) and 100 ng/mL cholera toxin respectively. HCC70 and BT-549 cells were cultured in RPMI-complete using ATCC's modified RPMI blend (ATCC) supplemented with 10% fetal bovine serum (FBS; R&D Systems) and 1% penicillin/streptomycin (P/S; Gibco). HCC1806, MDA-MB-453, and MDA-MB-231 cells were cultured in low-glucose Dulbecco's Modified Eagle Medium (DMEM; Gibco) supplemented with 10% FBS and 1% P/S to form DMEM-Complete. Lastly, the MCF7 cell line was cultured in DMEM-Complete supplemented with 0.01 mg/mL bovine insulin (Sigma). All cell lines were confirmed to be free of mycoplasma using a commercially available kit (InvivoGen).

### 4.3.2 Mammary Cell Transcriptomic Profiling

RNA expression data was obtained from the Cancer Dependency Map (DepMap) <sup>22,23</sup>, a comprehensive resource developed by the Broad Institute to identify genetic and chemical vulnerabilities across diverse cancer types. As part of the 24Q4 Public release <sup>24</sup>, DepMap provides genomic and transcriptomic profiles for a wide range of cancer cell lines, including RNA sequencing data for the six cell lines used in this study. This release includes updated data from



whole-genome and exome sequencing (copy number variation and mutation status), RNA sequencing (gene expression and fusion events), and genome-wide CRISPR-Cas9 knockout screens. Expression levels of VIM (vimentin) and EPCAM (EpCAM) were extracted from this dataset to quantitatively compare with protein-level expression observed through immunofluorescence staining.

**Table 4.1:** Mammary cell line information

Cell Line	Cell Type	Receptor Status	Reference
184B5 (CRL-8799 <sup>TM</sup> )	Normal Mammary Gland	-	25,26
MCF10A (CRL-10317 <sup>TM</sup> )	Fibrocystic Disease	-	27
MCF7 (HTB-22 <sup>TM</sup> )	Mammary Gland Adenocarcinoma	(ER+, PR+, HER2-)	28-30
MDA-MB-453 (HTB-131 <sup>TM</sup> )	Carcinoma	(ER-, PR-, HER2-)	29,31-33
HCC70 (CRL-2315 <sup>TM</sup> )	Primary Invasive Ductal Carcinoma	(ER-, PR-, HER2-)	31,32,34
HCC1806 (CRL-2335 <sup>TM</sup> )	Primary Squamous Cell Carcinoma	(ER-, PR-, HER2-)	31,34,35
MDA-MB-231 (HTB-26 <sup>TM</sup> )	Adenocarcinoma	(ER-, PR-, HER2-)	29,31,33,35-37
BT-549 (HTB-122 <sup>TM</sup> )	Ductal Carcinoma	(ER-, PR-, HER2-)	31,36,38

#### 4.3.3 Immunofluorescence Staining of Mammary Cell Lines

Immunofluorescent staining was performed to visualize epithelial and mesenchymal phenotypic markers in cells. Conjugated antibodies detecting EpCAM (ab237395, Abcam) and vimentin (ab202504, Abcam) were diluted to a final concentration of 0.1 µg/mL in phosphate-buffered saline (PBS; Gibco). The working stain solution was stored at 4°C for up to two weeks, while the remaining stock was stored at -20 °C for long-term use. Cells were seeded onto black-walled, clear-bottom 96-well plates (Corning) at a density of 10,000 cells/cm<sup>2</sup> and incubated for

14 hours to allow full adhesion and cytoskeletal spreading on the tissue culture polystyrene surface. Following attachment, cells were fixed with 4% (v/v) paraformaldehyde (PFA; Thermo Scientific) in PBS for 15 minutes, then permeabilized with 0.1% (v/v) Triton X-100 (Thermo Scientific) in PBS for another 15 minutes. Cells were then blocked with 3% bovine serum albumin (BSA; Invitrogen) for 30 minutes and subsequently incubated overnight at 4°C with the anti-EpCAM and anti-vimentin antibody solution. Nuclear staining was performed using NucBlue (Invitrogen), with a 20-minute incubation period. PBS washes were performed between all staining and blocking steps. Imaging was carried out manually at 20× magnification using a Cytation 1 imaging system (Agilent BioTek).

#### 4.3.4 Fluorescent Imaging of Mammary Cell Lines

Mammary cell lines were cultured and stained to assess cellular morphology and growth patterns. Each cell line was seeded into 6-well plates (Corning) and cultured in their respective growth media, as described in Section 4.3.1, until reaching approximately 50–70% confluence. Cells were fixed with 4% PFA in PBS for 30 minutes at room temperature, followed by two washes with PBS. For permeabilization and staining, a solution containing 1% (v/v) Tween 20 (Sigma-Aldrich), 10 µg/mL Hoechst 33342 (Thermo Fisher) to label nuclear DNA, and 1 µg/mL Fluorescein-5-Maleimide (Thermo Fisher) to visualize actin filaments was applied to the fixed cells. Cells were incubated in this staining solution for 1 hour at room temperature, protected from light. Following staining, cells were washed with PBS, and fluorescent images were acquired manually using a Cytation 1 imaging system (Agilent BioTek).

#### 4.3.5 Seeding Cells onto Cytoview Plates

Before cells were added to the CytoView-Z 96-well electrode plates (Axion Biosystems), the culture surface was treated with a 21.3  $\mu\text{M}$  poly-D-lysine solution and a media baseline test was performed as explained in Chapter 3. Each cell line was seeded at a density optimized to account for differences in growth rate and cell size, ensuring confluency at 24 hours. The non-cancerous 184B5 and MCF10A cells were seeded at 100,000 and 110,000 cells/cm<sup>2</sup> respectively. The MDA-MB-453 and HCC70 groups were seeded at the highest densities, 250,000 cells/cm<sup>2</sup> and 125,000 cells/cm<sup>2</sup> respectively, to ensure the highest possible surface coverage. The MCF7 and HCC1806 groups were seeded at 85,000 cells/cm<sup>2</sup> and the more elongated MDA-MB-231 and BT549 cells were seeded at 75,000 cells/cm<sup>2</sup>. To maintain humidity within the Maestro Z system, 8 mL of sterile deionized (DI) water was added to the peripheral reservoir of the plate. The plate was left to rest in a biosafety cabinet for 1 hour to allow the cells to attach and minimize edge effects. After one hour, the plate was docked in the Maestro Z system and cultured at 37°C and 5% CO<sub>2</sub>. High frequency impedance and transepithelial electrical resistance (TEER) measurements were automatically recorded at 1-minute intervals upon plate engagement.

#### 4.3.6 Evaluating Cell Proliferation, Barrier Integrity, and Migration

Cell proliferation and growth patterns were monitored by tracking high frequency (41.5 kHz) impedance through the AxisZ software compatible with the Maestro Z. At 24 hours, the plate was undocked, and the cells were visually checked for confluence using an EVOS FLc microscope (Invitrogen). To halt growth, all medium was changed to a nutrient-reduced formula, shown in Supplemental Table B.1, and the plate was redocked into the Maestro Z. The cells continued to culture for 12 hours while their metabolic function shifted, and cell growth ceased. Impedance was

collected continuously, while TEER was measured at confluence as resistance at a 1 kHz frequency current. A modified wound healing assay, outlined in Chapter 3, was used to measure cell migration through high frequency impedance. After 36 hours of migration, the experiment was terminated.

#### 4.3.7 Data Processing and Statistical Analysis

High-frequency impedance (41.5 kHz) and low-frequency resistance (1 kHz; TEER) data was exported from the AxisZ software via Microsoft Excel, where the rate of wound closure was then calculated by as the change in impedance from the time immediately after the scratch (0 hours) to 36 hours post-scratch. The 0-hour timepoint was defined as the measurement taken 5 minutes after the plate was redocked and impedance collection resumed, to account for transient spikes in impedance caused by handling-related perturbations. This change in impedance was then divided by the 36-hour interval to determine the rate of migration. Statistical analyses was performed using GraphPad Prism 10.2. Statistical significance was determined via ordinary one-way ANOVA.

### 4.4 Results

#### 4.4.1 Immunofluorescence Staining and Transcriptomic Profiling Confirm Epithelial-

#### Mesenchymal Heterogeneity

Immunofluorescence staining for EpCAM and vimentin was performed to assess the epithelial-mesenchymal phenotype of each mammary cell line. Imaging results, in combination with RNA sequencing data from the DepMap database <sup>24</sup>, confirmed heterogeneous expression of epithelial (EpCAM) and mesenchymal (vimentin) markers across the panel of cell lines tested.

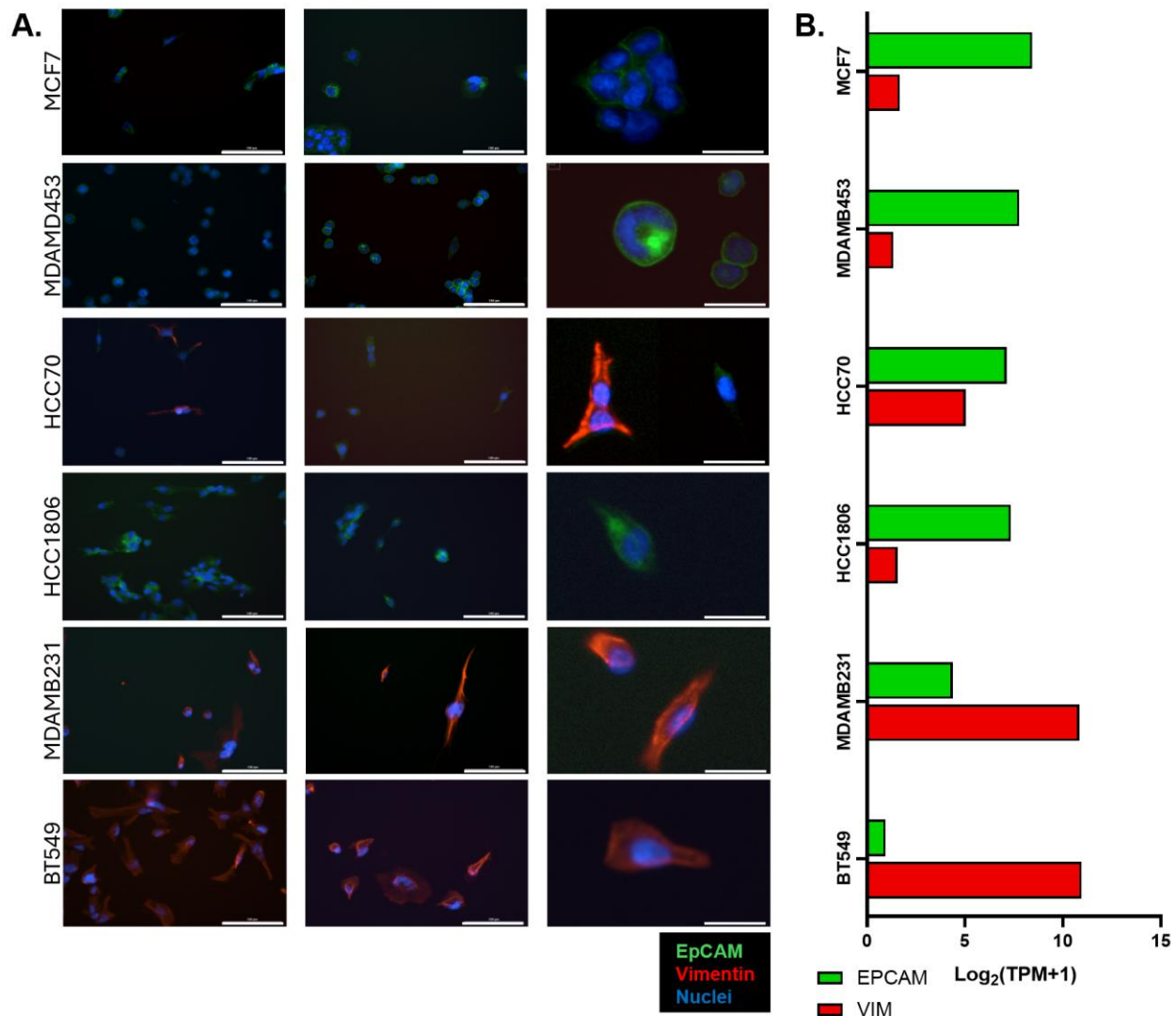


**Figure 4.1:** Epithelial-mesenchymal characterization of mammary cell lines. A) Representative immunofluorescence staining of mammary cell lines showing expression of EpCAM (green, GFP) and vimentin (red, TRITC), with nuclear counterstaining using Hoechst (blue, DAPI). Images in the left and middle columns were acquired at 20 $\times$  magnification (scale bars, 100  $\mu\text{m}$ ); the right column shows magnified regions from the corresponding images (scale bars, 20  $\mu\text{m}$ ). B) Corresponding gene expression levels of EPCAM and VIM in each cell line, obtained from the DepMap Portal<sup>22-24</sup>. RNA-seq values are presented as  $\text{log}_2(\text{TPM} + 1)$ , where TPM denotes transcripts per million.

Triple-negative breast cancer cell lines MDA-MB-231 and BT549 exhibited strong vimentin expression and minimal EpCAM expression (Figure 4.1), consistent with a mesenchymal phenotype. These cells also displayed prominent cytoskeletal projections, as seen in Figure 4.1A.

In contrast, MCF7 and MDA-MB-453 cells expressed high levels of EpCAM and low levels of vimentin, confirming their epithelial morphology.

HCC1806 cells showed moderately reduced EpCAM expression compared to MCF7 and MDA-MB-453 cells, along with a more elongated morphology. However, their overall phenotype remained predominantly epithelial, suggesting a potential intermediate or hybrid epithelial/mesenchymal state. This mixed phenotype, associated with cellular plasticity and enhanced metastatic potential, was more evident in the HCC70 cell line, which seemingly expressed both EpCAM and vimentin at substantial levels. Notably, Figure 4.1A highlights cell-to-cell variability in vimentin expression within the HCC70 population, further supporting the existence of phenotypic heterogeneity within this cell line.

#### 4.4.2 Impedance Reveals Proliferation Patterns and Surface Coverage in Mammary Cell Lines

As previously demonstrated in Chapter 3, high-frequency impedance is correlated with cell proliferation and surface coverage<sup>39-41</sup>. Therefore, impedance was measured across all mammary cell lines to explore the relationship between proliferation patterns and cell aggressiveness. Impedance values after 36 hours of proliferation, once each cell line reached confluency, are shown in Figure 4.2B. MCF10A and MCF7 cells exhibit significantly higher impedance than all other cell lines, indicating that they grow more tightly together and cover the growth surface more completely. This is consistent with known characteristics of their growth patterns, as shown in Figure 4.2A, where they form a tightly packed monolayer. In contrast, the normal mammary cell line 184B5 and all TNBC cell lines display markedly lower impedance, suggesting they do not cover the electrode surface as fully as MCF10A and MCF7 lines. High-frequency impedance provides insight into how each cell line proliferates and covers the growth surface. While

decreased proliferation is a hallmark of cancer invasion, it does not fully capture aggressive cancer behaviors. To further assess cell aggressiveness, TEER was measured in the same population to evaluate cell-to-cell barrier integrity.

#### 4.4.3 Transepithelial Electrical Resistance is Significantly Lower in Triple-Negative Cell Lines

The number of cell-to-cell connections can decrease as cancer cells undergo phenotypic changes and adopt more mesenchymal traits<sup>13,14,42</sup>. To evaluate this in our population of mammary cell lines, TEER was measured. TEER values, measured concurrently with impedance, were obtained after 36 hours of proliferation, once the cells had reached confluency, and are shown in Figure 4.2C. All TNBC cell lines exhibited significantly lower TEER values compared to the non-cancerous cells (184B5 and MCF10A) and the luminal MCF7 cells. This generally correlates with cell phenotype, as cells with reduced epithelial traits, like lower claudin and E-cadherin expression, show decreased barrier integrity. The MCF10A and MCF7 cells, which have the highest TEER values, exhibit a more epithelial phenotype and tighter cell-to-cell connections. The limitation of using TEER to quantify barrier integrity is that it can only be measured accurately at confluency, when the cells have formed a monolayer. This method can prove less accurate for cells, like the HCC70 cell line, that grow in dense patches but fail to fill in gaps in the growth surface even at confluence. Overall, these findings support our hypothesis that more aggressive cells, like TNBC, have lower barrier integrity, as reflected by their lower TEER values. To further quantify cell aggressiveness, a migration assay was performed.

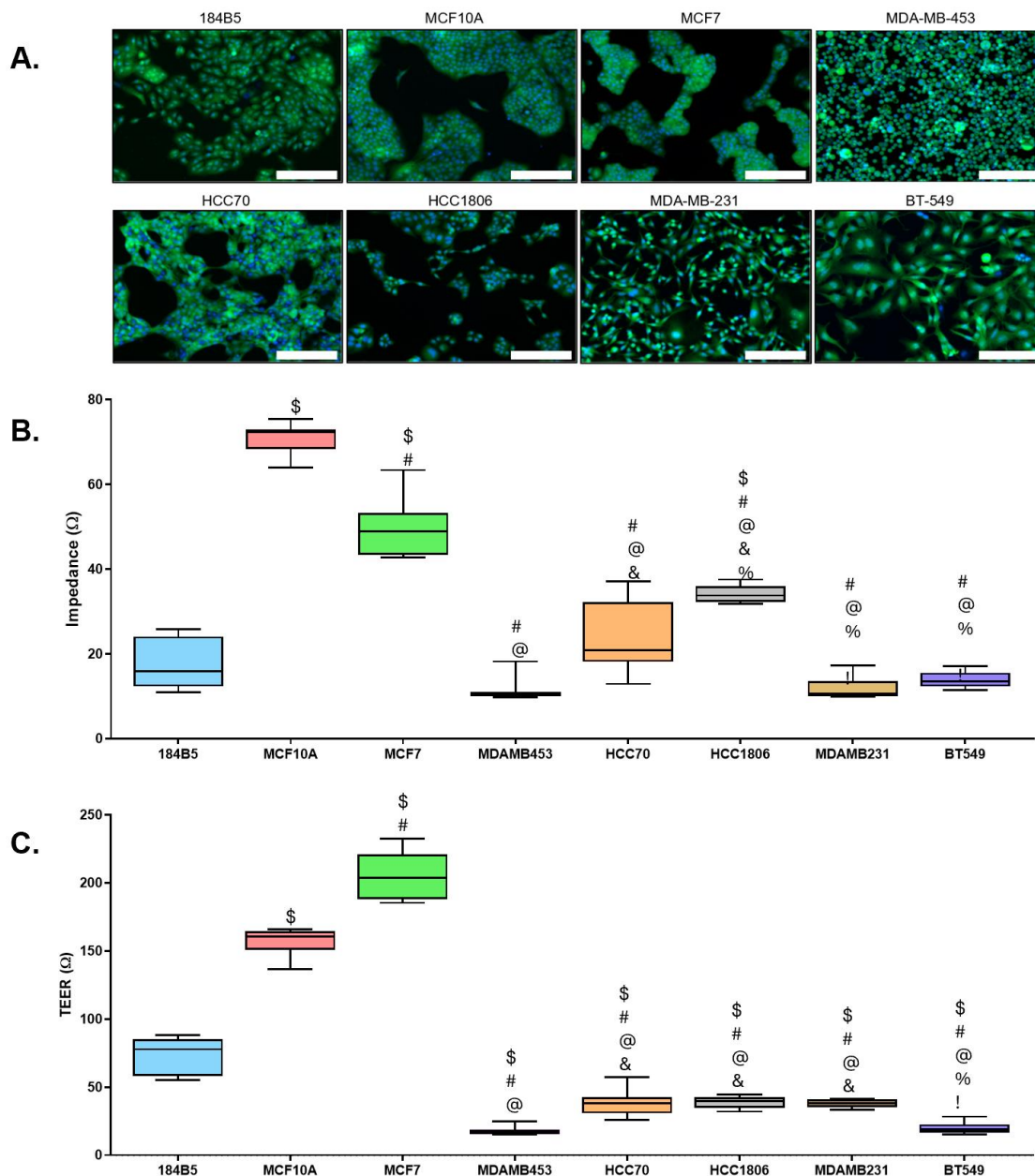


**Figure 4.2:** Representative images of mammary cell lines with impedance and transepithelial electrical resistance (TEER) values after 36 hours of proliferation. A) Cells were fixed and stained with Hoechst (blue) and fluorescein-maleimide (green) to indicate nuclei and cytoplasm, respectively. The white scale bar represents 200  $\mu\text{m}$ . Images are shown for all cell lines used in this study. B) High frequency (41.5 kHz) impedance and C) TEER (resistance at 1 kHz) measurements of mammary cell lines after 36 hours of proliferation, when each well had reached confluency. Data was obtained from 6 independent wells (n=6) per cell line. Statistical significance is indicated as follows: \$ indicates  $p < 0.0001$  compared to 184B5; # indicates  $p < 0.0001$  compared to MCF10A; @ indicates  $p < 0.0001$  compared to MCF7; & indicates  $p < 0.05$  compared to MDA-MB-453; % indicates  $p < 0.05$  compared to HCC70; and ! Indicates  $p < 0.05$  compared to HCC1806.



#### 4.4.4 Two-Dimensional Migration Reveals Aggressive Migration Patterns in Triple-Negative Cell Lines

To assess cell aggressiveness, two-dimensional (2D) cell migration was measured using a modified wound healing assay, where migration is tracked by changes in impedance (representing surface coverage). Impedance values immediately after the scratch and 36 hours post-scratch are shown in Figure 4.3A. To account for differences in growth patterns, impedance is normalized to the value at the time immediately prior to the scratch, when each well was confluent. Four of the five TNBC cell lines show a significant change in impedance over 36 hours, indicating migration. To further validate these results, the rate of migration was averaged over the 36-hour period, as shown in Figure 4.3B. The MDA-MB-453 and MDA-MB-231 groups were the only cell lines with significantly higher migration rates compared to the non-migratory MCF7 cells, suggesting that these cell lines are highly aggressive. In contrast, the HCC1806 and BT-549 groups exhibited moderate migration. Both the change in impedance over 36 hours and the rate of wound closure confirm that luminal MCF7 cells and triple-negative HCC70 cells show little to no migration. Both non-cancerous groups, 184B5 and MCF10A, show a negative rate of migration with the 184B5 cells showing a significant decrease in impedance over 36 hours. This indicates that these cell groups did not perform migration but began to die from long-term confluence-induced contact inhibition. Impedance, TEER, and rate of wound closure were measured in the same cell population and subsequently compared to identify patterns in impedance and TEER relative to migration potential.

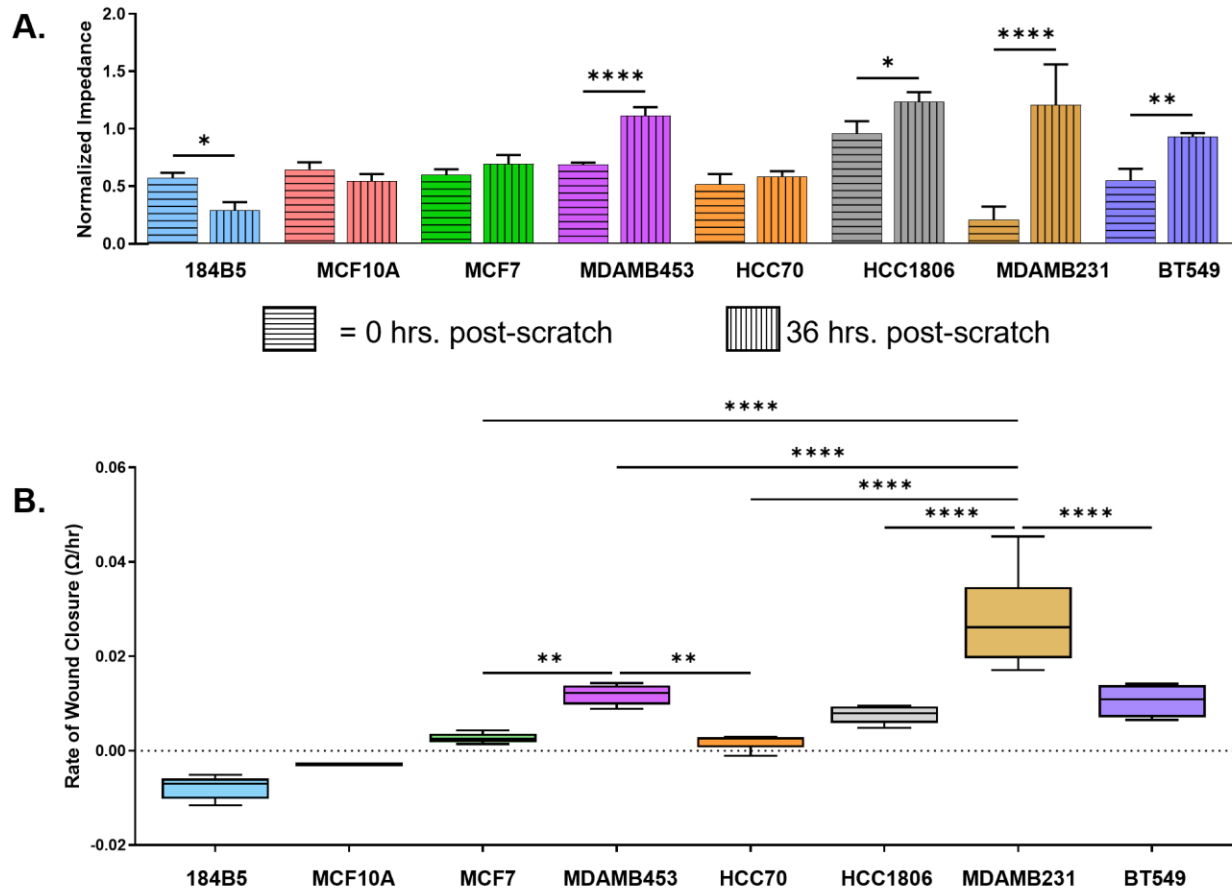


**Figure 4.3:** Rate of migration and impedance measurements during wound healing assay. A) Impedance values normalized to the point immediately prior to the scratch (confluency), showing impedance at both 0 and 36 hours after the scratch. B) Average rate of wound closure across 36 hours. Significance is only shown among cancer groups. Data was obtained from 4-6 independent wells (n = 4-6) across all cell lines. Statistical significance is indicated as follows: \* p < 0.05; \*\* p < 0.01; and \*\*\*\* p < 0.0001.

#### 4.4.5 Low Impedance and Low Transepithelial Electrical Resistance Are Linked with Cancer Aggressiveness

To investigate the relationship between epithelial barrier integrity and migratory behavior, impedance and TEER measurements at confluency were compared with wound closure rates. As shown in Figure 4.4A, cell lines demonstrating moderate (blue) to high (red) migratory capacity exhibit impedance values at confluency below 35.5 ohms. This finding suggests that highly migratory cell populations may achieve lower surface coverage at confluency, in contrast to less

migratory or non-aggressive cell lines, which do not display a consistent impedance profile. A comparable trend is evident in Figure 4.4B, where TEER values are analyzed in relation to migration rates. Aggressive cell lines consistently exhibit TEER values below 44.6 ohms, representing the lower spectrum of the range observed across mammary epithelial cell lines. This data imply that increased migratory potential is associated with reduced cell-cell adhesion and barrier function. While low impedance or TEER values alone are not exclusive indicators of aggressive migration, all highly migratory cell lines analyzed display reduced impedance and TEER values relative to the luminal MCF7 and non-tumorigenic MCF10A cell lines.

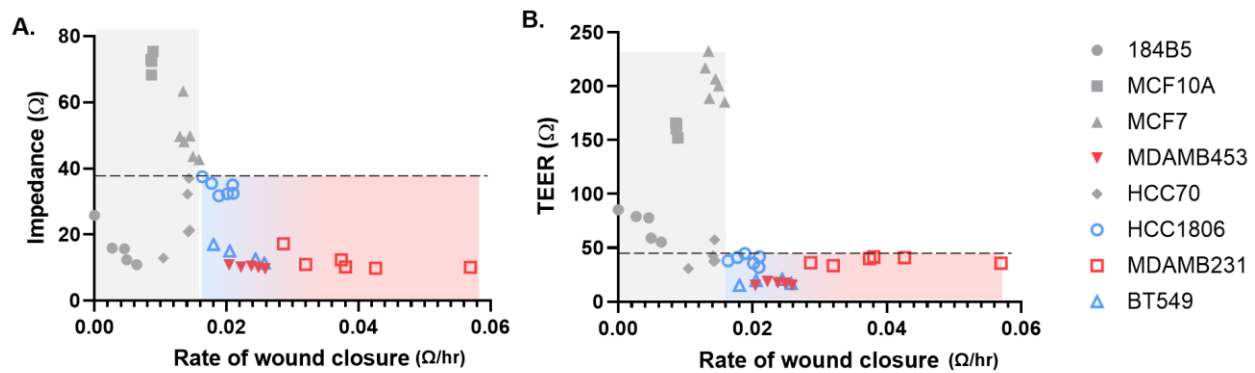


**Figure 4.4:** Impedance and transepithelial electrical resistance (TEER) compared to the rate of wound closure. A) High-frequency (41.5 kHz) impedance and B) TEER (resistance at 1 kHz) measurements of mammary cell lines after 36 hours of proliferation (confluency), compared with average rate of migration over 36 hours. Impedance, TEER, and rate of wound closure values are matched per well. Grey data points represent groups where no migration was performed (highlighted by a grey-shaded box). Blue data points represent groups (HCC1806 and BT549) where moderate migration occurred, and red data points represent groups (MDAMB231 and MDAMB453) with high migration (highlighted by a blue and red-shaded box). Dashed line represents the highest value of impedance and TEER recorded by the migratory cell lines, 35.5  $\Omega$  and 44.6  $\Omega$  respectively. Data were obtained from 4–6 independent wells ( $n = 4–6$ ) across all cell lines.

## 4.5 Discussion

These results demonstrate that bioelectronic measurements, like impedance and TEER, can capture functional differences in breast cancer cell behavior, particularly regarding cell spreading, barrier formation, and migration. The previous chapter established impedance spectroscopy as a tool for quantifying key cell properties. Building on that foundation, this chapter leverages impedance to investigate how EMT-related features correlate with metastatic potential across a panel of breast cancer cell lines.

EpCAM and vimentin expression highlight the epithelial-mesenchymal heterogeneity among the breast cancer cell lines analyzed. EMT is widely recognized as a hallmark of breast cancer metastasis, and cells exhibiting a more mesenchymal phenotype are generally expected to demonstrate higher migratory potential <sup>43,44</sup>. Our modified wound healing assay revealed a spectrum of migratory behaviors, with non-cancerous lines, MCF7, and HCC70 showing limited migration, a behavior measured in previous studies <sup>45,46</sup>. The BT-549, HCC1806, and especially MDA-MB-231 and MDA-MB-453 cells exhibited higher motility. These results support the role of EMT in enabling migration but also highlight the limitations of relying solely on morphological phenotype to predict metastatic potential.

Surprisingly, the MDA-MB-453 cell line exhibited significant migration despite its predominantly epithelial morphology. While previous work has reported variable behavior in this cell line <sup>46,47</sup>, our findings align with those of Xu et al., who observed comparable migration rates between MDA-MB-453 and the more mesenchymal MDA-MB-231 cells <sup>48</sup>. Interestingly, MDA-MB-453 cells are classified as triple-negative status, yet do not align with typical basal-like or claudin-low TNBC subtypes <sup>49</sup>. Instead, they belong to the luminal androgen receptor (LAR) subtype <sup>50,51</sup>, characterized by AR expression and a more epithelial-like gene signature. Despite

their epithelial morphology, these cells exhibit low expression of some tight junction genes such as CLDN1 (Supplementary Figure B.1) and lack strong junctional integrity<sup>22,24</sup>. This decoupling of epithelial morphology from junctional function may contribute to their high migratory behavior and underscores the complexity of using EMT markers in isolation to assess metastatic potential.

The HCC70 cell line presents a particularly complex case. Despite showing minimal migratory activity, it co-expresses both EpCAM and vimentin, with notable intrapopulation variability in vimentin levels. This phenotypic heterogeneity reflects a degree of plasticity often associated with increased metastatic potential and therapeutic resistance. However, in this study, that potential did not translate into migratory behavior, highlighting the limitations of using EMT marker expression alone to predict functional outcomes.

Further complicating interpretation, HCC70 cells exhibited low TEER values despite forming visible cell-cell junctions. Morphological inspection revealed large gaps in the monolayer (Figure 1A), likely disrupting overall barrier integrity. Yet at the molecular level, HCC70 cells expressed high levels of OCLN (Occludin) and other tight junction-associated genes (Supplementary Figure B.1)<sup>22-24</sup>, suggesting a strong inherent capacity for junctional connectivity<sup>52</sup>. This apparent mismatch between gene expression and barrier function underscores the importance of considering growth architecture and spatial organization when interpreting impedance-based measurements.

These findings reinforce that junctional gene expression, EMT marker status, and migratory behavior do not always align neatly in breast cancer models. Among all lines analyzed, MDA-MB-231 cells, known for their mesenchymal phenotype and low tight-junction expression, exhibited the most rapid and extensive migration, as expected. In contrast, HCC70's static yet transcriptionally ambiguous phenotype illustrates the nuanced relationship between EMT, junctional integrity, and metastatic potential.

## 4.6 Conclusion

This study reveals how diverse patterns of EMT marker expression, tight junction gene profiles, and migratory behavior intersect to shape metastatic potential in breast cancer cells. While EMT is often used as an indicator for aggressiveness, these findings illustrate that migratory potential is not always accurately predicted by a cell's phenotype or gene expression signature, reflecting the complexity of cancer cell behavior. For example, the high motility of MDA-MB-453 cells, despite their epithelial morphology, highlights the limitations of morphology-based predictions. Conversely, HCC70 cells exhibited strong expression of both epithelial and mesenchymal genes, suggesting phenotypic plasticity, yet showed little to no migration, emphasizing the influence of growth pattern and spatial organization on functional outcomes.

These discrepancies underscore the need for integrated, multidimensional approaches in studying cancer progression. While impedance and TEER provide a useful lens for examining barrier integrity and migration, their greatest value lies in complementing, not replacing, molecular and imaging-based methods. Together, such approaches can capture the full complexity of cancer cell behavior across diverse subtypes. In the future, combining impedance-based assays with high-throughput imaging and computational morphology profiling may offer a more comprehensive framework for assessing cancer aggressiveness. This study advances this broader goal and shows that functional assays capturing real-time cellular behavior can effectively elucidate the relationships between EMT, junctional integrity, and metastatic risk in breast cancer. Looking forward, integrating these techniques with image-based phenotyping and machine learning holds promise for enhancing the precision of metastatic behavior assessments.

## 4.7 References

1. Siegel, R.L., Kratzer, T.B., Giaquinto, A.N., Sung, H. & Jemal, A. Cancer statistics, 2025. *Ca* **75**, 10 (2025).
2. Sung, H., *et al.* Global cancer statistics 2020: GLOBOCAN estimates of incidence and mortality worldwide for 36 cancers in 185 countries. **71**, 209-249 (2021).
3. Park, M., *et al.* Breast cancer metastasis: mechanisms and therapeutic implications. *International journal of molecular sciences* **23**, 6806 (2022).
4. Giaquinto, A.N., *et al.* Breast cancer statistics 2024. *CA: a cancer journal for clinicians* **74**, 477-495 (2024).
5. Weinberg, R.A. *The biology of cancer*, (Garland science, 2013).
6. Brown, T.C., Sankpal, N.V. & Gillanders, W.E. Functional implications of the dynamic regulation of EpCAM during epithelial-to-mesenchymal transition. *Biomolecules* **11**, 956 (2021).
7. van der Gun, B.T., *et al.* EpCAM in carcinogenesis: the good, the bad or the ugly. *Carcinogenesis* **31**, 1913-1921 (2010).
8. Lambert, A.W., Pattabiraman, D.R. & Weinberg, R.A.J.C. Emerging biological principles of metastasis. **168**, 670-691 (2017).
9. Huang, J., *et al.* Cellular polarity pilots breast cancer progression and immunosuppression. *Oncogene*, 1-11 (2025).
10. VanderVorst, K., *et al.* Vangl-dependent Wnt/planar cell polarity signaling mediates collective breast carcinoma motility and distant metastasis. *Breast Cancer Research* **25**, 52 (2023).
11. Bhat, A.A., *et al.* Tight junction proteins and signaling pathways in cancer and inflammation: a functional crosstalk. *Frontiers in physiology* **9**, 1942 (2019).
12. Wibbe, N. & Ebnet, K. Cell adhesion at the tight junctions: new aspects and new functions. *Cells* **12**, 2701 (2023).
13. Kyuno, D., *et al.* Role of tight junctions in the epithelial-to-mesenchymal transition of cancer cells. *Biochimica et Biophysica Acta (BBA)-Biomembranes* **1863**, 183503 (2021).
14. Martin, T.A. & Jiang, W.G.J.B.e.B.A.-B. Loss of tight junction barrier function and its role in cancer metastasis. **1788**, 872-891 (2009).

15. Pan, C., *et al.* Research progress of Claudin-low breast cancer. *Frontiers in Oncology* **13**, 1226118 (2023).
16. Bussard, K.M., Mutkus, L., Stumpf, K., Gomez-Manzano, C. & Marini, F.C. Tumor-associated stromal cells as key contributors to the tumor microenvironment. *Breast Cancer Research* **18**, 1-11 (2016).
17. Villanueva-Duque, A., *et al.* Leptin induces partial epithelial-mesenchymal transition in a FAK-ERK dependent pathway in MCF10A mammary non-tumorigenic cells. *International Journal of Clinical and Experimental Pathology* **10**, 10334 (2017).
18. Pallegar, N.K., Garland, C.J., Mahendralingam, M., Vilorio-Petit, A.M. & Christian, S.L. A novel 3-dimensional co-culture method reveals a partial mesenchymal to epithelial transition in breast cancer cells induced by adipocytes. *Journal of mammary gland biology and neoplasia* **24**, 85-97 (2019).
19. Hill, B.S., Sarnella, A., D'Avino, G. & Zannetti, A. Recruitment of stromal cells into tumour microenvironment promote the metastatic spread of breast cancer. in *Seminars in cancer biology*, Vol. 60 202-213 (Elsevier, 2020).
20. Bijian, K., *et al.* Targeting focal adhesion turnover in invasive breast cancer cells by the purine derivative reversine. **109**, 2810-2818 (2013).
21. Indra, I., *et al.* An in vitro correlation of mechanical forces and metastatic capacity. **8**, 015015 (2011).
22. Institute, B. DepMap Portal Website. (2025).
23. Tsherniak, A., *et al.* Defining a cancer dependency map. *Cell* **170**, 564-576. e516 (2017).
24. DepMap, B. DepMap 24Q4 Public. (Figshare+, 2024).
25. Stampfer, M.R. & Bartley, J.C. Induction of transformation and continuous cell lines from normal human mammary epithelial cells after exposure to benzo [a] pyrene. *Proceedings of the National Academy of Sciences* **82**, 2394-2398 (1985).
26. Walen, K.H. & Stampfer, M.R. Chromosome analyses of human mammary epithelial cells at stages of chemical-induced transformation progression to immortality. *Cancer genetics and cytogenetics* **37**, 249-261 (1989).
27. Soule, H.D., *et al.* Isolation and characterization of a spontaneously immortalized human breast epithelial cell line, MCF-10. *Cancer research* **50**, 6075-6086 (1990).
28. Mota, A.d.L., *et al.* Molecular characterization of breast cancer cell lines by clinical immunohistochemical markers. *Oncology letters* **13**, 4708-4712 (2017).



29. Subik, K., *et al.* The expression patterns of ER, PR, HER2, CK5/6, EGFR, Ki-67 and AR by immunohistochemical analysis in breast cancer cell lines. *Breast cancer: basic and clinical research* **4**, 117822341000400004 (2010).
30. Soule, H.D., Vazquez, J., Long, A., Albert, S. & Brennan, M. A human cell line from a pleural effusion derived from a breast carcinoma. *Journal of the national cancer institute* **51**, 1409-1416 (1973).
31. Lehmann, B.D., *et al.* Identification of human triple-negative breast cancer subtypes and preclinical models for selection of targeted therapies. **121**, 2750-2767 (2011).
32. Li, Y., *et al.* Targeted immunotherapy for HER2-low breast cancer with 17p loss. *Science translational medicine* **13**, eabc6894 (2021).
33. Cailleau, R., Olive, M. & Cruciger, Q.V. Long-term human breast carcinoma cell lines of metastatic origin: preliminary characterization. *In vitro* **14**, 911-915 (1978).
34. Gazdar, A.F., *et al.* Characterization of paired tumor and non-tumor cell lines established from patients with breast cancer. *International journal of cancer* **78**, 766-774 (1998).
35. Volk-Draper, L.D., Rajput, S., Hall, K.L., Wilber, A. & Rana, S. Novel model for basaloid triple-negative breast cancer: behavior in vivo and response to therapy. *Neoplasia* **14**, 926-IN913 (2012).
36. Ramadan, W.S., *et al.* Interplay between epigenetics, expression of estrogen receptor- $\alpha$ , HER2/ERBB2 and sensitivity of triple negative breast cancer cells to hormonal therapy. *Cancers* **11**, 13 (2018).
37. Cailleau, R., Young, R., Olive, M. & Reeves Jr, W. Breast tumor cell lines from pleural effusions. *Journal of the National Cancer Institute* **53**, 661-674 (1974).
38. Lasfargues, E.Y., Coutinho, W.G. & Redfield, E.S. Isolation of two human tumor epithelial cell lines from solid breast carcinomas. *Journal of the National Cancer Institute* **61**, 967-978 (1978).
39. Chiu, S.-P., *et al.* Application of ECIS to assess FCCP-induced changes of MSC micromotion and wound healing migration. *Sensors* **19**, 3210 (2019).
40. Ebrahim, A.S., *et al.* Functional optimization of electric cell-substrate impedance sensing (ECIS) using human corneal epithelial cells. *Scientific Reports* **12**, 14126 (2022).
41. Anwer, S. & Szaszi, K. Measuring cell growth and Junction Development in epithelial cells using electric cell-substrate impedance sensing (ECIS). *Bio-protocol* **10**, e3729-e3729 (2020).

42. Brown, M.S., *et al.* Phenotypic heterogeneity driven by plasticity of the intermediate EMT state governs disease progression and metastasis in breast cancer. *Science advances* **8**, eabj8002 (2022).
43. Roy Burman, D., Das, S., Das, C. & Bhattacharya, R.J.M.B.R. Alternative splicing modulates cancer aggressiveness: role in EMT/metastasis and chemoresistance. **48**, 897-914 (2021).
44. Santos, J.M., Hussain, F.J.N. & cancer. Higher glucose enhances breast cancer cell aggressiveness. **72**, 734-746 (2020).
45. Liu, Y., *et al.* CTC-race: single-cell motility assay of circulating tumor cells from metastatic lung cancer patients. *ACS nano* **18**, 8683-8693 (2024).
46. Hwang, H.J., *et al.* Endothelial cells under therapy-induced senescence secrete CXCL11, which increases aggressiveness of breast cancer cells. *Cancer letters* **490**, 100-110 (2020).
47. Ziperstein, M.J., Guzman, A. & Kaufman, L.J. Breast cancer cell line aggregate morphology does not predict invasive capacity. *PLoS One* **10**, e0139523 (2015).
48. Xu, X., *et al.* VSP-17 suppresses the migration and invasion of triple-negative breast cancer cells through inhibition of the EMT process via the PPAR $\gamma$ /AMPK signaling pathway. *Oncology reports* **45**, 975-986 (2021).
49. Prat, A., *et al.* Phenotypic and molecular characterization of the claudin-low intrinsic subtype of breast cancer. *Breast cancer research* **12**, 1-18 (2010).
50. Moore, N.L., *et al.* An androgen receptor mutation in the MDA-MB-453 cell line model of molecular apocrine breast cancer compromises receptor activity. *Endocrine related cancer* **19**, 599 (2012).
51. Robinson, J.L., *et al.* Androgen receptor driven transcription in molecular apocrine breast cancer is mediated by FoxA1. *The EMBO journal* **30**, 3019-3027 (2011).
52. Martin, T.A., Mansel, R.E. & Jiang, W.G. Loss of occludin leads to the progression of human breast cancer. *International journal of molecular medicine* **26**, 723-734 (2010).

## CHAPTER 5

# TWO-DIMENSIONAL SINGLE CELL MORPHOLOGY AS AN INDICATOR OF BREAST CANCER AGGRESSIVENESS

---

Higgins, K. S.; Watts, L. B. and Gomillion, C. T. *To be submitted to Computers in Biology and Medicine.*

## 5.1 Abstract

Cell morphology reflects the combined outputs of genetic and signaling pathways and is becoming increasingly recognized as a functional readout of cancer cell behavior. In breast cancer, particularly in triple-negative breast cancer (TNBC), morphological variation has been linked to metastatic potential and cellular plasticity, but the full extent of this relationship remains unknown. Despite growing interest, few studies have comprehensively analyzed how morphology and cell phenotypic behaviors correlate across diverse TNBC models. Here, we demonstrate that cell morphology features can quantitatively predict epithelial-mesenchymal status, cell normality, and migration behavior across a panel of eight mammary cell lines, including one luminal breast cancer line and five TNBC lines, using high-throughput image analysis.

CellProfiler™ cell image analysis software was employed to extract quantitative single-cell morphological features from cellular- and nuclear-stained images, linking these features with migration measurements across all cell lines. Specific morphological traits, including cell elongation, nuclear irregularity, and cellular protein texture, captured meaningful variation in epithelial-mesenchymal state, cell normality, and motility. These results underscore the utility of cell morphology as a highly dimensional proxy for aggressive behavior in breast cancer and support the use of image-based phenotyping to explore functional heterogeneity in aggressive cancer subtypes.

## 5.2 Introduction

Cell morphology serves as a powerful phenotypic readout that captures the integrated output of gene expression, signaling, and cytoskeletal architecture. In cancer biology, particularly in breast cancer, cell shape has long been proposed as a critical element of cell behavior, including migration, invasion, and metastatic potential<sup>1-3</sup>. Morphological traits not only reflect the underlying biology of the cell but can also predict functional behaviors. For example, breast cancer cell shape has been shown to correlate with extracellular matrix (ECM) invasion in 3D environments, while morphological heterogeneity can indicate tumor cell plasticity and malignant progression<sup>3,4</sup>.

Breast cancer primarily arises from epithelial cells, which in normal tissue are highly organized, maintain apicobasal polarity, and exhibit contact inhibition. In contrast, malignant epithelial cells often lose polarity, adopt disorganized tissue architectures, and proliferate uncontrollably. Morphologically, cells with an epithelial-like appearance are more differentiated and are characterized by tight cell-to-cell junctions, resulting in limited motility<sup>5</sup>. In comparison, mesenchymal-like cells, often associated with the epithelial-to-mesenchymal transition (EMT), exhibit more elongated shapes, weakened cell-to-cell adhesions, and a higher proliferative and invasive potential<sup>6</sup>. This morphological distinction is reflected at the molecular level where luminal breast cancers (typically hormone receptor-positive) often retain epithelial morphology, while triple-negative breast cancer (TNBC) subtypes are more frequently mesenchymal-like<sup>7</sup>.

Nonetheless, significant phenotypic diversity exists even within the same molecular subtypes. For example, work by Hapach et al. demonstrated that subpopulations within the TNBC cell line MDA-MB-231 can adopt distinct morphologies and utilize different metastatic programs *in vivo* depending on their epithelial or mesenchymal state<sup>8</sup>. These findings highlight the

limitations of static molecular classifications and underscore the need to better understand the range of morphological and behavioral traits in breast cancer. Since single-cell morphology is an easily observable and quantifiable trait, it offers a powerful window into the otherwise complex and heterogeneous nature of cancer progression.

Additionally, single-cell morphology provides advantages over conventional molecular profiling in that it can capture population-level heterogeneity and may correlate better with emergent behaviors like migration and metabolic activity. In this work, cell morphology is analyzed across eight mammary cell lines and compared with migration potential, measured in Chapter 4. Together, these analyses aim to examine how cell line morphological features relate to cell type classification and aggressive migration, a preliminary step in the metastatic process.

CellProfiler<sup>TM</sup>, a high-throughput image analysis platform that enables automated quantification of cell features from microscopy images <sup>9,10</sup>, was employed to carry out this analysis. CellProfiler<sup>TM</sup> can extract measurements describing cell and nuclear shape (e.g., area, eccentricity), staining intensity, and texture features, like granularity and spatial variation. Among these, Haralick texture features, derived from gray-level co-occurrence matrices, quantify second-order statistics in pixel intensity, capturing patterns like contrast, entropy, and homogeneity within cellular compartments <sup>11</sup>. These features are particularly useful for assessing subcellular protein organization and cytoskeletal rearrangement, which are hallmarks of dynamic cell states. For example, texture measures from actin staining can reveal the presence of stress fibers, lamellipodia, or filopodia, all structures associated with migration and invasive potential <sup>12</sup>.

In this analysis, eight mammary cell lines are examined, including two non-cancerous epithelial lines (MCF10A and 184B5) and six breast cancer lines. Notably, five of the cancer lines represent TNBC, a clinically aggressive and molecularly diverse subtype lacking expression of the

estrogen receptor, progesterone receptor, and HER2. While several of these cell lines have been independently characterized, they have not, to our knowledge, been analyzed together in a single, morphologically focused study. By applying high-throughput morphological profiling across this diverse panel, we provide one of the most comprehensive comparative analyses to date of TNBC cell morphology. These lines span a wide range of phenotypes, from compact epithelial-like morphologies to highly elongated mesenchymal-like states, offering a unique opportunity to study the relationship between shape, heterogeneity, and migratory behavior across the epithelial-mesenchymal spectrum. This integrative approach allows for the exploration of both cell line variability and intra-line heterogeneity, providing valuable insight into the cellular plasticity and functional diversity of breast cancer.

## **5.3 Materials and Methods**

### **5.3.1 Cell Lines**

All cell lines were purchased from American Type Culture Collection (ATCC) and cultured at 37°C and 5% CO<sub>2</sub> atmosphere. 184B5 and MCF10A cells were cultured in Mammary Epithelial Growth Medium (MEGM; Lonza) supplemented with 1 ng/mL cholera toxin (Sigma-Aldrich) and 100 ng/mL cholera toxin respectively. HCC70 and BT-549 cells were cultured in RPMI-complete using ATCC's modified RPMI blend (ATCC) supplemented with 10% fetal bovine serum (FBS; R&D Systems) and 1% penicillin/streptomycin (P/S; Gibco). HCC1806, MDA-MB-453, and MDA-MB-231 cells were cultured in Dulbecco's Modified Eagle Medium (DMEM; Gibco) supplemented with 10% FBS and 1% P/S to form DMEM-Complete. Lastly, the MCF7 cell line was cultured in DMEM-Complete supplemented with 0.01 mg/mL bovine insulin

(Sigma). All cell lines were confirmed to be free of mycoplasma using a commercially available kit (InvivoGen).

### 5.3.2 Cell Staining and Imaging

Cells were seeded into black-walled 96-well plates (Corning) at a density of 10,000 cells/cm<sup>2</sup> to enhance contrast between cell borders and facilitate identification of cytoskeletal projections. After a 15-hour incubation to allow for attachment and spreading, cells were fixed with 4% paraformaldehyde (PFA; Thermo Fisher) in phosphate-buffered saline (PBS; Gibco) for 30 minutes at room temperature, followed by two PBS washes. Permeabilization and staining were performed using a solution containing 1% (v/v) Tween-20 (Sigma-Aldrich), 10 µg/mL Hoechst 33342 (Thermo Fisher) for nuclear labeling, and 1 µg/mL Fluorescein-5-Maleimide (Thermo Fisher) for cell protein visualization. Cells were incubated in this staining solution for 1 hour at room temperature, protected from light. After staining, cells were rinsed with PBS, and fluorescence imaging was performed using the Cytation 1 Cell Imaging Multimode Reader (Agilent Biotek). Each well was imaged using a 4×4 montage (16 fields of view) for both nuclear (DAPI) and cellular (GFP) channels, resulting in 32 images per well and a total of 3,072 images per cell line.

### 5.3.3 Image Analysis with CellProfiler™

After image acquisition, high-throughput single-cell morphological analysis was performed on individual cells using CellProfiler™ (Broad Institute), an open-source image analytical platform. A custom pipeline was developed to quantify morphological features from each cell (key features described in Supplemental Table C.1). Image metadata, including cell line



and location, were embedded, and DAPI and GFP channels were merged to generate overlaid images. These images were aligned and cropped to uniform size and illumination was normalized within each cell line dataset using the background and applied with a median smoothing filter.

Following preprocessing, segmentation was performed to identify individual nuclei and cells. Nuclei were segmented using adaptive Otsu thresholding, and corresponding cells were delineated via a propagation method. For each segmented object, numerous morphological features were quantified, including size, shape descriptors (e.g. form factor, solidity, extent, eccentricity), fluorescence intensity, texture metrics, and number of neighboring cells.

For reference and segmentation verification, overlay images showing segmented cell and nuclear boundaries were generated and exported. All extracted data and associated metadata were stored in SQL database files. These databases were processed in RStudio (Posit Software), where filtering steps were applied to remove segmentation artifacts. Objects smaller than 500 pixels<sup>2</sup> were excluded to prevent any false cell identification, and only isolated (non-touching) cells (i.e. those with zero recorded neighbors) were retained for further analysis. The final datasets were exported to Excel for downstream statistical analysis.

#### 5.3.4 Principal Component Analysis of CellProfiler™ Data

Following cell morphology quantification in CellProfiler™, individual cell measurements were aggregated into per-well mean values using RStudio to account for cell-to-cell variability. A similarity matrix of CellProfiler™ features was generated using Morpheus (Broad Institute), and features with a high Pearson correlation coefficient ( $r \geq 0.90$ ) were removed to reduce multicollinearity and minimize risk of model overfitting. This filtering resulted in 48 retained features describing cell and nuclear shape, stain intensity, and texture. Z-scores were then

calculated for the per-well averages, and features with absolute z-scores greater than 3 ( $|z| > 3$ ) were classified as outliers and excluded from further analysis. This threshold identifies extreme values while preserving the core data distribution, assuming approximate normality. Finally, principal component analysis (PCA) was conducted in RStudio to reduce dimensionality. PCA loadings, scores, and eigenvalues were analyzed to interpret the contribution of retained features to morphological variation.

#### 5.3.5 EMT Gene Expression Analysis Using DepMap RNA-Seq Data

RNA-seq gene expression data was obtained from the DepMap Project, a resource developed by the Broad Institute that compiles genetic and molecular profiling data from a diverse panel of human cancer models. Expression values ( $\log_2[\text{TPM} + 1]$ ) were used to compare EMT gene expression patterns with results from PCA of the breast cancer cell lines used in this study. A panel of 39 EMT-related genes was assembled based on established markers reported in relevant literature<sup>13-22</sup>. The results were visualized as a robust z-score heatmap generated in Morpheus and hierarchical clustering of cell line expression data was performed using Pearson correlation and average linkage.

#### 5.3.6 Univariate Statistical Analysis

Violin plots were generated using GraphPad Prism (version 10.2), and statistical significance was assessed using one-way ANOVA. Individual morphology features were normalized to the mean of the normal 184B5 cell line to highlight relative increases or decreases in comparison to the control group. Heatmaps of CellProfiler features and EMT-associated

genomic data, shown in Figure 5.2 and 5.4 respectively, were created in Morpheus using a robust z-score method.

## **5.4 Results**

### **5.4.1 Observable Difference in Morphology Among All Eight Cell Lines**

A total of 330 features related to cellular and nuclear morphology were measured, including parameters describing shape, staining intensity, and texture. As expected, significant morphological variation was observed across the eight mammary cell lines (Figures 5.1 and 5.2), particularly in cell shape-related features, like form factor, extent, and maximum Feret diameter. Most cancerous lines exhibited a higher max Feret diameter and lower form factor and extent compared to the normal epithelial 184B5 line (Figure 5.2 B, C, and D), indicating a more elongated shape with increased cytoskeletal projections, a phenotype broadly associated with mesenchymal traits. Among the cancerous lines, MCF7 showed the greatest morphological similarity to 184B5, consistent with its more epithelial-like behavior. In contrast, MDA-MB-453 cells displayed morphological features that deviated from the typical cancer-associated phenotype, exhibiting a more rounded and compact shape, which distinguishes it from other breast cancer lines. While these individual morphological features offer insight into cell line-specific variation, they do not fully capture the complexity of phenotype across the dataset. Therefore, to reveal underlying patterns and reduce dimensionality, principal component analysis (PCA) was applied and composite axes of morphological variation were identified.

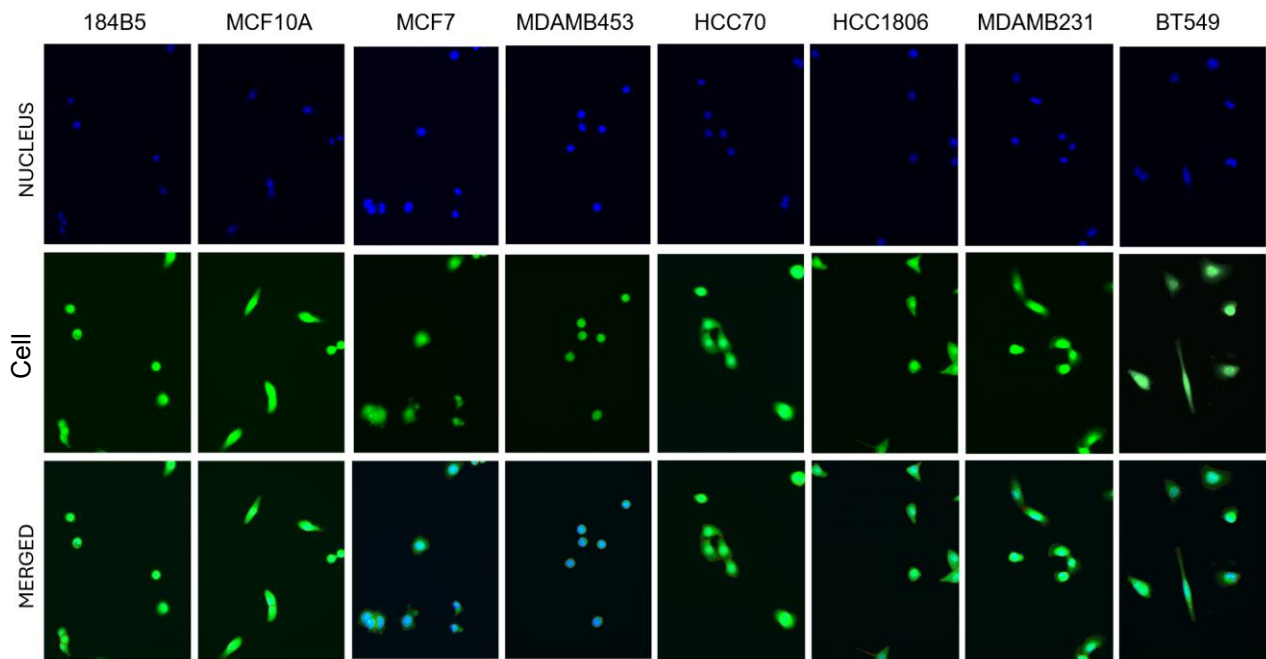


**Figure 5.1:** Representative images of stained mammary cell lines. The DAPI channel labels nuclei, while cells are visualized via the GFP channel. The bottom row presents an overlay of the DAPI and GFP channels, with segmentation borders from CellProfiler indicating nuclear (yellow) and cell (red) boundaries.

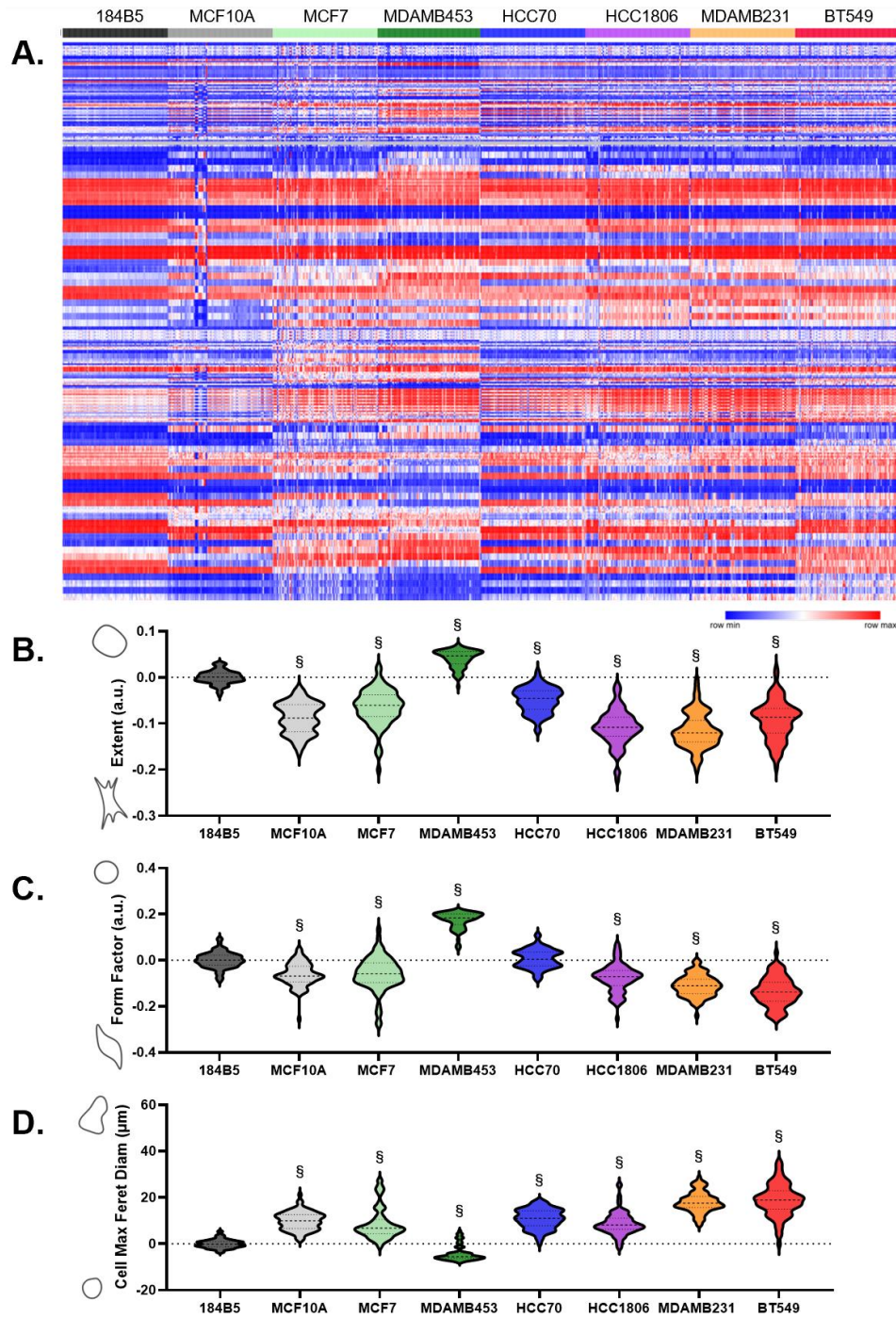


**Figure 5.2:** Mammary morphology features. A) Heatmap displaying all morphological features extracted using the CellProfiler pipeline. Each column represents the average z-score per well, grouped by cell line, and each row corresponds to one of 330 quantified cellular or nuclear variables. B) Violin plot of cell extent, reflecting how well each cell fits within its bounding box. C) Violin plot of cell form factor, representing cell circularity. D) Violin plot of maximum Feret diameter, indicating the longest measurable axis of the cell. All violin plots are normalized to the normal mammary epithelial cell line 184B5. Statistical significance compared to 184B5 is denoted as: §  $p < 0.0001$ .

#### 5.4.2 PCA Shows a Distinction Between EMT State and Normality

To better understand how combinations of features contribute to morphological diversity, PCA was performed, producing composite dimensions that summarize the most significant variations in the dataset. After reducing redundant variables using a similarity matrix, 48 features related to cell and nuclear morphology were used. Principal component 1 (PC1) accounted for 30.1% of total variance, while PC2 accounted for an additional 13.4%. Plotting the cell lines along PC1 and PC2 (Figure 5.3A) revealed a clear separation among groups. The normal 184B5 line and the highly epithelial MDA-MB-453 cells occupy distinct positions from the rest of the cell lines, suggesting these components capture meaningful biological differences. When PC1 and PC2 are examined individually (Figure 5.3B and 5.3C), additional structure appears. PC1 seems to reflect EMT-related morphological traits. Cell lines with low PC1 scores, like the rounded, epithelial-like MDA-MB-453 line, exhibit compact morphology, while lines with high PC1 scores, like MDA-MB-231 and BT-549 cells, are more elongated and mesenchymal-like. PC2, by contrast, seems to separate normality from malignancy. The 184B5 line has the lowest PC2 score, while all cancerous lines show elevated PC2 values. The non-tumorigenic MCF10A cells, which originate from fibrocystic tissue, have the second-lowest PC2 score, suggesting an intermediate state that is distinct from both normal and malignant profiles. Taken together, PC1 appears to capture variation related to EMT state, while PC2 reflects a dimension of cellular normality or deviation from it. To better understand the biological relevance of these components, the individual morphological features most strongly influencing PC1 and PC2 were analyzed next.

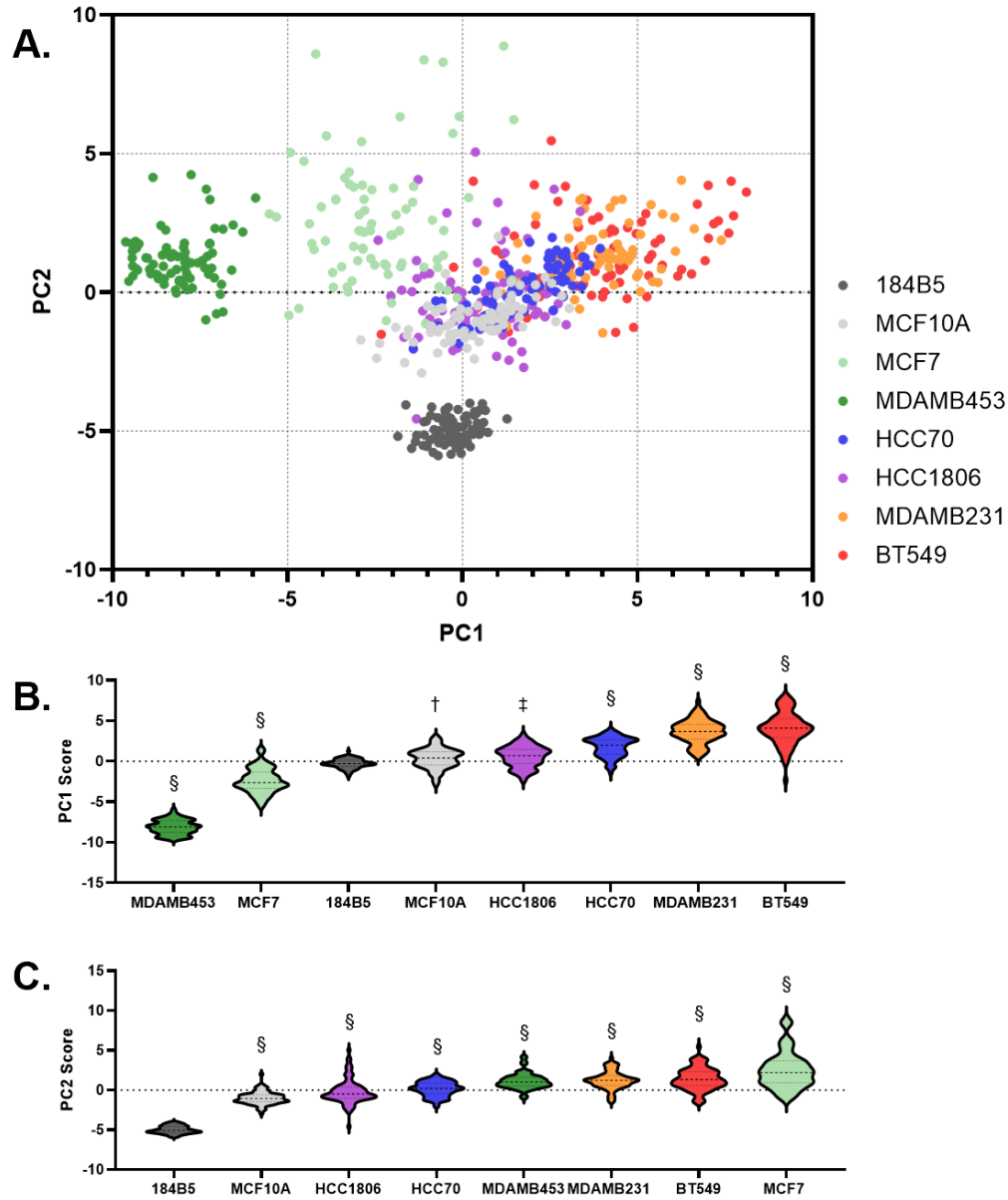


**Figure 5.3:** Principal component analysis (PCA) of cell and nuclear morphology across mammary cell lines. PCA was performed on morphological features extracted from 8 mammary cell lines, with each data point representing the average morphology of cells imaged in a single well. A) Scatter plot of the first two principal components (PC1 and PC2), where PC1 primarily separates epithelial-like from mesenchymal-like morphologies, and PC2 is associated with the degree of normality among the cell lines. Data points are colored by cell line, highlighting morphology-based clustering. B) Violin plot of PC1 scores by cell line, showing variation along the epithelial–mesenchymal axis. C) Violin plot of PC2 scores by cell line, reflecting differences related to normal versus transformed cell states. Each point represents one well;  $n = 76\text{--}84$  wells per cell line. Significance compared to the normal cell line, 184B5: †  $p < 0.05$ , ‡  $p < 0.001$ , §  $p < 0.0001$ .

#### 5.4.3 PC1 Reflects EMT-Related Phenotypic Plasticity, Integrating Cell Shape, Intensity Asymmetry, and Nuclear Texture Features

A PCA loadings plot (Figure 5.4A) was created to identify the morphology features most strongly associated with principal components 1 and 2. Multiple variables related to cell and nuclear shape, texture, and intensity contributed to PC1, which appears to capture EMT-related phenotypic variation. Among these, the cell-to-nucleus area ratio emerged as the most influential feature. This ratio was calculated as the difference between the nuclear area and the remaining cytoplasmic area of the cell, not overlapping with the nucleus. The epithelial breast cancer cell lines MCF7 and MDA-MB-453 exhibited significantly higher cell-to-nucleus ratios than all other lines, including the non-cancerous controls. In contrast, more mesenchymal-like cancer cell lines showed cell-to-nucleus ratios lower than the normal 184B5 cells. This pattern may reflect complex interactions between cytoplasmic spread and nuclear area. While MCF7 and MDA-MB-453 cells exhibit a similar epithelial shape to the normal 184B5 cell lines, they are also characterized by relatively large nuclei (Figure 5.4C), explaining their elevated cell-to-nucleus ratios as compared to the normal cell line. This highlights the multifaceted nature of EMT-associated morphological variation. To confirm the morphology relationship with EMT status, gene expression data from the DepMap portal was analyzed (Figure 5.4D). Hierarchical clustering of 39 EMT-related genes across the breast cancer cell lines using Pearson correlation and average linkage revealed a pattern consistent with the morphological PCA results (note: DepMap portal includes only cancer lines). This supports the conclusion that morphology features derived from cell and nuclear staining are sufficient to capture key EMT-related phenotypes. Next, we investigated the specific morphological features contributing to PC2 and their relationship to cell normality.



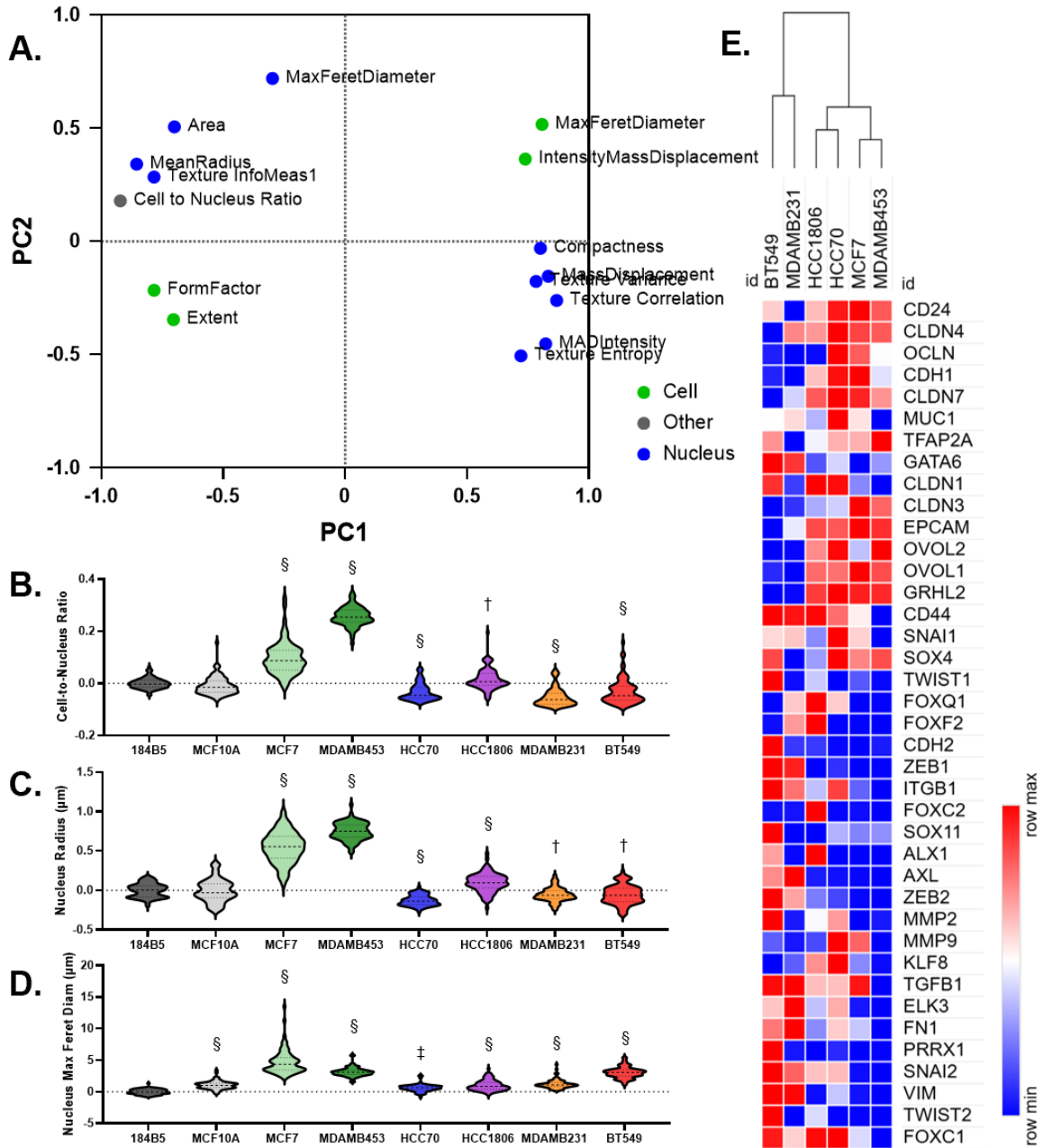


**Figure 5.4:** Features driving separation between EMT and normal cell states. A) Loadings plot for principal components PC1 and PC2, highlighting morphology variables with absolute loading scores > 0.7. Variables contributing to the first two components are color-coded: cell-related (green), nucleus-related (blue), and other (grey). B) Violin plot of the cell-to-nucleus area ratio, normalized to the mean of the 184B5 group. This is the most influential feature in PC1. C) Violin plot of nuclear radius, also normalized to the 184B5 group mean, representing another key contributor to PC1. D) Violin plot of nuclear maximum Feret diameter, similarly normalized. This is the most influential feature in PC2. E) Heatmap of EMT-associated gene expression, sourced from the DepMap Portal. Pearson correlation and average linkage were used for hierarchical clustering of cell lines. Each point represents one well; n = 76–84 wells per cell line. Significance compared to the normal cell line, 184B5: † p < 0.05, ‡ p < 0.001, § p < 0.0001.

#### 5.4.4 Nucleus Maximum Feret Diameter is Correlated with PC2 and Normality

Among all measured variables, only nuclear maximum feret diameter (MFD), which quantifies the longest axis of the nucleus, had a strong loading score for PC2 ( $|\text{loading}| > 0.7$ ), indicating it is the primary contributor to this principal component (5.4D). An increased MFD can reflect either an overall increase in nuclear size, potentially related to elevated ploidy, or irregular nuclear shape, both common features in malignancy. All cell lines exhibited a higher mean MFD compared to the non-malignant 184B5 cell line, indicating abnormal nuclear morphology across both cancerous and non-cancerous cell types. MCF10A cells, although non-tumorigenic, also showed an elevated MFD, though to a lesser extent than the cancer groups. This suggests a partial departure from normal nuclear architecture, possibly related to their fibrocystic origin. MFD values align with previous observations of nuclear radius (Figure 5.4C), which was highest in the epithelial breast cancer cell lines MCF7 and MDA-MB-453. Given their large nuclear size, it follows that these cell lines would also have elevated MFD values. Together, PC1 and PC2 highlight distinct and biologically meaningful axes of morphological variation (EMT-related features and nuclear abnormalities) that distinguish cell lines by functional and phenotypic state.

#### 5.4.5 Cellular Protein Distribution Patterns Drive a Morphological Signature Correlated with Cell Migration

To further investigate potential links between cell morphology and cellular aggressiveness, the contributions of PC3 and PC4 were examined. While PC4 explains 9% of the total variance, less than the more dominant PCs, it exhibited a partial correlation with migratory potential across cell lines. Specifically, PC4 values increased along a gradient that broadly mirrored the progression from non-tumorigenic to highly aggressive phenotypes (Figure 5.5.). Although not perfectly

aligned with migration rates, which followed a slightly different order, the general trend suggests that PC4 captures morphological changes relevant to migratory behavior.

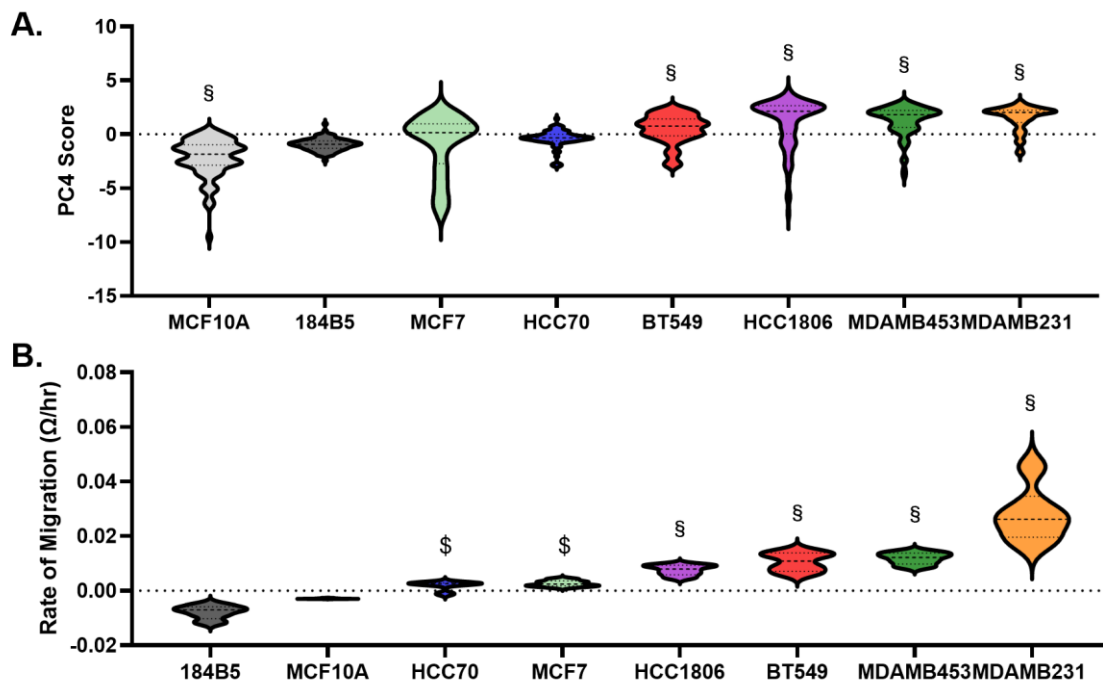


**Figure 5.5:** A Potential link between migration and cell morphology. A) Violin plot of PC4 scores by cell line, ordered from lowest to highest average score. Each data point represents one well;  $n = 76\text{--}84$  wells per cell line. B) Violin plot of the rate of migration ( $\Omega/\text{hr}$ ) for each cell line, determined in chapter 4. Cell groups are ordered from lowest to highest average rate of migration. Data was obtained from 4-6 independent wells ( $n = 4\text{--}6$ ) across all cell lines. Significance compared to the normal cell line, 184B5: †  $p < 0.05$ , §  $p < 0.01$ , ‡  $p < 0.001$ , §  $p < 0.0001$ .

To better understand the biological meaning of PC4, we examined its feature loadings. Two features related to the cellular stain, maximum intensity and difference entropy, had the strongest contributions to PC4 ( $|\text{loadings}| > 0.7$ ). Maximum cellular protein intensity could reflect localized enrichment of actin structures such as lamellipodia or stress fibers, while difference entropy, a Haralick texture metric, quantifies spatial complexity in protein organization. Together, these features suggest that PC4 represents a morphological signature characterized by both the intensity and heterogeneity of protein distribution, which could be linked to the cytoskeletal

remodeling observed in migratory and aggressive cells, something that can be measured via an actin-specific stain in future studies. These findings suggest that even lower-variance components like PC4 can reveal biologically meaningful patterns.

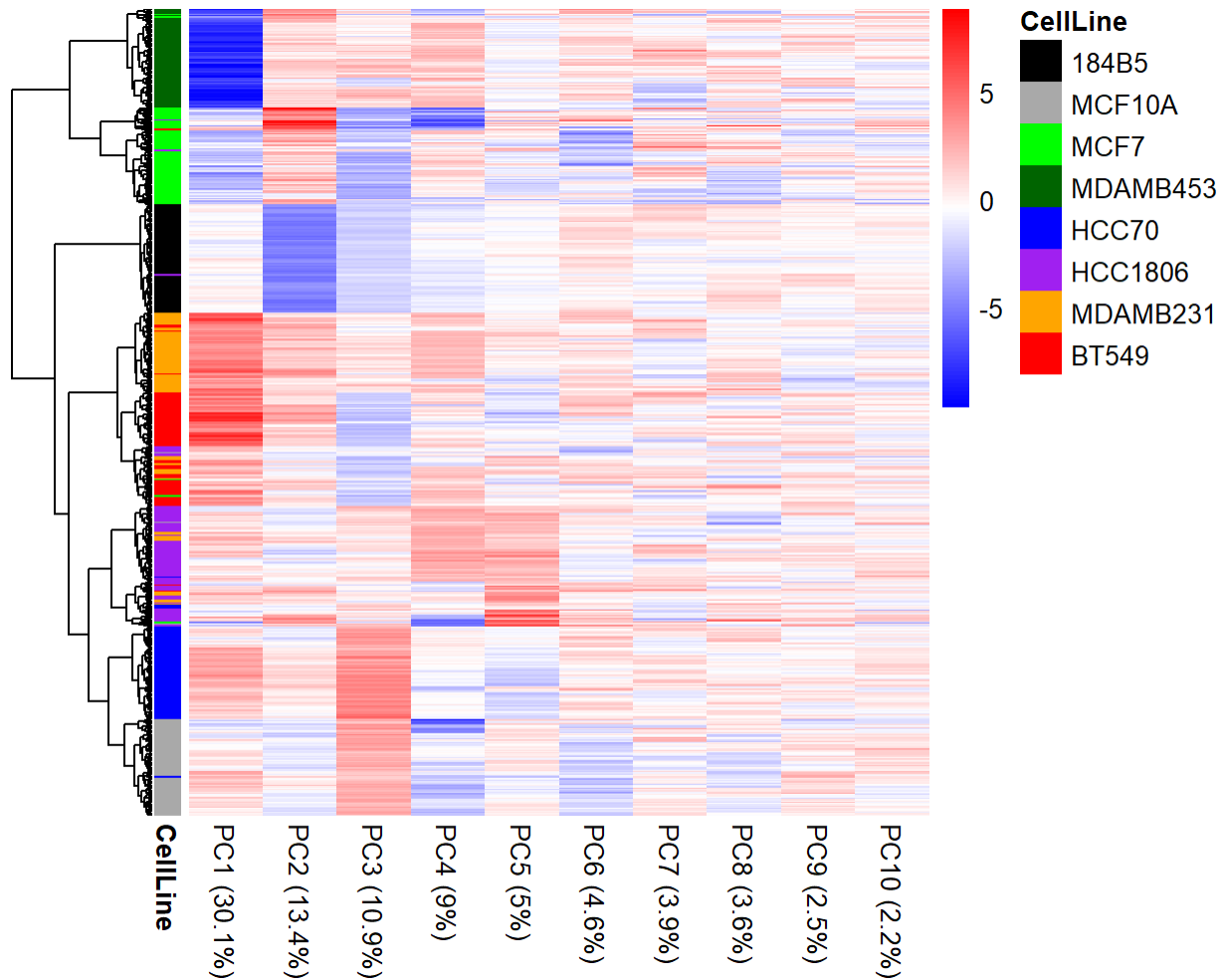


**Figure 5.6:** Heatmap of the first 10 principal components (PCs) derived from averaged cell morphology data across 8 mammary cell lines. Each row represents a single well, where the values reflect the mean morphological features of cells within that well. Columns correspond to the first 10 PCs, which capture the major sources of variation in the dataset. Hierarchical clustering of the wells was performed using Ward's minimum variance method to reveal patterns and similarities in morphological profiles across cell lines.

#### 5.4.6 Principal Component Analysis Emphasizes EMT as Primary Driver of Morphological Variation and Highlights Subtle Heterogeneity within Cell Lines

To assess overall patterns across the mammary cell lines, a heatmap of the first 10 principal components, together accounting for over 85% of the variance in the dataset (Supplementary Figure C.1), was created and is shown in Figure 5.6. PC1, which explains the largest proportion of variance, is primarily associated with EMT. Accordingly, much of the observed cell separation and hierarchical clustering reflects differences along the epithelial-mesenchymal phenotypic axis. Interestingly, non-cancerous and cancerous cell lines do not form entirely distinct clusters, suggesting that, while normality is detectable through PC2, it contributes less to the overall variance than EMT-related morphological changes. Hierarchical clustering also reveals that, generally, replicates from the same cell line cluster together, however, some wells are clustered separately from their counterparts. This highlights the inherent heterogeneity within breast cancer cell lines and underscores the complexity of analyzing cancer-associated phenotypes through morphological profiling.

### 5.5 Discussion

This study presents a comprehensive morphological analysis of eight mammary cell lines by integrating high-throughput imaging with PCA. By analyzing 48 of the 330 originally measured features, encompassing cell and nuclear morphology, texture, and staining intensity, distinct morphological traits associated with biological processes like EMT, cellular normality, and cancer aggressiveness were identified. The first principal component (PC1), accounting for the largest portion of variance (30.1%), was strongly associated with features traditionally linked to EMT, including cell elongation, reduced cellular extent, and increased cytoskeletal projections<sup>5,23</sup>. These morphological changes are consistent with mesenchymal transformation, a commonly researched

process in cancer metastasis. The association of PC1 with EMT was further corroborated by its correlation with gene expression signatures from EMT-related genes in cancer cell lines, provided by the DepMap Portal <sup>24</sup>, reinforcing the value of morphological features as a proxy for underlying transcriptional state.

Among all contributing features, the cell-to-nucleus ratio emerged as the most influential. This metric, calculated as the ratio of nucleus area to the remaining cell area, captures a combination of both nuclear size and overall cell morphology. Notably, MCF7 and MDA-MB-453 cells exhibited the highest cell-to-nucleus ratios. Both of these lines are compact and epithelial-like in morphology, but are distinguished by having relatively large nuclei <sup>25</sup> (Figure 5.3C). This combination results in a high nucleus-to-cell proportion, driving their elevated cell-to-nucleus ratio and lower PC1 scores. In contrast, the non-cancerous epithelial cell lines, 184B5 and MCF10A, while also epithelial in shape, have significantly smaller nuclei relative to their overall cell size, resulting in a lower cell-to-nucleus ratio. This distinction highlights the strength of this feature in capturing both aspects of cell identity: nuclear enlargement, which is often associated with malignancy <sup>26-28</sup>, and overall cell shape, linked to EMT status <sup>5,29</sup>. Thus, the cell-to-nucleus ratio serves as a composite marker that integrates information about both cellular elongation and nuclear size, two dimensions of morphological change that are key to differentiating between cancerous and non-cancerous, as well as epithelial and mesenchymal states. Despite its utility, however, the cell-to-nucleus ratio, and PC1 more broadly, does not effectively distinguish between cancerous and non-cancerous cell lines. This separation is better captured along the second principal component, PC2, which isolates differences in nuclear morphology more directly.

PC2, the second most significant component (13.4% variance), primarily separated the normal epithelial 184B5 cells from all other lines, based largely on nucleus morphology. This

correlates with previous studies of cell <sup>30-35</sup> and tissue <sup>26,35-37</sup> nucleus morphological analysis as an indicator of genomic instability and prognosis. Distorted or enlarged nuclei may indicate dysregulated DNA replication, aneuploidy, genomic instability, or genetic mutations that compromise the stability and function of the nuclear envelope <sup>27</sup>. Additionally, components of the nuclear envelope interact with both chromatin and transcription factors, contributing to the spatial regulation of gene transcription and expression <sup>27,38</sup>, validating the use of nuclear morphology as an indicator of cellular transformation and malignancy. The most influential feature on PC2 was nuclear MFD, which captures the longest axis of the nucleus. Elevated MFDs in all atypical lines suggest widespread nuclear irregularities across both malignant and non-malignant cells <sup>31,39</sup>. While MCF10A cells are non-tumorigenic, their elevated MFD and intermediate PC2 score reflect a partial deviation from normal nuclear architecture, consistent with their origin from fibrocystic disease tissue and a behavior that has been recorded in previous studies <sup>40-42</sup>. A comprehensive 3D morphometric analysis demonstrated that MCF10A cells possess larger nuclei and a higher nucleus-to-cytoplasm volume ratio compared to normal HME1 cells <sup>40</sup>. Additionally, MCF10A nuclei exhibited increased chromatin clumping and irregularities in nuclear shape, indicating structural deviations from typical normal epithelial cells. These findings suggest that MCF10A cells, despite being non-malignant, display nuclear features that are not entirely representative of normal breast epithelium, correlating with our results. These findings indicate that nuclear elongation and irregularity are morphological features that vary along a range, rather than serving as binary markers of tumorigenicity.

Further analysis of PCs 3 and 4 revealed that even components accounting for relatively low variance (10.9% and 9% respectively) can reflect biologically meaningful behaviors. Specifically, PC4 was moderately associated with cell migration rates, measured in Chapter 4, and

was driven by cell stain-related features: maximum intensity and Haralick texture difference entropy. Maximum cellular protein intensity could reflect concentrated F-actin structures like lamellipodia, filopodia, and stress fibers <sup>43</sup>, which are indicative of cytoskeletal remodeling associated with aggressive behavior <sup>12,44</sup>. The Haralick difference entropy metric captures spatial complexity in protein distribution, with higher values indicating more heterogeneous and dynamic protein staining. These observations suggest that PC4 distinguishes a signature of cell protein organization and may indicate cytoskeletal reorganization, a known facilitator of cell motility. This is something that can be evaluated in the future using an F-actin-specific stain, like phalloidin. Furthermore, it would be interesting to analyze this relationship with respect to collective cancer cell migration, a process that enables non-invasive follower cells to migrate alongside metabolically active leader cells <sup>45,46</sup>. These leader cells tend to have a mixed epithelial-mesenchymal phenotype, where the leading edge undergoes cytoskeletal reorganization and can exhibit actin-rich protrusions, while the trailing edge retains cell-to-cell junctions and epithelial characteristics <sup>47</sup>. This uneven distribution of F-actin may be measurable through Haralick texture features, providing additional areas of exploration with this technique. Although PC4 did not perfectly predict migration behavior, the observed trends support the utility of morphological features in capturing functional states like migratory potential.

Combined PCA and hierarchical clustering analyses (Figure 5.6) highlighted EMT as the dominant axis of morphological variation while also revealing intra-cell line heterogeneity. Replicate wells of the same cell line generally clustered together, but occasional deviations may point to phenotypic variability within cell lines. This heterogeneity aligns with the known plasticity of cancer cells and underscores the limitations of using static or single-feature markers to define



complex cell states. Overall, these findings highlight the value of morphological analysis not only for classifying cell types but also for assessing heterogeneity within cellular populations.

In summary, this study demonstrates that high-dimensional morphological profiling, coupled with PCA, uncovers biologically relevant axes of variation across mammary cell lines. EMT-associated features dominate the morphological landscape, while nuclear abnormalities and cellular protein dynamics emerge as secondary, but informative, signatures linked to transformation and motility. Although migration behavior did not strongly correlate with any single morphological axis, the trends observed reflect the multifaceted nature of cancer cell behavior and the challenges inherent in modeling metastatic potential. Future studies may benefit from focusing on morphological heterogeneity within aggressive cell lines to better understand its relationship with migration potential, a direction we pursue in Chapter 6. Overall, this multidimensional approach offers valuable insights into cellular heterogeneity and tumor progression in breast cancer.

## **5.6 Conclusion**

This study establishes a framework for leveraging high-throughput and highly dimensional morphological profiling to uncover the biological underpinnings of breast cancer heterogeneity. By integrating imaging-based metrics with PCA, axes of variation linked to EMT, nuclear transformation, and cytoskeletal remodeling, three hallmarks of cancer progression, were identified. These findings reveal that complex morphological traits, particularly the cell-to-nucleus ratio, nucleus MFD, and cellular texture features, can serve as composite biomarkers that encapsulate key cellular states beyond simple cancer versus normal classification. Moreover, the partial discrimination of non-tumorigenic but atypical lines like MCF10A underscores the nuanced

spectrum of phenotypic states present across mammary cell models. The presence of heterogeneity, even within well-characterized cell lines, highlights the dynamic nature of cancer cell identity and challenges the use of static molecular labels to capture functional potential. While migration behavior did not align neatly with any single morphological component, its reasonable association with PC4 reinforces the notion that motility is regulated by complex, multifactorial processes. Collectively, this work supports the use of comprehensive morphological analysis as a scalable and insightful method for dissecting cancer cell behavior and provides a foundation for future investigations into how morphological heterogeneity contributes to tumor aggressiveness.

## 5.7 References

1. Keren, K., *et al.* Mechanism of shape determination in motile cells. **453**, 475-480 (2008).
2. Lee, J., Ishihara, A., Theriot, J.A. & Jacobson, K.J.N. Principles of locomotion for simple-shaped cells. **362**, 167-171 (1993).
3. Baskaran, J.P., *et al.* Cell shape, and not 2D migration, predicts extracellular matrix-driven 3D cell invasion in breast cancer. **4**, 026105 (2020).
4. Weinberg, R.A. *The biology of cancer*, (Garland science, 2013).
5. Nurmagambetova, A., Mustyatsa, V., Saidova, A. & Vorobjev, I. Morphological and cytoskeleton changes in cells after EMT. *Scientific Reports* **13**, 22164 (2023).
6. Lehmann, B.D., *et al.* Identification of human triple-negative breast cancer subtypes and preclinical models for selection of targeted therapies. **121**, 2750-2767 (2011).
7. Geoffroy, M., *et al.* Pro-apoptotic effect of  $\Delta 2$ -TGZ in “claudin-1-low” triple-negative breast cancer cells: involvement of claudin-1. **165**, 517-527 (2017).
8. Hapach, L.A., *et al.* Phenotypic heterogeneity and metastasis of breast cancer cells. **81**, 3649-3663 (2021).
9. Carpenter, A.E., *et al.* CellProfiler: image analysis software for identifying and quantifying cell phenotypes. *Genome biology* **7**, 1-11 (2006).
10. Lamprecht, M.R., Sabatini, D.M. & Carpenter, A.E. CellProfiler™: free, versatile software for automated biological image analysis. *Biotechniques* **42**, 71-75 (2007).
11. Haralick, R.M., Shanmugam, K. & Dinstein, I.H. Textural features for image classification. *IEEE Transactions on systems, man, and cybernetics*, 610-621 (2007).
12. Leggett, S.E., Hruska, A.M., Guo, M. & Wong, I.Y. The epithelial-mesenchymal transition and the cytoskeleton in bioengineered systems. *Cell Communication and Signaling* **19**, 32 (2021).
13. Felipe Lima, J., Nofech-Mozes, S., Bayani, J. & Bartlett, J.M. EMT in breast carcinoma—a review. *Journal of clinical medicine* **5**, 65 (2016).
14. Dimitrova, Y., *et al.* TFAP2A is a component of the ZEB1/2 network that regulates TGF $\beta$ 1-induced epithelial to mesenchymal transition. *Biology direct* **12**, 1-17 (2017).
15. Song, Y., *et al.* GATA6 is overexpressed in breast cancer and promotes breast cancer cell epithelial–mesenchymal transition by upregulating slug expression. *Experimental and molecular pathology* **99**, 617-627 (2015).

16. Wu, R.-S., *et al.* OVOL2 antagonizes TGF- $\beta$  signaling to regulate epithelial to mesenchymal transition during mammary tumor metastasis. *Oncotarget* **8**, 39401 (2017).
17. Fan, C., *et al.* OVOL1 inhibits breast cancer cell invasion by enhancing the degradation of TGF- $\beta$  type I receptor. *Signal transduction and targeted therapy* **7**, 126 (2022).
18. Wang, Z., *et al.* GRHL2 regulation of growth/motility balance in luminal versus basal breast cancer. *International Journal of Molecular Sciences* **24**, 2512 (2023).
19. Nehme, Z., Roehlen, N., Dhawan, P. & Baumert, T.F. Tight junction protein signaling and cancer biology. *Cells* **12**, 243 (2023).
20. Pei, S., *et al.* The Role of the Fox Gene in Breast Cancer Progression. *International Journal of Molecular Sciences* **26**, 1415 (2025).
21. Le Minh, G., *et al.* Kruppel-like factor 8 regulates triple negative breast cancer stem cell-like activity. *Frontiers in oncology* **13**, 1141834 (2023).
22. Debnath, P., Huirem, R.S., Dutta, P. & Palchaudhuri, S. Epithelial–mesenchymal transition and its transcription factors. *Bioscience reports* **42**, BSR20211754 (2022).
23. Sun, B., Fang, Y., Li, Z., Chen, Z. & Xiang, J. Role of cellular cytoskeleton in epithelial-mesenchymal transition process during cancer progression. *Biomedical reports* **3**, 603-610 (2015).
24. Institute, B. DepMap Portal Website. (2025).
25. Kenny, P.A., *et al.* The morphologies of breast cancer cell lines in three-dimensional assays correlate with their profiles of gene expression. **1**, 84-96 (2007).
26. Abel, J., *et al.* AI powered quantification of nuclear morphology in cancers enables prediction of genome instability and prognosis. *NPJ Precision Oncology* **8**, 134 (2024).
27. Chow, K.-H., Factor, R.E. & Ullman, K.S. The nuclear envelope environment and its cancer connections. *Nature Reviews Cancer* **12**, 196-209 (2012).
28. Singh, I. & Lele, T.P. Nuclear morphological abnormalities in cancer: a search for unifying mechanisms. in *Nuclear, chromosomal, and genomic architecture in biology and medicine* 443-467 (Springer, 2022).
29. Brown, M.S., *et al.* Phenotypic heterogeneity driven by plasticity of the intermediate EMT state governs disease progression and metastasis in breast cancer. *Science advances* **8**, eabj8002 (2022).

30. Phillip, J.M., Han, K.-S., Chen, W.-C., Wirtz, D. & Wu, P.-H. A robust unsupervised machine-learning method to quantify the morphological heterogeneity of cells and nuclei. *Nature protocols* **16**, 754-774 (2021).
31. Kim, D.-H., *et al.* Volume regulation and shape bifurcation in the cell nucleus. *Journal of cell science* **129**, 457-457 (2016).
32. Caicedo, J.C., *et al.* Nucleus segmentation across imaging experiments: the 2018 Data Science Bowl. *Nature methods* **16**, 1247-1253 (2019).
33. Wu, P.-H., *et al.* Evolution of cellular morpho-phenotypes in cancer metastasis. *Scientific reports* **5**, 18437 (2015).
34. Park, J., *et al.* Classification of circulating tumor cell clusters by morphological characteristics using convolutional neural network-support vector machine. *Sensors and Actuators B: Chemical* **401**, 134896 (2024).
35. Ma, J., *et al.* The multimodality cell segmentation challenge: toward universal solutions. *Nature methods* **21**, 1103-1113 (2024).
36. Binder, A., *et al.* Morphological and molecular breast cancer profiling through explainable machine learning. *Nature Machine Intelligence* **3**, 355-366 (2021).
37. Mueller, J.L., *et al.* Rapid staining and imaging of subnuclear features to differentiate between malignant and benign breast tissues at a point-of-care setting. *Journal of Cancer Research and Clinical Oncology* **142**, 1475-1486 (2016).
38. Zuleger, N., Robson, M.I. & Schirmer, E.C. The nuclear envelope as a chromatin organizer. *Nucleus* **2**, 339-349 (2011).
39. Yang, W., Tian, R. & Xue, T. Nuclear shape descriptors by automated morphometry may distinguish aggressive variants of squamous cell carcinoma from relatively benign skin proliferative lesions: a pilot study. *Tumor Biology* **36**, 6125-6131 (2015).
40. Nandakumar, V., *et al.* Isotropic 3D nuclear morphometry of normal, fibrocystic and malignant breast epithelial cells reveals new structural alterations. *PloS one* **7**, e29230 (2012).
41. Munne, P.M., *et al.* TP53 supports basal-like differentiation of mammary epithelial cells by preventing translocation of deltaNp63 into nucleoli. *Scientific Reports* **4**, 4663 (2014).
42. Qu, Y., *et al.* Evaluation of MCF10A as a reliable model for normal human mammary epithelial cells. *PloS one* **10**, e0131285 (2015).

43. Mo, Y., *et al.* Quantitative structured illumination microscopy via a physical model-based background filtering algorithm reveals actin dynamics. *Nature communications* **14**, 3089 (2023).
44. Jerrell, R.J. & Parekh, A.J.A.b. Cellular traction stresses mediate extracellular matrix degradation by invadopodia. **10**, 1886-1896 (2014).
45. Vilchez Mercedes, S.A., *et al.* Decoding leader cells in collective cancer invasion. *Nature Reviews Cancer* **21**, 592-604 (2021).
46. Parlani, M., Jorgez, C. & Friedl, P. Plasticity of cancer invasion and energy metabolism. *Trends in cell biology* **33**, 388-402 (2023).
47. Mayor, R. & Etienne-Manneville, S. The front and rear of collective cell migration. *Nature reviews Molecular cell biology* **17**, 97-109 (2016).

CHAPTER 6

DISTINCT MORPHOLOGICAL SUBTYPES WITHIN THE AGGRESSIVE MDA-MB-231  
BREAST CANCER CELL LINE

---

Higgins, K. S.; Watts, L. B. and Gomillion, C. T. *To be submitted to Biotechnology and Bioengineering.*

## 6.1 Abstract

Tumor heterogeneity is a defining characteristic of many aggressive cancers and is associated with therapeutic resistance and poor prognosis. Even established cell lines like MDA-MB-231 cells, commonly used to model triple-negative breast cancer, display significant phenotypic diversity at the single-cell level. In this study, cell line heterogeneity was investigated by isolating and expanding individual clonal colonies from single MDA-MB-231 cells. Clonal outgrowth revealed a spectrum of growth behaviors and morphologies, including a unique colony (denoted as NC) that exhibited self-aligned, web-like architecture, suggestive of intrinsic collective migration behavior.

High-content imaging and quantitative analysis captured over 300 features related to cell and nuclear morphology, while principal component analysis (PCA) discerned differences in cell shape and nuclear architecture. These components correspond to known indicators of genomic instability, proliferation, and metastatic potential. K-means clustering identified three distinct morphological groups, though some colonies remained unclassifiable due to morphological ambiguity. To assess functional heterogeneity, quantitative impedance-based assays were performed to measure proliferation, cell-to-cell connectivity (transepithelial electrical resistance; TEER), and migration. Impedance and TEER values varied widely across colonies, including those within the same morphological cluster, suggesting that morphology traits alone do not fully predict dynamic behavior in this cell line. Migration rates were generally comparable across colonies, when compared to the parental MDA-MB-231 group, suggesting an alternative migratory strategy previously overlooked by the traditional epithelial-to-mesenchymal transition model.

Together, these findings demonstrate substantial clonal heterogeneity within the MDA-MB-231 cell line and highlight the value of combining single-cell clonal expansion with



morphological and functional profiling. This approach enables the identification of interesting phenotypes, like the self-aligning NC colony, which may hold relevance for understanding collective metastasis behaviors, mechanobiology, and drug resistance in heterogeneous tumor populations.

## 6.2 Introduction

Intratumoral heterogeneity remains one of the most significant challenges in cancer biology, contributing to drug resistance, disease progression, and metastatic spread <sup>1,2</sup>. Among triple-negative breast cancers (TNBC), this heterogeneity is particularly pronounced, with distinct subpopulations within a tumor exhibiting variable behaviors in proliferation, migration, invasiveness, and therapeutic response <sup>3-5</sup>. The MDA-MB-231 cell line, a widely studied model for TNBC, is representative of this complexity, possessing mesenchymal-like features, high motility (as validated in Chapter 5), and significant genetic heterogeneity. Despite its frequent use in mechanistic and therapeutic studies, the degree of functional and morphological diversity that persists in this popular cell line remains underexplored.

Current efforts to understand the implications of cancer cell heterogeneity have turned to clonal isolation strategies, in which individual cells from a parental population are expanded to form daughter colonies <sup>6-10</sup>. This approach allows researchers to uncover subpopulations within a heterogeneous cell line and define population characteristics that may be masked in bulk analyses, providing insights into how heterogeneity affects population behavior and phenotype. The process of clonal expansion can impose selective difficulties, as large cell populations are not easily obtained <sup>11</sup>, and the relationship between observable morphological traits and underlying cellular function remains complex and incompletely understood. Therefore, this study uses small cell populations to quantify both cell morphology traits and their dynamic behaviors.

High-throughput image analysis and subsequent morphometric feature quantification has been previously shown to act as a unique readout of cell phenotypic behaviors <sup>6,12,13</sup>. Using the morphology analysis principles outlined in Chapter 5, subtle variations in nuclear architecture, cell shape, and cytoskeletal organization can be captured. These features can then be linked to

biological processes like proliferation, chromosomal instability, and epithelial-to-mesenchymal transition (EMT), which play critical roles in tumor progression <sup>14-17</sup>. Furthermore, clustering techniques can help categorize morphologically distinct subpopulations, potentially defining deeper genomic patterns and epigenetic differences within the parental cell line <sup>6,13</sup>.

Yet morphology alone cannot capture the full spectrum of cancer cell metastatic behavior. Therefore, quantitative bioelectronic assays that can provide real-time insights into dynamic properties like cell proliferation, adhesion, and barrier formation complement cell morphology information well <sup>18-20</sup>. When combined with wound healing or migration assays, as done in Chapters 3 and 4, these tools offer a broader perspective on how structural traits relate to key behaviors relevant to migration and metastasis. Discrepancies between morphological classification and functional output highlight the need to integrate both static and dynamic phenotyping to more accurately define cell states.

In this context, the present study explores phenotypic and functional diversity within clonal colonies derived from the MDA-MB-231 line. By combining morphometric profiling, unsupervised clustering, and impedance-based functional analysis, we aim to deepen our understanding of how heterogeneity manifests at the single-cell level, and how it may contribute to broader patterns of behavior in aggressive breast cancers.

## **6.3 Materials and Methods**

### **6.3.1 Cell Culture**

MDA-MB-231 cells were obtained from the American Type Culture Collection (ATCC) and maintained at 37 °C in a humidified atmosphere with 5% CO<sub>2</sub>. Both the parental cell line and derived clonal colonies were cultured in Dulbecco's Modified Eagle Medium (DMEM; Gibco)

supplemented with 10% fetal bovine serum (FBS; R&D Systems) and 1% penicillin-streptomycin (P/S; Gibco), denoted as DMEM-complete. For the impedance-based wound healing assay, a nutrient-reduced medium was used, consisting of DMEM supplemented with 2% FBS and 1% P/S. The parental cell line was verified to be free of mycoplasma contamination using a commercially available detection kit (InvivoGen).

### 6.3.2 Isolating MDA-MB-231 Clonal Colonies

Clonal colonies were derived from passage 7 of the parental MDA-MB-231 cell line. Cells in the logarithmic phase of growth were detached using 0.05% Trypsin-EDTA (Gibco), and the resulting cell pellet was resuspended and serially diluted to a final concentration of 1,000 cells/mL. A volume of 1  $\mu$ L of this diluted suspension was seeded into each well of a 96-well plate (Corning). Wells were inspected using an EVOS FL Digital Inverted Fluorescence Microscope (Invitrogen), and those containing a single cell were documented. Subsequently, 200  $\mu$ L of DMEM-complete was added to each selected well. Media was changed every three days to minimize cell disturbance. Colonies were allowed to grow until a dense patch formed, at which point they were transferred to a 24-well plate. Cells were progressively expanded to 6-well plates and eventually to T-75 flasks. A portion of each colony was used for cell staining and imaging, while the remaining cells were cryopreserved for future use.

### 6.3.3 Cell Staining and Imaging

Cells were seeded into black-walled 96-well plates (Corning) at a density of 10,000 cells/cm<sup>2</sup> to enhance contrast between cell borders and facilitate identification of cytoskeletal projections. After a 15-hour incubation to allow for attachment and spreading, cells were fixed

with 4% paraformaldehyde (PFA; Thermo Fisher) in phosphate-buffered saline (PBS; Gibco) for 30 minutes at room temperature, followed by two PBS washes. Permeabilization and staining were performed using a solution containing 1% (v/v) Tween-20 (Sigma-Aldrich), 10 µg/mL Hoechst 33342 (Thermo Fisher) for nuclear labeling, and 1 µg/mL Fluorescein-5-Maleimide (Thermo Fisher) for cell protein visualization. Cells were incubated in this staining solution for 1 hour at room temperature, protected from light. After staining, cells were rinsed with PBS, and fluorescence imaging was performed using the Cytation 1 Cell Imaging Multimode Reader (Agilent Biotek). Each well was imaged using a 4×4 montage (16 fields of view) for both nuclear (DAPI) and cellular (GFP) channels, resulting in 32 images per well and a total of 3,072 images per colony.

#### 6.3.4 Image Analysis with CellProfiler™

After image acquisition, high-throughput single-cell morphological analysis was performed on individual cells using CellProfiler™ (Broad Institute), an open-source image analytical platform. The custom pipeline developed in Chapter 5 was used to quantify morphological features from each cell colony. Image metadata, including cell colony and location, were embedded, and DAPI and GFP channels were merged to generate overlaid images. These images were aligned and cropped to uniform size and illumination was normalized within each cell line dataset using the background and applied with a median smoothing filter.

Cell processing and segmentation was performed as described in Chapter 5. For reference and segmentation verification, overlay images showing segmented cell and nuclear boundaries were generated and exported. All extracted data and associated metadata were stored in SQL database files. These databases were processed in Rstudio (Posit), where filtering steps were

applied to remove segmentation artifacts. Objects smaller than 500 pixels<sup>2</sup> were excluded to prevent any false cell identification, and only isolated (non-touching) cells (i.e. those with zero recorded neighbors) were retained for further analysis. The final datasets were exported to Excel for downstream statistical analysis.

#### 6.3.5 Principal Component Analysis of CellProfiler™ Data

Following cell morphology quantification in CellProfiler™, individual cell measurements were aggregated into per-well mean values using RStudio to account for cell-to-cell variability. A similarity matrix of CellProfiler features was generated using Morpheus (Broad Institute), and features with a high Pearson correlation coefficient ( $r \geq 0.90$ ) were removed to reduce multicollinearity and minimize risk of model overfitting. This filtering resulted in 45 retained features describing cell and nuclear shape, stain intensity, and texture. Z-scores were then calculated for the per-well averages, and features with absolute z-scores greater than 3 ( $|z| > 3$ ) were classified as outliers and excluded from further analysis. This threshold identifies extreme values while preserving the core data distribution, assuming approximate normality. Finally, principal component analysis (PCA) was conducted in RStudio to reduce dimensionality. PCA loadings, scores, and eigenvalues were analyzed to interpret the contribution of retained features to morphological variation.

#### 6.3.6 Clustering Clonal Colonies

Principal components 1 through 10 were used to cluster clonal colonies into morphologically distinct groups. Four clustering algorithms were evaluated: k-means clustering, hierarchical clustering, density-based spatial clustering, and Gaussian mixture modeling. Among

these, k-means clustering with a cluster size of three provided the best fit, as determined by silhouette analysis (see Supplementary Figure D.1). Various distance metrics were tested within the k-means framework, including Euclidean, Manhattan, Mahalanobis, and cosine distances, but all resulted in similar clustering outcomes. Two clonal colonies, designated NH and MA, did not cluster consistently and exhibited data points distributed across all three groups. As a result, these colonies were excluded from further analysis to maintain a focus on morphologically distinct and well-defined clusters.

#### 6.3.7 Impedance-based Proliferation and Migration Assay

Cell proliferation, barrier integrity, and migration were evaluated as described in Chapter 3 using the Maestro Z system (Axion Biosystems). Wells were coated with 21.3  $\mu$ M poly-D-lysine (Sigma-Aldrich) in deionized water to promote cell adhesion. Cell colonies were seeded at a density of 90,000 cells/cm<sup>2</sup> in complete DMEM growth medium. Once confluence was reached, the medium was replaced with a nutrient-reduced formulation. After 12 hours, a scratch was introduced to each well, followed by a medium change with fresh nutrient-reduced medium. Cell impedance and TEER data were exported from the Axis Z software to evaluate proliferation, barrier function, and migration rates, following the same analytical procedures detailed in Chapter 3.

#### 6.3.8 Univariate Statistical Analysis

Violin plots were generated using GraphPad Prism (version 10.2), and statistical significance was assessed using one-way ANOVA. Individual morphology features were

normalized to the mean of the normal 184B5 cell line to highlight relative increases or decreases in comparison to the control group.

## **6.4 Results**

### **6.4.1 Observed Differences in Clonal Colony Growth and Behavior**

A total of 13 clonal colonies were isolated and expanded from a mycoplasma-free population of MDA-MB-231 cells, as illustrated in Figure 6.1. During expansion, clear visual differences in growth behavior emerged among colonies. While some wells seeded with a single cell failed to proliferate beyond a few cells over a 25 day period, others quickly developed into dense patches within the 96-well plates (Figure 6.1A). The degree of patch density varied, suggesting differential abilities of clonal groups to migrate and spread across the growth surface. In addition to differences in single-cell morphology, distinct growth patterns were observed across colonies. Notably, one colony (denoted as NC) exhibited an organized, web-like alignment pattern (Figure 6.1B, right image), unlike the more disorganized morphology seen in others. Quantitative morphological analysis using CellProfiler confirmed measurable differences between colonies. These are visualized in a heatmap representing all 330 features analyzed (Figure 6.2B). Based on these findings, dimensionality reduction was subsequently applied to further explore and characterize the diversity among clonal colonies.



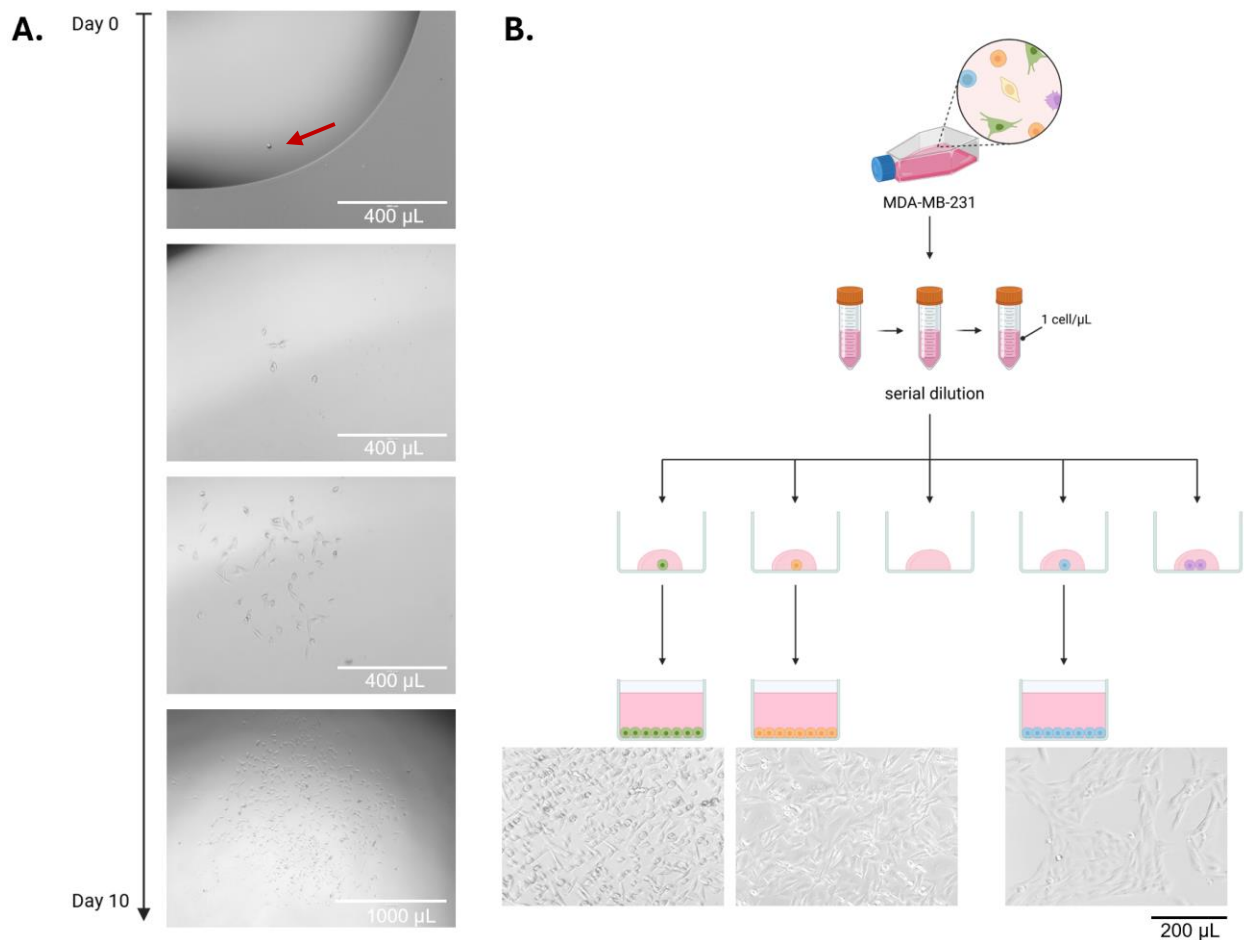


**Figure 6.1:** Clonal colony expansion. A) Representative images showing the expansion of a colony from a single cell (marked with a red arrow) over a 10-day period. B) Illustration of the procedure for growing clonal colonies from the parental MDA-MB-231 cell line. A cell suspension was serially diluted to achieve a final concentration of 1,000 cell/mL. A 1  $\mu$ L droplet was placed into each well, and wells containing a single cell were cultured to form colonies. The images at the bottom highlight the different cell morphologies and growth patterns observed across various colonies.

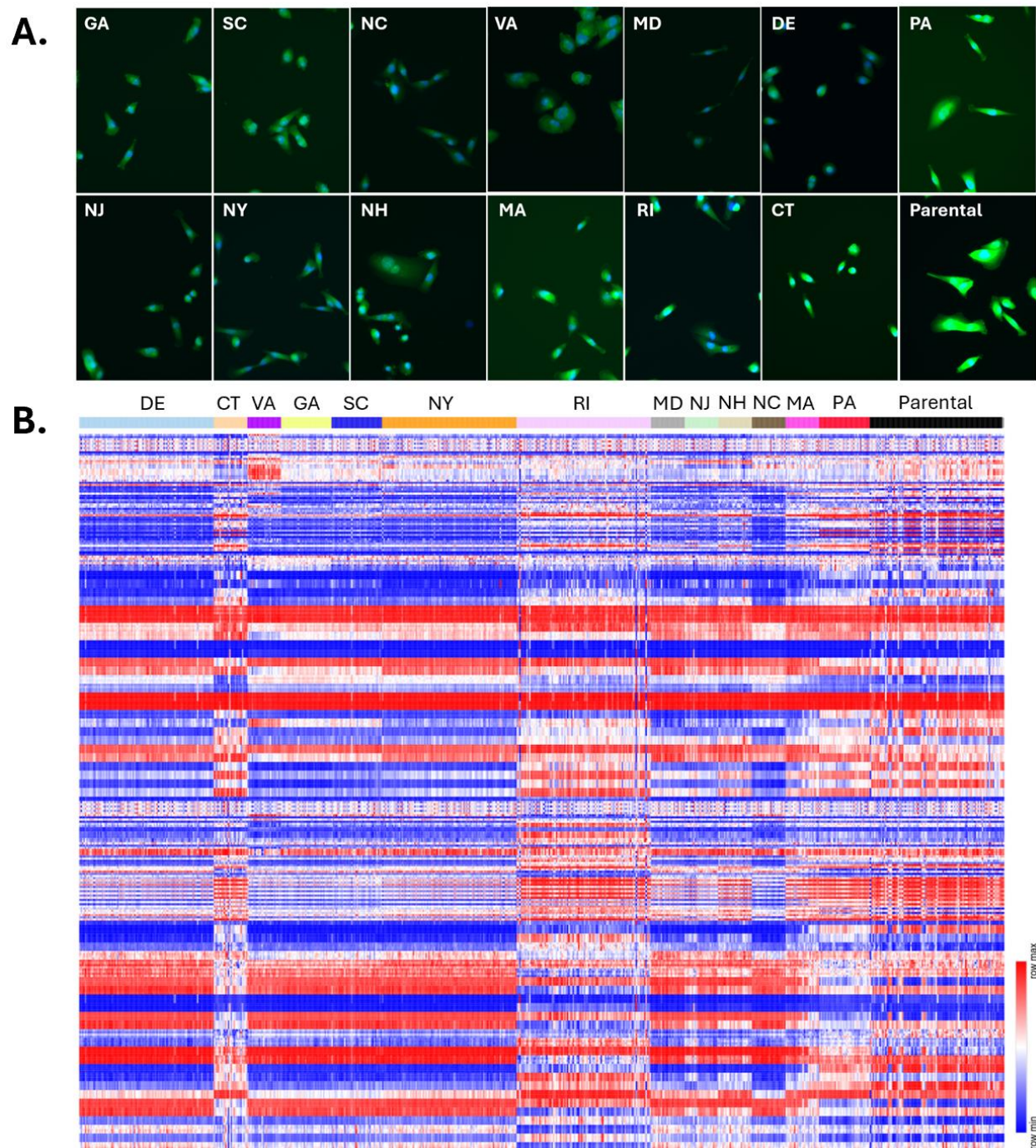


**Figure 6.2:** Clonal colony characterization using CellProfiler. A) Representative images of clonal colonies alongside the parental MDA-MB-231 cell line. B) Heatmap summarizing morphological features extracted via the CellProfiler pipeline. Each column represents the average z-score for a single well, grouped by colony identity, while each row corresponds to one of 330 quantified cellular or nuclear features.

#### 6.4.2 Morphological Variation Among Clonal Colonies Mapped by PCA

After eliminating variable redundancy using a similarity matrix, 45 features related to cell and nuclear morphology were selected for principal component analysis (PCA). When plotting the two most significant components, PC1 and PC2, clonal colonies were distributed across all quadrants (Figure 6.3A), indicating a wide range of morphological diversity. Analysis of the features contributing to each principal component revealed that PC1 was primarily associated with nuclear morphology, while PC2 was more closely related to cellular morphology. Lower PC1 values, observed in the parental cell line and colonies RI, PA, and CT, were significantly correlated with high nuclear entropy and irregular nuclear shapes, potentially reflecting disorganized or heterogeneous chromatin structure. In contrast, higher PC1 values, seen in colonies DE, VA, GA, SC, NY, and NC, were linked to increased nuclear stain intensity, greater texture variance, and larger or more structured nuclei. These features suggest that PC1 may capture differences in nuclear activity or chromatin organization, potentially reflecting variations in proliferation, genomic instability, and metastatic potential.

PC2, on the other hand, was strongly influenced by cell shape descriptors like perimeter and eccentricity. Colonies with higher PC2 scores, including the parental MDA-MB-231 cell line, exhibited more elongated and irregular cell shapes, indicative of a more mesenchymal-like morphology. In contrast, lower PC2 scores were associated with rounder, more compact cells, suggesting lower migratory or invasive potential. To explore these interpretations further, colonies were grouped based on their morphological profiles derived from PCA, and dynamic cellular behaviors were subsequently assessed using the impedance-based assay developed in Chapter 3.

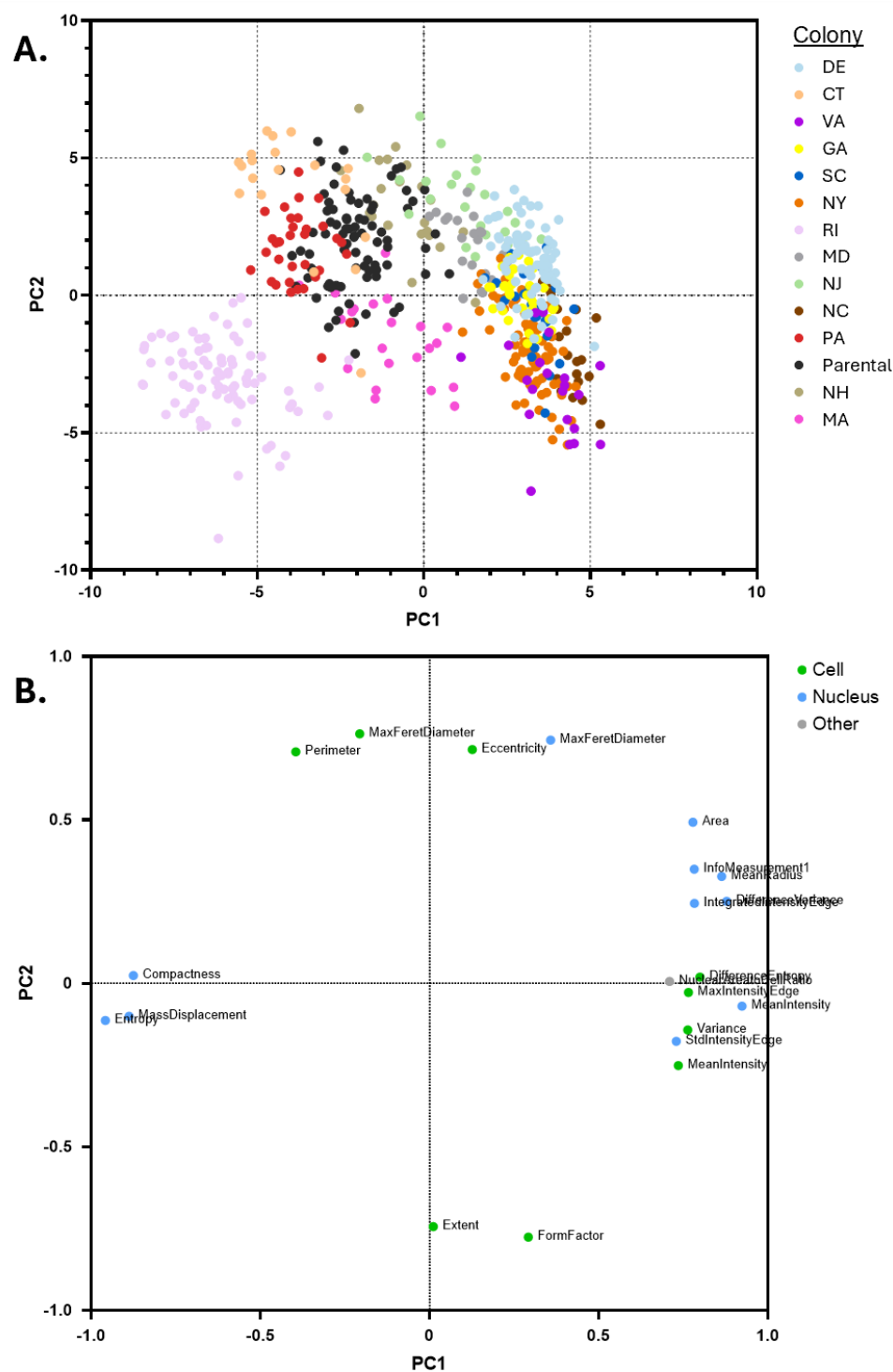


**Figure 6.3:** Principal component analysis (PCA) of morphological features in MDA-MB-231 clonal colonies. A) Scatter plot of the first two principal components (PC1 and PC2), illustrating morphology-based clustering of individual clonal colonies. Data points are color-coded by colony identity. B) Loadings plot for PC1 and PC2, showing morphological features with absolute loading scores > 0.7. Features are color-coded by type: cell-related (green), nucleus-related (blue), and other (gray).

### 6.4.3 Clonal Colonies Cluster into Three Distinct Morphological Groups

To categorize clonal colonies based on morphological features, multiple clustering algorithms were evaluated, including k-means clustering, hierarchical clustering, density-based clustering, and Gaussian mixture modeling. These methods were compared using silhouette scores, which assess how well each data point fits within its assigned cluster (Supplementary Figure D.1). The analysis identified k-means clustering with three clusters as the best-fitting model. When k-means clustering was applied to the PCA-transformed dataset using the first 10 principal components, three well-separated morphological groups emerged, with most colonies being clearly classified (Figure 6.4). Two colonies, NH and MA, did not cluster cleanly, displaying data points scattered across all three groups. Therefore, these colonies were excluded from further analysis due to their morphological ambiguity.

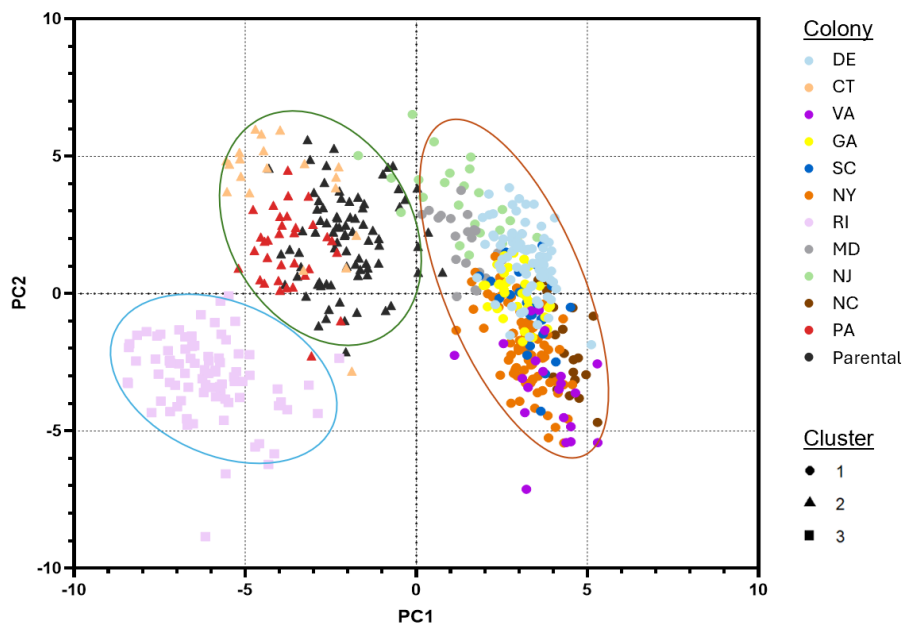


**Figure 6.4:** Morphology-based grouping of clonal colonies via k-means clustering. K-means clustering ( $k = 3$ ) was applied to PCA-transformed morphological data to classify clonal colonies into distinct groups based on cell and nuclear features. Colonies NH and MA were excluded from clustering due to inconsistent morphology and lack of clear cluster assignment.

#### 6.4.4 Impedance Analysis Reveals Functional Heterogeneity Among Clonal Colonies

To investigate dynamic cellular behaviors and assess the relationship between 2D morphology and functional traits like motility, impedance-based measurements were performed using our developed quantitative wound healing assay. Impedance and TEER were recorded at the point immediately prior to the wound scratch, when cell colonies had reached maximum confluence (Figure 6.5A, B). High-frequency impedance (41.5 kHz) serves as an indicator of cell proliferation and surface coverage, while TEER indicates cell-to-cell connectivity.

Both impedance and TEER values varied across clonal colonies, demonstrating heterogeneity, not only between individual lines, but also within morphologically defined clusters. Notably, all clonal groups deviated from the parental MDA-MB-231 cell line, though the direction and magnitude of these differences were inconsistent. Some colonies exhibited higher impedance and TEER values than the parental line, while others were lower, suggesting that functional behavior does not uniformly track with morphological traits.

Migration rate, measured post-scratch (Figure 6.5C), showed only modest variation across clonal colonies. Colonies SC and VA exhibited increased migratory activity, whereas RI and MD showed reduced migration relative to the parental line. Regardless, overall differences in migration rates were limited, indicating that most clonal colonies retained comparable motility to the heterogeneous parental population. These results suggest that dynamic cell behaviors like proliferation, migration, and cell-to-cell connectivity do not correlate strongly with the morphological clusters identified in this study.

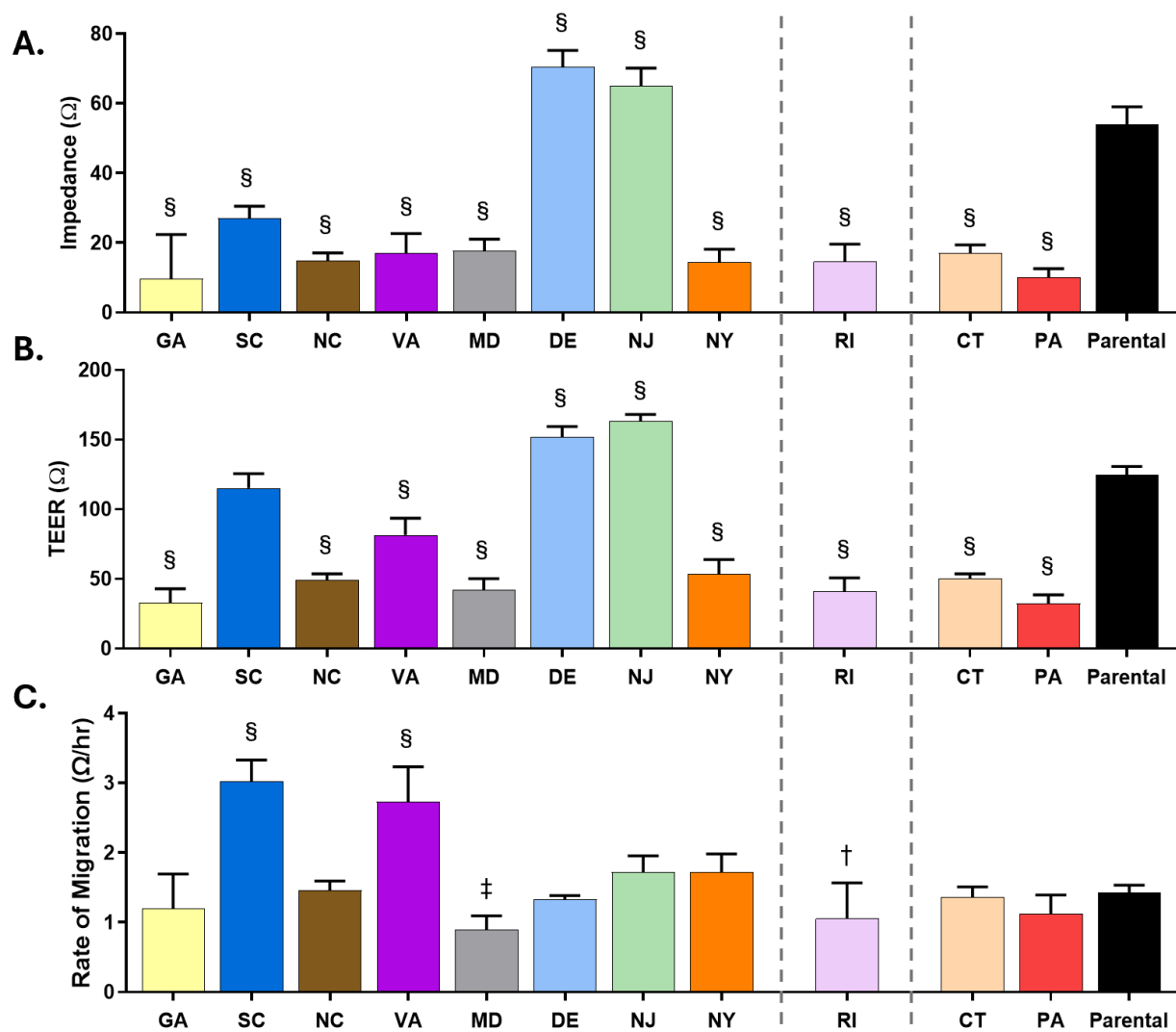


**Figure 6.5:** Functional differences among clonal colonies in proliferation, barrier integrity, and migration. A) Impedance measurements at confluence, reflecting cell proliferation and surface coverage. B) Transepithelial electrical resistance (TEER) at confluence, indicating cell-to-cell barrier integrity. C) Migration rate over 36 hours, calculated as the change in impedance over time ( $\Omega/\text{hour}$ ). Dotted lines delineate morphology-based groupings defined by k-means clustering. Each data point represents an average from 10–12 wells per colony or parental line. Statistical significance compared to the parental MDA-MB-231 line: †  $p < 0.05$ , ‡  $p < 0.01$ , §  $p < 0.0001$ .

## 6.5 Discussion

Differences were observed among colony behavior, even during the expansion process. The varying growth patterns and single-cell morphologies among the colonies reflect the diversity present in the heterogeneous parental MDA-MB-231 cell line. It is important to note that some



cells failed to expand into colonies, which could be attributed to several factors. First, successful expansion requires cells to be proliferative. However, as previously discussed, aggressive cancer cells often exhibit a tradeoff between proliferation and migration <sup>21</sup>. Cells with a more migratory phenotype may not thrive under standard culture conditions or achieve sufficient proliferation to form colonies. Additionally, population age may play a role, as even immortalized cell lines can show signs of genetic drift after long-term growth. These observations highlight an important consideration when using clonal expansion methods. Not all cells are equally capable of clonal outgrowth, and their failure to expand may carry biological significance related to metabolic status. Flow cytometry cell sorting offers an alternative means of separation and has previously been used to distinguish MDA-MB-231 cells based on EMT-related markers <sup>22</sup>. While this approach would reduce the number of population doublings required to obtain sufficient cell numbers, it would not yield the same degree of homogeneity as clonal isolation.

In addition to the single-cell differences observed across colonies, notable differences in growth patterns were also recorded. Most prominently, the NC clonal group exhibited a unique tendency to grow in highly aligned, web-like patches (Supplementary Figure D.2). Although this feature was not captured by our fluorescent image-analysis pipeline, due to its focus on non-touching, individually stained cells, it was clearly visible during colony expansion. This alignment likely reflects more than just a structural artifact. Rather, it may indicate an intrinsic cellular behavior reminiscent of collective migration, a process increasingly associated with migration and metastatic potential <sup>23-26</sup> that has been previously studied in MDA-MB-231 cells <sup>27</sup>. Notably, this organized behavior emerged even in the absence of exogenous extracellular matrix components, suggesting that these cells may be intrinsically predisposed to sense or replicate the aligned architecture of collagen fibers commonly found in the tumor microenvironment. Collagen



alignment has been shown to facilitate directional invasion, and tumor cells that preferentially align *in vitro* may exploit similar structures *in vivo*<sup>28,29</sup>. Thus, the NC clonal group's self-alignment could serve as a surrogate marker for an invasive phenotype, potentially driven by cytoskeletal dynamics, cell-cell adhesion, or altered mechanotransduction pathways. Future studies could explore this further by culturing these cells on ECM-mimicking substrates, performing live-cell imaging, or conducting an in-depth migration study, potentially uncovering key links between *in vitro* self-organization and *in vivo* aggressiveness.

PCA of quantified cell properties revealed notable variation between the parental MDA-MB-231 cell line and its daughter colonies. PC1 primarily captured features related to nuclear morphology, including differences in nuclear size, border irregularity, staining intensity, and texture. These traits are often associated with proliferation status, genomic instability, and metastatic potential. For example, enlarged nuclei suggest increased DNA content (polyploidy), which has been linked to heightened aggressiveness and drug resistance<sup>30</sup>. Similarly, increased nuclear texture may reflect chromosomal instability, another hallmark of metastatic capability<sup>15,31,32</sup>.

PC2 was more indicative of overall cell shape. Higher PC2 scores corresponded to elongated cell morphologies with pronounced cytoskeletal protrusions, while lower PC2 scores, like those observed in the RI colony, indicated a rounder and less elongated form. Despite this variation, all colonies originated from the MDA-MB-231 parental line, which has a mesenchymal-like, elongated phenotype (as established in Chapter 5). Thus, even the most circular colonies in this study remain more mesenchymal than epithelial, particularly when compared to mammary cell lines such as MDA-MB-453 examined in earlier chapters.

K-means clustering of morphological data grouped colonies into three distinct clusters. However, colonies NH and MA did not cluster cleanly. This could suggest that these colonies exhibit more average or intermediate nuclear morphology, particularly given their relatively low PC1 scores. Alternatively, their distribution across multiple clusters may indicate underlying heterogeneity within the colony itself, potentially arising from point mutations or subtle genomic shifts. Due to this clustering ambiguity, NH and MA were excluded from further analysis involving impedance measurements.

Impedance and TEER measurements varied across all colonies—even among those assigned to the same morphological cluster. Within the largest cluster (Cluster 1), significant differences emerged: colonies DE and NJ exhibited notably higher impedance and TEER values compared to the parental line, suggesting greater surface coverage and enhanced cell-cell connectivity. In contrast, other colonies within the same cluster (GA, SC, NC, MD, and NY) showed significantly lower values than the parental line. These discrepancies may partially reflect differences in growth rates. Although all colonies were seeded at equal density, they reached confluence at varying times (see Supplementary Figure D.3). Overall, migration rates were not significantly different for most colonies relative to the parental line, suggesting that the MDA-MB-231 cells may engage distinct or previously underappreciated mechanisms of migration that are not captured by traditional assays.

In the future, refinements in colony isolation methods could improve experimental consistency and reduce degradation over time. For example, future work might involve using lower passage numbers to derive colonies, limiting expansion periods, or employing alternative isolation techniques. While clonal colonies derived from the MDA-MB-231 line clearly demonstrate underlying heterogeneity within the parental population, this heterogeneity was not directly linked

to differences in migration potential in the current study. However, certain clonal populations, like the self-aligning NC colony, may represent promising models for future investigation. These colonies could be studied individually to explore specific mechanisms of cell migration, such as collective migration dynamics or interactions with collagen-aligned matrices.

## **6.6 Conclusion**

This study highlights the significant phenotypic and functional heterogeneity that exists within a single, widely used breast cancer cell line (MDA-MB-231). Results show that, through clonal expansion and quantitative profiling, even cells derived from the same tumor population can diverge in morphology and behavior dynamics. While dimensionality reduction and clustering techniques allowed for the identification of distinct morphological subtypes, an impedance-based analysis demonstrated that morphology alone does not fully predict cellular behavior. These findings underscore the importance of integrating both structural and dynamic phenotyping to better understand tumor cell heterogeneity. Future work would best be suited towards understanding the specific migration mechanisms and pathways of one or two select colonies. Together, these observations reinforce the value of clonal analysis in cancer metastasis research and suggest that cell-intrinsic heterogeneity could play a critical role in shaping tumor progression, therapeutic response, and metastatic capacity.

## 6.7 References

1. Zou, Y., *et al.* The single-cell landscape of intratumoral heterogeneity and the immunosuppressive microenvironment in liver and brain metastases of breast cancer. *Advanced Science* **10**, 2203699 (2023).
2. Wu, S.Z., *et al.* A single-cell and spatially resolved atlas of human breast cancers. *Nature genetics* **53**, 1334-1347 (2021).
3. Zhou, S., *et al.* Single-cell RNA-seq dissects the intratumoral heterogeneity of triple-negative breast cancer based on gene regulatory networks. *Molecular Therapy Nucleic Acids* **23**, 682-690 (2021).
4. So, J.Y., Ohm, J., Lipkowitz, S. & Yang, L. Triple negative breast cancer (TNBC): Non-genetic tumor heterogeneity and immune microenvironment: Emerging treatment options. *Pharmacology & therapeutics* **237**, 108253 (2022).
5. Oshi, M., *et al.* Immune cytolytic activity is associated with reduced intra-tumoral genetic heterogeneity and with better clinical outcomes in triple negative breast cancer. *American journal of cancer research* **11**, 3628 (2021).
6. Wu, P.-H., *et al.* Single-cell morphology encodes metastatic potential. **6**, eaaw6938 (2020).
7. Khan, G.N., Kim, E.J., Shin, T.S. & Lee, S.H. Heterogeneous cell types in single-cell-derived clones of MCF7 and MDA-MB-231 cells. *Anticancer Research* **37**, 2343-2354 (2017).
8. Kang, Y., *et al.* A multigenic program mediating breast cancer metastasis to bone. *Cancer cell* **3**, 537-549 (2003).
9. Nguyen, A., Yoshida, M., Goodarzi, H. & Tavazoie, S.F. Highly variable cancer subpopulations that exhibit enhanced transcriptome variability and metastatic fitness. *Nature communications* **7**, 11246 (2016).
10. Brix, N., Samaga, D., Belka, C., Zitzelsberger, H. & Lauber, K. Analysis of clonogenic growth in vitro. *Nature protocols* **16**, 4963-4991 (2021).
11. Kapadia, C.D., *et al.* Clonal dynamics and somatic evolution of haematopoiesis in mouse. *Nature*, 1-9 (2025).
12. Alizadeh, E., *et al.* Cellular morphological features are predictive markers of cancer cell state. *Computers in biology and medicine* **126**, 104044 (2020).

13. Bemmerlein, L., *et al.* Decoding single cell morphology in osteotropic breast cancer cells for dissecting their migratory, molecular and biophysical heterogeneity. *Cancers* **14**, 603 (2022).
14. Binder, A., *et al.* Morphological and molecular breast cancer profiling through explainable machine learning. *Nature Machine Intelligence* **3**, 355-366 (2021).
15. Singh, I. & Lele, T.P. Nuclear morphological abnormalities in cancer: a search for unifying mechanisms. in *Nuclear, chromosomal, and genomic architecture in biology and medicine* 443-467 (Springer, 2022).
16. Yang, W., Tian, R. & Xue, T. Nuclear shape descriptors by automated morphometry may distinguish aggressive variants of squamous cell carcinoma from relatively benign skin proliferative lesions: a pilot study. *Tumor Biology* **36**, 6125-6131 (2015).
17. Nurmagambetova, A., Mustyatsa, V., Saidova, A. & Vorobjev, I. Morphological and cytoskeleton changes in cells after EMT. *Scientific Reports* **13**, 22164 (2023).
18. Anwer, S. & Szaszi, K. Measuring cell growth and Junction Development in epithelial cells using electric cell-substrate impedance sensing (ECIS). *Bio-protocol* **10**, e3729-e3729 (2020).
19. Biosystems, A. Impedance - General. Vol. 2024 (Author, Axionbiosystems.com, 2024).
20. Biosystems, A. Axis Z User Guide. in *Software Manual for the Maestro Impedance System* (Author, 2021).
21. Ahmed, M. & Kim, D.R. Life history dynamics of evolving tumors: insights into task specialization, trade-offs, and tumor heterogeneity. *Cancer Cell International* **24**, 364 (2024).
22. Fietz, E.R., *et al.* Glucocorticoid resistance of migration and gene expression in a daughter MDA-MB-231 breast tumour cell line selected for high metastatic potential. *Scientific reports* **7**, 43774 (2017).
23. Debets, V.E., Janssen, L.M. & Storm, C. Enhanced persistence and collective migration in cooperatively aligning cell clusters. *Biophysical journal* **120**, 1483-1497 (2021).
24. Basan, M., Elgeti, J., Hannezo, E., Rappel, W.-J. & Levine, H. Alignment of cellular motility forces with tissue flow as a mechanism for efficient wound healing. *Proceedings of the National Academy of Sciences* **110**, 2452-2459 (2013).
25. Zisis, T., *et al.* Disentangling cadherin-mediated cell-cell interactions in collective cancer cell migration. *Biophysical Journal* **121**, 44-60 (2022).

26. Stehbens, S.J., Scarpa, E. & White, M.D. Perspectives in collective cell migration—moving forward. *Journal of Cell Science* **137**, jcs261549 (2024).
27. Zhang, X., Chan, T. & Mak, M. Morphodynamic signatures of MDA-MB-231 single cells and cell doublets undergoing invasion in confined microenvironments. *Scientific reports* **11**, 6529 (2021).
28. Gurrula, R., *et al.* Quantifying breast cancer-driven fiber alignment and collagen deposition in primary human breast tissue. *Frontiers in Bioengineering and Biotechnology* **9**, 618448 (2021).
29. Koorman, T., *et al.* Spatial collagen stiffening promotes collective breast cancer cell invasion by reinforcing extracellular matrix alignment. *Oncogene* **41**, 2458-2469 (2022).
30. Zhou, X., *et al.* Polyploid giant cancer cells and cancer progression. *Frontiers in Cell and Developmental Biology* **10**, 1017588 (2022).
31. Abel, J., *et al.* AI powered quantification of nuclear morphology in cancers enables prediction of genome instability and prognosis. *NPJ Precision Oncology* **8**, 134 (2024).
32. Zuleger, N., Robson, M.I. & Schirmer, E.C. The nuclear envelope as a chromatin organizer. *Nucleus* **2**, 339-349 (2011).

## CHAPTER 7

### CONCLUDING REMARKS AND RECOMMENDATIONS FOR FUTURE WORK

#### 7.1 Concluding Remarks

Breast cancer (BC) metastasis remains one of the leading causes of cancer-related deaths among women. There is a significant need to better understand the fundamental mechanisms driving metastasis, particularly the complex phenotypic changes that tumor cells undergo during disease progression. A deeper understanding of these processes could lead to earlier detection of metastatic cells and improved therapeutic strategies.

One key mechanism implicated in metastasis is the epithelial-to-mesenchymal transition (EMT), during which epithelial-like cells, typically cuboidal in shape and tightly adhered to the basement membrane, adopt a more elongated, mesenchymal-like morphology. This transformation is closely associated with increased motility and invasiveness. EMT plays a central role in tumor progression by linking changes in cell shape to alterations in gene expression, phenotype, and metastatic behavior. Because morphology is both highly indicative of cellular state and relatively easy to quantify, it serves as a valuable proxy for studying the molecular underpinnings of cancer progression. Still, the exact relationship between cell shape and metastatic potential remains incompletely understood.

This dissertation investigates that relationship by analyzing single-cell morphology both across various breast cancer cell lines and within a highly aggressive subpopulation. The goal is to identify measurable morphological features that correlate with metastatic behavior. To achieve

this, we developed a novel approach that combines Electric Cell-substrate Impedance Sensing (ECIS) with high-throughput imaging to more precisely and objectively characterize cancer cell traits.

A key advantage of this methodology is its compatibility with small cell populations, making it highly relevant for clinical applications where tissue biopsies often yield limited material. Our approach enables the assessment of cell morphology, growth dynamics, migration, and response to external stimuli using fewer than two million cells, well within the range typically obtained from patient-derived samples.

The resulting dataset provides new insights into the cellular features that influence breast cancer metastasis, while also offering a scalable framework for evaluating cancer cell behavior. By capturing detailed morphological and biophysical profiles from minimal sample input, this work supports the development of more efficient and clinically applicable diagnostic tools.

Overall, this dissertation advances the goal of establishing robust, quantitative methods for assessing breast cancer aggressiveness. Through the integration of impedance- and image-based analyses, it highlights the diagnostic and research potential of single-cell morphology in understanding and predicting metastatic progression.

Chapter 2 reviewed current *in vitro* modeling techniques used to study breast cancer metastasis, with an emphasis on cell invasion and spread within mammary tissue. While 2D models cannot fully replicate the complexity of the human body, they offer valuable advantages, such as precise control of experimental variables and compatibility with high-throughput analysis methods like automated imaging. These features make 2D systems particularly suitable for preliminary cell analysis and large-scale screening.



Additionally, the chapter highlighted 3D modeling approaches, including bioprinting and microfluidics, which better mimic physiological conditions such as dynamic flow, extracellular matrix composition, and cell–cell interactions. Despite these strengths, 3D systems face limitations, like high costs (e.g., bioinks in bioprinting) and a lack of standardization. Thus, choosing the appropriate model depends heavily on the specific research question. As research demands evolve, there is a pressing need to refine existing models and develop new platforms that improve reproducibility, enable more accessible data quantification, and support personalized cancer modeling.

Towards the goal of enhancing quantification, the chapter introduced bioelectronic assays as a promising technique. While these assays may lack the specificity of some biochemical methods, they allow for continuous, non-invasive monitoring of cell behavior and require only small cell populations, making them ideal for studies involving patient-derived biopsy samples. The remaining chapters build on this foundation, aiming to quantify mammary cell characteristics and validate single-cell morphology as a meaningful readout of cancer aggressiveness and metastatic potential. The work is conducted in 2D systems to leverage their compatibility with machine learning pipelines and impedance-based migration measurements.

Chapter 3 presented a preliminary bioelectronic assessment of breast cancer cell proliferation and motility, establishing impedance sensing as a reliable, non-invasive method to evaluate metastatic behavior. This approach streamlines wound-healing assays by enabling real-time, quantitative monitoring of cell migration. Three breast cancer cell lines were analyzed for spread, proliferation, barrier integrity, and migratory capacity. Additionally, responses to leptin, a proinflammatory cytokine, demonstrated the sensitivity of impedance measurements in detecting cell behavior changes. These findings aligned with previous migration studies and further

emphasized leptin's role in promoting proliferation and weakening cell–cell barriers, highlighting the potential of bioelectronic assays for broader adoption in cancer research.

Chapter 4 expanded upon the impedance-based approach by applying the developed protocols to a panel of eight mammary cell lines with varying metastatic tendencies. Quantitative measurements revealed distinct behavioral patterns aligned with known levels of aggressiveness. Notably, MDA-MB-453 cells exhibited high migratory activity despite maintaining epithelial morphology, challenging the assumption that epithelial-to-mesenchymal transition (EMT) status alone determines metastatic potential. These results underscore the value of integrating dynamic impedance measurements and TEER with traditional morphological assessments, advocating for a more nuanced and multi-parametric evaluation of metastatic capacity. This chapter laid the groundwork for integrating machine learning and image-based phenotyping to further enhance assessment precision.

Chapter 5 introduced high-throughput image analysis combined with machine learning to evaluate single-cell morphology as a predictive marker of cancer cell function. Using the same eight cell lines from Chapter 4, cell morphology metrics were extracted from cellular- and nuclear-stained images via CellProfiler. These features were then correlated with migration behavior and EMT status. The analysis identified key morphological traits, including cell elongation, nuclear irregularity, and cell protein texture, that effectively differentiated between normal and cancerous cells and between mesenchymal and epithelial phenotypes. These findings validated morphology as a high-dimensional, quantifiable proxy for aggressive behavior and highlighted image-based phenotyping as a powerful method for characterizing functional heterogeneity in breast cancer.

Chapter 6 built upon previous findings by assessing heterogeneity within a single aggressive cell line, the triple-negative MDA-MB-231 cell line. Thirteen sub-populations were

derived via low-density seeding and analyzed for both morphology and dynamic behavior. K-means clustering of morphological features identified three distinct groups with varying structural profiles. Subsequent impedance measurements revealed functional diversity among these sub-clones, including differences in proliferation, migration, and barrier integrity, but ultimately did not correlate with morphology groupings. These findings demonstrate that significant heterogeneity can exist even within a well-characterized cell line, emphasizing the importance of sub-clonal analysis in understanding metastatic potential.

Collectively, this work presents a comprehensive overview of breast cancer metastasis modeling and introduces a multi-faceted framework that integrates bioelectronic impedance sensing, high-throughput image analysis, and machine learning. This combinatorial approach enables more nuanced and scalable assessments of metastatic behavior, offering new avenues for both research and clinical application in personalized cancer modeling.

Altogether, this work highlights a broader opportunity to bridge experimental biology with computational analysis in healthcare research. While machine learning tools are increasingly applied to biological datasets, these tools are often developed without a deep understanding of the cellular mechanisms that generate the data. By integrating biologically grounded measurements, such as cell morphology, dynamic cell behaviors, and gene expression, this study demonstrates how computational pipelines can be informed through biological and mechanistic insight. This approach enhances both the interpretability and relevance of machine learning outputs, ultimately supporting the development of more effective and clinically meaningful models. As precision medicine continues to evolve, these interdisciplinary strategies will be essential for advancing personalized diagnostics and therapeutic decision-making. This dissertation therefore contributes

not only to cancer research, but also to the growing intersection of data science and experimental biology, an area with vast potential for future discovery.

## **7.2 Recommendations for Future Work**

The studies presented in this dissertation contribute to the validation of single-cell morphology as a meaningful readout associated with cancer aggressiveness and metastatic potential. To further expand and strengthen these findings, several directions for future work are recommended.

### **7.2.1 Validate Findings Across Additional Mammary Cell Lines**

This study offers a detailed look at a broad set of mammary cell lines, with a particular focus on triple-negative breast cancer. While we were able to identify meaningful patterns, like connections between cell shape and dynamic behaviors, the ability to measure how strong or reliable these patterns are is limited. This is mainly due to the small sample sizes, as in the limited number of cell lines used, which make it harder to apply statistical tools that typically help confirm whether such patterns are likely to hold up across broader datasets (confidence intervals, etc.). To address this, future studies should expand the current cell line panel to include additional cells, particularly those found in the peritumoral microenvironment (e.g. fibroblasts). This would allow for a more robust analysis of motility, morphology, and the ability to distinguish cell types within a heterogeneous population. A suggested list of additional cell lines is provided in Supplementary Table E.1.

### 7.2.2 Alternative Methods for Evaluating Cancer Cell Aggressiveness

In this study, 2D migration served as the primary metric for evaluating cancer cell aggressiveness and metastatic potential. This method, while widely used and easily quantifiable via impedance measurements, captures only the initial step of metastatic escape from the primary tumor<sup>1-4</sup>. Nonetheless, recent studies have questioned its clinical relevance as a predictor of *in vivo* metastatic behavior<sup>5-9</sup>. For example, subpopulations of MDA-MB-231 cells with low migratory ability have still demonstrated metastatic competence when injected into mammary fat pads of SCID mice<sup>10</sup>. Other research has identified mechanisms by which weakly migratory cancer cells can stimulate stromal cells through microvesicle signaling and enhance dissemination<sup>11</sup>. In all, these findings emphasize that migration alone may not fully capture metastatic potential.

To address this limitation, it is recommended that future work incorporate assays that better mimic the tumor microenvironment and more complex steps of the metastatic cascade, such as intravasation. One promising approach is to use an impedance-based endothelial barrier disruption assay (methods described in Appendix E). In a preliminary study, human umbilical vein endothelial cells (HUVECs) were cultured on a collagen IV-coated electrode plate to simulate the basement membrane and endothelial layer. Cancer cell lines were then seeded onto this monolayer, and changes in barrier integrity were measured via TEER (trans-endothelial electrical resistance), as shown in Figure 7.1. Notably, while MDA-MB-231 cells caused significant and sustained barrier disruption, MDA-MB-453 cells, despite showing high migration in earlier assays (Chapter 4), had no measurable effect on HUVEC integrity. This highlights the importance of using complementary metrics to assess aggressiveness.

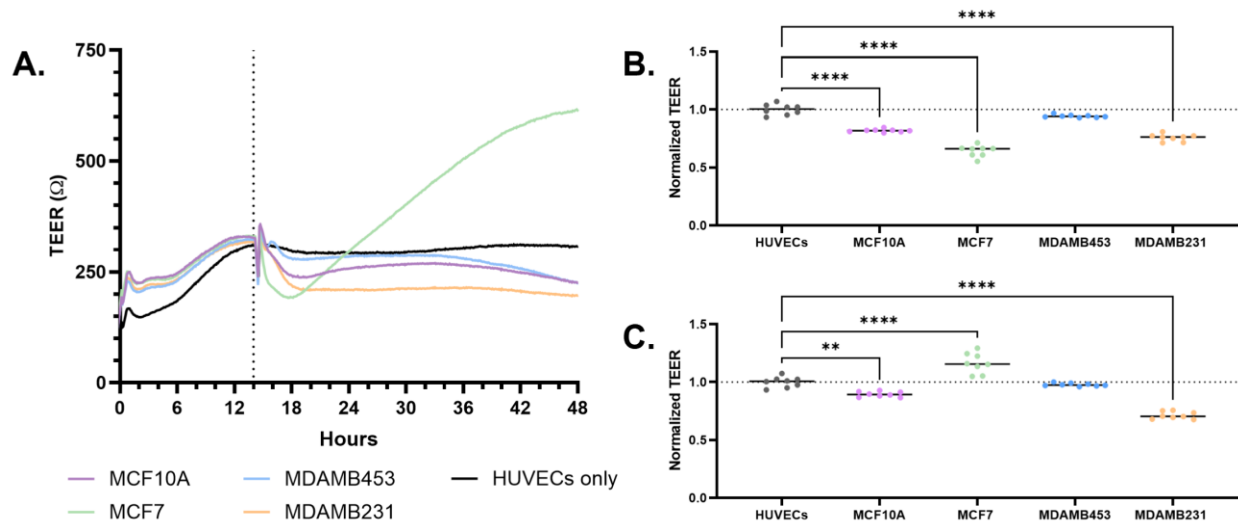


**Figure 7.1:** Breast cancer cells disrupt endothelial barrier integrity. A) Trans-endothelial electrical resistance (TEER) measurements over time for a monolayer of human umbilical vein endothelial cells (HUVECs). The HUVEC monolayer formed during the initial 13 hours. At this point (indicated by the grey line), cancer cell lines (MCF7, MDA-MB-453, MDA-MB-231) or the non-cancerous control line (MCF10A) were introduced. Barrier integrity was monitored for an additional 35 hours. Undosed wells (HUVECs only) served as a control. B) TEER values 3 hours after cell dosing, normalized to the average TEER of the undosed HUVEC control group. C. TEER values after 12 hours of dosing, also normalized to the undosed control. (n = 8)

Interestingly, MCF10A (a non-tumorigenic control) induced modest barrier disruption, suggesting that minimal TEER changes are not exclusive to malignant cells. MCF7 cells initially decreased barrier integrity but later appeared to increase it. This dynamic behavior could be due to paracrine signaling, possibly involving VEGF secretion by MCF7 cells, prompting HUVECs to reinforce their junctions via reciprocal signaling<sup>12</sup>. Alternatively, the observed TEER increase might be a measurement artifact resulting from MCF7 cells spreading over the HUVEC layer and increasing electrical resistance. This hypothesis could be tested using live-cell staining and imaging of the co-culture system. Overall, these preliminary findings support the utility of this assay in assessing metastatic potential beyond migration alone.

### 7.2.3 A Closer Look into Migration Mechanisms and Their Morphological Expression

Beyond evaluating alternatives to migration-based assays, future studies should also focus on understanding the specific mechanisms of migration and if they are morphologically linked. In Chapter 6, clonal analysis suggested that collective migration may support the high motility observed in MDA-MB-231 cells. In collective migration, invasive leader cells coordinate movement with non-invasive follower cells, an emerging concept in metastatic progression<sup>13,14</sup>.

Leader cells often display a hybrid epithelial–mesenchymal phenotype, featuring mesenchymal-like cytoskeletal restructuring at the leading edge and retained epithelial cell-to-cell junctions, and epithelial characteristics at the trailing edge<sup>15</sup>. Morphological signatures of this phenotype could be identified using Haralick texture features, as discussed in Chapter 5, to quantify cytoskeletal organization and reorganization with an F-actin stain like phalloidin. These techniques could be applied across cell lines or within specific clones to explore the mechanistic underpinnings of collective migration and their association with quantifiable cell features.

### 7.2.4 Further Exploration of Clonal Development and Intra-cell Line Heterogeneity

Finally, clonal analysis should be expanded to include a wider range of cell lines and more comprehensive characterization metrics. Isolating clones from additional aggressive lines, like HCC1806, and BT-549, would enable the recognition of broader trends related to cancer cell heterogeneity. It is also advised to use ultra-low passage parental lines and to minimize clonal expansion, maintaining clonal integrity and reducing the risk of genetic drift.

In addition to expanding the number of clonal colonies, deeper characterization of each clonal population would enhance the interpretation of observed phenotypes. Proteomic and transcriptomic profiling could provide molecular context for behavioral differences between

clones, even among those with similar morphologies. These high-dimensional datasets could be analyzed using PCA, clustering, or other modeling approaches introduced in Chapters 5 and 6. Clonal forming efficiency (CFE), which reflects the proportion of single cells that form colonies, can provide insight into clonogenic potential and may correlate with the presence of cancer stem-like cells<sup>16</sup>. Lastly, doubling time and growth rates are straightforward measurements of proliferative capacity that could be linked to migratory and invasive behaviors.

Taken together, these recommendations outline a multifaceted path forward for building upon this dissertation work. Expanding cell line diversity, incorporating alternative functional assays, dissecting migration mechanisms, and deepening clonal characterization will collectively refine our understanding of how cell morphology relates to cancer aggressiveness and metastatic behavior.



### 7.3 References

1. Palmer, T.D., Ashby, W.J., Lewis, J.D. & Zijlstra, A. Targeting tumor cell motility to prevent metastasis. *Advanced drug delivery reviews* **63**, 568-581 (2011).
2. Van Zijl, F., Krupitza, G. & Mikulits, W. Initial steps of metastasis: cell invasion and endothelial transmigration. *Mutation Research/Reviews in Mutation Research* **728**, 23-34 (2011).
3. Fares, J., Fares, M.Y., Khachfe, H.H., Salhab, H.A. & Fares, Y. Molecular principles of metastasis: a hallmark of cancer revisited. *Signal transduction and targeted therapy* **5**, 28 (2020).
4. Liu, Z., *et al.* Cancer cells display increased migration and deformability in pace with metastatic progression. *The FASEB Journal* **34**, 9307-9315 (2020).
5. Tormoen, G.W., Cianchetti, F.A., Bock, P.E. & McCarty, O.J. Development of coagulation factor probes for the identification of procoagulant circulating tumor cells. *Frontiers in Oncology* **2**, 110 (2012).
6. Padmanaban, V., *et al.* E-cadherin is required for metastasis in multiple models of breast cancer. *Nature* **573**, 439-444 (2019).
7. Fietz, E.R., *et al.* Glucocorticoid resistance of migration and gene expression in a daughter MDA-MB-231 breast tumour cell line selected for high metastatic potential. *Scientific reports* **7**, 43774 (2017).
8. Chen, A., *et al.* Reduction in migratory phenotype in a metastasized breast cancer cell line via downregulation of S100A4 and GRM3. *Scientific reports* **7**, 3459 (2017).
9. Johnstone, C.N., *et al.* Functional and genomic characterisation of a xenograft model system for the study of metastasis in triple-negative breast cancer. *Disease models & mechanisms* **11**, dmm032250 (2018).
10. Hapach, L.A., *et al.* Phenotypic heterogeneity and metastasis of breast cancer cells. **81**, 3649-3663 (2021).
11. Schwager, S.C., *et al.* Weakly migratory metastatic breast cancer cells activate fibroblasts via microvesicle-Tg2 to facilitate dissemination and metastasis. *Elife* **11**, e74433 (2022).
12. Azzarito, G., Visentin, M., Leeners, B. & Dubey, R.K. Transcriptomic and functional evidence for Differential effects of MCF-7 breast Cancer cell-secretome on vascular and lymphatic endothelial cell growth. *International Journal of Molecular Sciences* **23**, 7192 (2022).

13. Vilchez Mercedes, S.A., *et al.* Decoding leader cells in collective cancer invasion. *Nature Reviews Cancer* **21**, 592-604 (2021).
14. Parlani, M., Jorgez, C. & Friedl, P. Plasticity of cancer invasion and energy metabolism. *Trends in cell biology* **33**, 388-402 (2023).
15. Leggett, S.E., Hruska, A.M., Guo, M. & Wong, I.Y. The epithelial-mesenchymal transition and the cytoskeleton in bioengineered systems. *Cell Communication and Signaling* **19**, 32 (2021).
16. Brix, N., Samaga, D., Belka, C., Zitzelsberger, H. & Lauber, K. Analysis of clonogenic growth in vitro. *Nature protocols* **16**, 4963-4991 (2021).

## APPENDIX A

### SUPPLEMENTARY MATERIALS FOR CHAPTER 3

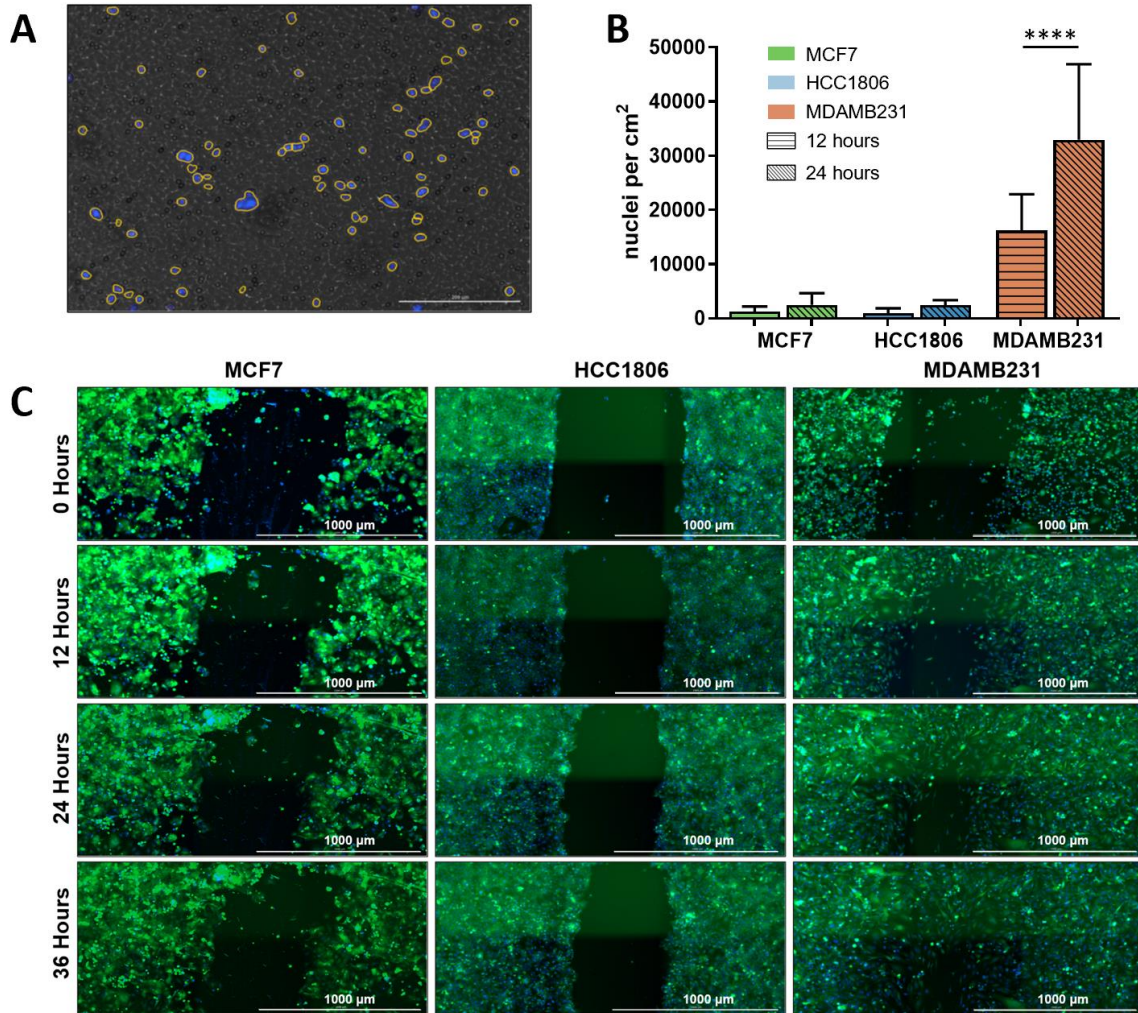


**Figure A.1:** A) Example of an image of nuclei (blue) migrated to through the transwell membrane. The top of the insert was swabbed to remove the non-migrated cells so only the migrated cells were left. The HCC1806 nuclei were counted using Gen5 software's object count analysis, adding a yellow border around each counted nucleus. B) Quantitative results of the transwell migration object count for 12 and 24 hours. \*\*\*\* indicates a statistically significant comparison where  $p > 0.0001$ . (n=12 images for each cell line/timepoint) C) Stitched images of wound closure of cell monolayers using a traditional wound healing method, where cells are stained green and nuclei are blue.



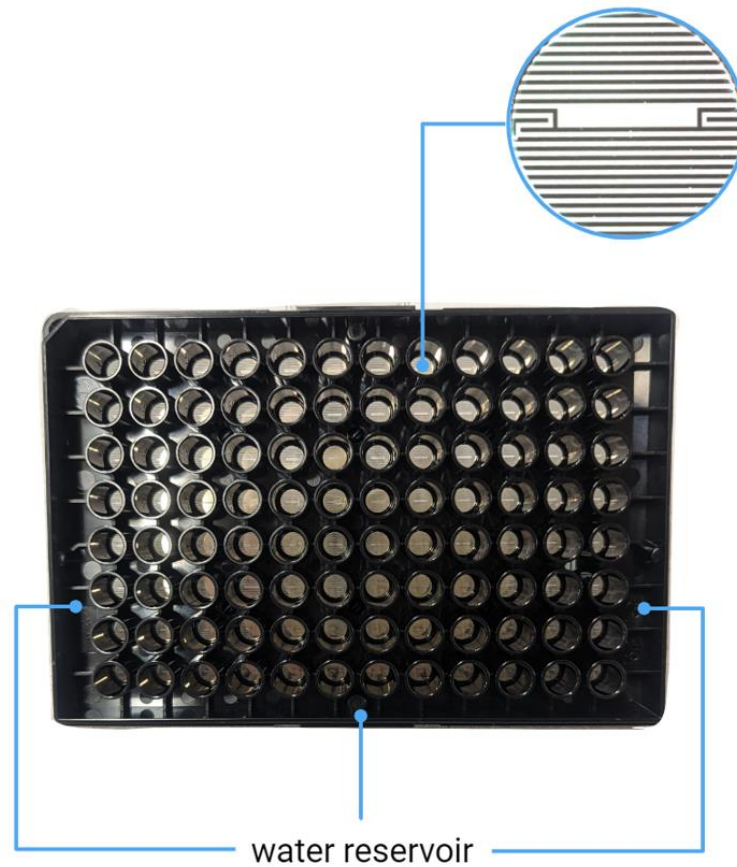


**Figure A.3:** Cytoview-Z plate. Each well contains one gold electrode on the culture surface, with a viewing window in the middle to visualize/image cells (top). To maintain humidity and minimize edge effects, the wells are bordered by a water reservoir (bottom).

## APPENDIX B

### SUPPLEMENTARY MATERIALS FOR CHAPTER 4

**Table B.1:** Nutrient reduced media formulations

Cell Line	Basal Media	Growth Supplements	Nutrient-reduced Supplements
184B5 (CRL-8799)	MEBM	MEGM SingleQuots (without GA-1000), 1 ng/mL CTX	-
MCF10A (CRL-10317)	MEBM	MEGM SingleQuots (without GA-1000), 100 ng/mL CTX	-
MCF7 (HTB-22)	DMEM	10% FBS, 1% P/S, 0.01 mg/mL insulin	2% FBS, 1% P/S
MDA-MB-453 (HTB-131)	DMEM	10% FBS, 1% P/S	2% FBS, 1% P/S
HCC70 (CRL-2315)	RPMI	10% FBS, 1% P/S	2% FBS, 1% P/S
HCC1806 (CRL-2335)	DMEM	10% FBS, 1% P/S	2% FBS, 1% P/S
MDA-MB-231 (HTB-26)	DMEM	10% FBS, 1% P/S	2% FBS, 1% P/S
BT-549 (HTB-122)	RPMI	10% FBS, 1% P/S	2% FBS, 1% P/S

Abbreviations: MEBM, Mammary Epithelial Basal Media; MEGM, Mammary Epithelial Growth Media; CTX, cholera toxin; DMEM, Dulbecco's Modified Eagle Media; FBS, fetal bovine serum; P/S, penicillin/streptomycin; RPMI, Roswell Park Memorial Institute Media

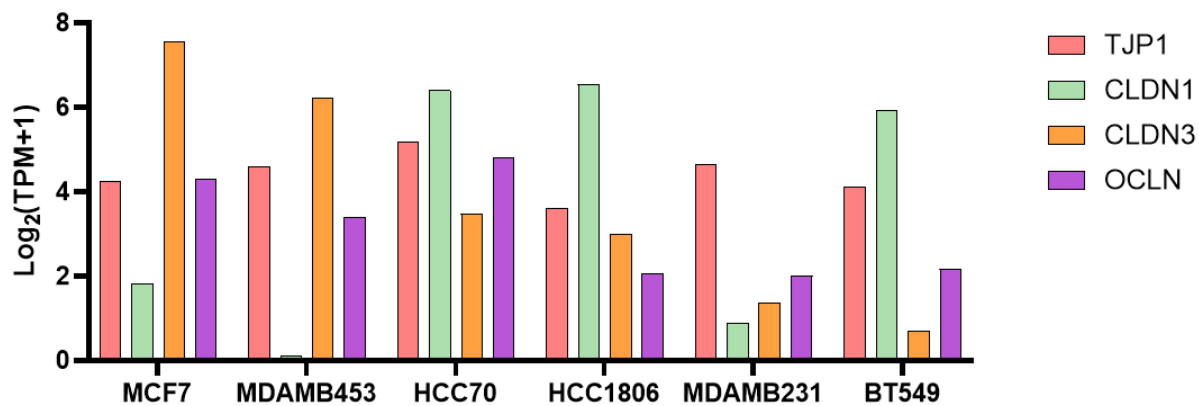


**Figure B.1:** Expression of tight junction-associated genes in each breast cancer cell line, sourced from the DepMap Portal. RNA-seq gene expression values are shown as  $\log_2(\text{TPM} + 1)$ , where TPM denotes transcripts per million. TJP1 corresponds to Zonula Occludens-1 (ZO-1); CLDN1 and CLDN3 represent claudins 1 and 3, respectively; OCLN denotes occludin.

## APPENDIX C

### SUPPLEMENTARY MATERIALS FOR CHAPTER 5

**Table C.1:** Significant features measured with CellProfiler

Feature	PC1 Interpretation
<i>Area/Shape Features</i>	
Extent	Ratio of the object's area to the area of its bounding box; measures how well the object fills its bounding box.
Form Factor	Calculated as $4 \cdot \pi \cdot \text{Area} / \text{Perimeter}^2$ ; A circularity measure where 1 indicates a perfectly circular object.
Max Feret Diameter	The longest distance between any two points along the object's boundary; a measure of object length.
Area	Total number of pixels within the object's boundary; represents object size.
Compactness	Measure of how densely packed the object is. A filled circle will have a compactness of 1, with irregular objects or objects with holes having a value greater than 1.
Mean Radius	The mean distance from the object's centroid to its boundary.
Cell-to-Nuclear Area Ratio	Ratio of the cell area to the nuclear area; indicates the relative size difference between nucleus and the cytoplasm not overlapping with the nucleus.
<i>Intensity Features</i>	
Mass Displacement	Distance between the intensity-weighted centroid and the geometric centroid; reflects asymmetry in intensity distribution.
MAD Intensity	Median Absolute Deviation of pixel intensities; a robust measure of intensity variation within the object.
Max Intensity	Maximum pixel intensity within the object; indicates the brightest pixel.
<i>Haralick Texture Features</i>	
Difference Entropy	Feature from Haralick analysis that quantifies local intensity contrast within an image.
Entropy	Feature measuring randomness or complexity in intensity values; higher entropy implies more complexity.
Variance	Measure of intensity dispersion or spread in the object's pixel values.
Correlation	Feature indicating the linear dependency of grey levels between neighboring pixels.
Info Measurement 1	Feature that quantifies how much information one can predict from the neighboring pixel intensities.



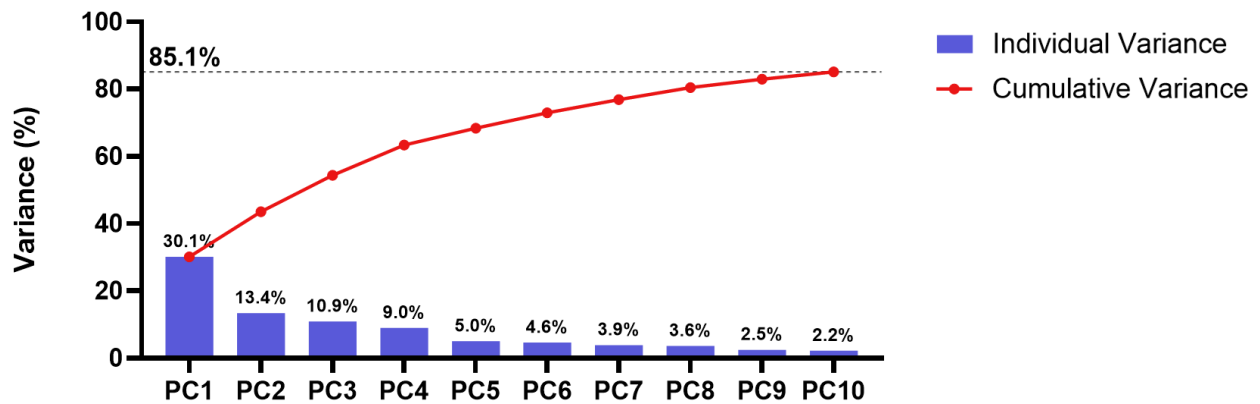


**Figure C.1:** Cumulative and individual variance explained by the first 10 principal components (PCs). Together, these PCs account for 85.1% of the total variance in the dataset. The bars represent the individual variance explained by each PC, while the line indicates the cumulative variance.

## APPENDIX D

### SUPLEMENTARY MATERIALS FOR CHAPTER 6

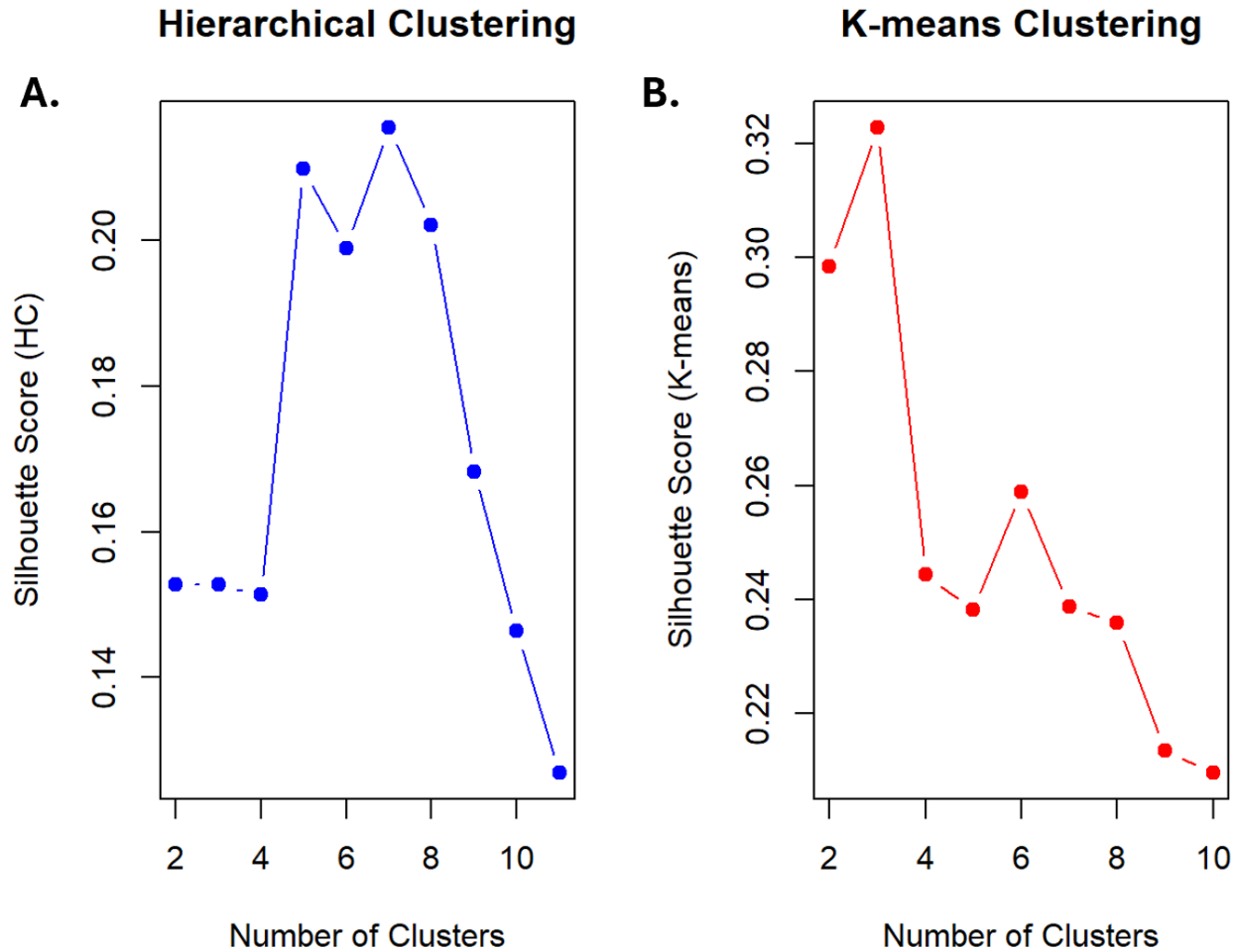


**Figure D.1:** Evaluation of Clustering Methods Using Silhouette Scores. Silhouette scores for A) hierarchical and B) k-means clustering across a range of cluster numbers (2–11). The highest silhouette score was observed for k-means clustering with  $k = 3$ , indicating that this method and cluster number best fit the PCA-transformed morphological data.

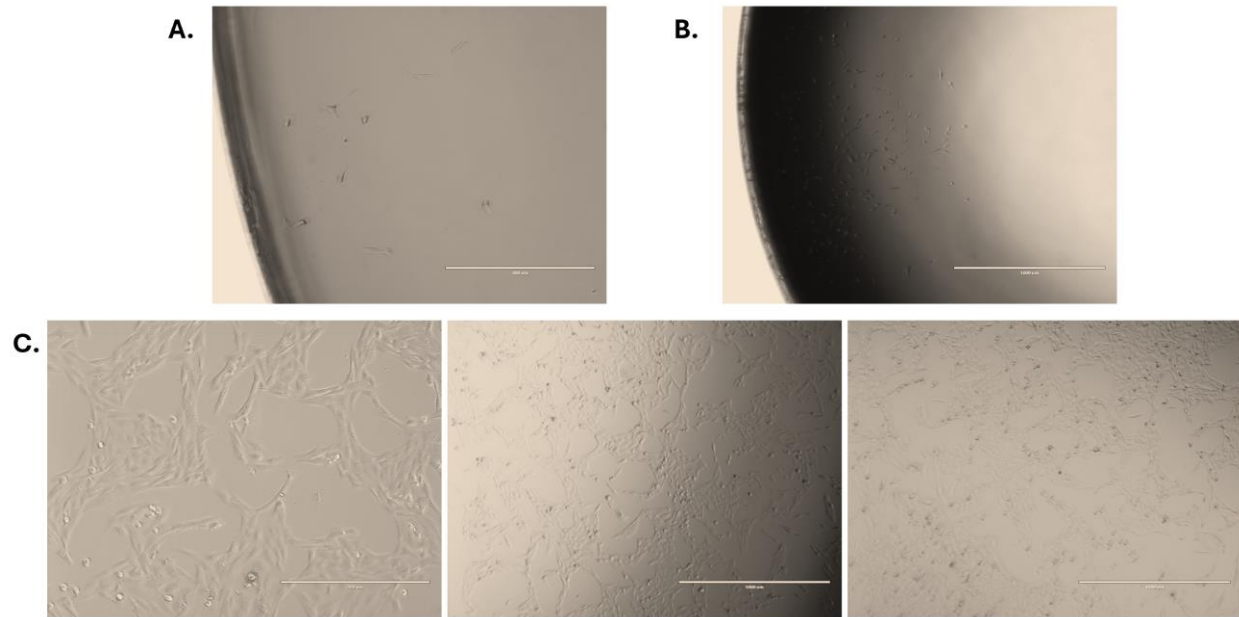


**Figure D.2:** NC clonal colony expansion over time. A. Cell growth observed 4 days after single-cell seeding. B. Colony expansion at 10 days in culture, showing increased cell density. C. Colony morphology at 23 days, where cells exhibit self-alignment along the tissue culture polystyrene surface.

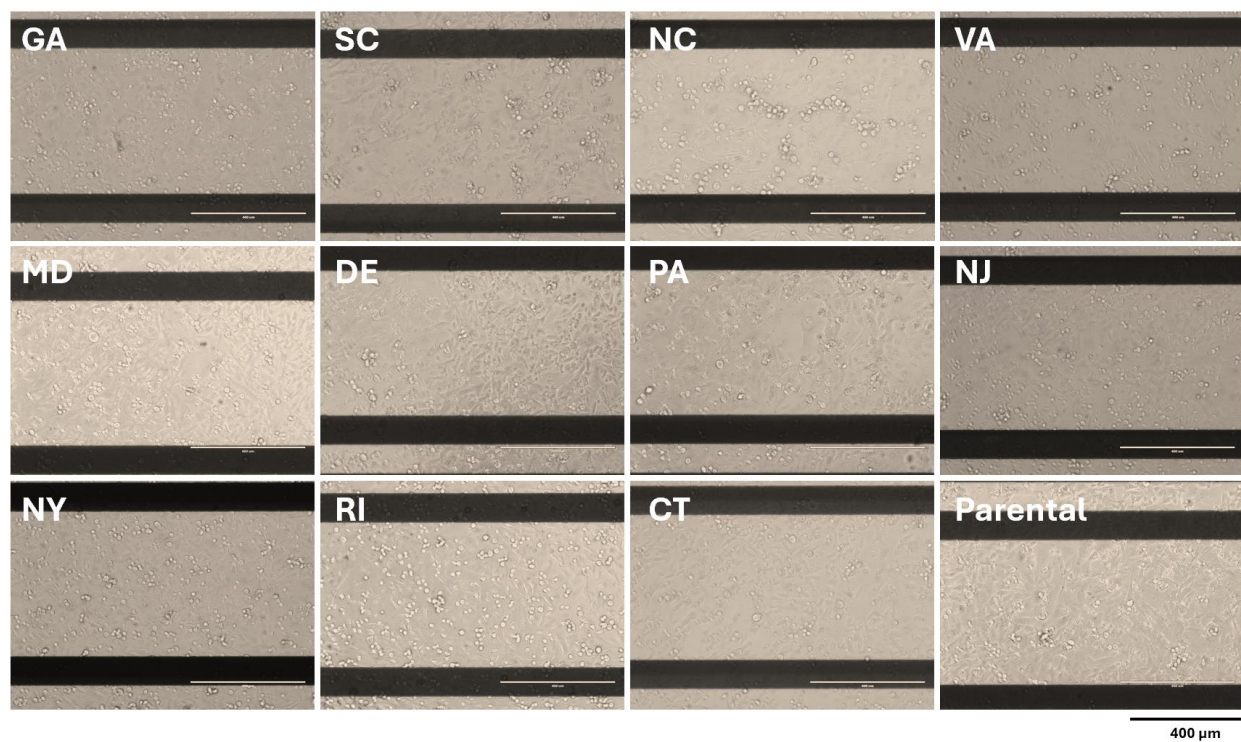


**Figure D.3:** Representative bright phase images of clonal colonies. Images are taken from the viewing window of the Cytoview-Z plate, immediately prior to creating the scratch.

## APPENDIX E

### SUPPLEMENTARY MATERIALS FOR CHAPTER 7

**Table E.1:** Additional cell lines to include in future work

<b>Cell Line</b>	<b>Cell Type</b>
Hs27 (HTB-122)	Fibroblast
AG11132 (from Coriell Institute)	Epithelial
BT-20 (HTB-19)	Carcinoma TNBC
MDA-MB-468 (HTB-131)	Adenocarcinoma TNBC
MDA-MB-436 (HTB-122)	Adenocarcinoma TNBC
MDA-MB-157 (HTB-24)	Carcinoma, Medullary TNBC
Hs 578T (HTB-122)	Carcinoma TNBC

Abbreviations: TNBC, Triple-negative breast cancer

## **E.1 Supporting Methods**

### **E.1.1 HUVEC and Mammary Cell Culturing**

Human umbilical vein endothelial cells (HUVECs; CC-2519, Lonza) were cultured in Endothelial Cell Growth Medium-2 (EGM-2; Lonza) following the manufacturer's protocol. To prevent degradation from repeated warming and cooling, the necessary volume of EGM-2 was aliquoted at a time and warmed in a water bath only once per use. Mammary cell lines MCF10A, MCF7, MDA-MB-453, and MDA-MB-231 were cultured in their respective standard growth media, as detailed in Appendix B, Table B.1.

### **E.1.2 Experimental Seeding and Impedance Analysis**

Each well of a 96-well CytoView-Z impedance plate (Axion Biosystems) was coated with 50  $\mu$ L of a 50  $\mu$ g/mL collagen IV solution (Abcam), prepared in sterile glacial acetic acid (Sigma-Aldrich). The plate was incubated at room temperature for one hour and then washed with phosphate-buffered saline (PBS; Gibco). Following this, the plate was inserted into the Maestro-Z impedance system (Axion Biosystems) to collect a media-only baseline, as outlined in Chapter 3. HUVECs were seeded at a density of 70,000 cells/cm<sup>2</sup>. According to Lonza's guidelines, complete endothelial barrier formation occurs within 12 to 16 hours. After 13 hours, TEER measurements confirmed barrier establishment, indicating a stable monolayer. At this point, the plate was undocked and brought to the biosafety hood for dosing with the mammary cell lines. 100  $\mu$ L of media were removed from each well and mammary cells (MCF10A, MCF7, MDA-MB-453, MDA-MB-231) were added at a density of 10,000 cells/cm<sup>2</sup> in fresh EGM-2 to dose the wells. Undosed control wells received 100  $\mu$ L of fresh EGM-2 to serve as vehicle-only HUVEC controls.

The plate was subsequently returned to the Maestro-Z instrument, and changes in trans-endothelial electrical resistance (TEER) were monitored continuously for an additional 35 hours.